Distributed Fiber Optics Sensing for Crack Monitoring of Concrete Structures

Antoine Bassil

To cite this version:

Antoine Bassil. Distributed Fiber Optics Sensing for Crack Monitoring of Concrete Structures. Civil Engineering. Université de Nantes, 2019. English. NNT : . tel-02951164

HAL Id: tel-02951164
https://hal.science/tel-02951164

Submitted on 1 Oct 2020

THESE DE DOCTORAT DE

L'UNIVERSITE DE NANTES
COMUE UNIVERSITE BRETAGNE LOIRE

ECOLE DOCTORALE N° 602
Sciences pour l'Ingénieur
Spécialité : *Génie Civil*

Par
Antoine BASSIL

Distributed Fiber Optics Sensing for Crack Monitoring of Concrete Structures

Thèse présentée et soutenue à l'IFSTTAR, le 26 Novembre 2019
Unité de recherche : Institut Français des Sciences et Technologies des Transports, de l'Aménagement et des Réseaux IFSTTAR
Thèse N° :

Rapporteurs avant soutenance :

Joan Ramon Casas	Professor	Universitat Politècnica de Catalunya
Branko Glisic	Professor	Princeton University

Composition du Jury :

Président :	Eugen Brühwiler	Professor	EPFL
Examinateurs :	Emmanuel Marin	Professeur des Universités	Université Jean Monnet
Dir. de thèse :	Dominique Leduc	Maître de Conférences, HDR	Université de Nantes
Co-dir. de thèse :	Odile Abraham	Ingénieur Divisionnaire des TPE, HDR	IFSTTAR
Encadrant :	Xavier Chapeleau	Chargé de Recherche	IFSTTAR

Invité(s)

Jean Marie Henault	Ingénieur de Recherche	Electricité de France EDF

Contents

List of Figures

List of Tables

Acknowledgments

First, I would like to start by thanking my supervisors Xavier Chapeleau, Dominique Leduc and Odile Abraham for the patient guidance, encouragement and advice they have provided throughout my time as their PhD student. Their guidance helped me in all the time of research and writing of this thesis. I have been extremely lucky to have supervisors who cared so much about my work, and who responded to my questions and queries so promptly. I would like to also thank Dr. Sylvie Lesoille and Dr.Virginie Gaillard for their yearly examination of my work and their insightful comments.

Besides my supervisors, I would like to thank the rest of my thesis committee: Prof.Eugen Brühwiler, Prof.Joan Casas, Prof.Branko Glisic, Prof.Emmanuel Marin and Dr.Jean-Marie Henault, for their insightful comments and encouragement, but also for the hard questions which incented me to widen my research from various perspectives.

I would like to thank all the members of SII Laboratory for their continued support and for providing an exciting and funny work environment. Performing the important number of experimental tests would not have been possible without the big help of Jean-Philippe Gourdon and Ivan Guéguen. Moreover, I am thankful for Louis Marie Cottineau for his great mentorship and guidance.

During these last three years, I felt part of a big family called IFSTTAR, the reason I decided to become a board member of the PhD students association. Therefore, I would like to thank those whom I had the chance to work with, those who helped in my project management and to all the PhD students that I met and they became my friends.

The thesis has been performed within the framework of the European project Infrastar (infrastar.eu), which has received funding from the European Union's Horizon 2020 research and innovation programme under the Marie Skłodowska-Curie grant agreement No 676139. The grant is gratefully acknowledged. I thank all the members of this wonderful European family that made all the events I attended from training weeks to implementation days such an eye-opening experience. Moreover, I would like to thank INFRASTAR project manager Hakim Ferria for his endless support, especially when it came to interpersonal and communication skills.

I spent three months at BAM federal institution (Berlin, Germany) and three months in EPFL university (Lausanne, Switzerland), where I had the chance to collaborate with fantastic researchers. More specifically, I would like to thank Prof.Eugen Brühwiler and Dr.Ernst Niederleithinger who provided me the opportunity to join their team and who gave me access to the laboratory and research facilities. Moreover, and without the precious support of Xin Wang and Bartłomiej Sawicki, it would not be possible to conduct very interesting part of this research work.

Last but not least, I would like to express my deepest gratitude to my family and friends. This dissertation would not have been possible without their warm love and continued patience.

Introduction

That infrastructure matter to growth is now relatively well recognized and widely understood among practitioners and policy makers. The population of 21st century, depends on a complex and extensive system of infrastructures. Thus, better quality of infrastructures helps maintain quality of life, facilitate private investment, raise productivity, and improve jobs and income levels for many. This is why civil engineering plays a critical role in planning, developing, building and maintaining this infrastructure stock.

The neglection and excessive use of the existing public infrastructures in many developed countries has led to accelerated deterioration of bridges, buildings and transportation systems. For example, in United States alone, one bridge in nine is rated as structurally deficient while the average age of nations bridges is just 42 years (while bridges are designed for 75 to 100 years). In like manner, many countries in Europe are having the same problem where half a million bridges, built right after the Second World War, are beyond their 50 years of life. The increase in weight of trucks raising the accumulated loads, the change in environmental conditions, the widespread corrosion of steel rebars and overall deterioration and aging led to unsatisfactory conditions of these infrastructures with the situation becoming imminent to a global infrastructure crisis [1]. Moreover, the continuous growth in worldwide population and the climate changes (increasing the probability of natural hazards) are increasing the need for housing and better infrastructures.

Nowadays, reinforced concrete is the most employed material in the construction industry, but the global trend is to reduce its consumption rate and thus to change the focus from “design of new structures” to “maintenance of the current constructions” [2]. The only way to guarantee their normal operation and to prevent damage or failure caused by the different fluctuating operational and environmental loads over decades is by continuous monitoring of their health condition. Achieving this task before the structure becomes in dire need of attention and cost of repair approaches the cost of replacement, requires tools capable of mixing numerical modeling and measurement techniques in order to provide a good inspection-monitoring and reinforcement-rehabilitation plans.

Morandi bridge collapse in Genoa (14/8/2018).

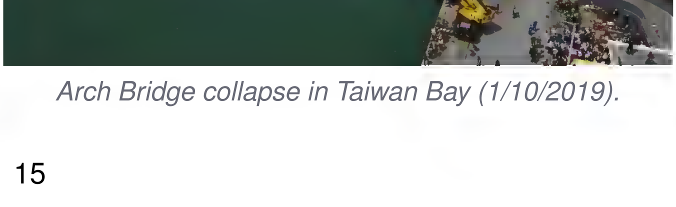

Arch Bridge collapse in Taiwan Bay (1/10/2019).

In this way, INFRASTAR (Innovation and Networking for fatigue and Reliability Analysis of Structures - Training for Assessment of Risk) ITN project, funded by the Horizon 2020 program, addresses three major challenges: (1) Early damage monitoring using NDT techniques, (2) advanced modeling of concrete fatigue behavior and (3) probabilistic approaches of structures reliability under fatigue phenomenon. As one of the 12 PhD subjects and part of the monitoring and auscultation work package, the scope of this thesis stands at the investigation of a new strain sensing technology called Distributed Fiber Optics Sensing DFOS technique. This technique led to a breakthrough in the sensing field by providing distributed strain measurements over the length of the structures, using a tiny and non-intrusive optical fiber. Thus, this technique brings a substantial amount of data that can help design, maintenance and operation engineers to study long-term degradation phenomena, particularly fatigue of structures.

The network of academic and industrial partners in INFRASTAR project helped bringing together different expertise to make this research work more transverse and mature. A three-month secondment in BAM (Bundesanstalt für Materialforschung und -prüfung) research institute helped in the evaluation of the performance of this novel technique compared to other Non-destructive evaluation techniques like Coda Wave Interferometry and Digital Image Correlation techniques. In addition, during a three-month secondment in MCS (Structural Maintenance and Safety) laboratory in EPFL university (Ecole Polytéchique Fédérale de Lausanne), a collaboration resulted in applying DFOS technique for monitoring of UHPFRC (Ultra High Performance Reinforced Concrete) structures and studying the fatigue life of the optical fiber sensors.

The 12 early stage researchers and the partners in INFRASTAR ITN project.

This thesis work aims to provide a better understanding of the distributed strains measured by the fiber optics sensing technique in the case of damaged reinforced concrete structures. In other words, we want to examine the relationship between the strain measured over the length of an embedded or surface-mounted optical fiber and the strain in the concrete material figuring a crack discontinuity. For this purpose, we investigate the different strain transfer theories for a better understanding of this phenomenon and we propose a new analytical model that is more adapted for the case of fractured concrete material. Based on this model, a methodology is developed in order to achieve good estimation of micro and macro cracks openings. The final purpose of this work is to propose a multiple crack monitoring system for reinforced concrete infrastructures capable of providing early crack detection, accurate localization and continuous quantification of their openings.

The thesis is organized around four chapters. The first chapter presents the state of the art on fiber optics sensors applications in civil engineering. We start by presenting the Structural Health Monitoring (SHM) concept and the different traditional sensors used for this purpose. Then, we present the different distributed fiber optic sensing techniques, as well as some recent applications on real scale structure for structural health monitoring. In addition, a focus on cracking behavior of reinforced concrete structures is presented. The advantages of distributed fiber optics sensing over other available techniques for crack monitoring are also discussed.

The second chapter focuses on the strain transfer from the host material to the fiber core. As this strain transfer happens through a stack of layers usually surrounding the optical fiber (the sensing element), the strain measured by the fiber could differ from the strain in the host material. Based on the existing literature, a three-layer strain transfer model is discussed in the case of continuous and discontinuous host material. The simplifying assumptions and boundary conditions are also argued. As this model assumes an elastic behavior of different layers and a perfect bonding at the interfaces, the elasticity limits and the most probable post-elastic phenomena are presented. Their effect on the measured strain response is developed for a better understanding of this phenomenon. Finally, a new strain transfer model capable of handling the imperfect interfacial bonding is presented. This model is more realistic, as perfect bonding with concrete is hardly achieved through embedded and glued sensors. The model is then extended to multi-layers system for a better modeling of complex cases where the optical fiber is surrounded by different protective and adhesive layers.

The third chapter presents an experimental study based on wedge splitting tests instrumented with embedded and surface-glued optical cables. Part the tests aim to validate the proposed strain transfer model for concentric and non-concentric layer configurations. The capacity of accurate estimation of crack openings by model fitting to measured strain from DFOS techniques is evaluated. The other part focused on the influencing conditions and limitations of the analytical model. Robust cables for on-site application and thin optical fibers for laboratory applications were tested. In addition, the influence of concrete hardening, bonding lengths and epoxy adhesive aging are all examined for embedded and surface-mounted optical cables.

The fourth chapter deals with reinforced concrete structures. Early crack detection using distributed fiber optics sensing technique is compared to coda wave interferometry technique and other traditional sensors like LVDT and strain gauges. The possibility of a dual DFOS and CWI techniques implementation for crack monitoring is briefly discussed. Then, three-point bending tests were performed on laboratory-size reinforced concrete specimens. In order to achieve accurate small crack openings estimations, accounting for the strain in host material, the influence of rebars, concrete hardening and formation of surrounding microcracks are all argued. Finally, we investigate the case of monitoring multiple crack openings in a real scale reinforced concrete beam. The estimated crack openings are compared to LVDT sensors and DIC technique. In-depth crack opening estimations and view of a continuous crack monitoring system for civil infrastructures are also discussed.

Chapter I

State of the Art: Monitoring of civil infrastructures using Distributed Fiber Optics sensors

> ”Somewhere in me is a curiosity sensor. I want to know what’s over the next hill. You know, people can live longer without food than without information. Without information, you’d go crazy.”
>
> *Arthur C. Clarke*

Contents

I.1. Context

I.1.1. Importance of Structural Health Monitoring (SHM) in the civil engineering field

Civil infrastructures owners must manage their heritage sustainably, guarantee the safe operation of facilities while ensuring the safety of people, the structure and the environment. However, concrete structures and their operating conditions evolve and the regulatory constraints may also modify during the life of the structure. Therefore, how can the owner ensure, throughout the life of the structure, that the structure meets functional requirements and potentially evolving constraints? The structure's monitoring strategy, which is part of the maintenance policy, must answer this problem.

Several criteria are available to help the owners in setting up the monitoring strategy for a structure. It starts from a risk analysis that takes into account the functional and regulatory requirements, the safety, the operating and environmental conditions, the knowledge of the behavior and pathologies of the materials and the structure, the operating loss costs and the life of the structure. The result is the definition of the physical quantities to be characterized, the type of monitoring, the possible instrumentation, the frequency and the processing methodology of the measurements, as well as the measures to be taken (safety measures, repair works) according to the results obtained compared to thresholds derived from calculations.

Nowadays, structural surveillance is mainly based on periodic visual inspections. In the case of suspected or existing damage, a possible short-term failure of the structure, or in the case of exceptional structural design where the behavior in service is needed, more detailed investigations are conducted. Auscultation requires the intervention of a competent team and the use of special techniques to estimate the properties of the materials. These techniques can be based on destructive testing performed on samples taken from the structure and analyzed in the laboratory, or on non-destructive methods implemented directly on the structure and which can be calibrated on the samples taken. The evaluation of the work concludes to the diagnosis of the state of the structure. A prognosis of the evolution of the state of the structure can also be deduced. At this stage, it could be decided to perform a more detailed monitoring of the structure, for a fixed period (one year minimum), by increasing the periodicity of visual inspections, or by instrumenting the structure. The measurements commonly performed include global and local displacement and deformation measurements of the structure to monitor the stress, deflection or crack openings.

In most cases, the sensors are installed on the surface of existing structures. On the other hand, in the case of new structures, the sensors can be installed as soon as the structure is built and can therefore be embedded in the concrete material. A major difficulty in the surveillance of civil engineering structures is to make sure that the measurements are representative of the behavior of the structure, which generally has a large surface area and a large volume. Thus, a key step in the development of the instrumentation plan is to define the number, the location (global or local zones) and the measurement base of the sensors to be deployed on the structure, while rationalizing the quantity of these sensors [3]. The use of several measurement techniques, for the estimation of the same parameter is often implemented in order to ensure the redundancy and the continuity of the series of measurements.

The SHM concept was developed primarily for aeronautics around 1990 and more recently for civil engineering [3]. The SHM consists in massively instrumenting the structure using different types of sensors in order to obtain a representative image of the state of health of the structure. The main idea is to compare the "as-is" structural condition, which includes the damage, fatigue, load distribution, etc., to the "as-built" structural condition, which comes from the structural design. Then, the analytical models can be updated so that the structural safety condition can be evaluated based on the "as-is" model [4]. In terms of complexity and sophistication, SHM systems can be classified into four levels (Figure 1-1). While a level 1 SHM system is only capable of detecting the damage, a level 2 system can also localize the damage. A SHM system reaches level 3 when it is able to provide information about the severity of the damage. Finally, level 4 SHM system, assessing the safety of the structure and the need for maintenance operations, is the most complex and costly level. For many reasons, SHM systems are now highly expensive to operate mainly due to time consuming, cumbersome and expensive installation of sensors and their data acquisition. Another main bottleneck is the fact that the spatial resolution of the obtained measurements depends on the total number of deployed sensors, which may result in less accurate damage localization. To date, the majority of research activities in the SHM area are focused on developing sensing technologies to acquire the data and create damage detection algorithms [5]. These measurement systems must meet the requirements defined by the structure's owner in specifications that describe in particular the expected functions and the constraints of use for the intended application. For this purpose, the selected solutions must be qualified for the user to be assured of their performance in response to the needs. The requirements on measuring systems must define the measurand, the metrological characteristics (measurement basis, sensitivity, tolerated errors, service life, etc.). In addition, the ease and speed of installation on the structure, the resistance to environmental conditions (mechanical stress due to handling, concrete pouring, ...), chemical aggression (basic pH of the concrete for installation in concrete, sunshine, humidity, salts for a siding installation), and the size of the sensor (to limit the effects of inclusion ...), should be all indicated. The aim is to determine the performance of the measurement system for the given application and to estimate the associated uncertainties, depending on the influencing parameters (environment, implementation, acquisition and processing of measures). In order to separate the sources of uncertainties and to understand the phenomena involved, the successive steps introduce a growing number of parameters, should start with configurations in the laboratory, through representative models of the application in a controlled environment and finish with an implementation on-site. Each step is conducted through experiments and modeling.

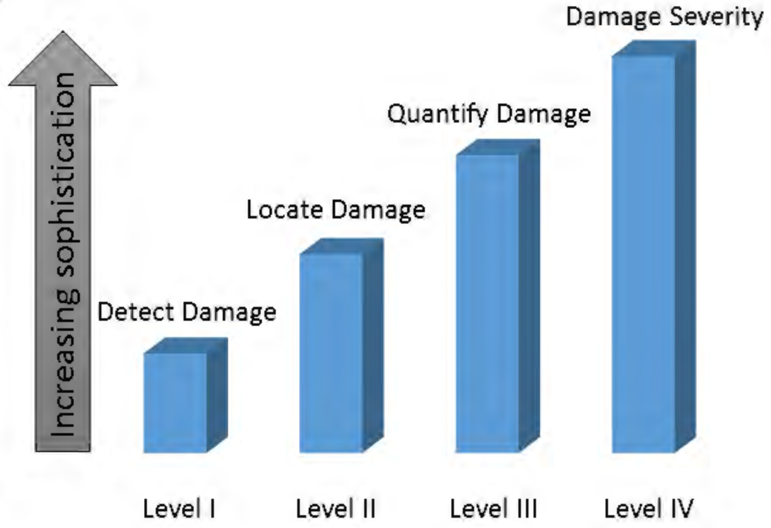

Figure 1-1: Classification of SHM systems based on their capabilities

I.1.2. Traditional monitoring systems for strain measurements

To supervise the health condition of a civil structure, from a global approach, it is mainly important to follow the stress variation over the length of the structure. While it is nearly impossible to measure the stress, strain is correlated to the stress by Hooke's law. Thus, any change in stress field is reflected through a change in the strain field. In addition, many other correlated parameters relevant for the evaluation of the structural health condition can be derived from static and dynamic strain and displacement measurements, such as the inclination and the differential settlement. Strain levels are usually determined at the design stage and they are associated to a safety factor varying considerably between different types of structures. For concrete and steel structures, their working range is usually limited to several hundred micro strains, and could be increased by crack formation. Sensors have to detect changes between one order in magnitude smaller (1/10), at least, and two orders (1/100), requested. For this reason, the strain accuracy can be of the order of 10 μm/m. The local strain measurement base should be usually 2 to 3 times the dimensions of the aggregates and therefore, varying around 2 cm to 5 cm. The measurement range depends on the application. Likewise precision, spatial resolution and temperature/strain separation have to create for users an added-value and be economically justifiable [6].

Moreover, local damage monitoring seems also paramount. Local damage behaves as cracks, fatigue, slip, debonding, effective force-resistance area losses, etc. Strain is an alternative parameter, which can be used to describe deformation, study the crack opening and even detect the slip and debonding. In terms of crack monitoring, the crack signature (leading to strain localization) should allow early detection and accurate localization of multiple close microcracks with a crack spacing in the order of several centimeters. For the estimation of crack openings, the crack opening threshold that must be measured is of the order of 200 μm. In addition, the life of the sensor must be equal to that of the structure, that is to say up to 100 years for some types of infrastructures like bridges. In order to to evaluate these parameters and reply to the desired specifications, structural engineers have always pursued surface inspection or high quality strain and displacement sensors.

The conventional surface inspection techniques are topometry and photogrammetry, and more recently lasergrammetry and Digital Image Correlation (DIC) [7]. With these techniques, it is possible to obtain the displacement and deformation fields observed on the surface of the structure, ranging from one to several thousand square meters. The error depends on many parameters including the characteristics of the optics, the distance between the means of measurement and the structure, external conditions,etc. In addition, new NDT techniques like Coda Wave Interferometry (CWI) [8, 9] and acoustic emission techniques [10, 11, 12, 13] can achieve crack detection and quantify parameters for crack identification, like the location, opening and height of the cracks.

As for traditional strain and displacement sensors, those used for monitoring civil structures have either a short base of a few centimeters, such as vibrating wire extensometers and strain gauges designed for point measurements, or a long base up to several meters, such as Invar wire extensometers associated with Linear Variable Differential Transducer (LVDT) (Figure 1-2). By averaging the measurement over the total gage base, provide a global information on the strain inside the structure [14]. Sensors are either embedded in the host material during the structure construction phase, or fixed on the surface. In the first case, they give in-depth information of the structural behavior, but they are no more accessible *a posteriori*, which may cause problems with their maintenance and their metrological monitoring. In the second case, they remain accessible and therefore they can be calibrated periodically. However, they bring on surface information whose behavior may differ from the core of the structure.

These techniques are at different levels of maturity. In some cases, and due to the fact of being used in a wide range of applications (like strain gauges), the systems are subject to standards and calibration procedures. In other cases, where the systems are specific to the field of civil engineering (like vibrating wire extensometers) and despite having been used for structural monitoring for decades, there are no existing standards or calibration procedures.

The most used type of extensometers in the industrial field is the resistive strain gauge. The

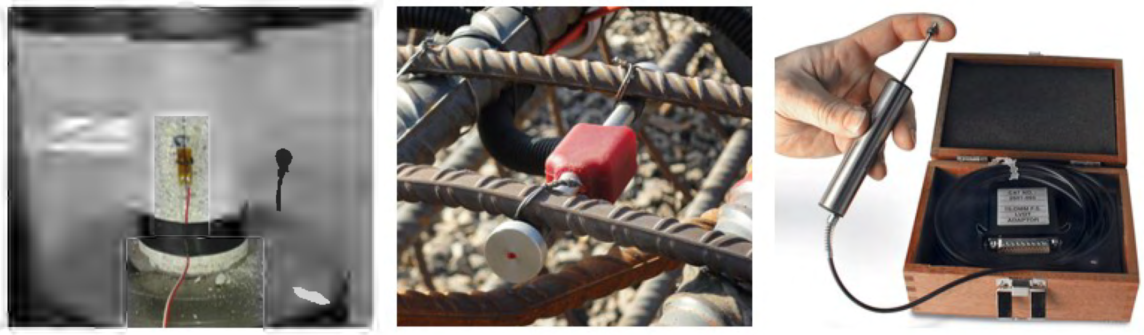

Figure 1-2: Strain gauges, a vibration wire sensor and a LVDT sensor.

operating principle is based on the fact that their electrical resistance varies according to their deformation. Normally, a gauge consists of a grid formed by thin strips of metallic film, fixed on an insulating support, bonded to the structure, and protected from the environment. Small in size, from millimeters to centimeters, it allows discrete measurements. The measurement range can vary from $\pm 10\ \mu\mathrm{m/m}$ to $\pm 200\,000\ \mu\mathrm{m/m}$ with an uncertainty of about 0.1%. In the field of civil engineering, gauges are mainly used to measure the deformations of passive steels, but can also be installed on cementitious materials. Preliminary preparation of the surface (grinding or sanding) before using a specific glue is adapted to the support of the gauge and the nature of the material to be instrumented.

The displacement sensor type LVDT, another sensor widely used in the industry, is an inductive sensor. The displacement to be measured is imposed on a ferromagnetic core by means of a guiding rod. The displacement of this moving part, induces a voltage variation in a secondary circuit, which is coupled to a primary circuit with a sinusoidal voltage. Depending on the product, the measuring range varies between $\pm$ 1 mm to $\pm$ 500 mm, with an error of about 0.002%. In practice, in the field of civil engineering, the LVDT sensor is associated with a metal rod positioned vis-à-vis the guiding rod. Each element is attached to a metal square. The metal rod is usually an Invar rod to limit the influence of temperature. The measuring system is anchored to the structure with the measurement base equal to the distance between the two anchor points. This measuring system is fixed on the surface of the structure and is often used to measure cracks opening. Some products make it possible to make global measurements on the structure by integrating the displacement on a base of measurement of several meters.

Figure 1-3: LVDT sensors installed on site on the left of a 1 m Invar bar [15].

Vibrating wire extensometers have been developed particularly for civil engineering applications and have been used in concrete substrates since the 1930s. The operating principle lies in the vibration of a steel wire anchored mechanically between two clips. The measurement base corresponds to the distance between the clips and is typically 11 cm, guaranteeing the representativeness of the local strain measurement compared to the centimeter size of the aggregates. The measuring range is of the order of $\pm$4000 $\mu\mathrm{m/m}$. The estimated uncertainty is in the order of $\pm$10 $\mu\mathrm{m/m}$ [16]. On the other hand, there is no standard for this measurement system, in particular on a calibration method and periodic calibrations.

I.2. Technology of Fiber Optics Sensors (FOS)

I.2.1. Fundamentals of FOS

In addition to traditional sensors, it is now possible to instrument the structures with a new generation of sensors based on optical fibers. For more than a decade, FOSs became increasingly popular, particularly for SHM applications where they became the second most used sensing technology in this field [17]. This is all due to the following advantages [18]:

- They are highly resistant to chemical degradation; hence, they can survive in aggressive environments (under water, in high humidity environment, near corroded rebar).
- They do not have electrical components, thus they are immune to high voltage and cannot be destroyed by lightning stroke.
- They are small-sized and light weighted, so they do not have a big influence on the host material behavior and can be mounted in very tight areas like anchor rods, in cable or rebar, in composite materials used to reinforce structural elements like Fiber Reinforced Polymers and Textiles Reinforced Mortar.
- They are electromagnetically passive and this is why they are the first choice measurement for energy industry for offshore wind turbines and oil platforms instrumentation.
- They exhibit multiplexing property and distributed measurements. Therefore, it reduces drastically the cost of wiring installations and allows the monitoring of a large section of the structure contrary to point sensors that require predicting the critical hot spots in the structure before their installation.

An optical fiber is a flexible, transparent fiber made of very pure glass (silica) not much wider than a human hair that acts as a wave guide, to transmit light between the two ends of the fiber [19]. As we can see in Figure 1-4a, an optical fiber consists of a central core surrounded by a cladding. Since silica optical fiber is pure elastic and brittle, a primary coating formed of one or many concentric layers of materials is added to protect the optical fiber, to avoid its breakage and to ascertain its long-term stability. For standard telecom fibers, the typical diameters of the core and the cladding are 10 $\mu\mathrm{m}$ and 125 $\mu\mathrm{m}$ respectively.

In order to confine the light into the core, the index of refraction of the cladding has to be marginally lower than that of the core $n_{\text{clad}} < n_{\text{core}}$. To slightly change Silica's index of refraction, either fluorine or various oxides such as B_2O_3, GeO_2 or P_2O_3 are added. The small relative difference:

$$\Delta = \frac{n_{\mathrm{core}}^2 - n_{\mathrm{clad}}^2}{2n_{\mathrm{core}}^2} \approx \frac{n_{\mathrm{core}} - n_{\mathrm{clad}}}{n_{\mathrm{core}}} \tag{I.1}$$

varies between 0.1% and 1% (0.3% for standard telecom fibers). Total Internal Reflection is the most common guiding mechanism in the optical fiber (Figure 1-4(b)). This optical phenomenon occurs when a ray of light in the core strikes the cladding at an angle larger than the critical angle θ_c with respect to the surface's normal line:

$$\theta_c = \sin^{-1}\left(\frac{n_{\text{clad}}}{n_{\text{core}}}\right) \tag{I.2}$$

In this case, the ray of light is reflected in the core without passing through the core-cladding interface. The acceptance angle:

$$\theta_a = \sin^{-1}(n_{\text{core}}\sqrt{2\Delta}) \tag{I.3}$$

determines the cone of external rays that can be guided by the fiber and forms an essential parameter for light coupling in and out of the fiber.

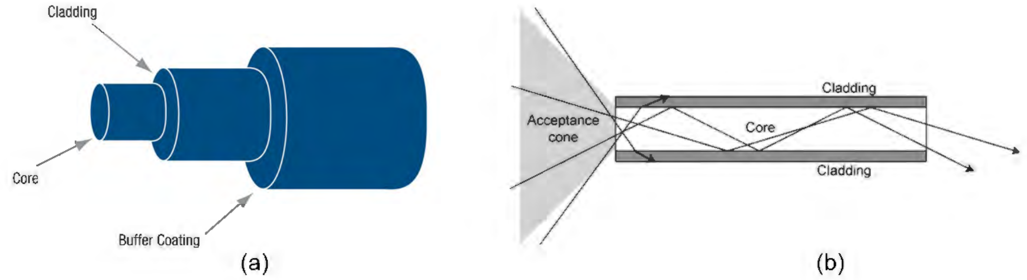

*Figure 1-4: **(a)** Different components of a fiber optic. **(b)** Guided light and internal reflection in the optical fiber.*

Intensity loss in optical fibers is a paramount feature. It is due to material absorption, light scattering, wave guide and bend losses. Outside the absorption bands shown in Figure 1-5, an exponential attenuation in the optical power of the guided light coupled to the fiber P_0 can be observed:

$$P(z) = P_0 e^{-\alpha z} \tag{I.4}$$

with $P(z)$ the power remaining after a z distance propagated by the light and α the attenuation coefficient indicating the rate of optical power loss in dB/km. This attenuation coefficient due to Rayleigh scattering depends on the size of the particles relative to the wavelength of light λ and is given by the hollowing approximate formula:

$$\alpha(\lambda) = \alpha_0 \frac{\lambda_0}{\lambda^4} \tag{I.5}$$

where "α_0=1.7dB/km" and "λ_0=0.85μm". We can notice from Figure 1-5 that to guarantee a good light transmission in the optical fiber with the longest propagation distance, the light wavelength has to vary near 1550 nm, where the light exhibits the minimum loss value (0.2 dB/km).

Optical fibers can be classified into two categories (Figure 1-6):

- Single-Mode optical Fibers (SMF) with a small core diameter (5-10 μm), where the light beam travels straight through the fiber with no reflections from the core-cladding sidewalls. For this reason, they are used in all modern long-range communication systems.
- Multi-Mode optical Fibers (MMF) with a large core diameter (50-1500 μm), where the index of refraction of light changes inside the fiber core. They are mainly applied for medium-range communications (such as local area networks) and where high power densities are needed (such as medical and industrial laser power delivery).

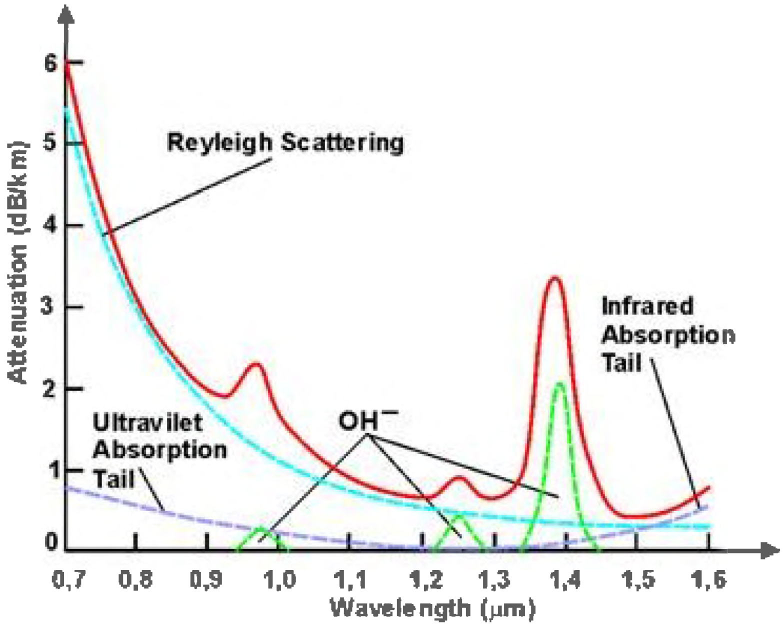

Figure 1-5: Optical power losses in the silica fiber with respect to light wavelengths.

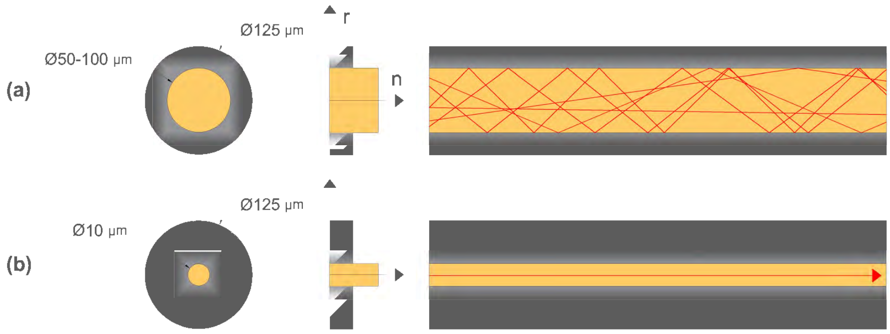

Figure 1-6: Difference in diameter and propagation of light between (a) Multimode and (b) Single mode optical fibers.

The general operating principle of Fiber Optic Sensor (FOS) consists on converting the information about quantities like strain, temperature or pressure into a modulated signal of either the intensity, the phase, the polarization, the wavelength or the transit time of light in the fiber. The information is deported out of the measurement area into an interrogator. Therefore, the measurement chain comprises a remote interrogator connected to one or several optical fibers, specifically packaged and adapted to the medium due the fragility of the optical fibers.

There are different ways to classify FOS depending of which criteria are being considered, e.g., the nature of transduction, the measurand induced modulation, the magnitude to be measured, the number of measurement points and the gauge length over which the measurand is averaged. Based on the last two criteria, FOSs can be divided into categories as shown in Figure 1-7.

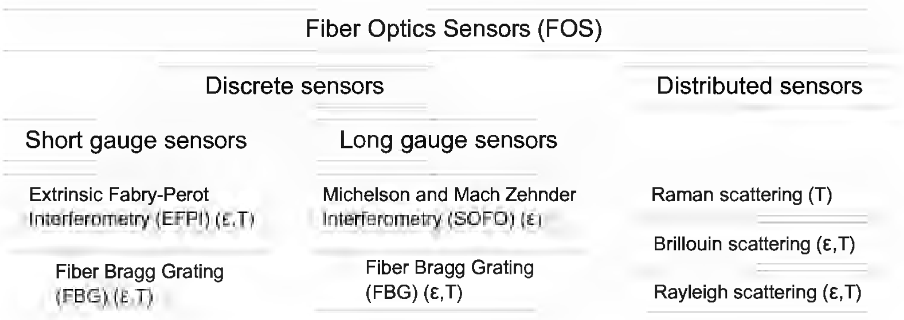

Figure 1-7: FOSs divided according to the gauge length [20]

I.2.2. Overview on discrete FOS

They are called discrete sensors due to the effect that they provide one discrete measurement point at the instrumented location. Contrary to traditional strain or temperature sensors, these sensors can be multiplexed and therefore measurement systems become capable of measuring at different specific points in the structure based on interference principles. Some FOS have been specifically developed to be embedded in civil engineering structures, similar to traditional sensors [3]. The gauge length or measurement base can range from 10 cm to several meters, which makes it possible to carry out either local or global measurements on structures.

Michelson interferometric sensors rely on signal interference from two optical fiber arms terminated by mirrors. The first fiber is linked to anchors while the second stay loose inside the sensor [21]. A specific sensor was developed for civil engineering applications, named SOFO [3] (1-8), estimates the deformation and self-compensates the temperature effects. These sensors can be either embedded in the concrete material, similar to vibrating wire sensors, or glued on the surface, similar LVDT sensors.

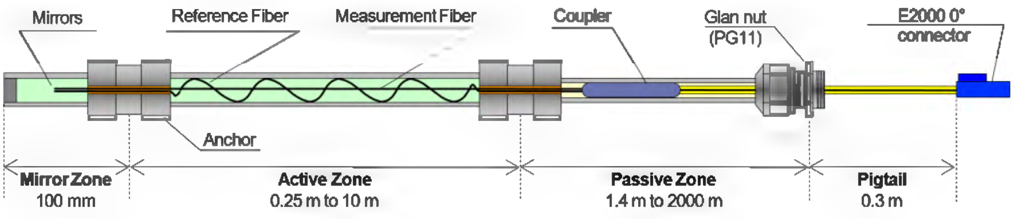

Figure 1-8: SOFO fiber optic sensors based on Michelson interferometer (Excerpt from SMARTEC).

Fabry-Perot sensors consists of a capillary tube containing two portions of cleaved optical fiber and separated by an air gap of few micrometers constituting an interferometric cavity [3]. The sensor is encapsulated in a packaging adapted to the intended application with the fiber portions bonded normally to the capillary tube over a typical characteristic length of 10 mm (Figure 1-9). For civil engineering, several ways of encapsulations are possibly similar to those of vibrating wires sensors [22]. As the substrate and the attached tube are strained, the reflected interference signal varies in response to the changes in cavity spacing.

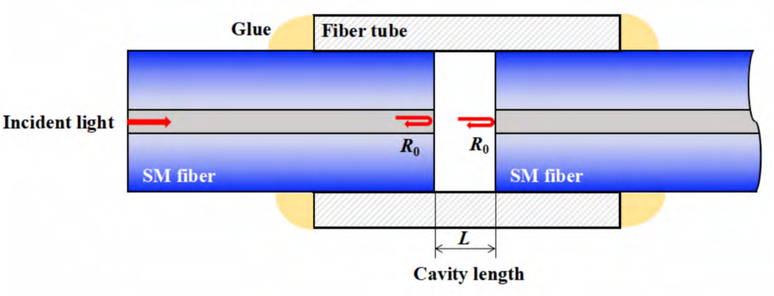

Figure 1-9: Typical structure of an Extrinsic Fabry–Perot Interferometer (EFPI) sensor fabricated with two SMFs and a short fiber tube[23]

Fiber Bragg Grating (FBG) sensors are the number one FOSs used in monitoring of different engineering structures especially civil structures. Due to the periodical variation of the core's refractive index over several millimeters to centimeters Bragg grating, only the part of light with a wavelength equal to Bragg's wavelength $\lambda_B = 2n_{eff}\Lambda$ is reflected (Figure 1-10). As a result, any temperature or strain variation induces a variation in grating period and consequently, a shift in Bragg's wavelength $\Delta\lambda_B$ to the following equation:

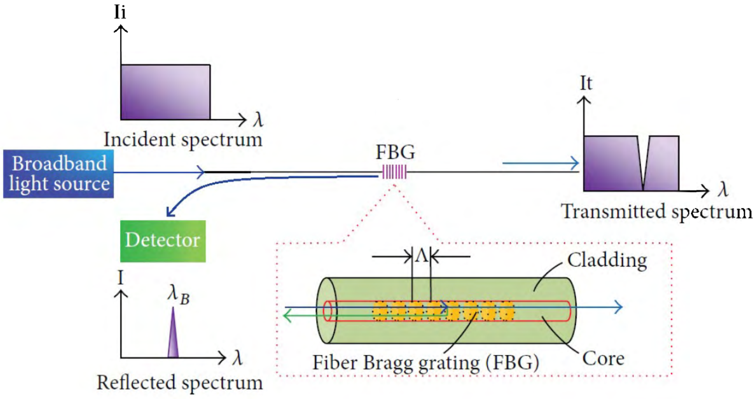

Figure 1-10: Measurement principal of FBG sensors [24].

$$\frac{\Delta\lambda_B}{\lambda_B} = \alpha\Delta T + \beta\Delta\epsilon \tag{I.6}$$

Where α and β are constant coefficients depending on the thermal and mechanical properties of the optical fiber and varies respectively in the order of 7.8 10^{-6} $^{\circ}C^{-1}$ and 0.78. Since the measurand (strain or temperature) is encoded to wavelength shift, FBG sensors are independent from intensity fluctuations of the source or lost in intensity during the light path [25]. In addition, due to wavelength multiplexing capabilities, several sensors can be integrated in one single mode optical fiber. The number of Bragg gratings in a fiber is a compromise between the spectral width of the reflected peak, the spectral width of the light source used and the expected range of measurement. The same interrogator can interrogate several fibers. In the case where the sensor is to be embedded in the structure, the fiber is surrounded by several protective layers similar to those of the vibrating wire or SOFO sensors (Figure 1-11a). However, when the sensor is mounted on the surface of the structure, it is configured similar to the strain gauges, in the form of a patch to be glued (Figure 1-11b). Guidelines and testing procedures for characterizing the FBG sensor when bonded exist. For this reason, FBG sensors reached nowadays two thirds of FOSs applied in different fields like aeronautic, civil engineering, renewable energy and medicine.

(a) *(b)*

Figure 1-11: Fiber Bragg Grating sensor adapted ***(a)*** *to be embedded and* ***(b)*** *mounted on the surface for monitoring of civil engineering structures. (Excerpt from CEMENTYS)*

I.2.3. Distributed sensing techniques

Large infrastructures need high number of sensing points in order to cover all the hidden structural information. Complicated techniques have been explored and studied for system identification and damage detection. Notwithstanding, the performance of these techniques based on high-level algorithms may decrease due to external interference that can mask the real damage, such as temperature variations, load changes, outliers and missing data in monitoring results [26]. Following this urgent need, Distributed Optical Fiber Sensors (DOFS) were introduced as a promising candidate for SHM applications. The difference between these systems and previously mentioned sensors is their ability to provide simultaneous local and global information [27]. The result of an acquisition is a continuous profile of the scattering phenomenon of the light, over a certain range of the optical fiber, and with a defined measurement step that can be changed by the user. The measurement system consists of a remote interrogator connected to a standard optical fiber. The measurement step or gage length of these systems varies from 1 meter to fewer than 1 millimeter.

The laser injected into the optical fiber is a monochromatic wave characterized by a frequency ν_0, therefore a wavelength λ_0. Due to different types of non-uniformities in the Silica medium, part of the wave are scattered away from its main direction and another part is absorbed by the material. As the optical fiber is a wave guide that favors the two directions of propagation, only the backscattered part propagates in the medium, opposite to the main direction of propagation of the incident wave. At the microscopic scale, the scattered wave spectrum is highlighted through three main scattering phenomena: Rayleigh, Brillouin and Raman (1-12). Rayleigh scattering is a quasi-elastic scattering where the scattered photons maintain the same frequency as the incident light. This phenomenon

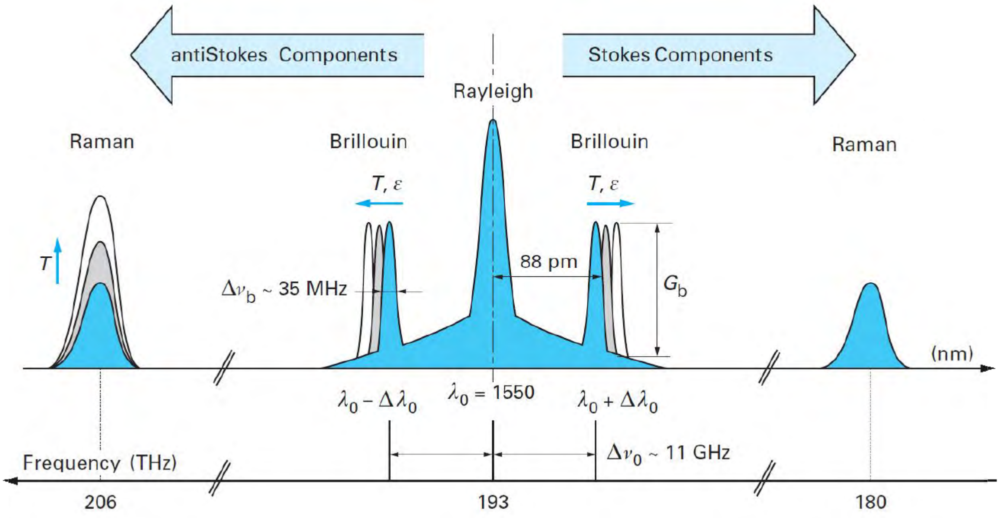

Figure 1-12: Rayleigh, Raman and Brillouin back-scattering intensity in silica fibers (excitation at $1550\ nm$*)* [17]

is due to impurities or density fluctuations of the refractive index on a scale smaller than the optical wavelength. It is affected by temperature and strain variation. On the other hand, Brillouin scattering phenomenon is due to an inelastic scattering mechanism in the medium. The energy exchange between the medium and the propagating light leads to a wavelength shift between the incident and backscattered light. In the frequency domain, it is manifested by: Stokes frequency $\nu_S = \nu_0 - \nu_B$ and Anti-Stokes frequency $\nu_{AS} = \nu_0 + \nu_B$. This frequency shift ν_B is sensitive to temperature and strain variations. Raman phenomenon is also due to the inelastic scattering mechanism, but it is only sensitive to the molecular vibrations (mainly due to the temperature of the material). In terms of energy in the silica medium, this mechanism is more important than Brillouin phenomenon and therefore leads to greater frequency shifts. Only the Raman anti-Stokes component amplitude is affected by temperature variation.

These interactions occur at each point of incidence of light. By analyzing the backscattered light spectrum, it is then possible to obtain information on the temperature and the deformation at each location of the silica fiber. This distributed measurement systems operate based on two main techniques:

- Optical Time Domain Reflectometry (OTDR): It is the most used technique. The technique consists on propagating a light pulse in the optical fiber and measuring the returned light intensity as a function of time. The time the backscattered light takes to be detected allows the localization of the event (Figure: 1-13). The spatial resolution is then a function of the width of the light pulse normally equal to 10 ns resulting in a resolution of about 1 m. Using OTDR technique, any gain or loss in light intensity due to a change in refractive index, in ModeField Diameter (MFD) or a change in material density (Fresnel peaks) can be analyzed over tens of kilometers with a metric spatial resolution (Figure 1-14).

- Optical Frequency Domain Reflectometry (OFDR): This technique relies on frequency modulation. The incident light wave is a quasi-continuous wave whose frequency varies linearly with time. The Fourier transform of the backscattered signal corresponds to a temporal trace of the intensity of the backscattering. The OFDR technique achieves a much better spatial resolution than the OTDR (up to 1mm) because the spatial resolution depends this time on the inverse

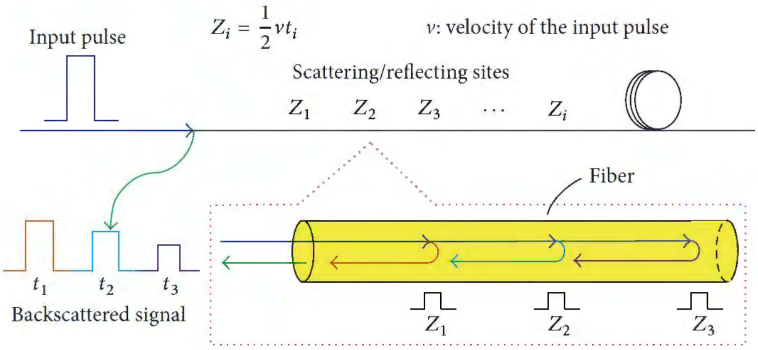

Figure 1-13: Optical Time Domain Reflectometry measurement principal [24].

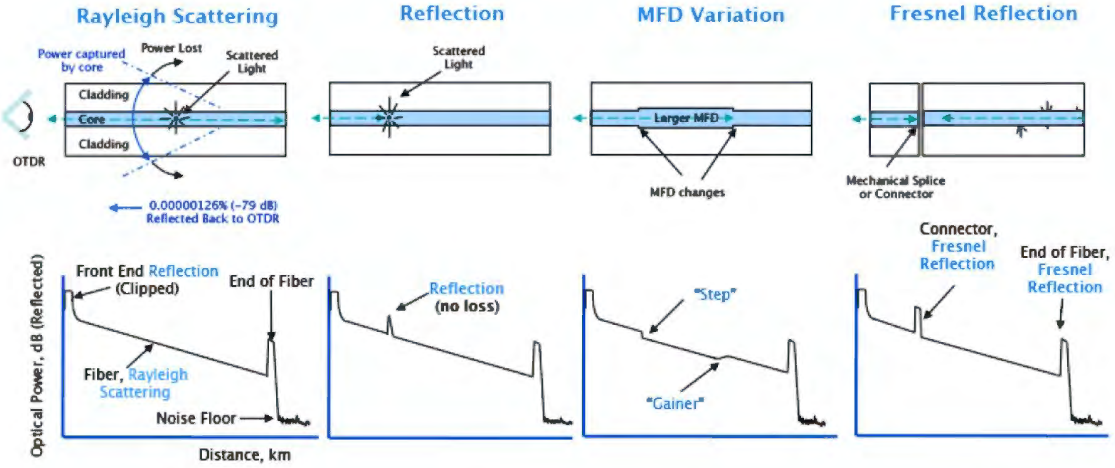

(1a) (1b) (1c) (1d)

Figure 1-14: Different events behind the change in attenuation trace measured by an OTDR system [28] of the frequency range of the source. However, it can reach lower distance range (maximum 2 km) compared to the OTDR, mainly due to the time cohesion length limit and the phase noise of the light source [29].

The measurement systems based on backscattering phenomena are relatively new: the first Raman interrogators were marketed in the late 1990s, the first Brillouin devices in 2000 and the first Rayleigh interrogator in 2007.

Techniques based on Brillouin back-scattering phenomenon like Brillouin Optical Time Domain Reflectometry (BOTDR) and Brillouin Optical Time Domain Analysis (BOTDA) were first presented. But the main limitations of these techniques turned around the low spatial resolution (typically between 25 cm and 1 m). Later on, this problem was resolved with new sensing techniques based on Rayleigh backscattering like Optical Backscattering Reflectometry (OBR) and Tunable Wavelength Coherent Optical Time Domain Reflectometry (TW-COTDR) giving the possibility to obtain centimeters to millimeter spatial resolution for strain measurements. These techniques filled a range of applications not easily covered by Brillouin DOFS systems like cracks detection in civil engineering structures [30]. Today, there are also interrogators able to perform Brillouin and Rayleigh backscattering based strain measurements in the same fiber.

The applications targeted by the distributed measurement systems correspond to the monitoring of objects with large linear length or large areas. The purpose of monitoring is often the detection of events whose location is unpredictable like cracks, fires, leaks, slip or movement, third party aggression; and the objects are paths of electric cables, wells, pipelines and civil engineering structures like bridges, tunnels, dikes, dams, buildings.

Raman Optical Time Domain Reflectometry R-OTDR interrogators analyze the Raman backscattering phenomenon that leads to the generation of two symmetrical frequencies as shown in Figure 1-12. While the intensity of stokes signal I_S is almost free from temperature influence, the intensity of Anti-Stokes signal I_{AS} is strongly related to the variation of temperature. The advantage of R-OTDR technique lies in its high insensitivity to mechanical perturbations applied to the fiber, its independence from the intensity value of the initial pulse and local and distributed fiber losses [17]. R-OTDR technique is nowadays a mature temperature sensing technique applied mainly in Oil and gas industry to monitor temperature gradient due to fluid flows in high-pressure reservoir [31] or fluid diversion along the well bore [32]. These DFOS systems were also applied to monitor one of the world's largest steam-flood operations conducted on Sumatra Island in Indonesia [33] where the surveys helped to identify bypassed or unswept oil zones in the steam-flood patterns.

During the Brillouin scattering phenomenon, an acoustic wave is created which weakens the light pulse. This loss of energy leads to a change in the position of central frequency peak of the original light pulse. In [34], the authors discovered that this frequency shift is linearly dependent on the variation of strain and temperature:

$$\Delta\nu_B = C_\epsilon \Delta\epsilon + C_T \Delta T \tag{I.7}$$

Where C_T and C_ϵ stand for the Brillouin temperature-frequency and strain-frequency coefficients. The Brillouin scattering can be spontaneous or stimulated. The technique based on the former is Brillouin Optical Time Domain Reflectometry BOTDR, while the one based on the latter is the Brillouin Optical Time Domain Analysis BOTDA. The main advantage of BOTDR technique lies in the need to access just one fiber end [34, 35, 36]. However, the lower efficiency of the spontaneous Brillouin effect leads to long measurement times. Thus, BOTDA technique was developed to overcome this drawback by using two counter propagating lasers: a pulse laser and a continuous laser. The backscattered light is stimulated when the frequency difference between the two lasers becomes equal to the Brillouin frequency shift. Figure 1-15 shows an example of Brillouin Gain Spectrum (BGS). Pre-Pump Pulse

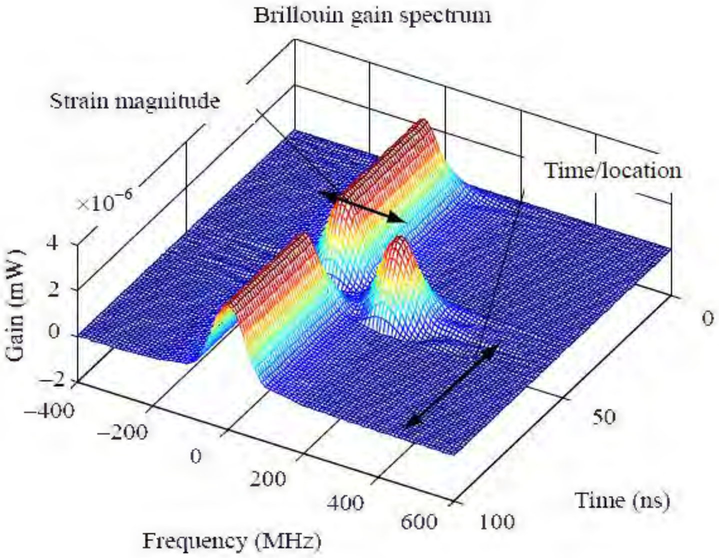

Figure 1-15: Example of Brillouin Gain Spectrum (BGS) from BOTDA technique due to a strain variation [6].

Brillouin Optical Time Domain Analysis PPP-BOTDA came as a breakthrough technology for Brillouin systems reducing the spatial resolution from 1 m to 10 cm [37, 6, 38].

Brillouin DOFSs were applied in security field of critical infrastructures. "Smart Fence" project is a good example, where optical sensors helped detecting any intrusion on a 670 m perimeter of an electrical substation [39]. Dams also constitute an ideal structure to apply DOFS technology, in particular Brillouin based techniques, taking into consideration the big scale of dams and the presence of water. These systems were applied to monitor the risk of flooding in inspection galleries (Ex: Plavinu dam in Latvia and Solina gravity dam in Poland) [40]. By integrating optical fibers into geosynthetics, these techniques were able to monitor any critical deformation in the dike's body due to an erosion or slope failure (Figure 1-16) [18]. Maybe one of the main fields of application of Brillouin techniques is oil and gas energy industry. In order to prevent big environmental and property damages due to leaks in pipelines, transporting gas, oil or any other fluid, interrogators based on BOTDR and BOTDA techniques were implemented to detect cracks down to 0.1 mm [40, 41]. These monitoring systems have proved to be more adequate than existing traditional leak detection technologies (Figure 1-17). Since

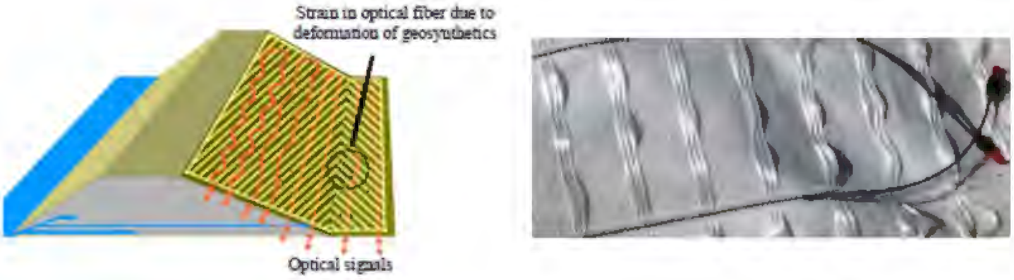

Figure 1-16: (a) The instrumentation of the river dike and (b) the combination of optical fibers with the geotextiles [18]

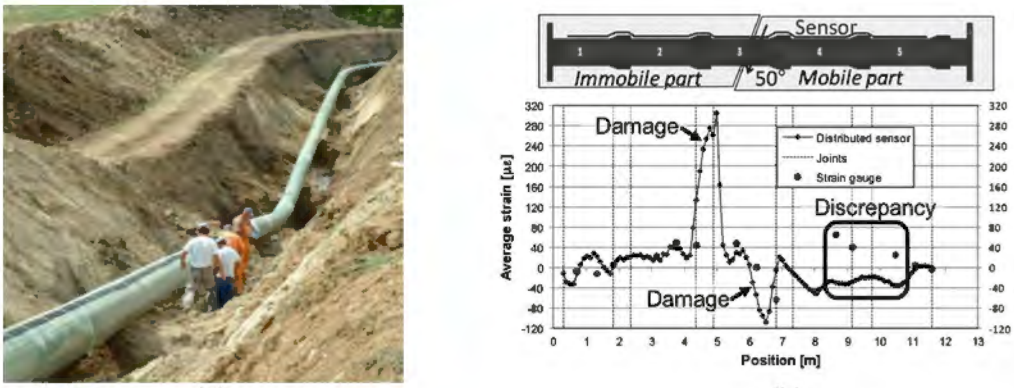

(a) (b)

Figure 1-17: (a) Instrumentation of pipelines near Rimini in Italy [41] (b) Results of the test and damage detected [42].

2005, many bridges were instrumented with Brillouin DFOS systems to monitor different early and long-term behaviors of reinforced concrete and steel [43, 44]. Monitoring systems based on BOTDR were introduced to monitor rehabilitated reinforced concrete bridges with externally post-tensioned tendons [45]. A good example of complete monitoring projects on a long structure in service is the Götaälv Bridge (Figure 1-18a). The SHM system used BOTDA technique is planned for 15 years aiming to detect effects of aging and long-term loading like creep and fatigue. Recently, a BOTDA system combined with other types of sensors was implemented to monitor different parameters as long-term creep and shrinkage, post-tensioning forces, bending, shear, and torsional cross sectional stiffness, etc., in the concrete deck of Streicker Bridge [46] (Figure 1-18b).

(a) (b)

*Figure 1-18: **(a)** Götaälv Bridge in Gothenburg, Sweden. **(b)** Streicker Bridge in Princeton, United States [47].*

During their fabrication, the silica optical fibers present tiny fluctuations in their refractive index. This heterogeneous property constitutes a kind of fingerprint for each optical fiber [48]. A Swept Wavelength Interferometry (SWI) technique can be used to divide the whole length of the fiber into several short sections (in the orders of centimeters) so that the Rayleigh backscattering pattern can be measured as function of the fiber length over a fixed spatial resolution. Then, the Optical Backscattering Reflectometry (OBR), shown in Figure 1-19, transforms the small segments of the backscattering pattern into the frequency domain using Fourier transform. By comparison to a reference pattern,

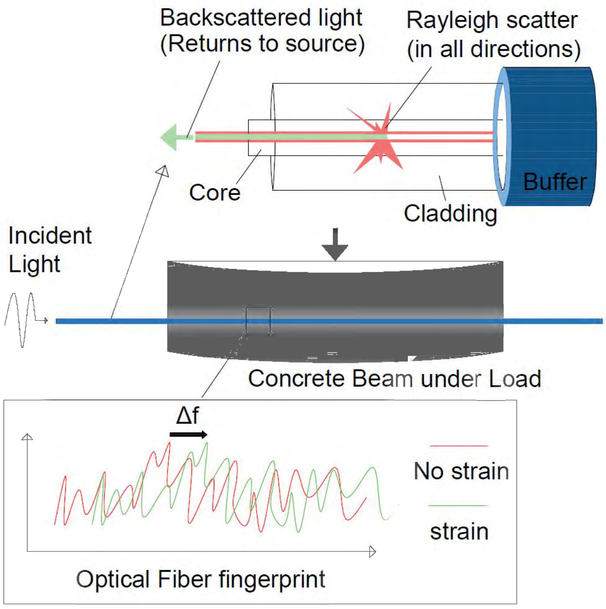

Figure 1-19: Optical Backscattering Reflectometry OBR working principle.

the frequency shifts of the spectrum are calculated. This frequency shifts $\Delta\nu$ are proportional to temperature and/or strain as follows:

$$\frac{\Delta\nu}{\nu} = K_T\Delta T + K_\epsilon\Delta\epsilon \tag{I.8}$$

The temperature coefficient K_T is the sum of thermal expansion and thermo-optic coefficients corresponding to the optical fiber. The strain coefficient K_ε depends on the refraction index, the strain-optic coefficients and Poisson's ratio. For a standard monomode fiber, the calibrated K_T and K_ε are respectively -1.25 GHz/°C and -0.15 GHz/$\mu\epsilon$, for a 1550 nm wavelength. Thus, this measurement technique is much more sensitive to temperature variation than to a variation of deformation. This is one of the main weak points of this type of monitoring systems in the context of a deformation measurement application. Distributed measurement techniques based on Rayleigh backscattering have advantages over those using Raman and Brillouin scattering. Indeed, the spatial resolution is higher (of the order of millimeters) and the measurement uncertainties for temperature and deformation are lower (0.1°C and 1$\mu\epsilon$). On the other hand, they are limited in terms of measurement range to a few meters. Applications are therefore limited to objects like medium range bridges and laboratory tests of limited-size structures such as reinforced concrete beams ([49, 50]), or composite wind turbine blades ([51]), etc.

Recently, a new Rayleigh OTDR measurement technique was introduced [6]. By means of the tunable wavelength of a Distributed-Feedback Laser and frequency scanning, the power spectrum can be obtained, showing a random distribution in the Coherent OTDR trace that corresponds to the in-homogeneity of glass density in the fiber core. Therefore, this technique, called Tunable Wavelength Coherent Optical Time Domain Reflectometry TW-COTDR, provides a frequency shift from cross-correlation of Rayleigh scattering traces. Similarly to OBR technique, this frequency shift is related to strain and temperature. By using a time domain approach, this technique provides measurements for long distance with a centimeter spatial resolution [52]. Despite this great advantage, this technique presented correlation problems related to the way frequency shifts were obtained. Therefore, the Japanese company Neubrex, introduced this technique as a part of a hybrid interrogator (NBX-7020). By adding high precision Brillouin PPP-BOTDA, this instrument made it possible to separate the strain and temperature. Concerning the data processing, and as shown in Figure 1-20a, the Brillouin data improved correlation analysis and provided distance compensation while Rayleigh data made it possible to easily separate the temperature effects and filtered noise (Figure 1-20b).

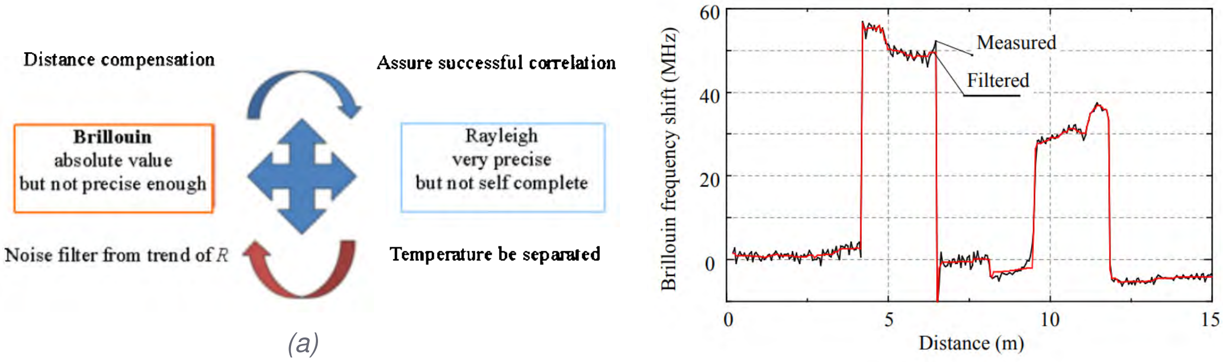

(a)

(b)

*Figure 1-20: **(a)** Hybrid Brillouin-Rayleigh data analysis scheme. **(b)** Example of Brillouin central frequency filtered using the Rayleigh shift [6].*

The OFDR techniques can deliver important benefits in civil engineering since it can be used for health monitoring of structures, such as big buildings, dams, bridges or pipelines. Currently research is based on the cracking control, deformation and damage detection. In 2014, OBR technique was used to monitor the Black river bridge in Ontario, Canada. Results showed that this technique can be used to monitor strain, deflection in the structure and the location of different microcracks [53]. Recently, OBR measurement systems were also applied to monitor the Rideau Centre Expansion reinforced concrete building [54], as well as the rehabilitation of a historical building used as hospital and the enlargement of Sarajevo Bridge in Barcelona [55].

Table 1-1 compares different properties of DOFS systems.

Backscattering phenomena	Raman	Brillouin			Rayleigh	
Sensing technique	**R-OTDR**	**BOTDR**	**BOTDA**	**PPP-BOTDA**	**TW-COTDR**	**OBR**
Measurement range	1 km - 37 km	50 km	150 km	0.5 - 10 km	21 km	70 m-2 km
Spatial resolution	1 cm - 17 m	1 m	2 m	2 - 50 cm	10 cm - 1 m	5.2-1.3 mm
Strain accuracy	-	60 με	20 με	20 με	0.5 με	1 με
Strain range	-	±30000 με	±30000 με	±30000 με	±15000με	±12000 με
Temperature accuracy	0.8°C - 3°C	2-3°C	1-2°C	0.75°C	0.05°C	0.1°C
Measurement time	<3 min	1-5 min	2-5 min	5 s	60 s	0.004-4 s
Dynamic measurement	No	No	Yes	No	No	Yes

Table 1-1: Measuring properties of different DOFS systems [24]

While their only limitation could be the sensing range for on-site applications, the millimeter spatial resolution and high accuracy of OBR measurement technique are what makes this technique more adapted than Brillouin and Raman OTDR systems for an application aiming to follow strain variations and achieving crack identification (detection, localization and quantification). The experimental work in this thesis is based on measurements from 3 different interrogation units based on OBR technique (manufactured by Luna). OBR4600 interrogator is the oldest version, with a limited spatial resolution of 10 mm and measurement rate of 0.25 Hz. In ODISI-B interrogators, the spatial resolution was improved to 1.3 mm with a measurement rate of 23.8 Hz, making it possible to perform continuous measurements during a quasi-static or cyclic load tests. While the last two units can interrogate only one optical fiber, the newest version of OBR interrogators, so-called ODISI 6000, adds the possibility of interrogating up to 8 optical fibers.

To conclude, these devices, incorporating the active components of the measurement system, are constantly evolving and are the subject of numerous research projects. The progress made today makes it possible to have commercial equipment with a performance comparable to that of traditional sensors, while having the additional functionality of having thousands of measurement points with a single optical fiber. The measurement chain presents the performance of the interrogators summarized in Table 1-1. Compared with the mentioned requirements for strain and crack monitoring in concrete structures, it is found that the distributed measurement systems are likely to meet the expressed needs. In order to improve the accuracy, it is recommended, during the instrumentation, to have point reference sensors close to the path of the fiber optic cable. In addition, and as the interrogators can be deported outside the measurement area, the user can position them in an easily accessible area from which it will be easy to carry out maintenance operations, or even to consider a subsequent replacement of devices while ensuring the temporal continuity of the measurements. This is particularly realistic in the context of civil engineering applications mentioned above, for which the required operating time is tens to hundreds of years.

I.2.4. Optical cables

As mentioned in the previous sections, the optical fiber is the actual sensor. However, for civil engineering applications, the optical fiber with its primary coating is very fragile. The solution is to protect the optical fiber with additional layers. This fiber and coating assembly, so-called cable, is more resistant and can reach several millimeters. The coatings serve mainly to protect the fiber against mechanical and chemical attack. However, and in order to be used as a sensor, the cable should also be conceived to guarantee an optimal mechanical and thermal transfer between the host material and the optical fiber. Nevertheless, and due to shear lag effect in the intermediate layers, there will be always a strain transfer error.

Different types of optical cables are available in the market. Among them, some are conceived to be embedded inside the structure during construction, while others are more suitable for surface installation on existing structures. These cables are formed of different materials, shaped in different forms. It can contain several monomode or multimode optical fibers to measure temperature and strain simultaneously. Depending on the application, some cables are reinforced by metal strands (to withstand high stresses in concrete) or inserted into geotextiles (for geomaterials [56]). Nowadays different companies are proposing several types of cables like Smartec, Sensornet and Neubrex and Brugg kabel AG.

The influence of these coatings has long been ignored by the manufacturers of interrogation systems with, in most cases, small information concerning the mechanical properties of the cable and its constituent elements, are available. However, suppliers often indicate that their products are versatile and are suitable to be used in different environments, like concrete, composites or pavements, and often without technical justification. In addition, the long-term behavior of these cables also remains unknown. In the last few years, some works have been done to try to lift this technology gap [57, 58, 59, 60], especially with the improved properties of the interrogation units.

By means of finite element simulations [59], Delepine-Lesoille et al. designed an optical cable with an external coating formed by a glass-epoxy composite braid as shown in Figure 1-21. The aim was to maximize the bonding with the host material. Henault et al. studied another type of optical cable from Sensornet. The cable had different intermediate layers between the sensing optical fiber and the sensed host material. However, despite its complicated configuration, the cable showed good performance in terms of strain and crack monitoring.

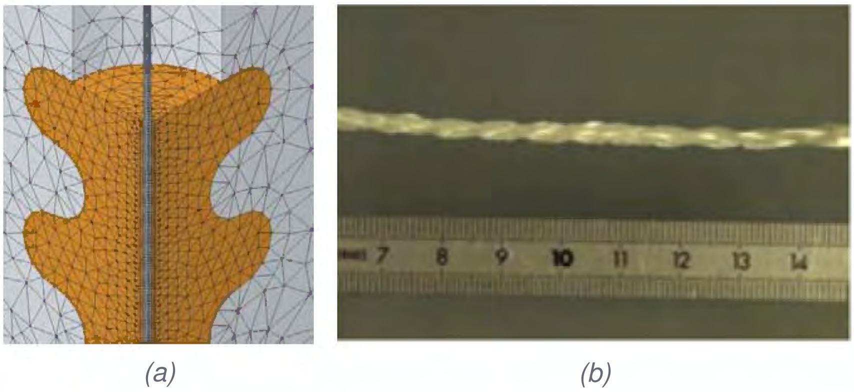
(a) (b)

*Figure 1-21: **(a)** Close view of the 3D mesh of the embedded cable. **(b)** a picture of spiral optical cable [59].*

In 2014, Hauswirth et al. studied the properties of a class of robust fiber optic cable prototypes produced by the cable manufacturer Brugg Kabel AG by performing experimental tests. Figure 1-22 show the different cables mainly designed to be directly embedded in soil. Except for the V1 cable (on the far left), the cables contain additional metallic protection sheaths in order to reach a higher level of robustness than usual fiber optic cables. By using a Rayleigh based interrogator (OBR4600), the authors showed that some cables showed some kind of slippage at high strain levels.

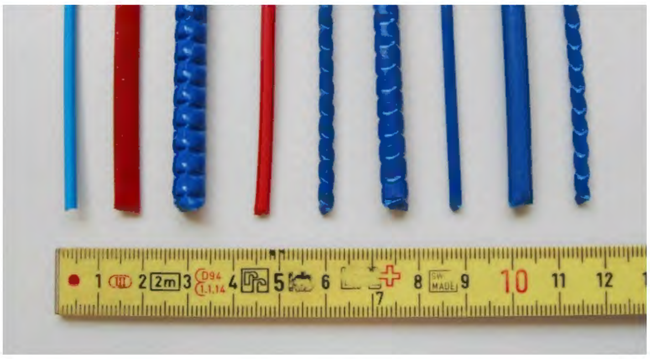

Figure 1-22: Different types of cable packages proposed by Brugg Kabel AG versions V1 to V9 (from left to right) [60] .

In addition, and when a crack occurs, there is a risk that a debonding at the surface of the specimen occurs due to localized strain near the crack. Thus, it can cause a plastic deformation in intermediate layers or slippage at the interfaces. In [61], and with the entire complicated phenomenon, the authors claim that it is still hard to monitor the crack openings quantitatively using an optical cable bonded along a host material and the idea of measuring strain near cracks is always a complicated problem. For this reason, the in-depth knowledge of the properties of different layers could help in understanding the mechanical strain transfer near cracks for the quantification of crack openings, particularly inside the structure where no robust and non-intrusive crack meters or NDT techniques can do the job.

I.3. Crack monitoring of concrete structures

I.3.1. Cracking in concrete

Cracks can occur in a Reinforced Concrete structure when it is subjected to bending, shear, torsion or tension loading. They may also arise from other phenomena, for example, shrinkage. As it is well known, the mechanical behavior of reinforced concrete structural members is highly affected by the formation of cracks during loading [62].

The crack presence on the surface can take various meanings and effects, according to the crack type. Indeed different cracks types can be distinguished. Gerard et al. [63] have defined active cracks as those affecting mechanical and transfer properties; passive cracks are essentially disturbing mechanical properties, knowing that they are activated only when the structure is under load. Different definitions are given in the French standards [64]: a crack is active if its opening evolves depending on solicitations from various natures (thermal, hydraulic, mechanical); it is a passive one if its opening does not change under different loads.

The major obstacles to be overcome are related to the multiple scale character of these problems, involving the formation of tiny dissipative zones preceding the cracks (fracture crack process zones), and the material instabilities caused by the progressive deterioration of the mechanical properties in these zones [62].

When the concrete material is under tension stress, cracks propagate perpendicularly to the main tensile stress. The degradation of concrete material starts through micro-cracking diffusion in the matrix of cement paste as shown in Figure 1-23. When concrete tensile strength is reached, a softening phase starts due to the coalescence of several micro cracks induces a macro-crack. This macro crack represents a localized crack as a discontinuity of the material.

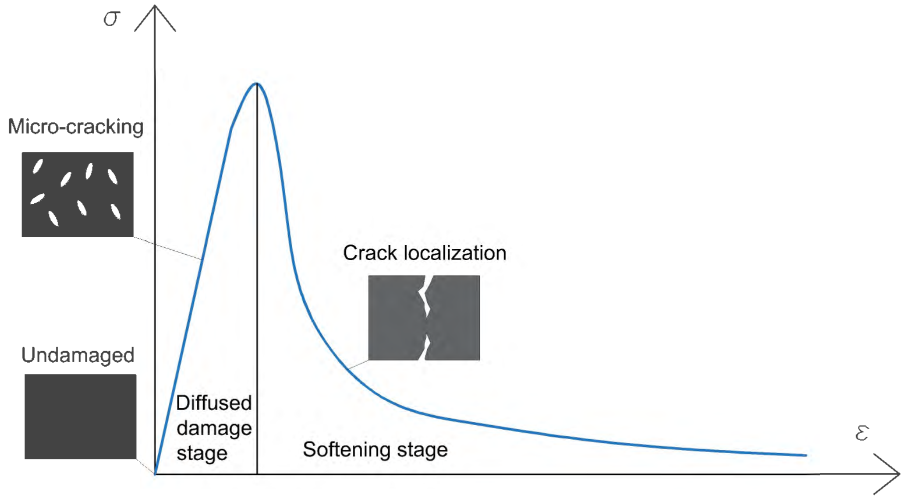

Figure 1-23: Behavior of concrete material under tension loading and its damage evolution.

A lot of work was dedicated for studying the cracking behavior of reinforced concrete structures. Two types of experiments were mainly performed. The first one is tensile tests on RC prismatic element in which one steel bar reinforcement was cast inside a concrete volume and the crack propagation can be seen on the concrete surface. The second one is three points or a four point bending tests, with or without the presence of a notch on the mid-span of the beam.

First tensile tests were performed by Goto [65]. The cracks were dyed by injecting ink into the specimens (Figure 1-24a). After finishing the test, the specimens were split into two parts and the

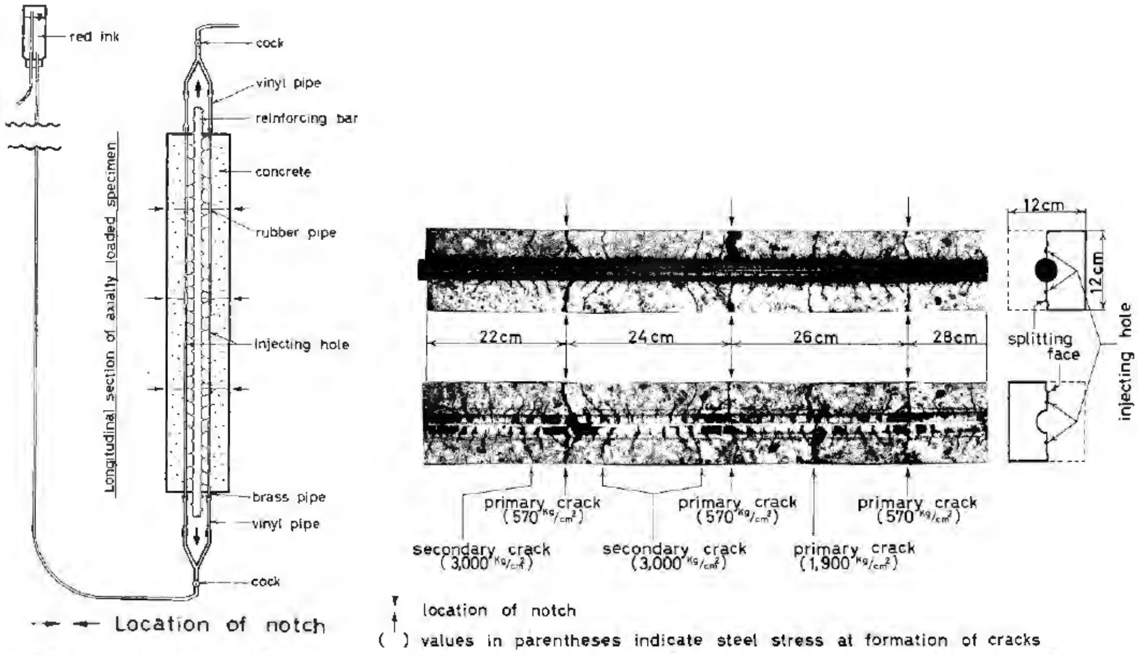

(a) Test configuration with the ink.   (b) The longitudinal splitting face with a 32 mm of bar diameter.

Figure 1-24: Tensile test performed by Goto [65].

dyed cracks were investigated to see the damage occurred around the steel bar. In this study, four types of cracks were classified: the primary crack, the secondary crack, the internal crack and the longitudinal crack. The primary crack was a radial crack that propagated to the concrete surface (notched) while internal cracks were the cracks appeared in between two ribs which could propagate to the concrete surface for higher loading forming the secondary crack. The action of the ribs to the concrete abutment created a radial deformation around the steel bar that provoked the longitudinal cracks initiation at the face of the primary crack. In 2010, Borosnoyoi et al. [66] performed similar tensile tests in order to study the in-depth crack propagation. Epoxy resin was injected in order to preserve the crack openings inside the specimen after the end of the test. Whilst the crack opening or width is usually considered to be constant within the concrete cover, the authors showed that effect of different concrete cover levels on the variation of both internal and surface crack openings as shown in Figure 1-25. Another study of tensile tests was performed by Michou [67] (Figure 1-26a) where multiple transverse cracks were localized during the loading (Figure 1-26b) using DIC. For a quantitative point of view, the evolution of the maximum crack opening for each specimen is presented in Figure 1-26c. The first crack propagation for three specimens occurred at the same load level with approximately $200\ \mu m$ of crack width for each specimen. Moreover, the sum of the crack opening (Figure 1-26d) for the three specimens presented a good similarity.

Many studies performed four-point and three point tests on reinforced concrete beams with a rectangular section [68, 69]. These studies showed that the bending cracks propagated from the bottom part in a vertical direction reaching the neutral axis of the beam. The quantification of surface crack openings showed different values of the maximum crack opening for beams with different dimensions, showing the effect of the structural size. Oliver et al. [62] compared numerical simulations to three-point bending beams tested by Ruiz et al. [70] in order to investigate bars/concrete interface system (Figure 1-27a). The results showed a propagation of the main macro-crack as well as the development of an orthogonal micro-cracking pattern in the concrete surrounding the rebar as shown

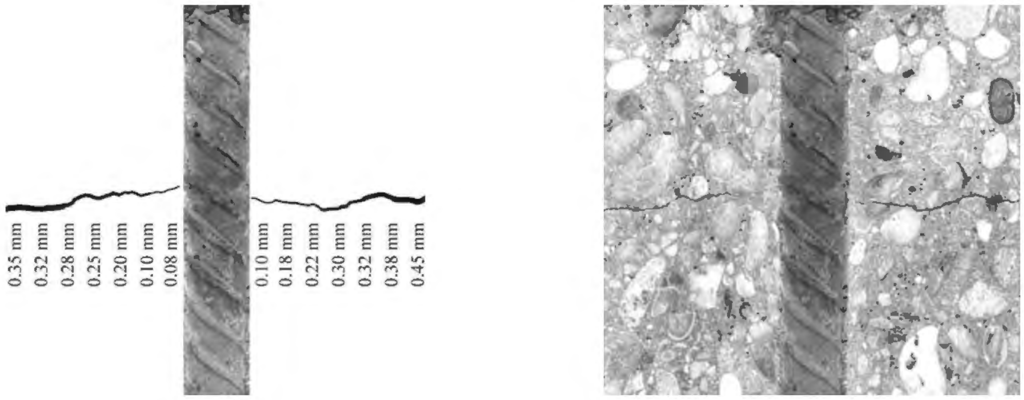

Figure 1-25: Variation of crack width during a tensile test with a concrete cover of 50mm [66].

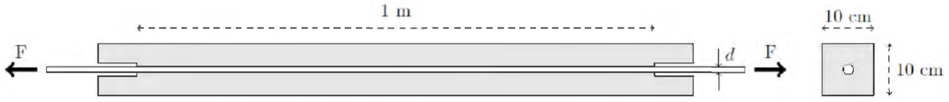

(a) The configuration of the Tie beam specimen.

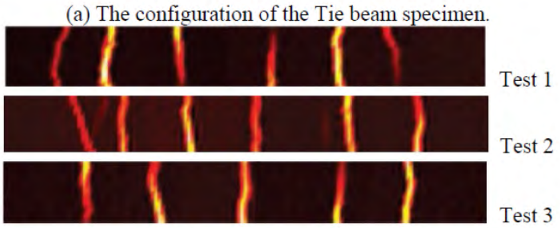

(b) The cracking pattern of the three specimens at the yielding point of the steel bar.

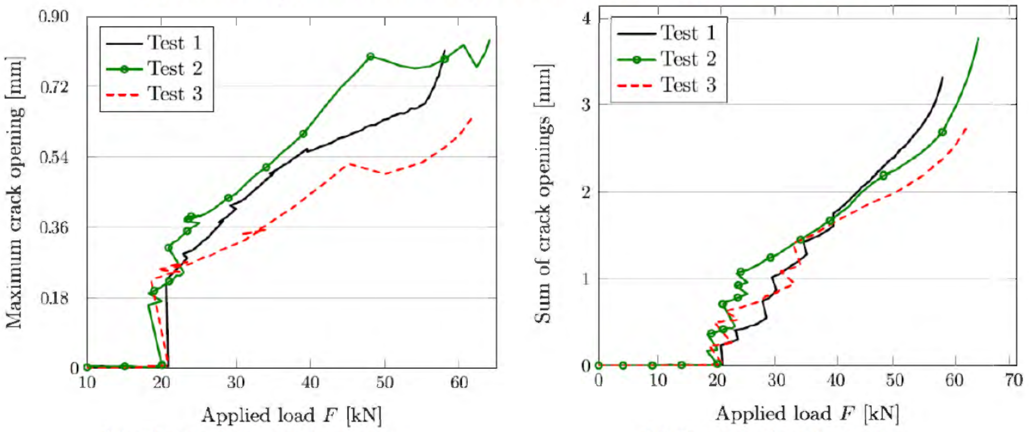

(c). The maximum crack opening

(d) The sum of crack opening

Figure 1-26: Results of tensile tests performed by Michou [67].

in Figure 1-27b.

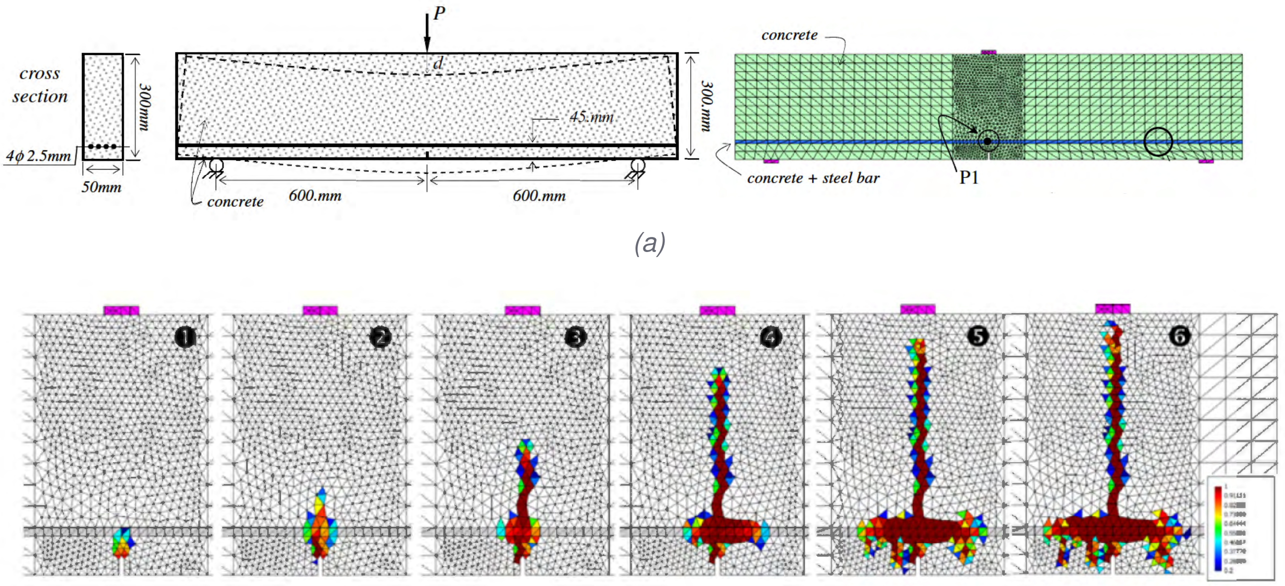

(a)

(b)

*Figure 1-27: **(a)** Numerical simulation corresponding to a three-point bending test on a RC beam. **(b)** Active crack pattern at different stages of the RC beam behavior [62].*

In addition, cracks density and opening are parameters conditioning rebars corrosion, even for very thin cracks (100 μm opening) [71]. Crossing cracks (cracks opened through all the thickness of a concrete element) are identified as very detrimental alteration regarding structural viability. Indeed, in such a case, fluids can easily flow through the crack, developing material leaching and, therefore, making easier aggressive fluids penetration within material. For a non-crossing crack, the partial self-fill in of crack with dust and corrosion products can generally be observed. It is a favorable factor, reducing the ingress of external fluids [72].

To conclude, the crack opening in a reinforced concrete structures can vary between wide limits and cannot be estimated precisely. The French standards [64] as well as Eurocode 2 [73] distinguish crack types according to their opening and establish rules to ensure the durability and limit the crack opening. Up to this acceptable limit of crack, the functioning of structures is not considered impaired. The maximum acceptable value of crack width is 300 μm for all exposure classes under the action of quasi-permanent combination of loads. The lower recommended crack width limit may be used for a special condition, such as in a case of water-retaining structures and even in absence of durability problems, a maximal opening of 400 μm is required to preserve safety aspect of the structure. During the design process, the engineers have to control the maximum crack width of structures [74]. However, once existing cracks are observed, their activity and depth must be accounted for, according to their influence on damaging process [75].

I.3.2. NDT techniques and sensing systems for crack identification

Nowadays, visual inspection is the acclaimed method for the crack inspection. However, along with the works presented in the previous section, there were some developments on the methods used to monitor the cracks propagation and quantify their crack openings. In the manual inspection, the sketch of the crack is prepared manually, and the conditions of the irregularities are noted. Since the visual approach completely depends on the specialist's knowledge and experience, it lacks objectivity in the quantitative analysis. Having information about the type, number, width and length of the cracks on the structural surface gives insight about the earliest degradation level and carrying capacity of the concrete structures [76]. The crack detection may be of many types depending on the parameter with which the crack detection is made possible. Some of the objective which makes this analysis possible: length, width, depth, position, surface and direction of propagation of the crack [77].

SHM aims to achieve cracks detection at an early stage of crack development and in general, cracks are randomly distributed to the structure. Nowadays, there are other techniques as Smart Films [78, 79], or Image processing [80, 81] for crack monitoring. A classical tool such as the crack-measuring-microscope allows measuring the crack width on the surface of the structure. The user has to make a direct contact to the specimen to measure the opening which is sometimes inconvenient. Crack Opening Displacement (COD) gauge is another tool that can be used to measure the crack tip opening [82, 83] for notched beams. Meanwhile, for larger structures where crack positions are unknown, Digital Image Correlation is favored.

The Digital Image Correlation (DIC) was originally developed by Sutton et al. [84] to study the evolution of the displacement field of a specimen subjected to a mechanical loading. This technique has been established experimentally to measure the crack opening, the crack spacing and the cracking pattern in concrete materials domain [82, 69, 68, 85, 86, 67]. The DIC technique is a contact-less measurement method that acquires images in digital format and performs the analysis based on the observation of a light-dark pattern (applied to the surface of the beam). The image of the pattern is divided into sub-image areas (so-called facets). These facets and their movement, due to the applied load, are identified and followed using the images taken during the test. Therefore, this system allows measuring the available vertical and horizontal displacement fields of a set point on a surface [82]. The observation of the behavior beyond the failure point of a material is possible. The latest DIC system uses two synchronously triggered cameras. Since the cameras are calibrated photogrammetrically in a stereo arrangement (Figure 1-28a), the 3D coordinates of the corresponding material areas can be determined from the image positions of the facets, which lead to calculating displacement and deformation parameters while correcting any slight in-depth movement (forward or backward) of the specimen during the test.

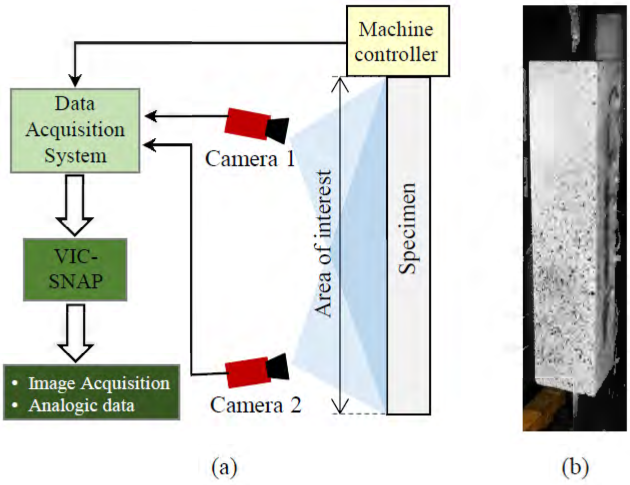

*Figure 1-28: **(a)** Sketch of the DIC system. **(b)** RC prismatic specimen with the speckle pattern [67].*

To use DIC, a speckle pattern (in black and white colors) is applied on the region of interest (Figure 1-28b). This speckle can be made by a spray paint forming a random pattern. During the test, the digital cameras capture successively the white or black dots following the deformation or the displacement of the specimen. An iterative procedure of correlation using Fourier transform is necessary. From this procedure, we can obtain displacement field that can be used for further analysis. Furthermore, with some refinement and color gradation, the crack pattern can be reproduced visually. In a work using DIC by Michou et al. [67], pre-stressed beams were subjected to a four-point bending load. The extraction of the crack opening was obtained from the displacement field. In Figure 1-29a, a representation of a displacement field is shown in 3D. The crack width is measured at the level of the passive reinforcement on the bottom part of the beam. So, along with the line AB, a displacement field is extracted and results in a stair-shaped curve as presented in Figure 1-29b. The jumping value in horizontal displacement indicates the crack opening. Then, multiple linear interpolations are used to obtain the crack opening. Evidently, the accuracy of the crack measurement depends on several parameters, such as the quality of the photography, the lighting (brightness and contrast) and the speckle pattern.

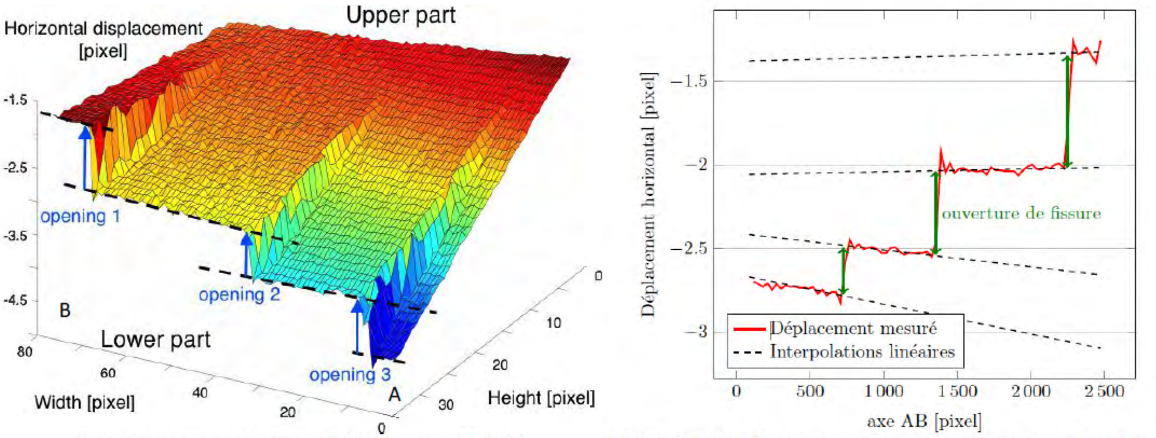

(a). 3D representation of displacement field. (b). Multiple linear regression to obtain crack width.

Figure 1-29: Extraction of the COD from the displacement fields measured by DIC [67].

I.3.3. DFOS techniques for crack identification: a promising tool

Many research studies on the ability to implement distributed sensing techniques using a single optical fiber to detect crack formation had been performed. DOFSs techniques based on measuring losses with OTDR technique and micro-bending in a single fiber optic were developed for crack detection by correlating the losses to the number of cracks and crack openings [87, 88, 89, 90, 91, 92]. However these methods are very limited in practical applications.

In the case of DOFSs based on Brillouin backscattering, methods to measure cracks in concrete structural elements were developed for BOTDR and BOTDA systems offering a spatial resolution of 1 m [93, 94, 95]. All these methods have been well established in laboratories with acceptable results, but they can still be improved. Some recent research prototypes of Brillouin Optical Coherent Domain Analysis BOCDA technique figure a better spatial resolution close to 3 cm [96, 97]. The limitation of these techniques in terms of local damage detection is mainly related to the strain sensing accuracy around a crack in the concrete material, which is greatly influenced by the spatial resolution [43, 44]. As a matter of fact, the complicated strain distribution and its rapid variation within the spatial resolution, mainly decreases the strain measurement accuracy [98].

On the other hand, high spatial resolution in OBR measurement systems based on OFDR techniques contributed in achieving high sensitivity to crack propagation and a precise estimation of the cracks location over big areas of the structure [99], contrary to short gauge and long gauge sensors (Figure 1-30).

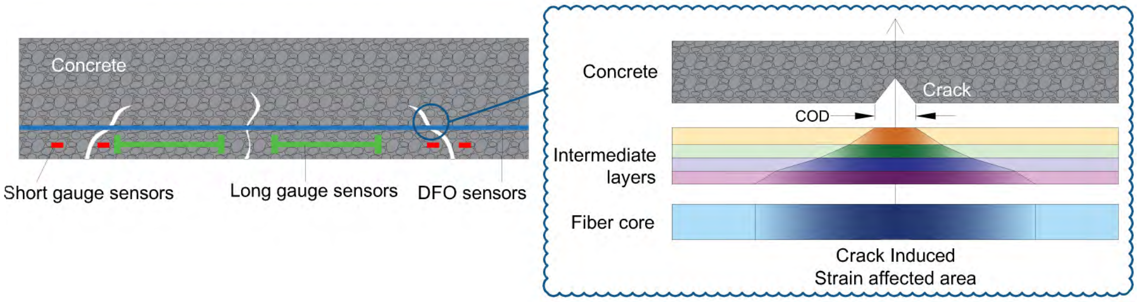

Figure 1-30: Crack detection using DFOS techniques [100].

Henault et al. [49] tested a reinforced concrete (Figure 1-31a) with two different optical fiber cables glued on the surface and embedded inside the concrete material as shown in Figure 1-31b. While DFOS strain values measured by an OBR system in the compression zone (level 1) and next to the neutral axis (level 2) remained consistent with those of the conventional Vibrating Wire Gauges (VWG) sensors, peaks in the strain profiles in the tension zone (level 3) correspond to the position of the cracks localized by visual inspection at high-loading levels (Figure 1-31c).

Rodriguez et al. [101, 102] confirmed the results established by Henault, by gluing an optical fiber with a primary coating on the surface of a RC slab. In addition, the authors proposed a method to obtain crack initiation, location and width in concrete structure subject to bending. The method is based on calibrating a finite element model of the structure using the millimetric spatial strain measurements using the OBR system. The experimental and theoretical strain distribution presented a relatively good fit.

Brault and Hoult [103, 54] adopted a method to evaluate the strain gradients in order to evaluate the crack widths. The interval over which the sum of strain gradients should be calculated is based crack spacing. The results showed that the FOS strain measurements from reinforced elements using the OBR4600 and a nylon coated fiber optic cable can be used to measure crack widths up to 300 μm. In addition, the authors detected irrecoverable strains due to the concentrated opening of a simulated crack, raising the question about whether their technique could be used to monitor cyclic or long-term behavior of concrete elements.

Recently, Fischer et al. [104] performed a four-point bending test on a reinforced concrete beam in order to investigate the effect of the application method (glued to the concrete surface, applied to reinforcing bars or directly embedded in concrete) and the configuration of the optical fiber cable on the robustness of the strain measurements. Therefore, in addition to Polyimide and Nylon-coated fibers, some of the previously mentioned robust measuring cables (V0, V1 and V9 from Brugg Kabel AG) were also investigated (Figure 1-32). The authors proposed an automated evaluation of the measured strain curves by assigning strain gradients intervals for each crack and defining the sum of strain gradients as the fiber elongation and thus the crack opening.

Sienko et al. [105] also performed a tensile axial test on a prismatic specimen instrumented with an optical fiber surrounded by a tight protective jacket.

Similar to [104], the crack widths were defined as the sum of fiber elongations (strains integral) within the sections between the cracks. Thus, despite using optical fibers in a tight jacket which mediates in the strain transfer, the results obtained were suitable for the assessment of the structural condition of the members under consideration within the range of 50 μm. The authors claimed that increased error in the estimated crack widths in the range of 100-300 μm, are due to the presence of

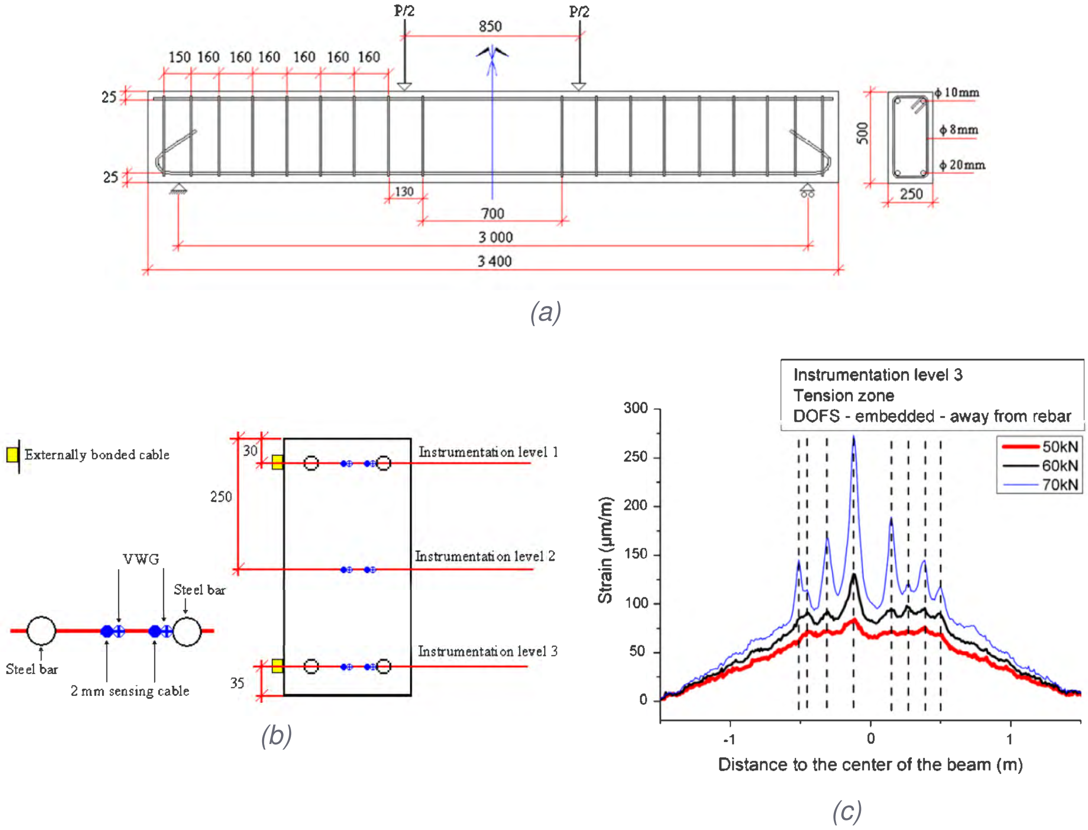

Figure 1-31: ***(a)*** *Shop drawing of the tested RC beam.* ***(b)*** *Positions of the Vibrating Wire Gauges (VWG) and optical fiber cables.* ***(c)*** *Peaks in the OBR distributed strain measurements corresponding to the location of multiple cracks [49].*

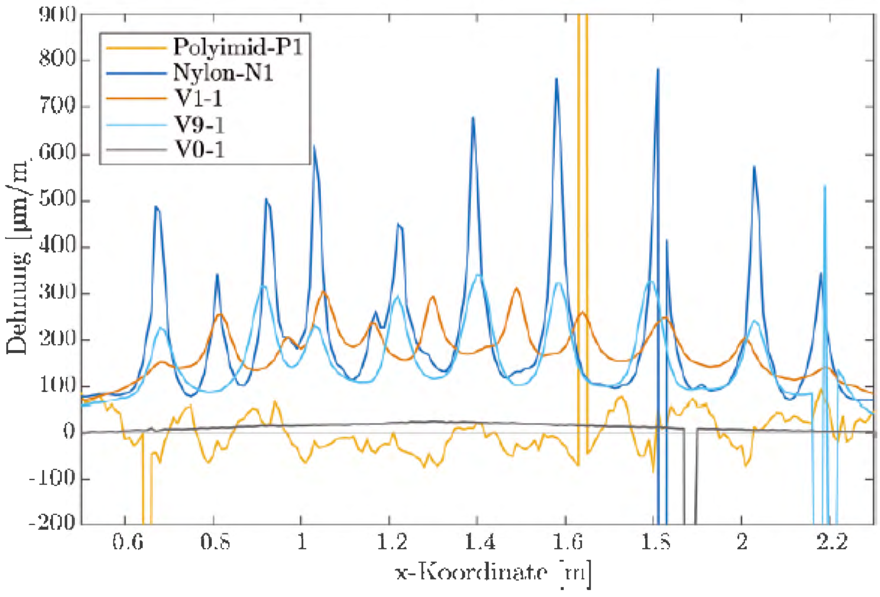

Figure 1-32: Spatial strain distribution of different types of optical cables in a cracked reinforced concrete beam [104] .

a tight plastic jacket protecting the glass core of the fiber. Therefore, attention should be paid to the limitations of adopting the model of strain transfer from the medium under test, through the protective layers, to the glass fiber. Thus, this work put the spot light on the necessity of taking into account many parameters such as adhesion between concrete and protective coating, adhesion between the protective coating and the glass core, parameters of adhesive agent used for the fiber installation on the concrete surface or reinforcing bars.

I.3.4. Strain transfer mechanism between the FOS and the host material

The mechanisms of strain transfer through the intermediate layers have been demonstrated through the spatially distributed measurements next to localized events (Figure 1-30) where the role of adhesion between the cable and the surrounding environment has long been argued. Some studies have notably led to the development of optical cables with rough exterior surface or with mechanical anchorages in order to optimize the adhesion of the cable to the environment of use. However, few works led to the experimental quantification of the adhesion of optical fiber sensors [106]. In most cases, the strain transfer was neglected because a the used sensor is an optical fiber with a simple Polyimide coating, known to have an extremely good adhesion [99, 50, 101]. However, the application of this type of sensor may have strong limitations for the long-term monitoring of exposed structures. Some studies were interested in the issues related to the installation of the sensors. Different types of adhesives are used to attach the optical fiber depending on the host material, like epoxy and cyanoacrylate commercial glue. While cyanoacrylate adhesive showed good performance on steel surfaces, epoxy adhesives were better for concrete material [107, 53].

In 2005, Bastianini et al. [43] highlighted that the crack propagation through the epoxy resin to the optical fiber leads to harsh localized shear stresses (Figure 1-33).

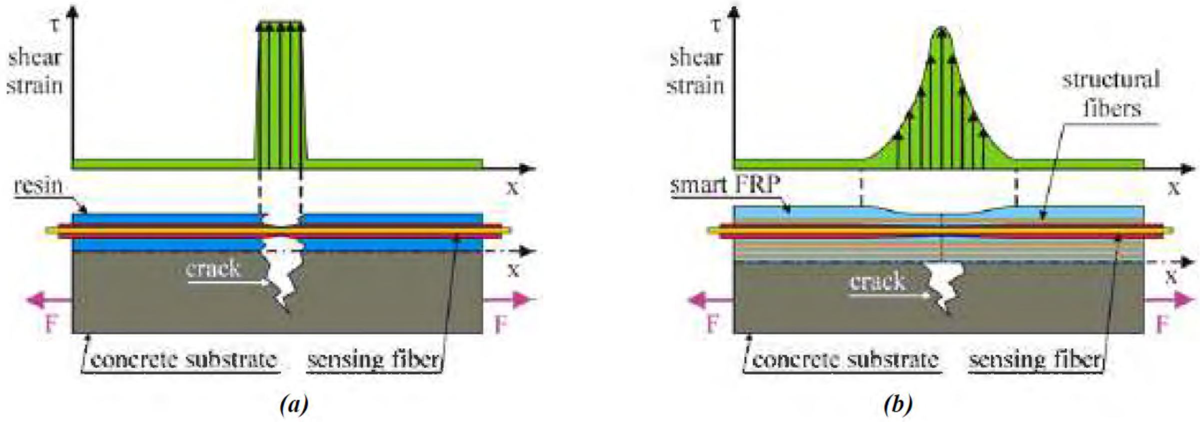

Figure 1-33: Illustration of the distribution of shear stress along the optical fiber in the case of (a) a fiber glued on the structure using epoxy resin or (b) a fiber embedded in a FRP (Fiber Reinforced Polymer) composite bonded to a cracked concrete material [43].

Imai et al. [96] confirmed this theory while using an interrogator with a 29 mm spatial resolution to measure strain profiles over the length of a glued fiber on a Fiber Reinforced Concrete (FRC) beam as shown in Figure 1-34.

The authors proposed that the measured strain by the DFOS system can be explained as the strain transfer from concrete to the optical fiber through the intermediate layers and by taking into account the characteristics of the interrogator (due to averaging over the spatial resolution).

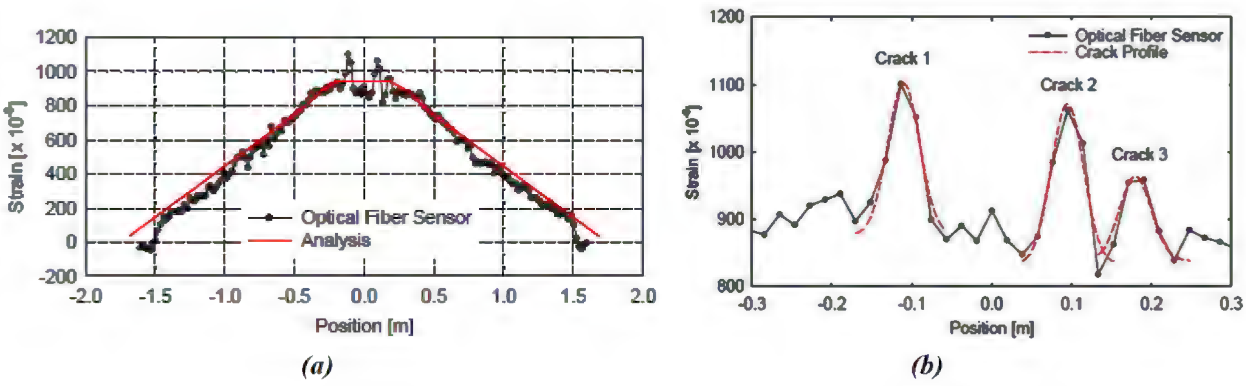

Figure 1-34: **(a)** Spatial strain profile **(b)** Zoom on the central part - measured by a Brillouin interrogator with 29mm spatial resolution, connected to an optical fiber glued on a UHPFRC beam [96].

In order to determine the strain transfer function characterizing the buffering effect of surrounding materials, the cracked concrete was modeled using Finite Element analysis (Figure 1-35a) and the distribution of the crack-induced strain on the sensing segment of the fiber was determined (Figure 1-35b). The authors also mentioned that the effect of the interrogation unit can be neglected when the spatial resolution is very small compared to the anchoring length.

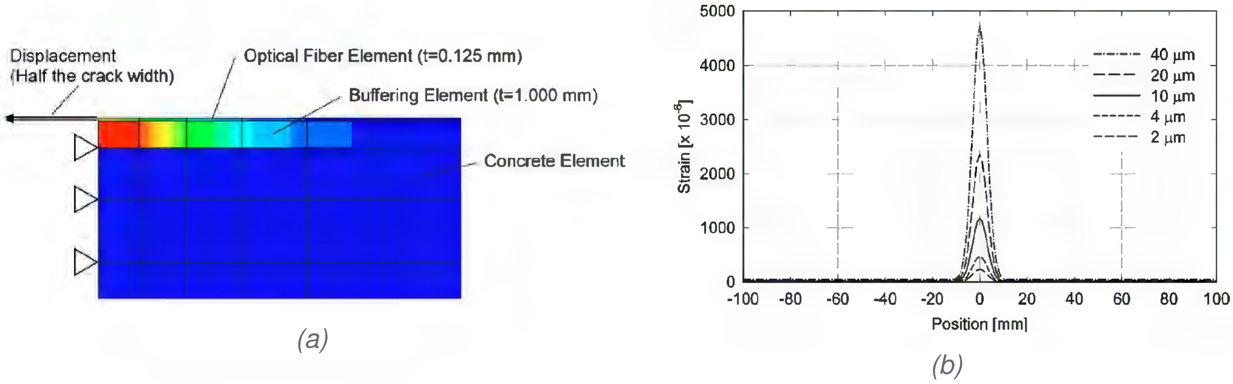

Figure 1-35: **(a)** Two-dimensional Finite Element model mesh used to model the optical fiber/buffering element/cracked concrete medium. **(b)** Strain distribution on the sensing segment of the fiber by Finite Element analysis [96].

Based on the same approach, Henault et al. [108, 57, 109] indicated that the measured strain by the DFOS system $\epsilon_{measured}$ is the result of the convolution of the strain in the host material $\epsilon_m(x)$ by a characteristic function of the interrogator F_{int} and a mechanical transfer function MTF(x) of the optical fiber/intermediate layers/host material system as follows:

$$\epsilon_{measured}(x) = \epsilon_m(x) \otimes F_{int} \otimes MTF(x) \tag{I.9}$$

Neglecting F_{int} leads to $\epsilon_{measured}$ equal to ϵ_f at the level of the optical fiber:

$$\epsilon_{measured}(x) = \epsilon_f(x) = \epsilon_m(x) \otimes MTF(x) \tag{I.10}$$

In addition, the authors assumed that the stress transfer process, carried out from the host material to the optical fiber is a linear mechanism and the MTF(x) of the cable is the impulse response of the mechanical system. Therefore, a crack occurring in the host material was assumed to generate a strain profile at the surface of the cable under the form of a Dirac distribution. As a result, modeling a cable embedded in a host material with a crack opening of 1 μm using Finite Element Modeling (Figure 1-36a), led to determine the cable's MTF(x) that can be fitted by an exponential function (Figure 1-36b) as follows:

$$MTF(x) = Be^{-A|x|} \tag{I.11}$$

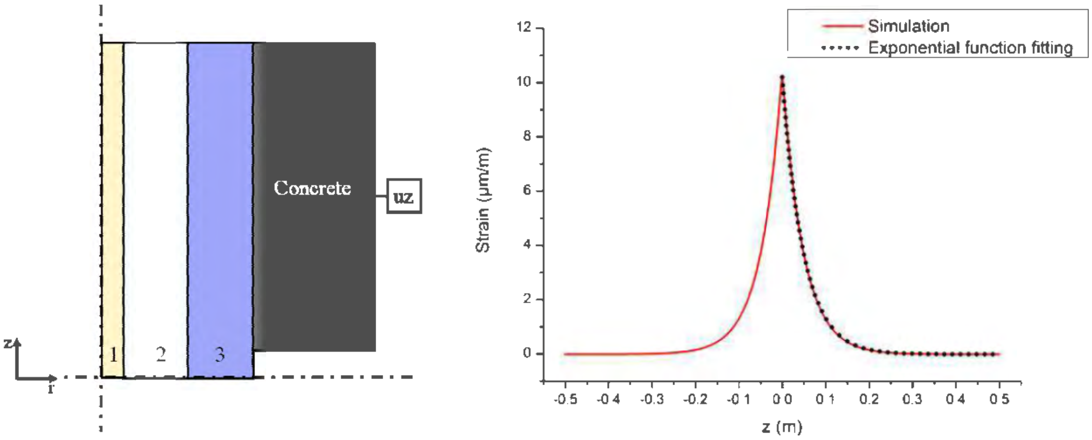

(a) *(b)*

*Figure 1-36: **(a)** Finite Element mesh used to model a cable configuration embedded in a cracked concrete medium. **(b)** Modeled strain profile at the level of the optical fiber MTF(x) [108].*

To perform the finite element simulations, it was important to determine the mechanical properties of the optical fiber/intermediate layers/host material system. In this direction, the authors performed axial tensile and pull-out tests to determine the modulus of elasticity and the stiffness at the interfaces. The biggest crack opening that cable/host material mechanical system can withstand while having an elastic behavior was found to be equal to 200 μm. Reaching this level of crack opening, debonding at the cable/concrete interface and softening of the Hytrel jacket was found to be the most critical failure mechanisms. Later in 2015, Billon et al. [109] deduced the same exponential shape function for another optical cable configuration conceived for concrete surface applications.

On the other hand, and since 2012, few analytical models have been proposed, mainly based on the strain transferring theories proposed for discrete optical fiber sensors. The lead-up equations and different assumptions and boundary conditions will be presented and discussed in the following chapter.

I.4. Conclusion

For civil infrastructures, the main functionality that civil engineers want to preserve in time is its mechanical strength. The tools implemented must allow the assessment of its safety. They must also provide elements to detect the appearance and the monitoring of the evolution of harmful pathologies in the structure. Global and local strain and displacements measurements, and the cracking of concrete, are indicators of the mechanical strength of the structure.

DFOS systems, composed of an interrogator and optical cable, allow spatial distributed strain measurements forming an undeniable asset for health monitoring on civil infrastructures. These techniques can replace many thousands of traditional sensors with only one optical fiber. For industrial use in the context of structural health monitoring, these measurement systems must meet the requirements of the structures owners. During the last decade, the interrogation unit properties improved significantly to almost reach those of the traditional sensors. On the other hand, the behavior of optical cables designed for strain measurements are poorly understood in short-term as well as in the long-term.

Bare optical fibers are fragile. They are protected with a coating giving a sort of ductility and decreasing the probability of rupture especially in cases where there is a stress concentrations (e.g. when a crack is created). Taking this into account, the complete strain transfer from the monitored structure to the sensor is not guaranteed. Many theoretical models have been proposed to deduce a mechanical transfer function while assuming an elastic behavior of the different layers (host material, coatings and bare fiber). Moreover, and during the propagation of a crack, combinations of different kind of phenomenon could happen in the materials. The post-elastic mechanisms of debonding or plasticity have to be discussed to optimize the crack identification process (detection, localization and quantification).

Hence, in this PhD work, these challenges will be approached. Contrary to several years back in time, with the new DFOS technique high performance (in terms of spatial resolution, repeatability, accuracy, etc.), conducting a thorough study of the mechanisms of strain transfer through intermediate layers and validating theoretical models for the optical fiber sensors is now possible and of paramount importance.

Chapter II

Strain transferring from host material to the optical fiber

> ”There are two possible outcomes: if the result confirms the hypothesis, then you’ve made a measurement. If the result is contrary to the hypothesis, then you’ve made a discovery.”
>
> *Enrico Fermi*

Contents

The widespread application of optical fiber sensing technology in structural health monitoring requires high confidence in the strain measurements, particularly in the presence of cracks. Strain transfer analysis, used to determine the action mechanism and to improve the precision of these sensors, is therefore an important issue.

Before introducing the basic equations of the elastic strain transferring theory, it is worth mentioning that historically, the problem of strain transfer through an optical fiber sensor has been studied in the field of short dimensional sensors like Bragg grating or interferometric sensors. Indeed, many research works focused on designing discrete sensors with improved strain transfer efficiency [110] and performing parametric studies of different mechanical and geometrical properties of multilayered sensors [111]. The objective of such studies is to better evaluate the calibration coefficient of a Bragg grating patch, intended to be embedded in or installed on the surface of a structure. Thus, this helps measuring the strain of the host structure as accurately as possible. Applications mainly concern the aeronautical [112], marine [113] and civil engineering [114] sectors.

On the other hand, research studies were also interested in exploring the effect of temperature [115], non-axial stresses [115] and the effect of static fatigue (creep) [116, 117, 118, 119]. In addition, analytical models [120, 121, 122] and Finite Element analysis [123, 124, 125] were investigated for surface bonded sensors. Moreover, Sun et al. [126] proposed a strain transfer model for a clamped Fiber Bragg Grating (FBG) sensor. Problems with strain gradient over the bonding length were also approached [127, 128, 129, 130].

In the next part of this PhD thesis, we will focus only on the strain transfer theory under longitudinal strain. One of the first research on strain transfer was conducted in 1998 by Ansari and Libo [131]. The authors proposed an analytical model for a Silica optical fiber/coating/host material mechanical system. This model is based on the so-called ”strain-lag” approach (or ”shear-lag” in the case of shear stress calculation) which was developed initially for the study of bonded assemblies in 1938 by Völkersen [132] and now commonly applied to bonded structural reinforcement composites. To establish a relationship between the strain in the host material $\epsilon_m(z)$ and the strain measured by the optical fiber $\epsilon_f(z)$, Ansari considers a uniform longitudinal strain $\epsilon_m(z) = \epsilon_m$ applied along the optical fiber. In addition, the strain in the center of the optical fiber is assumed to be equal to the one in the host material ($\epsilon_f(0) = \epsilon_m(0)$). From the equilibrium equations, he obtained :

$$\epsilon_f(z) = \epsilon_m \left(1 - \frac{\sinh(\lambda\,|z|)}{\sinh(\lambda\,L)}\right) \tag{II.1}$$

where λ is the strain lag parameter which depends on the fiber optic sensor's geometry and mechanical characteristics. This strain lag parameter is given by :

$$\lambda = \frac{2\,G_p}{r_f^2\,E_f\,\ln\left(\frac{r_p}{r_f}\right)} \tag{II.2}$$

where G_p is the shear modulus of the protective coating. E_f and r_f are the Young modulus and the radius of the bare optical fiber, respectively.

Ansari's model depicts well the strain transfer as long as $\lambda\,L > 5.3$, which guarantees the validity of the assumption $\epsilon_f(0) = \epsilon_m(0)$. When $\lambda\,L < 5.3$, the strain in the center of the optical fiber can be significantly different from the strain in the host material. Thus, in 2006, D. Li et al. [133] proposed an improvement of Ansari's model to overcome this limitation.

In view of the elements from the literature, this chapter is dedicated to discuss the strain-transferring mechanism. For this purpose, we need to explore first the fundamental mechanical properties of an optical fiber. Then, a general elastic strain transferring theory, based on D. Li [133] assumptions and boundary conditions, will be discussed in the case of continuous and fractured host materials. This theory is established by assuming an elastic behavior and perfect interfacial bonding of different layers composing the mechanical system. Therefore, the post-elastic strain transfer is also discussed and a new strain transfer analysis taking into account an imperfect bonding at the layer's interfaces is established for three-layer and multi-layer systems.

II.1. Fundamental mechanical properties of optical fibers

An optical fiber is a flexible transparent fiber made of very pure glass after being drawn from a molten glass perform. Silica is the most common material used for optical fibers, especially for sensing applications. These optical fibers made of fused silica are perfectly elastic until their breaking point. They are brittle when over stressed.

Typical mechanical properties of the optical fiber are listed in Table 2-1. These mechanical properties may vary around the values listed in the table due to different manufacturing processes. For most sensor applications, the strength of structural members to be measured is much lower than the strength of the silica fiber. The optical fiber can reach a maximum tensile strain of 100000 μm/m [134]. The presence of many microscopic flaws can lower the strength of the fiber from 4.8 GPa to 0.35 GPa. Typically, these fibers are proof tested by the manufacturers to 0.35 GPa, corresponding to 0.5 % of the strain. Fatigue tests showed that optical fibers have a long working life when its operating stress is a small fraction of the proof stress [135].

Material	Mechanical parameter	Values
Silica glass	Young modulus E (in GPa)	73
	Tensile strength σ_t (in GPa)	$3.5 - 48$
	Breaking strain ϵ (in $\mu\mathrm{m}/\mathrm{m}$)	100000
Acrylate coating	Young modulus E (in GPa)	0.7
	Tensile strength (in GPa)	0.026
	Poisson ratio ν	$0.17 - 0.48$
Polyimide coating	Young modulus E (in GPa)	2.4
	Tensile strength (in GPa)	0.13
	Poisson ratio ν	$0.17 - 0.48$

Table 2-1: Mechanical properties of the optical fiber [134].

As shown in Table 2-1, the Young modulus of the fiber core is typically much larger than that of the coating or the adhesive. As a matter of fact, the axial elastic displacements of the fiber and the host material can be very different. Thus, once a strain localization event appears at the level of the coating, it will be diffused and measured over an important length of the optical fiber.

II.2. Basics equations of the elastic strain transferring theory

The general framework used to describe the strain transfer from the host material to the core of a fiber optic sensor is relied on continuum mechanics. As shown in Figure 2-1, a three-layer model is considered in which the optical fiber is surrounded by a host material. The core of the optical fiber (of diameter 9 μm for a single mode fiber) and the optical cladding (of diameter 125 μm for a single mode fiber) are assumed to have similar mechanical properties. In the Figure, r_f and r_p are the radius of the bare optical fiber and of the protective coating, respectively. Moreover, the optical fiber is assumed to be bonded to the host material over a finite length ($2L$). The stress states of the optical fiber and the protective layer micro sections are illustrated in Figure 2-1b: σ, τ, u represent respectively the normal stress, the shear stress and the axial deformation exerted on the optical fiber (f), protective coating (p) and host material (m) layers.

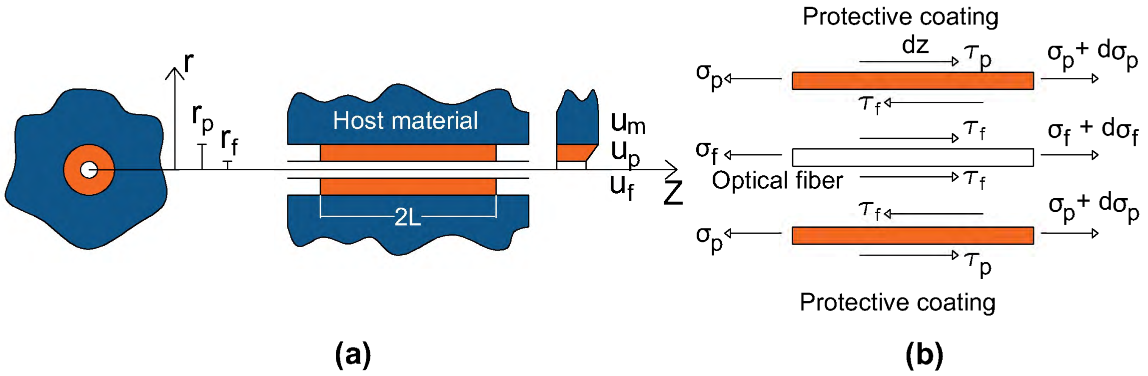

Figure 2-1: (a) Structure of the three layered system (b) stress state of the protective layer and the optical fiber micro sections.

The basic equations of the elastic strain transferring theory presented in this section are obtained by considering that all the constitutive layers of the strain transfer system (i.e. fiber core, protective coating and host material) are isotropic and behave in a linear elastic manner. Therefore, the stress/strain relationship can be expressed through the generalized Hooke's law:

$$\overline{\overline{\epsilon}} = S\overline{\overline{\sigma}} \tag{II.3}$$

where $\overline{\overline{\epsilon}}$ and $\overline{\overline{\epsilon}}$ are the stress and the strain tensor which are related by S usually called compliance tensor.

Given the geometry of the optical fiber, the cylindrical coordinates (r, θ and z) are well adapted to the strain transfer description and the generalized Hooke's law is given in this coordinate system by:

$$\begin{bmatrix} \epsilon_r \\ \epsilon_\theta \\ \epsilon_z \\ \gamma_{r\theta} \\ \gamma_{zr} \\ \gamma_{\theta z} \end{bmatrix} = \begin{vmatrix} \frac{1}{E} & -\nu & -\nu & 0 & 0 & 0 \\ -\nu & \frac{1}{E} & -\nu & 0 & 0 & 0 \\ -\nu & -\nu & \frac{1}{E} & 0 & 0 & 0 \\ 0 & 0 & 0 & \frac{1}{G} & 0 & 0 \\ 0 & 0 & 0 & 0 & \frac{1}{G} & 0 \\ 0 & 0 & 0 & 0 & 0 & \frac{1}{G} \end{vmatrix} \begin{bmatrix} \sigma_r \\ \sigma_\theta \\ \sigma_z \\ \tau_{r\theta} \\ \tau_{zr} \\ \tau_{\theta z} \end{bmatrix} \tag{II.4}$$

where:

- ϵ_i and σ_i are respectively the strain and normal stress in the i-direction
- γ_{ij} and τ_{ij} are respectively the engineering shear strain and the shear stress in the i-j plane
- E and G are the modulus elasticity in tension (or compression) and in shear respectively.
- ν is the Poisson's ratio

and

$$G = \frac{E}{2\,(1+\nu)} \tag{II.5}$$

The strain-displacement relationships in the cylindrical coordinates is also given by:

$$\epsilon_r = \frac{\partial u_r}{\partial r} \quad \text{(II.6a)} \qquad \gamma_{r\theta} = \frac{\partial u_\theta}{\partial r} + \frac{1}{r}\frac{\partial u_r}{\partial \theta} - \frac{u_\theta}{r} \quad \text{(II.6b)}$$

$$\epsilon_\theta = \frac{u_r}{r} + \frac{1}{r}\frac{\partial u_\theta}{\partial \theta} \quad \text{(II.6c)} \qquad \gamma_{\theta z} = \frac{1}{r}\frac{\partial u_z}{\partial \theta} + \frac{\partial u_\theta}{\partial z} \quad \text{(II.6d)}$$

$$\epsilon_z = \frac{u_z}{z} \quad \text{(II.6e)} \qquad \gamma_{zr} = \frac{\partial u_r}{\partial z} + \frac{\partial u_z}{\partial r} \quad \text{(II.6f)}$$

where u_i is the displacement in r, θ and z directions.

The assumptions used in the strain transfer analysis proposed by D. Li [133] are the following:

- The host material and the optical fiber are isotropic materials that deform essentially under the effect of a tensile stress (the Poisson ratio ν is neglected). So, only the longitudinal strain ϵ_z is taken into account and from Equation II.4, it is given by :

$$\epsilon_z = \frac{\sigma_z}{E} - \nu\left(\frac{\sigma_r}{E} + \frac{\sigma_\theta}{E}\right) \simeq \frac{\sigma_z}{E} \tag{II.7}$$

- The coating has a very low shear modulus G_p compared to those of the host material and silica fiber, so that :

$$\frac{r_p^2 - r_f^2}{r_f^2}\frac{E_p}{E_f} \ll 1 \tag{II.8}$$

- The coating deforms essentially under the effect of shear stress and the radial displacements u_r are assumed to be small compared to the axial displacements u_z (noted u_p in the coating). So from Equations II.4 and II.6f the shear stress $\tau_{z\,r}$ in the coating noted τ_p is given by:

$$\tau_p(r,z) = G_p\,\gamma_p(r,z) \simeq G_p\frac{\partial u_p}{\partial r} \tag{II.9}$$

- Since the protective layer is strained together with the optical fiber, the strain gradients are expected to be of the same order:

$$\frac{\mathrm{d}\epsilon_f(z)}{\mathrm{d}z} \simeq \frac{\mathrm{d}\epsilon_p(z)}{\mathrm{d}z} \tag{II.10}$$

  Noted that this assumption is the main difference with the Ansari's model.

- The bonding at the interfaces is perfect and therefore, the axial displacement in the fiber u_f, the protective coating u_p and the host material u_m are related as follows:

$$u_p(r_p,z) = u_m(r_p,z) \quad \text{and} \quad u_p(r_f,z) = u_f(r_f,z) \tag{II.11}$$

Considering the force equilibrium at each of the optical fiber and the protective layer, allows us to establish the following equations:

$$\tau_f(r_f,z) = -\frac{r_f}{2}\frac{\mathrm{d}\sigma_f(z)}{\mathrm{d}z} \tag{II.12}$$

$$\tau_p(r,z) = \frac{r_f}{r}\tau_f(z,r_f) - \frac{r^2 - r_f^2}{2r}\frac{\mathrm{d}\sigma_p(z)}{\mathrm{d}z} \quad \text{for } r_f \leq r \leq r_p \tag{II.13}$$

Replacing Equation II.12 in Equation II.13 leads to:

$$\tau_p(r,z) = -\frac{r_f^2}{2r}\frac{\mathrm{d}\sigma_f(z)}{\mathrm{d}z} - \frac{r^2 - r_f^2}{2r}\frac{\mathrm{d}\sigma_p(z)}{\mathrm{d}z} \tag{II.14}$$

According to assumption II.7, we also have:

$$\frac{\mathrm{d}\sigma_p(z)}{\mathrm{d}z} = E_p\frac{\mathrm{d}\epsilon_p(z)}{\mathrm{d}z} \quad \text{and} \quad \frac{\mathrm{d}\sigma_f(z)}{\mathrm{d}z} = E_f\frac{\mathrm{d}\epsilon_f(z)}{\mathrm{d}z} \tag{II.15}$$

Thus, Equation II.14 can be rewritten as follows:

$$\tau_p(r,z) = -\frac{E_f r_f^2}{2r}\frac{\mathrm{d}\epsilon_f}{\mathrm{d}z}\left(1 + \frac{r^2 - r_f^2}{r_f^2}\frac{E_p}{E_f}\right) \tag{II.16}$$

With the assumption II.8, this last relation can be simplified to:

$$\tau_p(r,z) = -\frac{E_f r_f^2}{2r}\frac{\mathrm{d}\epsilon_f}{\mathrm{d}z} = -\frac{E_f r_f^2}{2r}u_f''(z) \tag{II.17}$$

Taking assumption II.9 and integrating equation II.17 over the thickness of the protective coating allows us to calculate the shear deformation in the coating:

$$\Delta u_p(z) = u_p(r_p,z) - u_p(r_f,z) = \int_{r_f}^{r_p}\frac{\partial u_p}{\partial r}\mathrm{d}r = \frac{1}{G_p}\int_{r_f}^{r_p}\tau_p(r,z)\mathrm{d}r \tag{II.18}$$

By using the relation II.17, we can obtain :

$$\Delta u_p(z) = u_p(r_p,z) - u_p(r_f,z) = -\frac{r_f^2}{2}\frac{E_f}{G_p}\ln\left(\frac{r_p}{r_f}\right)u_f''(z) \tag{II.19}$$

As we assume a perfect bonding at the interfaces (assumption II.11), The displacement $\Delta u_p(z)$ can be expressed as a function of the displacements in the host material $u_m(r_p,z)$ and the fiber core $u_f(r_f,z)$:

$$\Delta u_p(z) = u_m(r_p,z) - u_f(r_f,z) = -\frac{r_f^2}{2}\frac{E_f}{G_p}\ln\left(\frac{r_p}{r_f}\right)u_f''(z) \tag{II.20}$$

which can be written as:

$$u_f''(z) - \lambda^2 u_f(z) = -\lambda^2 u_m(z) \tag{II.21}$$

where the strain lag parameter λ is equal to:

$$\lambda^2 = \frac{2\,G_p}{E_f r_f^2 \ln\left(\frac{r_p}{r_f}\right)} \tag{II.22}$$

Equation II.21 is the main equation that governs the strain transfer between different layers. Notice that the strain lag parameter λ is the same as one obtained by Ansari. However, the strain transfer function which can be deduced from Equation II.21 is different, as it will be demonstrated in the next section.

II.2.1. Strain transfer in a continuous host material

The differentiation of Equation II.21 yields:

$$\epsilon_f''(z) - \lambda^2 \epsilon_f(z) = -\lambda^2 \epsilon_m(z) \tag{II.23}$$

In the case of a continuous host material, the strain $\epsilon_m(z)$ can be assumed to be constant over the bonding length $2\,L$ and the solution of Equation II.23 yields the normal strain in the fiber core as:

$$\epsilon_f(z) = C_1 e^{\lambda\, z} + C_2 e^{-\lambda\, z} + \epsilon_m \tag{II.24}$$

where C_1 and C_2 are the integration constants. The symmetric nature of the three-layered structure and the fact that no more strain transfer between the fiber and the host material exists at both extremities ($z = L$ and $z = -L$), allow us to fix the following boundary conditions:

$$\epsilon_f(-L) = \epsilon_f(L) = 0 \quad \text{and} \quad \epsilon_f'(-L) = \epsilon_f'(L) = 0 \tag{II.25}$$

Hence:

$$C_1 = C_2 = -\frac{\epsilon_m}{2\cosh \lambda L} \tag{II.26}$$

and finally:

$$\epsilon_f(z) = \epsilon_m \left(1 - \frac{\cosh \lambda\, z}{\cosh \lambda L}\right) \tag{II.27}$$

Equation II.27 is the governing equation that describes the strain distribution along the fiber in the case of a uniform strain in the host material. This last relation, different from the strain transfer relation established by Ansari (see Equation II.1), allows to have $\epsilon_f(0) \neq \epsilon_m$. The latter is the main improvement in D. Li's model compared to Ansari's model.

Figure 2-2 presents the variation of the normalized longitudinal deformation for two different bonding length $2L$ equal to 40 cm and 80 cm with several values of λ fixed arbitrary.

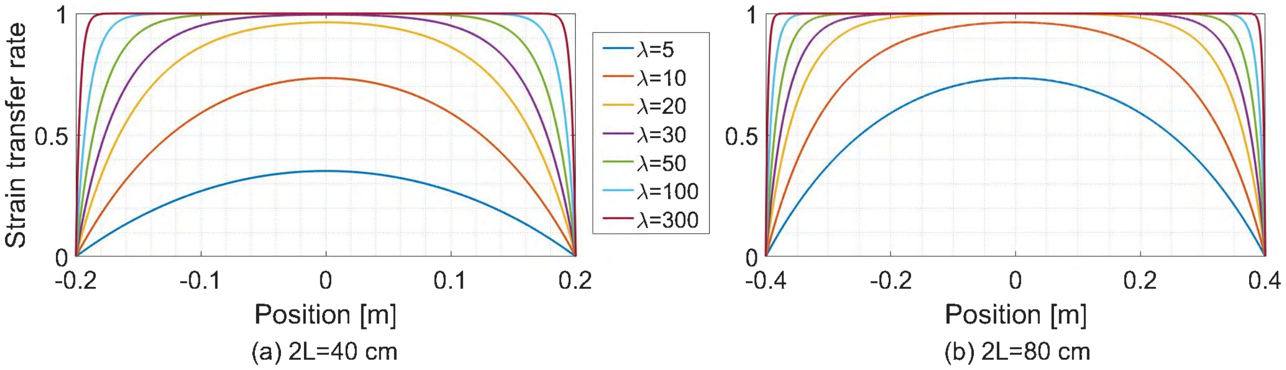

(a) 2L=40 cm (b) 2L=80 cm

*Figure 2-2: Variation of the strain transfer rate at the level of the optical fiber $\frac{\epsilon_f}{\epsilon_m}$ for different λ values and over a bonding length of **(a)** $2\,L$=40 cm and **(b)** $2\,L$=80 cm.*

These curves show that the strain at the level of optical fiber is not uniform over the bonding length and it could be quite different from the strain in the host material. An increase in the strain lag parameter λ leads to better strain transfer rates. In addition, for $\lambda >$30m^{-1} and $\lambda >$20m^{-1} corresponding to $2L$=40 cm and $2L$=80 cm respectively, we can observe that there exist a distance from the bonding end where the strain transfer can be considered as total.

In 2012, D. Li [134] generalized the strain transfer equation for a system composed of n intermediate layers. He obtained the same strain transfer function as in the case of the three-layer model:

$$\epsilon_f(z) = \epsilon_m \left(1 - \frac{\cosh(\lambda\, z)}{\cosh(\lambda\, L)}\right) \tag{II.28}$$

However, the strain lag parameter is different and is given by :

$$\lambda = \frac{2}{r_f^2 E_f \left[\sum_{i=2}^{n} \frac{1}{G_i} \ln\left(\frac{r_i}{r_{i-1}}\right) + \frac{1}{G_1} \ln\left(\frac{r_1}{r_f}\right)\right]} \tag{II.29}$$

where r_i and G_i are the inner radius and the shear modulus of the ith layer of protective coating, respectively.

This result puts the spotlights on the fact that strain lag parameter is a fundamental parameter in the strain transfer that includes all the mechanical and geometrical characteristics of the fiber optic sensor.

II.2.2. Strain transfer in a fractured host material

After applying the D. Li's model to the case of continuous material, we can now investigate the case of fractured host material. Figure 2-3 represents schematically a three-layer system figuring a discontinuity in the host material at $x = 0$. The width of this discontinuity is called the Crack Opening Displacement (COD).

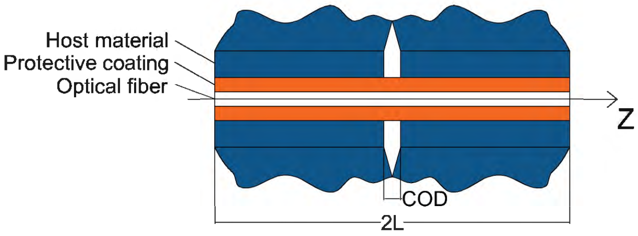

Figure 2-3: Three layered strain transfer system figuring a discontinuity in the host material.

Since 2012, three models (analytical and numerical) [97, 94, 136] were proposed to describe the strain transfer function in the presence of a crack in the host material. Figure 2-4 compares the way that the crack effect is introduced in these three strain transfer models.

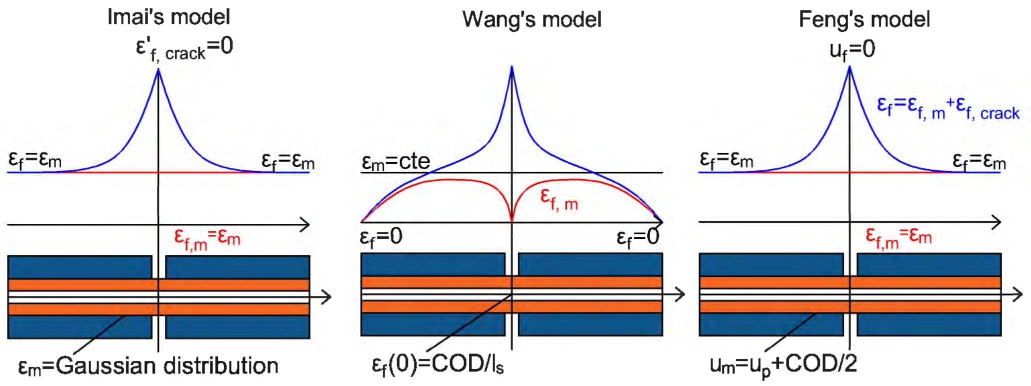

Figure 2-4: Comparison of different boundary conditions and crack-induced effect assumptions between the three analytical models proposed in the literature.

Imai et al. [97] adapted the assumption proposed previously by Duck et al. [137], by introducing the effect of a crack discontinuity in the host material as a Gaussian distribution at the contact interface with the protective coating:

$$\epsilon_m(r_p, z) = \epsilon_p(r_p, z) = \epsilon_m\, e^{-4\,\ln 2\left(\frac{z}{\Delta z_m}\right)^2} \tag{II.30}$$

This last equation is a function of the position z and the full width to half maximum Δz_m, which depends on the crack opening (COD). The authors use it as an input to finite element model and their results show that the crack-induced strain distribution in the optical fiber takes the form of an exponential distribution.

Wang et al. [138] fixed the strain at the crack location as the average the crack opening over the spatial resolution ℓ_s of the measurement instrument as follows:

$$\epsilon_f(z = 0) = \frac{\mathrm{COD}}{\ell_s} \tag{II.31}$$

It is clear that this assumption is mainly dependent on the spatial resolution, varying from a measuring instrument to another. As it takes into account the averaging effect of the interrogator, it seems to neglect the buffering effect of intermediate layers in the area surrounding the crack location. Therefore, this assumption seems to be a very simplifying approximation of the strain transfer mechanism next to crack location.

Feng et al. [94] introduced the COD in D. Li's model as an additional local discontinuity in the host material deformation field:

$$u_m(r_p, z) = \int_0^z \epsilon_m(z)\mathrm{d}z + \frac{\mathrm{COD}}{2} \quad \text{for} \quad z \geq 0 \tag{II.32}$$

For uniform strain in the host material: $\epsilon_m(z) = \epsilon_m$, the integral II.32 is simply $\epsilon_m\, z$ and Equation II.21 becomes for $z \geq 0$:

$$u_f''(z) - \lambda^2 u_f = -\lambda^2 \left(\frac{\mathrm{COD}}{2} + \epsilon_m\, z\right) \tag{II.33}$$

which general solution is:

$$u_f(z) = C_1 e^{\lambda\, z} + C_2 e^{-\lambda\, z} + \epsilon_m\, z + \frac{\mathrm{COD}}{2} \tag{II.34}$$

Differentiation of Equation II.34 with respect to z yields the normal strain in the fiber core:

$$\epsilon_f(z) = \lambda C_1 e^{\lambda z} - \lambda C_2 e^{-\lambda z} + \epsilon_m \tag{II.35}$$

where C_1 and C_2 are the integration constants.

As the deformation discontinuity only creates a localized strain in the vicinity of the crack location, the strain at an z position far away from the crack location should be only affected by the nominal strain of host material. As $-\lambda C_1 e^{\lambda z} \to \infty$ for $z \to \infty$, this mathematical term does not represent a solution for the discussed physical problem. As a result, C_1 can be assumed to be equal to 0.

In addition, considering a symmetrical response of the optical fiber allows us to assume $u_f(0) = 0$, leading to:

$$C_2 = -\frac{\mathrm{COD}}{2} \tag{II.36}$$

As a result, the final strain transfer equation can be written as follows:

$$\epsilon_f(z) = \epsilon_m + \frac{\mathrm{COD}}{2}\lambda e^{-\lambda |z|} \tag{II.37}$$

Figure 2-5 illustrates the strain variation over the length of the optical fiber for several values of λ and COD. We can clearly observe that an increase in λ leads to higher peak amplitude at the crack location (z=0), as well as a decrease in the length of the optical fiber affected by this crack-induced strain. On the other hand, an increase in COD leads to an increase in the peak amplitude without affecting the shape of the exponential and the affected region. The strain at the crack location (z=0) is equal to $\frac{\mathrm{COD}}{2}\lambda$ and therefore varies linearly in function of the crack opening.

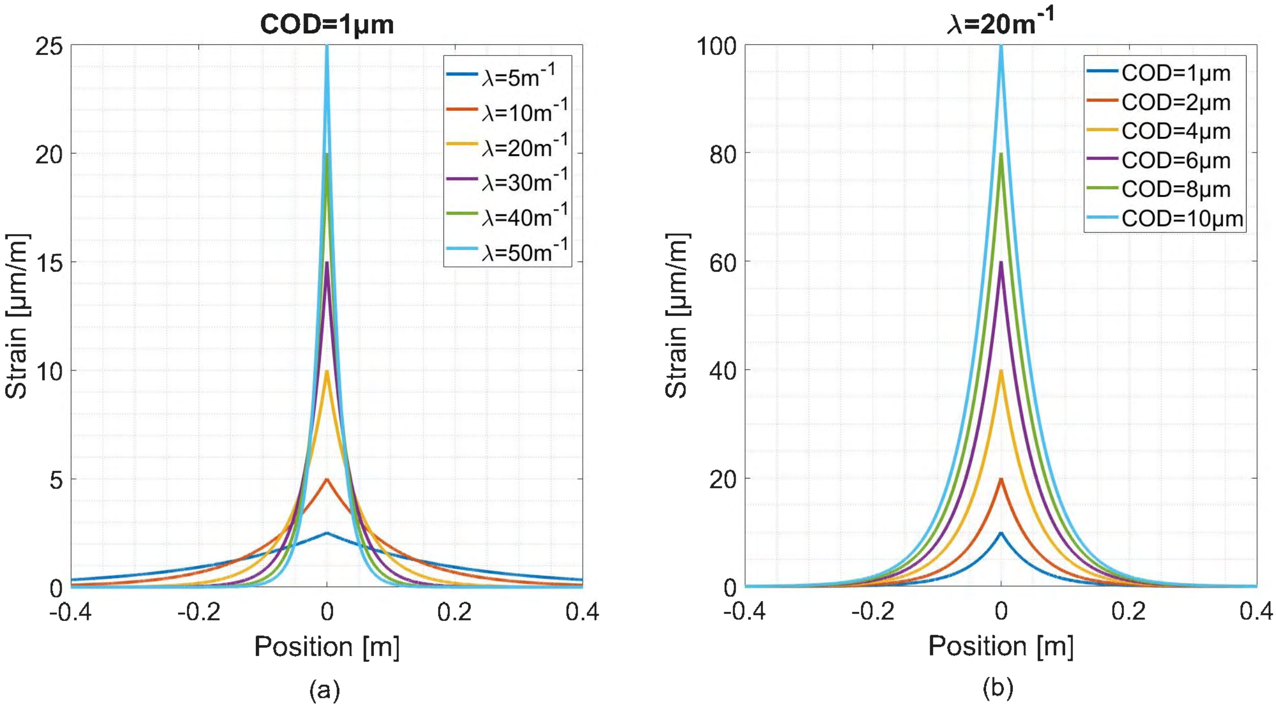

*Figure 2-5: Variation of the crack-induced strain $\epsilon_{f,crack}$ over the length of optical fiber for different **(a)** strain lag parameter λ and **(b)** crack openings COD values.*

II.3. Post-elastic strain transferring analysis

The strain transfer system reaches its elastic limit when a permanent deformation arises. Stresses beyond the elastic limit cause a material to yield or flow. For such materials the elastic limit marks the end of elastic behavior and the beginning of plastic behavior. For most brittle materials, stresses beyond the elastic limit leads to failure with almost no plastic deformation.

II.3.1. Debonding at the fiber core/coating interface

Imai et al. [97] considers that the fiber core usually experiences an interfacial slippage with the surrounding material. Therefore, the post-elastic behavior of the strain transfer system can be characterized through a bond-slip model. In order to simplify the problem, the authors assume a sudden softening model where debonding at the interface occurs when the stress reaches the maximum level (Figure 2-6). Therefore, exceeding the elastic limit leads to zero shear stress and a constant maximum bearing strain ϵ_{max} over the debonded region as follows:

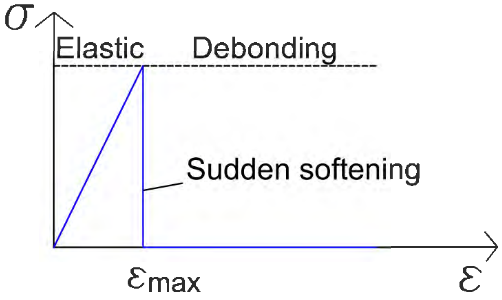

Figure 2-6: Debonding behavior of the coating layer.

$$\epsilon_f^{Deb}(z) = \epsilon_{max} \quad \text{for} \quad |z| < z^{Deb} \tag{II.38}$$

$$\epsilon_f^{Deb}(z) = \epsilon_f(z - z^{Deb}) \qquad \text{for } |\text{z}| > \text{z}^{\text{Deb}} \tag{II.39}$$

Figure 2-7 shows an example of the spatial strain distribution over the length of the optical fiber. During the debonding stage, z^{Deb} increases progressively with the crack opening as shown in Figure 2-7.

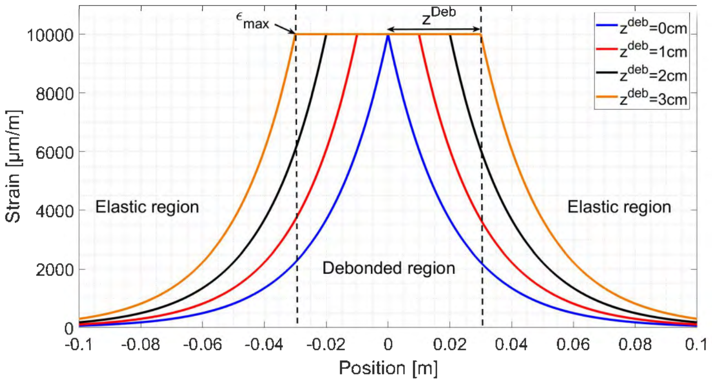

Figure 2-7: The spatial strain distribution during the post-elastic debonding stage for a critical COD$_{cr}$=400 μm, λ=50 m^{-1} and $2\,L$ =80 cm.

II.3.2. Plasticity of the coating layer

Taking into consideration that most of the coatings, especially polymer coatings, are elasto-plastic materials, Li et al. [139, 140] proposed a model that considers the coating as a perfectly elasto-plastic material as shown in Figure 2-8. Therefore, an elasto-plastic phase starts when the shear stress in the coating $\tau_p(z, r_f)$ reaches the critical yield level as follows:

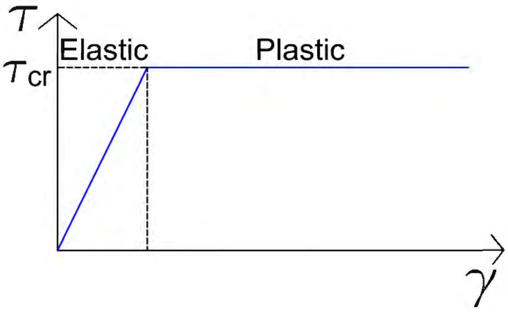

Figure 2-8: Elasto-plastic behavior of the coating layer.

$$\tau_p^p(z, r_f) = \tau_f^p(z, r_f) = \tau_{cr} \quad \text{for} \quad |z| \leq z^p \tag{II.40}$$

where $\tau_f^p(z, r_f)$ is the shear stress within the plastic region and z^p is the half-length of the plastic region. The silica glass in the optical fiber core behaves in a linear elastic manner all the way to fracture, and it has a much larger ultimate strength than the yield strength of the coating. Based on Equations II.12 and II.15, the following relationship can be established:

$$\frac{\mathrm{d}\sigma_f}{\mathrm{d}z} = E_f \frac{\mathrm{d}\epsilon_f}{\mathrm{d}z} = -\frac{2}{r_f}\tau_f(z) \tag{II.41}$$

and therefore, the strain measured by the optical fiber inside the plastic region can be given by integrating Equation II.41:

$$\epsilon_f^p(z) = -\frac{2\tau_{cr}}{E_f r_f}\, z + D_1 \quad \text{for} \quad |z| \leq z^p \tag{II.42}$$

where $D1$ is an integration constant.

Integrating of Equation II.42 yields the displacement in the fiber core:

$$u_f^p(z) = -\frac{2\tau_{cr}}{E_f r_f}\, z^2 + D_1\, z + D_2 \quad \text{for} \quad |z| \leq z^p \tag{II.43}$$

where $D2$ is an integration constant.

In the elastic region, and similar to Equations II.34,II.35 and II.16, the deformation, the strain and the shear stress in the fiber core can be expressed as follows:

$$u_f^e(z) = D_3\, e^{-\lambda\, z} + \epsilon_m\, z + \frac{\mathrm{COD}}{2} \quad \text{for} \quad |z| > z^p \tag{II.44}$$

$$\epsilon_f^e(z) = -\lambda\, D_3\, e^{-\lambda\, z} + \epsilon_m \quad \text{for} \quad |z| > z^p \tag{II.45}$$

$$\tau_f^e(z) = -\frac{\lambda^2\, E_f\, r_f}{2}\, D_3\, e^{-\lambda\, z} \quad |z| > z^p \tag{II.46}$$

where $D3$ is an integration constant.

To determine $D1$, $D2$ and $D3$, the three following boundary conditions, taking into account the continuity in the material, are imposed:

$$u^p_f(z^p) = u^e_f(z^p) \quad , \quad \epsilon^p_f(z^p) = \epsilon^e_f(z^p) \quad , \quad \tau^p_f(z^p) = \tau^e_f(z^p) = \tau_{cr} \tag{II.47}$$

which makes it possible to obtain:

$$D_3 = -\frac{2\tau_{cr}}{E_f r_f \lambda^2} e^{\lambda\, z^p} \tag{II.48}$$

$$D_2 = \frac{\mathrm{COD}}{2} - \frac{2\tau_{cr}}{\lambda\, E_f r_f}\left(z^p + \frac{1}{\lambda}\right) \tag{II.49}$$

$$D_1 = \epsilon_m + \frac{2\,\tau_{cr}}{E_f\, r_f}\left(z^p + \frac{1}{\lambda}\right) \tag{II.50}$$

Thus, the two resulting strain transfer equations can be written:

$$\epsilon^e_f(z) = \epsilon_m + \frac{2\,\tau_{cr}}{\lambda\, E_f\, r_f} e^{\lambda |z^p - z|} \quad \text{for} \quad |z| > z^p \tag{II.51}$$

$$\epsilon^p_f(z) = \epsilon_m + \frac{2\,\tau_{cr}}{E_f\, r_f}\left(\frac{1}{\lambda} + z^p - z\right) \quad \text{for} \quad |z| \leq z^p \tag{II.52}$$

The maximum elastic bearing strain $\epsilon^{e/p}_f$ can be calculated at $z = z^p$:

$$\epsilon^e_f(z^p) = \epsilon^{e/p}_f = \epsilon_m + \frac{2\tau_{cr}}{\lambda E_f r_f} \tag{II.53}$$

A boundary condition $u^p_f(0) = 0 = D_2$ allows us the establish a relationship between z^p and COD parameter as follows:

$$\mathrm{COD} = \frac{4\tau_{cr}}{\lambda\, E_f\, r_f}(z^p + \frac{1}{\lambda}) \tag{II.54}$$

Finally, Equation II.52 can be rewritten in function of λ and COD parameters as follows:

$$\epsilon^p_f(z) = \epsilon_m + \lambda\, \frac{COD}{2} - \frac{2\,\tau_{cr}}{E_f\, r_f}\, z \tag{II.55}$$

Thus, we can conclude that the strain at the level of optical fiber varies linearly with the crack opening at the crack location ($z = 0$) and at the same rate is as the one in the elastic stage. The beginning of the post-elastic phase corresponds to $z^p = 0$, which corresponds to critical crack opening COD_{cr} given by:

$$\mathrm{COD}_{cr} = \frac{4\,\tau_{cr}}{\lambda^2\, E_f\, r_f} \tag{II.56}$$

Figure 2-9 shows an example of the spatial strain spatial distribution during the elasto-plastic phase for strain lag parameter λ=50 m^{-1}, a critical crack opening COD$_{cr}$=400 μm and a bonding length 2 L=80 cm. We can observe that with the increase in z^p, the exponential strain distribution in the elastic region stays constant and moves towards the extremities of the optical fiber bonding length while the linear strain distribution in the plastic region keeps increasing.

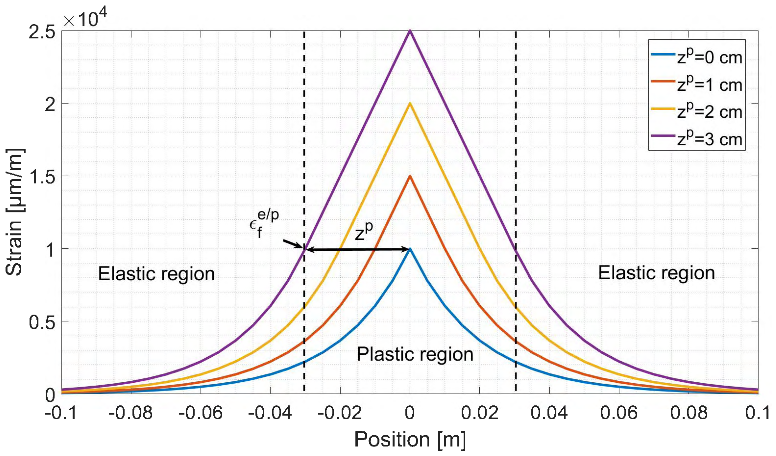

Figure 2-9: Spatial strain distribution during the elasto-plastic stage for a critical COD$_{cr} = 400\ \mu$*m,* $\lambda = 50$ *m*$^{-1}$ *and* $2\,L = 80$ *cm.*

II.4. Newly proposed strain transfer model: imperfect bonding theory

As mentioned previously, another fundamental assumption in the strain transfer theories proposed in the literature is the perfect bonding at all different interfaces. However, in reality, the mechanical properties of a resulting composed system in a bonding assembly depends not only on the properties of the materials but also on the properties of the interfaces between the materials. Good adhesion requires a strong interfacial bond as well as intimate contact. The bonding quality depends on many conditions like the cleanliness of the contact surface and its roughness. In addition, when an intermediate adhesive exists, mechanical properties of the adhesive, the good joint design and the adhesive bonding process (solidification and cure), all of these factors can affect the adhesion between two materials.

As the concrete material is a heterogeneous material, different concrete properties can affect the bond strength and coarse aggregate degradation, like the concrete compressive strength, the aggregate type and quantity, the tensile strength and fracture energy, voids, etc. Thus, the bonding between the optical fiber sensor and concrete cannot be always considered as perfect. One of the limited works to test the validity of the perfect bonding assumption is done by Henault et al. [108, 57], where the authors investigated the bonding of an embedded optical cable to a concrete substrate by performing pull-out tests (Figure 2-10a). From these tests, a deduced interface stiffness coefficient k_p varying around 1.1×10^9 Pa/m, together with other deduced mechanical properties (from performed tensile tests), were introduced in a finite element model representing the optical fiber/intermediate layers/concrete system. Compared to the perfect bonding case (where k_p is assumed equal to 10^{13} Pa/m), the simulation results presented in Figure 2-10b showed a decrease in λ to almost half its original value (decrease from 37 to 15 m^{-1}). These results proved that the stiffness at the cable/concrete interface is an important factor and therefore its effect on the strain transfer should be more deeply studied. In the next section, we proposed to complete the D. Li's model in order to extend the strain transfer analysis to handle imperfect interfaces.

II.4.1. Three-layer system

A good way to take into account the slip at the contact interface is to let off the axial displacement continuity condition. Thus, based on the current interfacial state at the coating/host material interface,

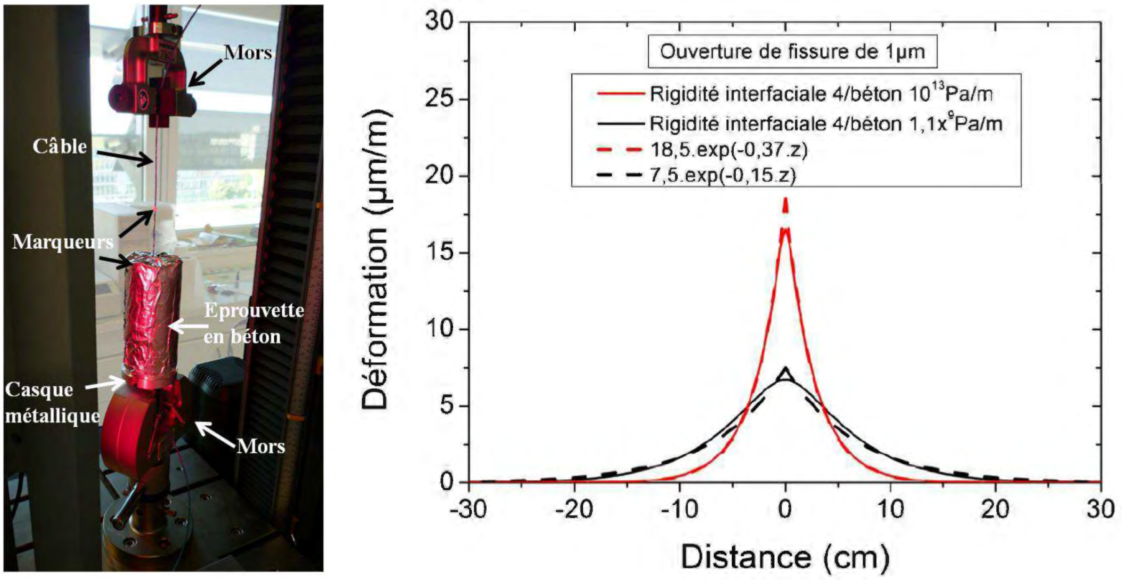

(a)

(b)

*Figure 2-10: **(a)** Pull-out test on an optical cable embedded inside a concrete specimen. **(b)** Strain distribution profiles for a COD=1 μm calculated by FEM for $k_p = 1\ GPa/m$ and $k_p = 10^4\ GPa/m$ [57].*

an axial displacement discontinuity is considered as follows:

$$\tau_p(r_p, z) = k_p\ (u_m(r_p, z) - u_p(r_p, z)) = k_p\, \Delta u_{m/p}(r_p, z) \tag{II.57}$$

As shown in Figure 2-11, $\Delta u_{m/p}$ represents the axial discontinuity and k_p represents the interface stiffness parameter and depicts the level of interfacial adhesion. Thus, $k_p = +\infty$ results in zero discontinuity or a perfect bonding and $k_p = 0$ results in zero interfacial shear stress or a debonded interface.

The generalized axial deformation compatibility equation can be written as follows:

$$u_m(r_p, z) = [u_m(r_p, z) - u_p(r_p, z)] + [u_p(r_p, z) - u_p(r_f, z)] + [u_p(r_f, z) - u_f(r_f, z)] + u_f(r_f, z) \tag{II.58}$$

Assuming a perfect bonding at the fiber/coating interface, $u_f(r_f, z) = u_p(r_f, z)$, and an imperfect bonding at the coating/host material interface yields:

$$u_m(r_p, z) = \Delta u_{m/p}(r_p, z) + \Delta u_p(z) + u_f(r_f, z) \tag{II.59}$$

According to Equations II.17, II.19 and II.57, $\Delta u_p(z)$ and $\Delta u_{m/p}(r_p, z)$ can be written as follows:

$$\Delta u_p = -\frac{E_f r_f^2}{2G_p} \ln\left(\frac{r_p}{r_f}\right) u_f''(z) \quad \text{and} \quad \Delta u_{m/p}(r_p, z) = \frac{\tau_p(r_p, z)}{k_p} = -\frac{E_f r_f^2}{2r_p k_p} u_f''(z) \tag{II.60}$$

Thus, Equation II.59 can be rewritten as follows in the case of constant strain in a fractured host material:

$$u_f''(z) - \lambda^2 u_f(z) = -\lambda^2 \left(\frac{\text{COD}}{2} + \epsilon_m\, z\right) \tag{II.61}$$

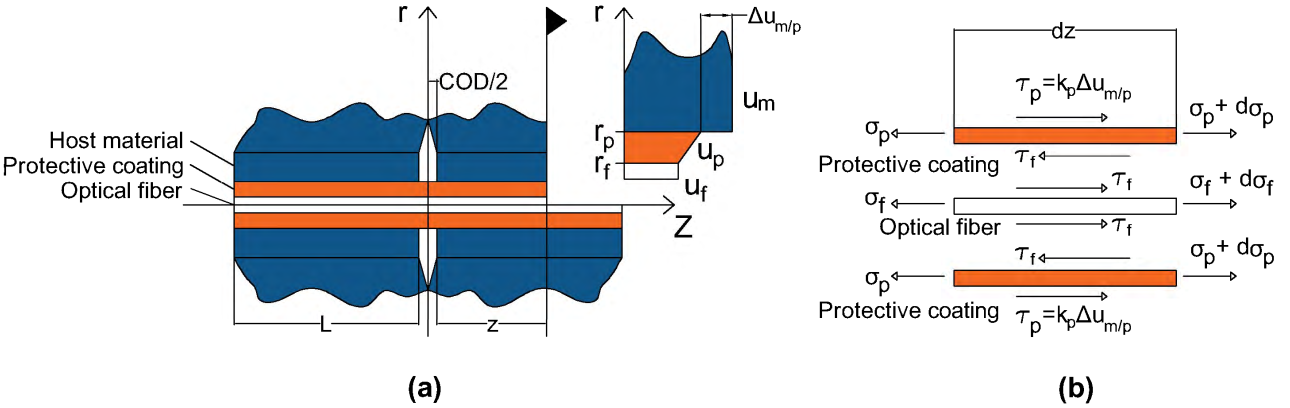

Figure 2-11: ***(a)*** *Three layers strain transfer system figuring a discontinuity in the host material and an imperfect bonding at the coating/host material interface and* ***(b)*** *the corresponding stress state at different layers.*

where the new strain lag parameter λ equation is given by:

$$\lambda^2 = \frac{2}{E_f\, r_f^2 \left[\frac{1}{G_p} \ln\left(\frac{r_p}{r_f}\right) + \frac{1}{k_p\, r_p}\right]} \tag{II.62}$$

Equation II.61 has the same form as Equation II.33 and the same solution as in the case of perfect bonding can be deduced:

$$\epsilon_f(z) = \epsilon_m + \frac{\text{COD}}{2}\lambda e^{-\lambda|z|} \tag{II.63}$$

As a result, even though the crack-induced distribution takes the same exponential form as in the case of perfect bonding theory, yet the strain lag parameter is dependent on the stiffness coefficient k_p through Equation II.5. When $k_p = +\infty$, a perfect bonding reign at the interface and the strain lag parameter equation becomes equal to Equation II.22 from the perfect bonding analysis. On the other hand, non-infinite bonding leads to decrease in λ values and thus a decrease in the amplitude of the crack-induced strain distribution and an increase in the crack affected region over the optical fiber length. Moreover, when the bonding quality degrades $k_p \to 0$ and $\lambda \to 0$, leading to a zero strain transfer. Thus, Henault's experimental results and FEM simulations are confirmed by the model that is proposed in this PhD memory.

II.4.2. Multi-Layer system

In civil engineering applications, additional intermediate layers usually surrounds the optical fiber, in order to improve the mechanical properties or the durability of the optical fiber sensor. Figure 2-12 shows a multiple layer model corresponding to the imperfect bonding strain transfer analysis. Based on the force equilibrium at each intermediate layer yields:

$$\tau_i(r,z) = \frac{r_{i-1}}{r}\tau_{i-1}(r_{i-1},z) \quad \text{for} \quad \mathrm{r_{i-1} \le r \le r_i} \tag{II.64}$$

Therefore, the shear deformation Δu_i can be written as follows :

$$\Delta u_i = \int_{r_{i-1}}^{r_i} \frac{\tau_i(r,z)}{G_i}\mathrm{d}r = \frac{\tau_f(r_f,z)}{G_i}\int_{r_{i-1}}^{r_i}\left(\frac{r_{i-1}}{r}\right)\left(\frac{r_{i-2}}{r_{i-1}}\right)...\left(\frac{r_f}{r_1}\right)\mathrm{d}r = \frac{\tau_f(r_f,z)}{G_i}\int_{r_{i-1}}^{r_i}\frac{r_f}{r}\mathrm{d}r \tag{II.65}$$

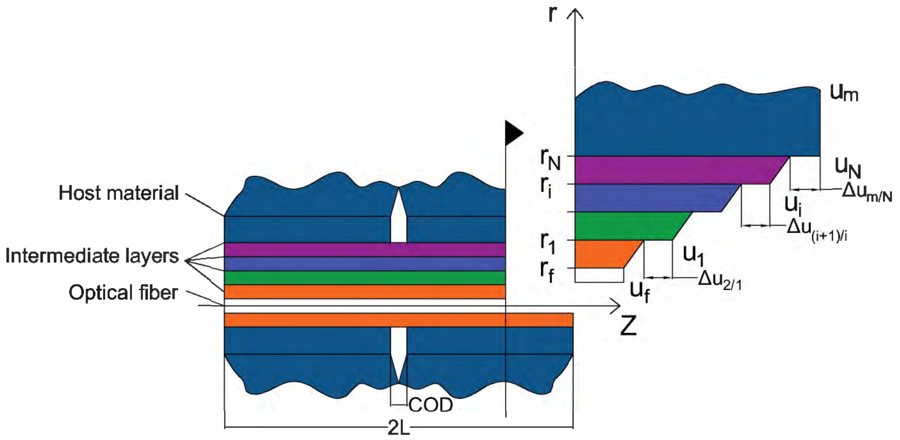

Figure 2-12: Multiple layers strain transfer system figuring a discontinuity in the host material and an imperfect bonding at different intermediate layers.

With Equations II.12 and II.15, this last relation becomes:

$$\Delta u_i = -\frac{r_f^2 E_f}{2}\frac{1}{G_i}\ln\left(\frac{r_i}{r_{i-1}}\right) u_f''(z) \tag{II.66}$$

Furthermore, the slip at interface $\Delta u_{i+1/i}$ can be written as follows:

$$\Delta u_{i+1/i} = \frac{\tau_i(r_i,z)}{k_i} = \frac{\tau_1(r_1,z)}{k_i}\left(\frac{r_{i-1}}{r_i}\right)\left(\frac{r_{i-2}}{r_{i-1}}\right)...\left(\frac{r_1}{r_2}\right) = \frac{\tau_1(r_1,z)}{k_i}\left(\frac{r_1}{r_i}\right) \tag{II.67}$$

Since $r_1\,\tau_1(r_1,z) = r_f\,\tau_f(rf,z)$ and with Equations II.12 and II.15, this last relation becomes:

$$\Delta u_{i+1/i} = -\frac{r_f^2\,E_f}{2}\,\frac{1}{r_i\,k_i}\,u_f''(z) \tag{II.68}$$

The multi-layer axial displacement compatibility equation is then given by:

$$u_m(r_N,z) = \sum_{i=1}^{N}\left[\Delta u_i + \Delta u_{i+1/i}\right] + u_f \tag{II.69}$$

$$= -\frac{r_f^2 E_f}{2}\left[\frac{1}{G_1}\ln\left(\frac{r_1}{r_f}\right) + \sum_{i=2}^{N}\frac{1}{G_i}\ln\left(\frac{r_i}{r_{i-1}}\right) + \sum_{i=1}^{N}\frac{1}{r_i\,k_i}\right] u_f''(z) + u_f(z) \tag{II.70}$$

This leads to the same second degree differential equation:

$$u_f''(z) - \lambda^2 u_f(z) = -\lambda^2\left(\frac{\mathrm{COD}}{2} + \epsilon_m\,z\right) \tag{II.71}$$

where the new strain lag parameter λ is written as follows:

$$\lambda^2 = \frac{2}{E_f r_f^2\left[\frac{1}{G_1}\ln\left(\frac{r_1}{r_f}\right) + \sum_{i=2}^{N}\frac{1}{G_i}\ln\left(\frac{r_i}{r_{i-1}}\right) + \sum_{i=1}^{N}\frac{1}{k_i\,r_i}\right]} \tag{II.72}$$

To sum up, whether a perfect bonding exist at the different interfaces of a three-layer system or a slip occurs with a finite and constant interfacial adhesion coefficient, the same exponential form of the crack-induced strain distribution will be observed. Moreover, introducing an additional protective or adhesive layer does not affect the strain distribution form when all different layers are behaving in an elastic manner. What differs each case is how the strain lag parameter is related to the characteristics of the system.

Based on these facts, this generalized yet simple analytical model can be fitted to the DFO strain measurements next to crack's locations and only two variable parameters need to be estimated: λ and COD. Any variation in λ can be an indicator of the behavior of the system, as it holds the mechanical properties of different constitution layers. At the same time, the fact that there is no need to calculate this parameter in order to continuously monitor the crack openings in a structure, is what makes this model particularly interesting.

II.4.3. Linear strain variation in host material

In this section, the constant strain assumption in host material will be dismissed and a linear strain variation is considered as follows:

$$\epsilon_m(z) = K(L-z) \tag{II.73}$$

This strain distribution can correspond to a three points bending test case with the loading force located at $z = 0$ as shown in Figure 2-13.

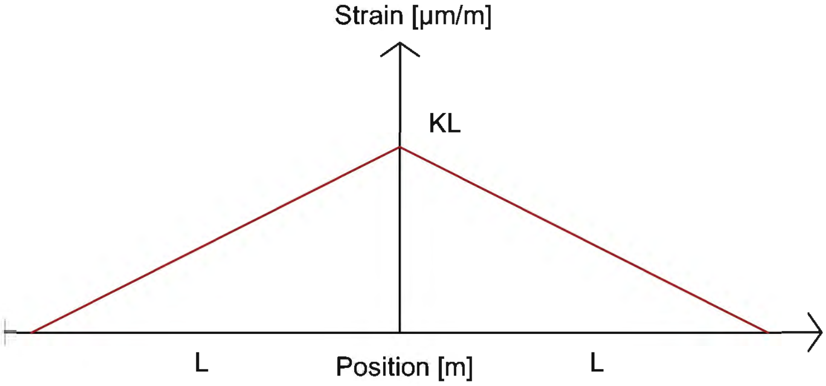

Figure 2-13: Linear strain variation in a three points bending test.

Therefore Equation II.32 can be written as follows:

$$u_f''(z) - \lambda^2 u_f(z) = -\lambda^2 \left(\int_0^z K(L-z')\mathrm{d}z' + \frac{\text{COD}}{2} \right) \quad \text{for} \quad z \geq 0 \tag{II.74}$$

$$= -\lambda^2 \left(K\left(L - \frac{z}{2}\right) z + \frac{\text{COD}}{2} \right) \tag{II.75}$$

The general solution of Equation II.74 holding the complementary function and particular integral is thus:

$$u_f(z) = Ce^{-\lambda z} + K\left(L - \frac{z}{2}\right) z + \frac{COD}{2} - \frac{K}{\lambda^2} \tag{II.76}$$

Considering a symmetrical response of the optical fiber $u_f(0) = 0$, leads to:

$$C = \frac{K}{\lambda^2} - \frac{COD}{2} \tag{II.77}$$

As a result, the final strain transfer equation can be written as follows:

$$\epsilon_f(z) = \lambda \left(\frac{COD}{2} - \frac{K}{\lambda^2} \right) e^{-\lambda z} + K(L - z) \tag{II.78}$$

This equation shows that the strain at the level of the optical fiber is equal the strain in the host material that varies linearly, added to the crack induced strain part figuring an additional term K/λ^2, compared to the constant strain case. Figure 2-14 shows the variation of this additional term for a peak strain KL=100μm/m equal to the maximum strain attained by concrete in reinforced concrete structures. We can clearly observe that an increase in λ and/or span length L leads to a decrease in the additional term value. For $L >$0.5m and $\lambda >$15m^{-1}, K/λ^2 is less than 1μm and thus can be neglected compared to the crack openings COD in materials like concrete.

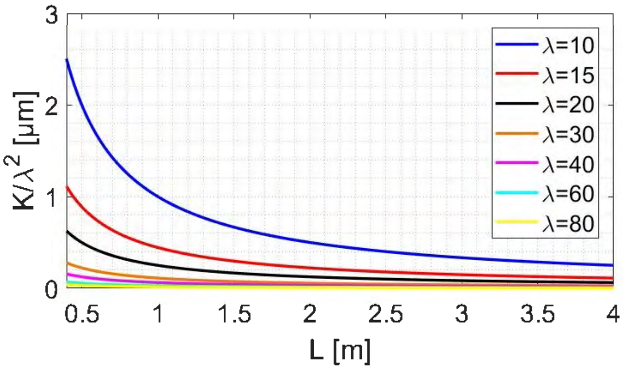

Figure 2-14: Variation of the additional term (K/λ^2) in the crack-induced strain $\epsilon_{f,crack}$ distribution in function of the span L for different strain lag parameter λ values.

II.5. Conclusion

To conclude, the mechanical properties of the optical fiber showed that the fiber core behaves as an elastic material until high strain values, the reason behind using it as a strain sensor. However the low strength of the surrounding material limits its sensing capacity. In order to study the effect of these intermediate layers existing between the host material (sensed material) and the fiber core (the sensor), a general strain transfer analysis was presented and discussed in the case of continuous and fractured host material.

In the case of continuous host material, it has been revealed that differences can exist between the strain measured by the fiber core and the strain in the host material. These differences can lead to errors in the measured strain and are mainly dependent on the strain lag parameter. This parameter holds the mechanical and geometrical properties of the fiber core and the intermediate layers and therefore an in-depth understanding of the strain lag parameter variation can help in the conception of the optical fiber sensor packages.

In the case of fractured host material, we chose to introduce the localized discontinuity due to crack propagation as an additional axial displacement in the host material. The final strain transfer equation includes the strain in the host material and an additional crack induced strain part. In some cases, this spatial strain distribution has an exponential form with a peak value at the crack location. The exponential shape is mainly dependent on the same strain lag parameter deduced in the case of continuous host material. In addition, the amplitude is also linearly dependent on the crack opening displacement. This linear relationship makes the optical strain sensor potentially capable of following the crack openings in a damaged host material, like a cracked concrete structure. For this purpose, choosing the optical fiber sensors packaging with the convenient strain lag parameter level seems to be of paramount importance. Low strain lag parameter values can affect the sensitivity of the sensors to small micro cracks propagation while high strain lag values can lead to high strain gradients, exceeding the limited strain measuring capacity of the DFOS interrogator.

The potential post-elastic phenomena have been discussed and their effect on the spatial strain distribution has been studied. As one of the surrounding materials reaches its maximum elastic stress limit, a sudden softening in the material leads to a constant bearing strain in the debonded area. However, if this surrounding layer is an elasto-plastic material, its post-elastic behavior corresponds to a linear strain increase in the plastic region.

Finally, we proposed an improved strain transfer analysis that can take into account a non-infinite bonding at the sensor/host material interface. This more realistic analytical model includes the slip or discontinuities at the interface by introducing an interfacial stiffness parameter. In the case of a fractured host material, the imperfect bonding strain analysis produces the same strain transfer equation (Equation II.63) as the perfect bonding strain analysis. However, the interfacial stiffness coefficient figures as an additional coefficient affecting the new strain lag parameter (Equation).

Given all these points, and in real structural health monitoring applications, the crack opening and strain lag parameter can be estimated by fitting the mechanical transfer equation to DFO strain measurements. As some potential drawbacks may arise from additional protective and adhesive layers, the new strain lag parameter equation handling the imperfect interfaces can be used to examine the condition of the contact interfaces and evaluate the adhesion levels. In the long run, the performance of the optical sensor can be monitored and new sensors and adequate adhesives with better bonding performance can be developed.

Chapter III

Experimental study of the crack-induced strain response in concrete material

> ”One accurate measurement is worth a thousand expert opinions.”
>
> *Grace Hopper*

Contents

In order to validate the mechanical strain transfer model proposed in Chapter 2 in the case of cracked concrete host material, it is important to perform stable mechanical tests on concrete specimens. In addition, as we are interested in developing a method for measuring crack openings, it is important to be able to create a mode 1 pure tensile crack in concrete with sufficient control of crack opening rate.

Therefore, this part of the thesis work is dedicated to validate the new proposed analytical model through wedge splitting tests, performed on concrete specimens instrumented with optical fiber cables. Embedded concentric optical fiber configurations will be studied, as well as surface mounted (in U-groove) and more complex non-concentric configurations. The limitations of the strain transfer model are discussed and the conditions that influence the estimated parameters like the crack opening and the strain lag coefficient are examined.

III.1. Wedge Splitting Test (WST)

The most direct way to follow the crack phenomenon is a uni-axial tensile test. But it is difficult to perform this type of test because of the extreme stiffness of the concrete material and the small deformations at failure. In practice, three-points bending test with a notch is the most used test to study the fracture mechanics of concrete. However, this type of test showed that it is not always stable due to the influence of the dead weight of the specimen. Thus, this instability can lead to problems in controlling the crack opening during the cracking process. Moreover, cracking in concrete material is more complex than homogeneous materials like steel or aluminum, due to the existence of the microcracking stage before a real macro crack appears. For this reason, it is important to perform tests on undamaged specimens and cover the crack initiation stage.

The Wedge Splitting Test (WST) was initially proposed by Linsbauer and Tschegg (in 1986) [141] and developed later by Brühwiler and Wittmann (in 1990) [142] for the study of fracture mechanisms in cementitious materials. Currently, it has been used for many years to not only characterize the mechanical properties at failure of different types of materials like concrete [143, 144, 145, 146], steel and fiber reinforced concrete [147, 148, 149], asphalt [150, 151] and wood, but also characterize the bonding of bi-materials [152]. The test consists on transforming a vertical force from a stiff steel profile to two splitting forces acting on the specimen. This is done through two loading devices inserted in a groove positioned at the center of the specimen. Thus, this simple test does not require a special loading configuration in order to create a vertical crack propagating in the middle of the specimen and splitting it into two halves.

Linsbauer and Tschegg [141] proposed a first version of the wedge force transmission system that is applied directly to inclined planes on the groove of the specimen (Figure 3-1). This first trial version had a major disadvantage due to significant frictional forces generated by the contact of the metallic wedge with the inclined planes of metal helmets. The wedge acted on a skew plane and had a wide angle which prevents its advancement.

In order to improve this first version, Brühwiler [153] developed a new system with a wedge steel frame transferring the load to rollers on the two sides of the specimen (Figure 3-2). The use of rollers and the small wedge angle highly reduced the friction effects.

Similar to Brühwiler's proposition, Tschegg [154] later proposed a modified version by introducing rollers into the load transmission parts. However, Tschegg kept the principle of the wedge acting inside the groove. This configuration was recently modified by Gharbi et al. [150] for testing asphalt interlayer systems with a circular groove.

In 1998, Trunk and Wittman [155] proposed stabilizing the test piece on two supports located under the center of gravity of each half of the specimen. While the aim was to reduce the effect of

Figure 3-1: First Wedge Splitting Test (WST) configuration proposed by Tschegg in 1986 [141].

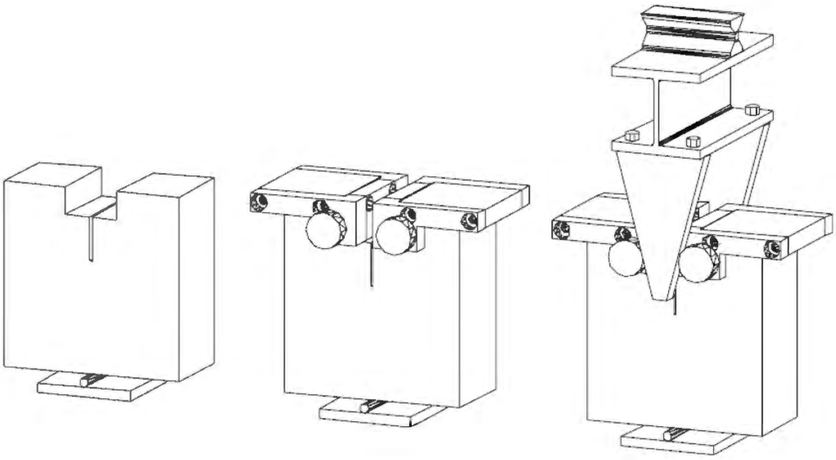

Figure 3-2: Wedge Splitting Test (WST) configuration proposed by Brühwiler in 1988 [153] .

self-weight in large concrete specimens, this proposal generated parasitic forces at the level of the two supports.

To conclude, we chose the Wedge Splitting Test proposed by Brühwiler over the other types of mechanical tests as it responds to all our following demands:

1. The test leads to the formation of only one propagating tensile crack.
2. The test allows us to reach high crack openings (in the order of several millimeters) before the failure of the specimen.
3. The test provides a stable fracture mechanism during the softening phase of concrete with less effect of the dead load, contrary to three-points bending test. Thus, it allows us to maintain a good control of the crack opening displacement variation rate. This last advantage is important in our case, where the DFO interrogation unit has limited measurement frequency and/or averaging the measurements is needed in some cases (as will be presented later in this chapter).
4. As the specimens size is relatively small and only one vertical actuator is needed, the test is more or less simple to carry out.

III.2. Test setup

Figure 3-3a shows the geometry of the wedge splitting specimen that is used to validate the strain transferring model in presence of a crack. Each of the 80×80×20 cm specimens are tested after at least 28 days of concrete curing. An 8x5 cm groove and a starter notch of a 40 cm characterizes the specimen shape. Based on the results of previous research works [142, 145], the height of the notch is chosen equal to half height of the specimen, in order to guaranty a vertical crack propagation. The notch is created by fixing a 2 mm thick steel plate in the molds before casting. The surfaces facing the concrete are painted with lubricating oil to reduce the friction between the plate and the concrete during demolding.

The loading configuration proposed by Brühwiler [142] is chosen for these experiments. One linear support with a width equal to 3 cm is located in the center of the wedge specimen and fixed to the lower plate of the testing machine. Each specimen had to be handled carefully to prevent unexpected failure and accurately positioned on the single support as shown in Figure 3-3b.

The main feature of the loading device is the use of wedges and rollers. It is composed of the three pieces shown in Figure 3-4. Two massive steel loading devices equipped with roller bearings on each side are fabricated to be placed on top of the specimen. A steel profile with two identical wedges is fixed at the upper plate of the testing machine. In [156], it has been proven that the use of rollers significantly improves the reproducibility of test results and reduces the fretting forces of rollers to less than 1%. As the vertical actuator force F_a and the horizontal splitting forces F_h are related as follows:

$$F_h = \frac{F_a}{2\tan\alpha} \tag{III.1}$$

the use of wedges with a small wedge angle ($2\alpha = 15°$) leads to almost completely transforming the vertical force into the two horizontal splitting forces with less reversible energy is stored in the loading frame. This stored energy is usually the reason behind a fast crack propagation at the moment of concrete tensile failure. In addition, small wedge angle leads to an increase in the actuator displacement with respect to the specimen deformation. As a result, better control of the crack opening can be achieved.

The fiber optic cables, to be tested, were whether embedded inside the specimen or glued in U-groove engraved on the surface. In order to make sure that the cables keep their same position,

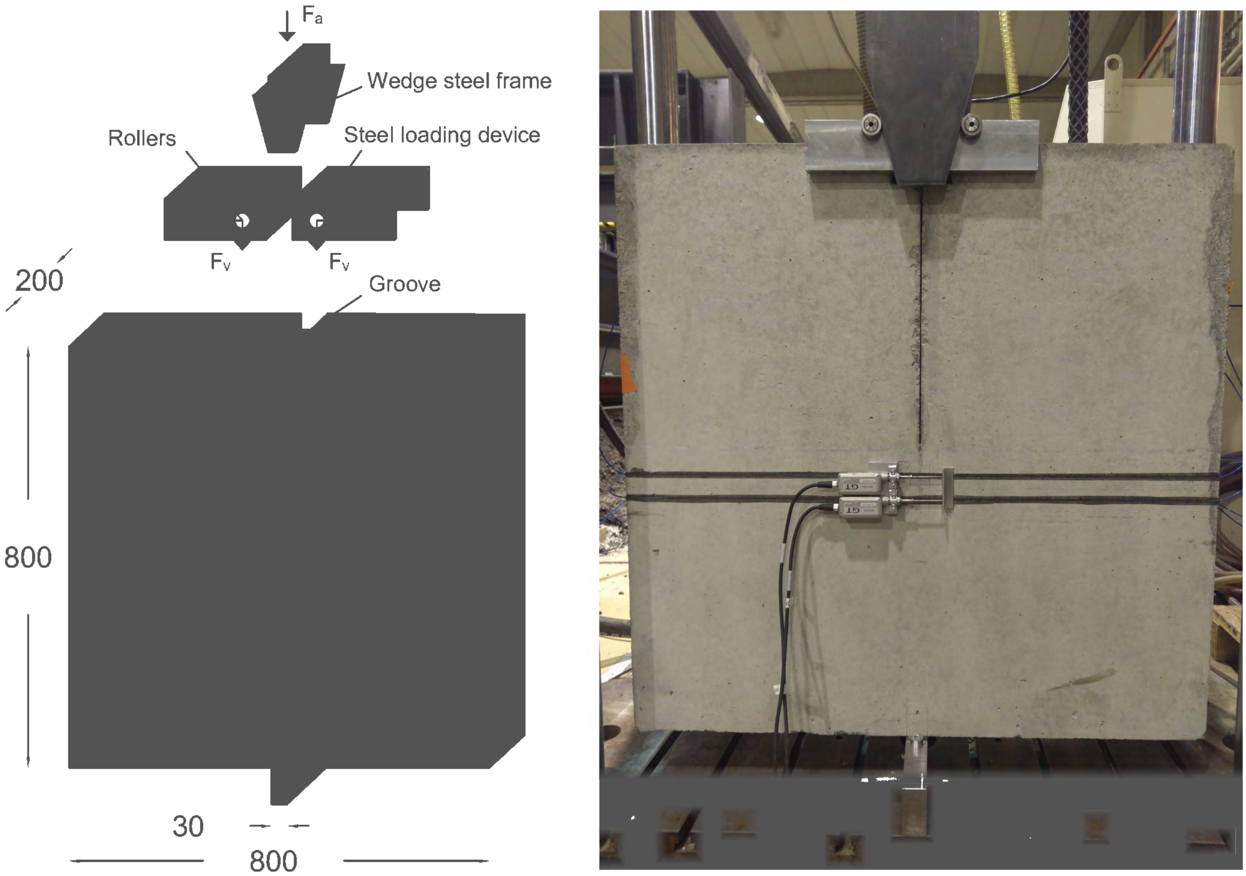

(a)

(b)

*Figure 3-3: **(a)** Shop-drawing of the testing set-up. **(b)** Front view of the loading arrangement and the concrete specimen instrumented with DFO and LVDT sensors.*

Figure 3-4: Mechanical pieces fabricated for the wedge splitting test.

they were strained (Figure 3-5a) and fixed to the two sides of the formwork using dominos (Figure 3-5b). After removing the formwork, a U-groove was sewed perpendicularly to the estimated vertical direction of the crack. The dimensions of the groove were adapted to the diameter of each type of fiber optic cable. After adding a first layer of epoxy glue, the cable is introduced inside (Figure 3-5c) and then covered with a second layer to fill the groove. To perform quantitative comparisons of the crack openings that will be estimated from the strain transfer model, LVDT sensors covering a 5 cm range are fixed at the level of the fiber optic lines from both sides of the specimen. They have a displacement precision of 1 μm and a measurement range of 10 mm. The sensors were calibrated before each test. Figure 3-6 shows a global view of the experimental setup during a wedge splitting test. A signal frequency generator was used to synchronize the LVDT and actuator force and displacement (from a HBM Spider 8 acquisition system) to the fiber optic measurements.

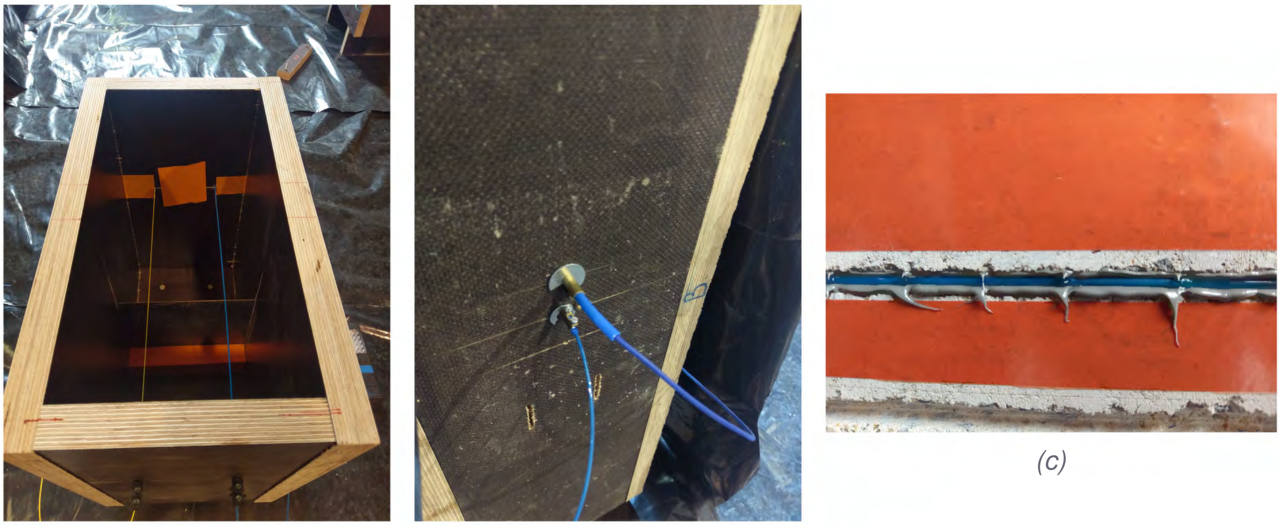
(a) *(b)* *(c)*

*Figure 3-5: **(a)** View of two fiber optic cables fixed from both sides of the formwork. **(b)** Fiber optic cable fixed to the formwork using dominos. **(c)** Fiber optic cable introduced inside a groove filled with epoxy glue.*

III.3. Fiber optics measurement system

During the tests, distributed strain measurements are performed using the ODISI–B interrogation unit (manufactured by Luna). The interrogator is based on the Optical Backscattering Reflectometry (OBR) technique capable of reaching a spatial resolution in the order of several millimeters (1.25-5.2 mm) and with a measurement frequency in the order of several Hz (23.8-250 Hz). It holds four operating modes which characteristics are presented in Table 3-1.

III.3.1. Repeatability at zero strain

As shown in Table 3-1, the repeatability of the strain measurements depends on the chosen operating mode. Figure 3-7a shows an example of the spatial strain profile measured using the high resolution mode over 80 cm of a standard optical fiber glued on the surface of a concrete specimen. The associated histogram shows that the strain measurements have the form of a normal distribution

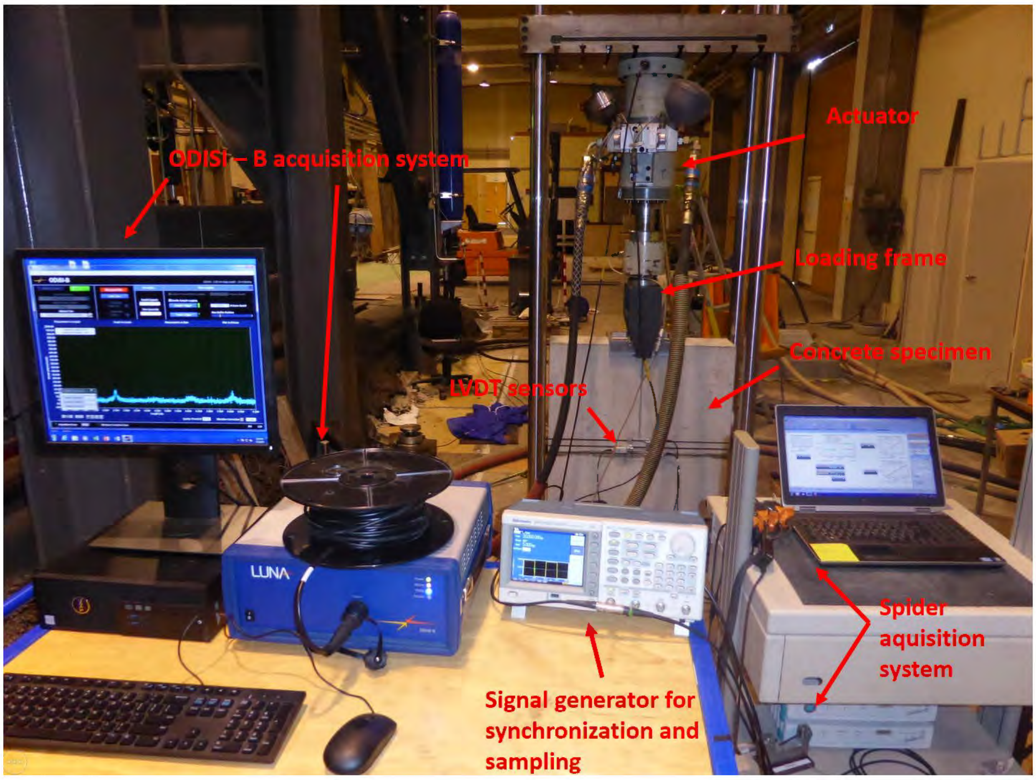

Figure 3-6: Experimental setup for the Wedge Splitting tests showing the specimen in the testing machine and the data acquisition system.

Mode of operation	**Maximum Sensing Length** (m)	**Acquisition Rate** (Hz)	**Sampling Interval** (mm)	**Spatial resolution** (mm)	**Repeatability at zero strain** (μm/m)	**Strain accuracy** (μm/m)	**Strain gradient tolerance** (μm/m)
Standard	10	100	2.6	5.2	$< \pm 5$	± 30	129
High Speed	2	250	2.6	5.2	$< \pm 10$	± 30	129
High Resolution	10	23.8	0.65	1.25	$< \pm 20$	± 25	517
Extended Length	20	50	2.6	5.2	$< \pm 5$	± 25	129

Table 3-1: ODISI-B modes of operation. (ODISI-B Users Guide 5.2.2)

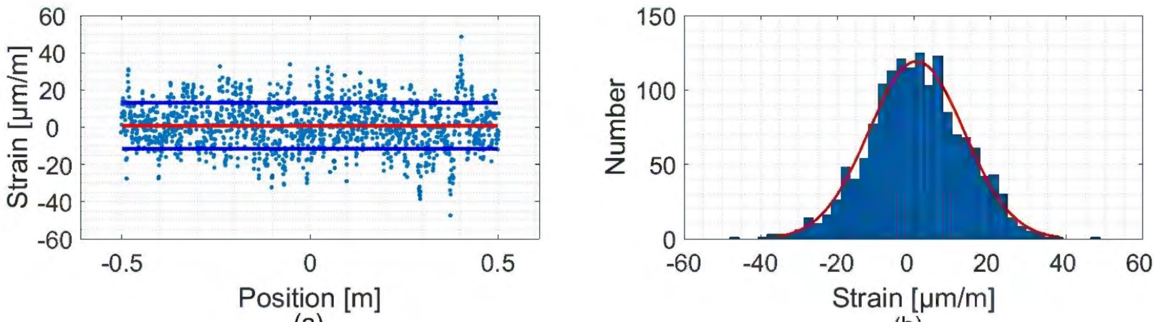

(a)

(b)

*Figure 3-7: Example of strain measurements obtained from the ODISI-B interrogator connected to an 80cm standard optical fiber: **(a)** Spatial distribution, **(b)** associated histogram and normal distribution fit.*

(Figure 3-7b). The calculated spatial dispersion over 100 consecutive measurements leads to a mean value of 0.3 μm/m and a standard deviation of 12.3 μm/m. With the standard operating mode, the results of 100 consecutive measurements performed led to a mean value of -0.1 μm/m and a standard deviation of 4.5 μm/m. These measurements are in accordance with the specifications given in Table 3-1.

Comparing the previous measurements to those performed before gluing the optical fiber to the specimen show a negligible influence of the instrumentation procedure whether by gluing the fiber on the surface or embedding it inside the concrete specimen. In addition, no remarkable difference in the strain repeatability is observed in function of the chosen type of optical fiber configuration whether the fiber core is surrounded by one primary coating or different layers of protection.

As a matter of fact, the quality of the strain measurements is mainly affected by Rayleigh intensity amplitude over the length of the optical fiber (Figure 3-8). To ensure that the interrogator reaches its measurement properties, an alignment check of the internal optical network is performed before each test and to prevent any important variation in the intensity amplitude over the length of the optical fiber, as shown in Figure 3-8. The quality of the ending and intensity loss due to a connection between two different optical fibers could also decrease the temporal repeatability and spatial dispersion of the strain measurements. Vibration of the fiber and the testing instruments can also affect the measurements. In order to overcome this issue, the first 20 cm of the sensing fiber is used to remove the vibration effect from the optical data prior to computing strain. Therefore, we had to ensure that the vibration correction region is left unstrained during the tests.

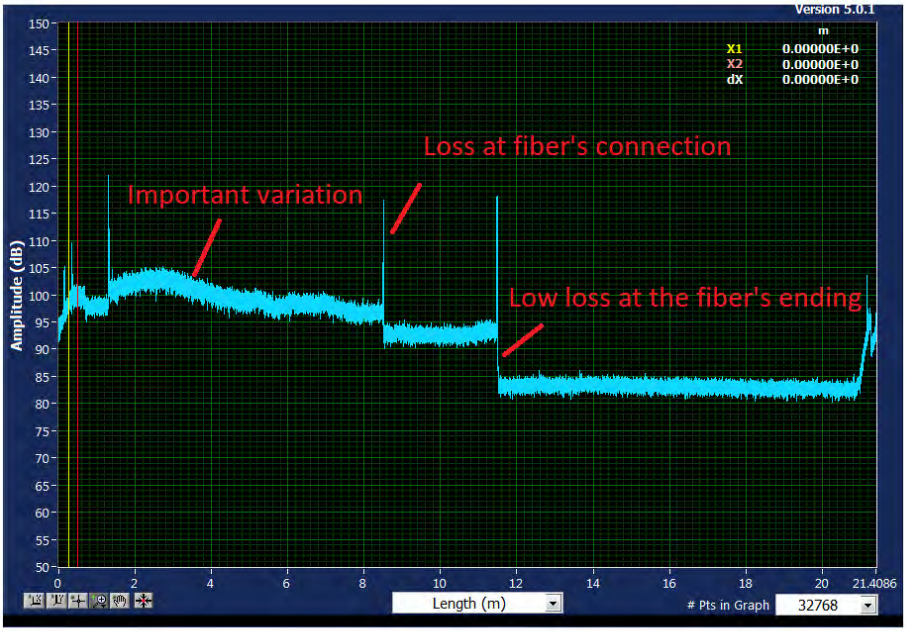

Figure 3-8: Bad preparation procedure leading to degradation in the strain measurement properties performed by ODISI-B interrogator.

III.3.2. Dropouts

Since the ODISI-B spectral shift calculation is dependent on the correlation between a measurement and a reference spectrum, if a strong correlation is not observed the second strongest peak can be any noise peak in the correlation background. This random nature of miscalculated points along the fiber causes them to be referred to as dropouts (NaN values). As mentioned in Chapter 2, the crack-induced strain distribution can take an exponential form, meaning that there will be high strain variations over the spatial resolution in the proximity of the crack location (Figure 3-9). As a result, the frequency of dropout measurements can increase in this area of rapid strain transitions. Moreover, the algorithm used to compute the spectral shift assumes a uniform strain across the spatial resolution. Thus, the presence of strain gradients will invalidate this assumption as strain gradients broaden the cross correlation peak. As a result, the strain gradient should be smaller than an allowable value ($\Delta\epsilon < \Delta\epsilon_{max}$). Based on these facts, the high resolution operating mode is the most suitable in our case for two reasons: high spatial resolution (ℓ_s) and strain gradient tolerance ($\Delta\epsilon_{max}$). This operating mode achieves a spatial resolution four times less than other modes and therefore, it leads to an important reduction in the strain variations across a one spatial resolution distance ($\Delta\epsilon$) as shown in Figure 3-9. In addition, the strain gradient tolerance value $\Delta\epsilon_{max}$ is four times higher in high resolution mode (517 μm/m) than other operating modes (129 μm/m). The only disadvantage of this operating mode is that high resolution leads to an increase in strain repeatability. Therefore, it will be hard to detect small strain gradients corresponding to small crack openings.

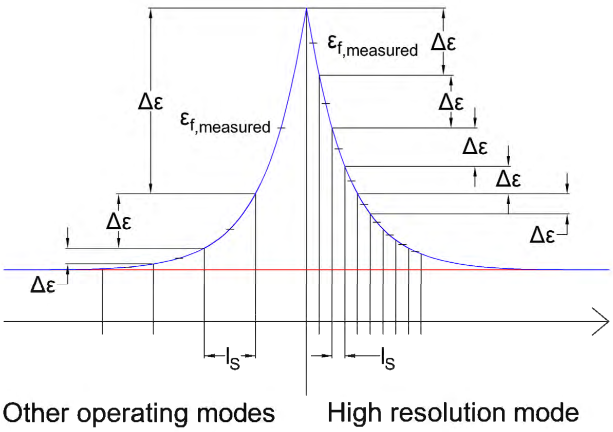

Figure 3-9: Variation of strain gradients over the crack-induced strain spatial distribution.

Another factor that can lead to the appearance of dropouts is the vibration of the sensing fiber. Figure 3-10 shows the number of dropouts over 80 cm of an optical fiber glued on one of the wedge splitting tests that experienced high vibration rates. We can observe random spatial distribution of dropouts frequency reaching a maximum of several thousands of dropouts over 30000 measurements. In order to solve this problem, performing a temporal rolling average over 10 consecutive measurements can help reducing the number of the dropout points and therefore increasing the quality of the measurements. As shown in Figure 3-10, dropouts completely disappeared in the 80 cm bonded length of the fiber after performing the temporal averaging.

III.3.3. Analyzing of DFO measurements

Each wedge splitting test was controlled under a vertical displacement rate of 0.2 mm/min and performed until the crack opening at all different optical fiber lines reached at least 2 mm. The ODISI-B interrogator was continuously measuring at a frequency equal to 20 Hz and therefore, a total of 70000-90000 measurements of strain profiles were taken during one hour for each test. Since the high resolution operating mode is used, each strain profile measurement along a 10 m length of the optical fiber corresponds to around 15000 measurement points. Each test resulted in a raw data file of around 200-400 GB. This file is then loaded in the ODISI-B Post Processing software. As the post-processing rate is limited to 1.25 Hz, the post-processing took around one day to generate a

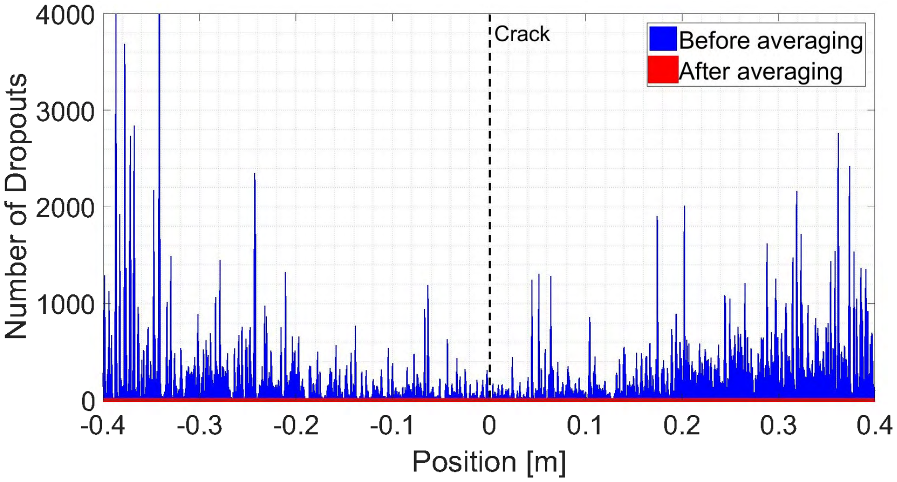

Figure 3-10: Number of Dropouts before and after a temporal rolling average of 10 consecutive measurements from high resolution mode and an acquisition rate of 20 Hz.

final strain measurement file of around 2 Gigabytes. In order to reduce the number of dropouts, the temporal rolling average of each 10 consecutive measurements is performed. Any NaN value in 10 consecutive measurements is not taken into account during the averaging process. As a result, only 10 consecutive NaN measurements can lead to a NaN value after averaging.

As a final step, the mechanical strain transfer model had to be fitted to the spatial strain profiles. The strain transfer equation presented in the previous chapter is adapted:

$$\epsilon_f(z) = \epsilon_m + \lambda \frac{\mathrm{COD}}{2} e^{-\lambda|z|} \tag{III.2}$$

COD and λ are chosen as variable coefficients while ϵ_m is neglected as the strain in the concrete material does not exceed the 100μm/m. For wedge splitting tests, the strain in concrete ϵ_m is very localized in the fracture process zone next to the notch tip. Moreover, the appearance of a macrocrack is usually accompanied by a strain release ($\epsilon_m \to 0$) .

The curve fitting toolbox from Matlab software is used to fit the measurements with Equation III.2. Geometrical irregularities in the specimens, heterogeneity in the concrete material and the existence of voids can show some asymmetric error in the measured strain distribution. All these local strain irregularities, as well as the risk of appearance of some outliers from the interrogation unit, can lead to unreliable parameter estimations. Therefore, the robust least square method is selected as it is less sensitive than ordinary least squares to large local changes in the data.

III.4. Analysis of concrete fracturing mechanism in wedge splitting tests

Before presenting the validation of the strain transfer model, it is important to demonstrate the stability of the wedge splitting test system developed at Ifsttar in the framework of this PhD thesis work. Therefore, three main parameters can be examined: the stress variation, the crack propagation and the variation of its opening at a fixed distance from the pre-existing notch during the wedge splitting tests.

Figure 3-11 shows the variation of the vertical actuator load and LVDT displacement measurements during one of the performed tests. All different wedge splitting tests were performed under a low actuator displacement rate of 0.2 mm per minute, in order to prevent any steep fall in load or a fast increase in cracks opening.

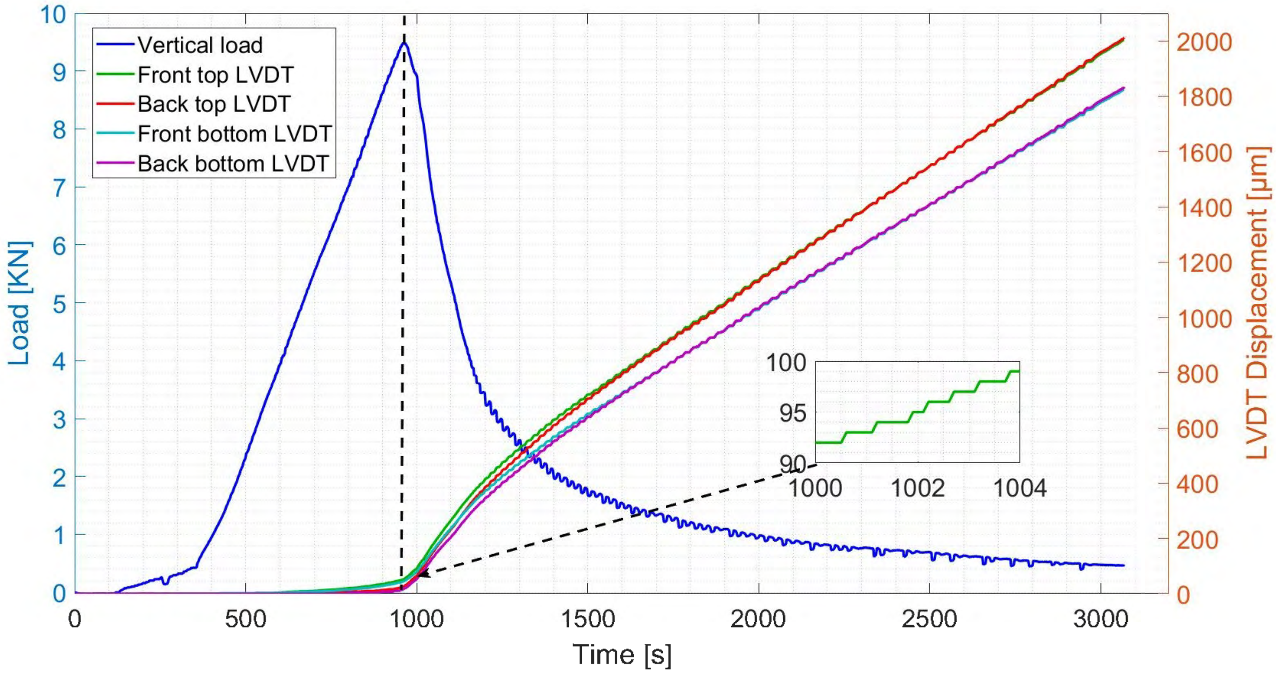

Figure 3-11: Variation of the vertical load and LVDTs displacement during the wedge splitting test.

In the beginning of the test, the load increases slowly as the specimen takes its most stable position. Then, a linear load increase is observed as the concrete material behaves in an elastic manner. After 960 s, the load reaches a maximum value of 9.5 kN followed by an exponential decrease. The same behavior was observed for all the performed tests.

The displacements measured by all different LVDT sensors show similar changes with a slow increase during the elastic stage followed by high increase during the macrocracking stage. As the crack propagates starting from the notch tip, LVDT sensors at the top level (3 cm from the notch) measure higher displacement values than the sensors fixed at the bottom level (6 cm from the notch). Differences between the front and back side measurements do not exceed the 20 μm at maximum load and decreases while the crack propagates towards the single support.

In the rest of this PhD work, the LVDT displacements will be considered as the reference measurements (termed measured COD). During the microcracking stage, before the peak load, the concrete strain reigning in the 5 cm area covered by the LVDT sensors can lead to COD measurement errors. In this area, a constant strain of 100 μm/m can lead to an additional 5 μm displacement measurement. This error disappears later during the macrocracking stage due to strain release. Putting aside this small measurement error, and before the peak load, we can assume that the LVDT displacement measurements mainly represent the sum of different micro crack openings in the fracture process zone. After the peak load, these measurements correspond clearly to the main macro crack opening.

Furthermore, as shown in Figure 3-11, the highest variation rate of around 2 μm per second is reached just after the peak load. Therefore, the rolling average of 10 consecutive fiber optics measurements is done over less than 1 μm change of crack opening (As the measurement frequency is 20 Hz) equal to the accuracy of the LVDT sensors. The crack can then then be considered as static during the time needed to perform the averaged strain profile measurement.

Figure 3-12 shows the load changes in function of the LVDT displacement for different tested specimens. This time, the LVDT displacements correspond to the average value between the front and back sides of the specimen, 3 cm below the notch tip. In total, ten concrete specimens were tested, where eight are 80×80×20 cm (Specimens 1-8) and three are 40×40×20 cm (Specimens 9-11). As a result, and except for specimen 1, peak loads varied between 9 and 11.3 kN for specimens 2-8 and 5.3 to 6.2 kN for specimens 9-11. This peak value differed from each specimen to another in function of their hardening time and the number and robustness of the instrumented optical cables. Moreover, the peak loads correspond to LVDT displacements of around 40 to 60 μm. Therefore, a measured COD of 50 μm is considered for the rest of the chapter as the limit separating the micro and macro cracking stages for the wedge splitting tests.

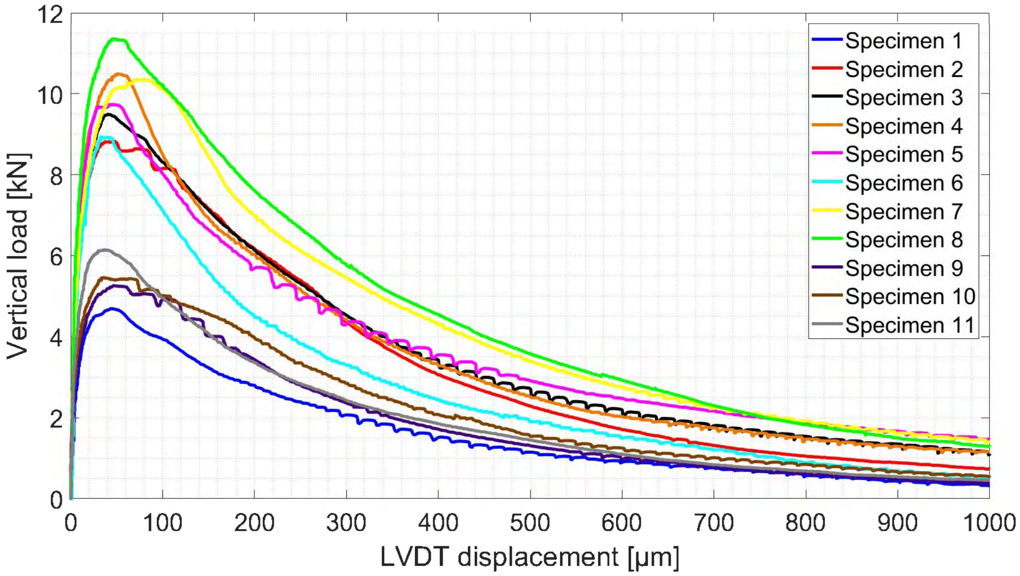

Figure 3-12: The vertical load vs COD diagram for the different Wedge splitting specimen from the two testing campaigns.

Finally, as no rapid increase in measured COD or steep fall in load levels can be observed from Figure 3-12, we can conclude that all the performed tests behaved as expected. In addition, it is important to mention that all the cracks propagated vertically towards the central support and inside the 5 cm range covered by the LVDT sensors, allowing us to measure the COD with high precision and at a controlled rate.

III.5. Validation of the mechanical strain transfer model

In this section, the fitting results of the strain profiles measured during wedge splitting tests will be presented. The examination of the strain residuals and the comparison of the estimated COD parameter to the reference measurements from LVDT sensors will enable us to validate the mechanical strain transfer model for different fiber optic cables.

III.5.1. Concentric cable configurations

Two types of concentric cable configurations are chosen for wedge splitting tests on Specimens 1 and 2:

- A three layers concentric configuration composed of an optical fiber surrounded by Hytrel coating with an external diameter of 900 μm (Figure 3-14). The optical fiber is sold by Thorlabs company.

- A five layers concentric configuration composed of an optical fiber surrounded by a multi-layer buffer, a strain transfer layer and an Ethylene Propylene Rubber (EPR) outer sheath with an external diameter of 2800 μm (Figure 3-14). This optical fiber is produced and sold by SOLIFOS company under the name “BRUsens V1”.

A photo of the two cables is shown in Figure 3-13. As illustrated in Figure 3-14, Specimen 1 is instrumented by embedding two lines of Thorlabs cable inside the concrete material (E1, E2) and gluing two lines on the surface of the specimen (S1, S2). In the same way, one line of BRUsens V1 cable was embedded inside Specimen 2 (E) and two lines are mounted on the surface (S1, S2).

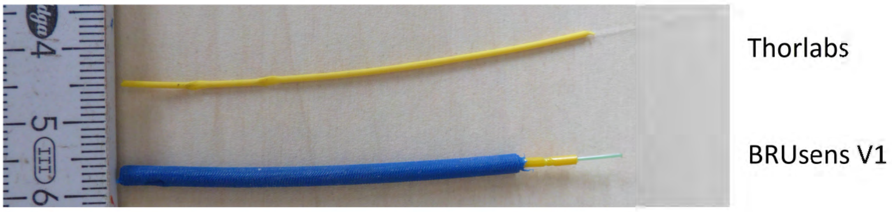

Figure 3-13: Photo of the Thorlabs and BRUsens V1 cables.

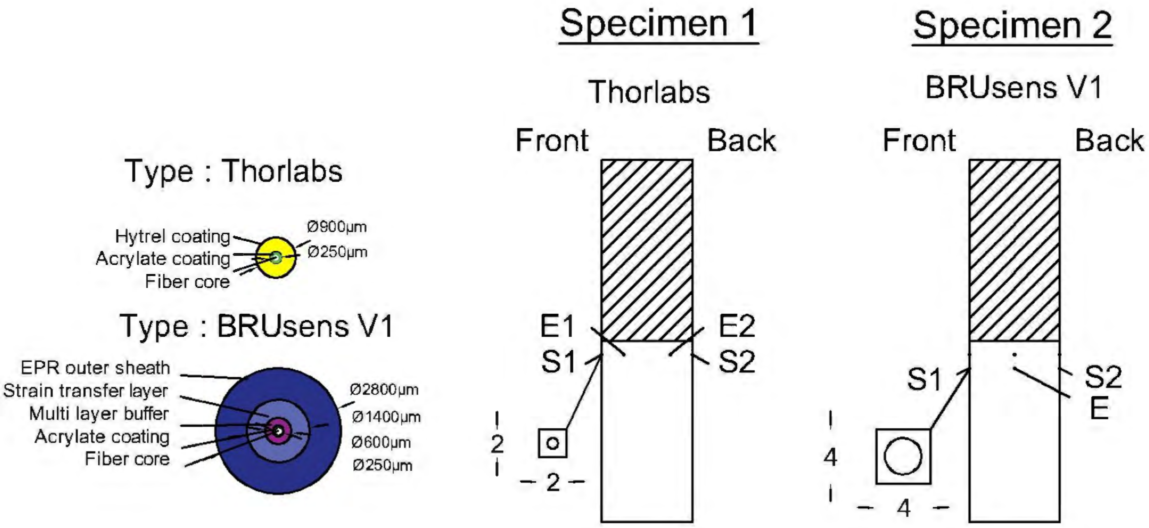

Figure 3-14: Schematic representation of the instrumentation policy of specimens 1 and 2 with T and BRUsens V1 concentric cable configurations.

For surface mounted lines, the size of the U-groove is chosen according to the cable’s external diameter of the optical cable while surrounding it with at least 500 μm of glue. Therefore, groove dimensions are fixed to 2×2 mm for Thorlabs surface mounted lines and 4×4 mm for BRUsens V1 cable.

The two components epoxy paste adhesive (Araldite 2014-1) is selected. The structural adhesive is resistant to high temperature, to water and various chemicals. With its low shrinkage property and non sagging up to 5 mm thickness, it can be definitely used to fill the gap between the optical fiber cable and the groove. The main mechanical properties are mentioned in Table 3-2.

Cure time	**Lap shear strength**	**Shear modulus**	**Tensile strength**	**Tensile modulus**	**Elongation at break**
4-7 hours	$>$14 MPa	1.2 GPa	26-28 MPa	3.5-4.35 GPa	7000-8000 μm/m

Table 3-2: Mechanical properties of the Araldite 2014-1 epoxy adhesive at 23° C.

III.5.1.1. Embedded optical cables

Embedding the Thorlabs and BRUsens V1 cables in the specimen forms a concentric multilayered system with the concrete as a host material and therefore, corresponds well to the symmetry of the mechanical model proposed in Chapter 2.

Figure 3-15 shows the spatial strain profiles measured by the ODISI-B interrogator over one embedded line for each optical cable type, together with the fits using Equation III.2 for different measured crack openings. For both types of cables, and at the beginning of the test (Figure 3-15a-left and Figure 3-15b-left), the measured spatial strain distribution figures an exponential variation and is in accordance with the proposed mechanical model. The residuals vary randomly around the zero line in the limits of the strain repeatability of the ODISI-B interrogator operating on high resolution mode (±20 μm/m). When the cracks opening increases, we observe an increased level of residuals in the area surrounding the location of the crack ($z = 0$). Instead of following the exponential variation, strain in this area tends to become constant, more likely due to a significant reduction in bond strength between the cable and the concrete material. This “close to debonding” behavior is normally a sort of degradation or microcracking in the fracture process zone (1-4 cm around the crack) with its heterogeneous nature and particle flaws subjected to important tensile stresses. Thus, when the bonding between the cable and concrete is stronger than the bonding between its aggregate particles, moderate strains could lead to the concrete breaking apart next to the crack location as shown in Figure 3-16 [157]. The Brusens V1 (Figure 3-15a) cable shows more important residuals than Thorlabs cable (Figure 3-15a), as its robustness and more important contact surface with concrete (the diameter is 3 times bigger than Thorlabs cable) could be main factors promoting this degradation phenomenon.

At the end of the test (Figure 3-15a-right and Figure 3-15b-right), the increase in the residuals observed next to the crack location is caused by a linear strain variation starting from the crack location and decreasing over a particular distance. The corresponding region (named later as “post-elastic region”) propagates progressively from the crack location to the optical fiber bonding limits under increased crack openings. Outside this region, the crack-induced strain distribution conserves its exponential shape.

As shown in Chapter 2, both debonding or plasticity phenomenon are initiated at the location of the crack, where the strain peak exists. Therefore, in order to accurately identify the crack opening limit separating these two stages, the strain measured at the location of the crack is plotted in Figure 3-17 as a function of the measured crack opening for different embedded lines. For both optical cables, we can clearly observe that the strain varies linearly in function of the crack opening during the first stage. This linear behavior, characterizing the first stage, constitutes a proof that all different layers behave in an elastic manner and thus can be called the “elastic stage”. Moreover, we can clearly detect the start of the second stage at a crack opening equal to 200 μm for Thorlabs cable and 400 μm for BRUsens V1 cable. This “post-elastic stage” is characterized by a non-linear strain variation under increased crack opening levels.

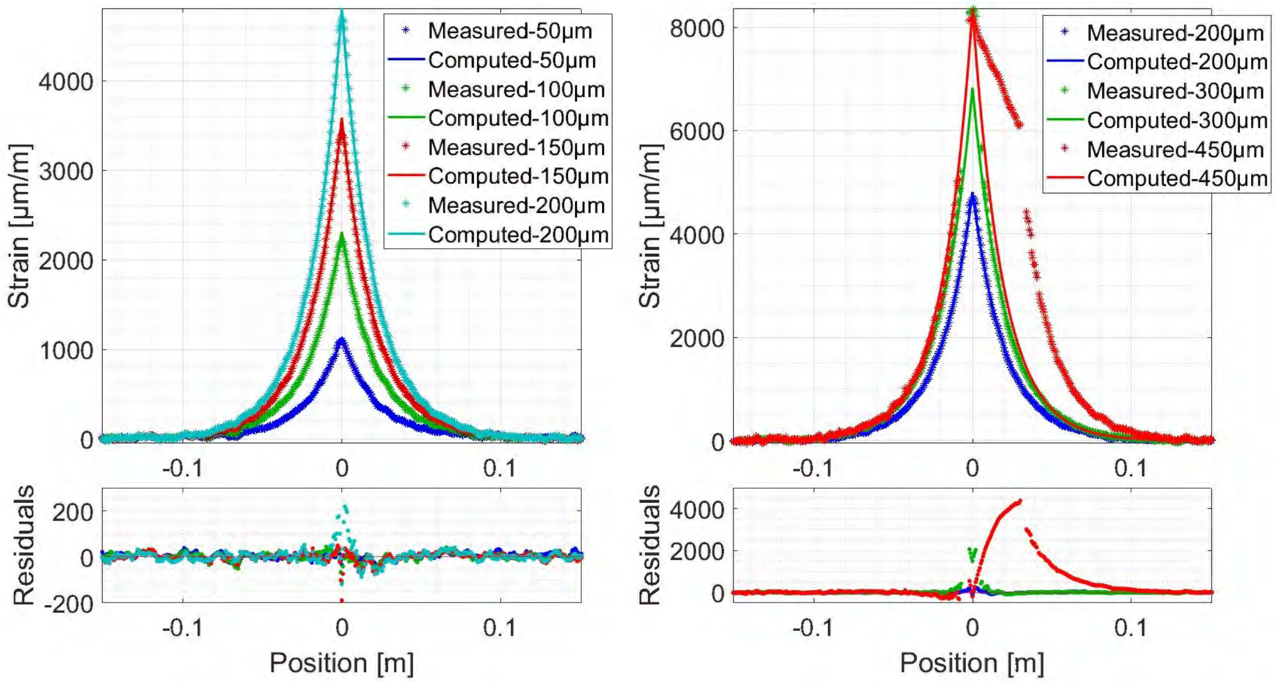

(a) E1 line from Specimen 1

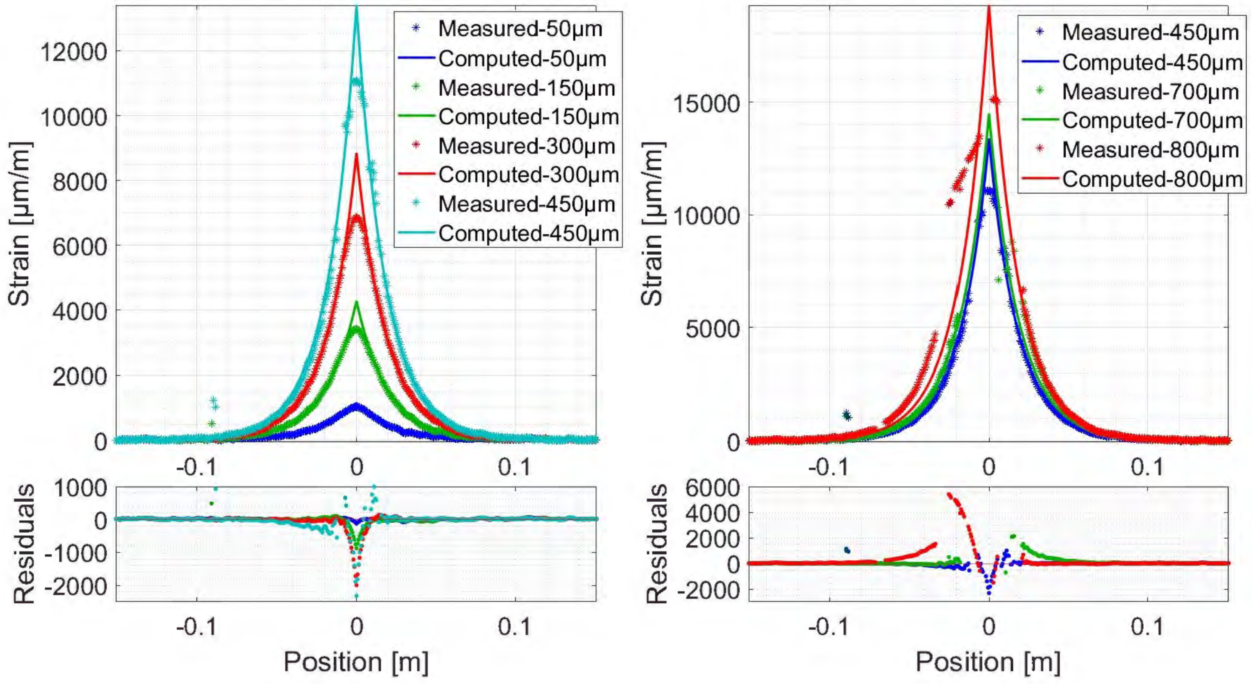

(b) E line from Specimen 2

Figure 3-15: Computed strain compared to the measured strain distribution and the corresponding residuals for different crack openings over ***(a)*** *Thorlabs and* ***(b)*** *BRUsens V1 embedded lines.*

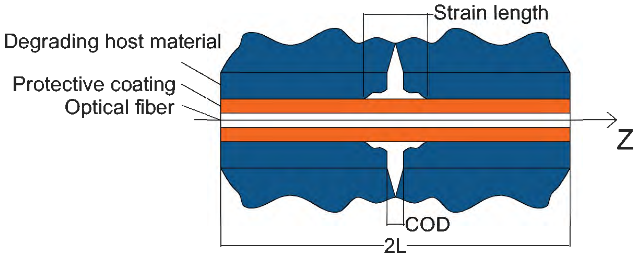

Figure 3-16: Strain length vs COD in a degrading host material.

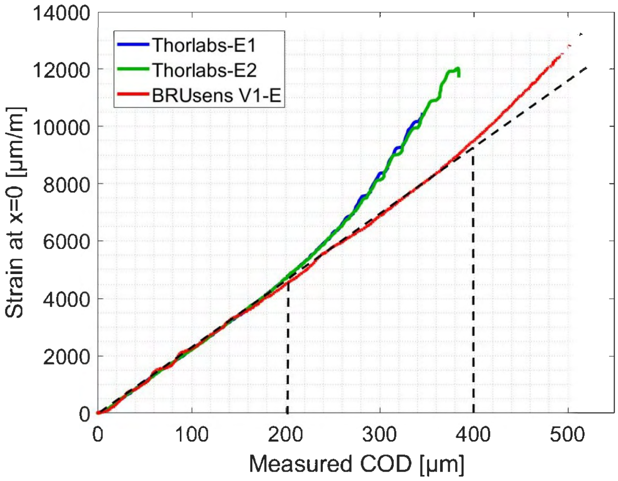

Figure 3-17: Variation of the DFOS strain measured at the location of the crack in function of the crack opening for different embedded Thorlabs and BRUsens V1 cable lines.

The numerical values of the estimated crack opening COD and strain lag λ parameters, corresponding to each measured strain profile from Figure 3-15, are shown in Table 3-3. The relative COD estimation error is then calculated with respect to the measured values from LVDT sensors as follows:

Thorlabs cable: E1 line from Specimen 1						
Strain lag parameter λ [m^{-1}]	45.9	47.5	48.4	48.4	49.1	38.1
Estimated COD [μm]	50.2	98.5	148.6	196.6	285.1	490.83
Measured COD [μm]	50	100	150	200	300	450
Absolute relative error [%]	0.4	1.5	0.9	1.7	5	9.1
BRUsens V1 cable: E line from Specimen 2						
Strain lag parameter λ [m^{-1}]	43.2	51.57	54.36	55.5	53.6	41.26
Estimated COD [μm]	53.4	166.3	328.4	482.5	542.5	694
Measured COD [μm]	50	150	300	450	700	800
Absolute relative error [%]	6.8	10.87	9.5	7.2	22.5	13.2

Table 3-3: Estimated parameters from the fitting and the calculated COD absolute relative error with respect to measured crack opening for Thorlabs and BRUsens V1 embedded lines.

$$\text{Absolute relative error} = 100\left(\frac{|\text{Estimated COD} - \text{Measured COD}|}{\text{Measured COD}}\right) \tag{III.3}$$

The table shows that the model does not only replicate the measured spatial strain distribution, it is also capable of achieving very precise estimations of the crack openings with the relative error varying around 0.5-2% for Thorlabs cable and 7-11% for BRUsens V1 cable. Under high crack openings exceeding the post-elastic stage limits for each cable, the estimations are less accurate as higher relative errors are observed (in red color).

For a more complete view of the estimated parameters variations, the relative error and the strain lag parameter are plotted in Figure 3-18 in function of the measured crack opening. An estimation of the parameters is performed every 10 μm change in the measured COD for Thorlabs lines and 20 μm for BRUsens V1 lines.

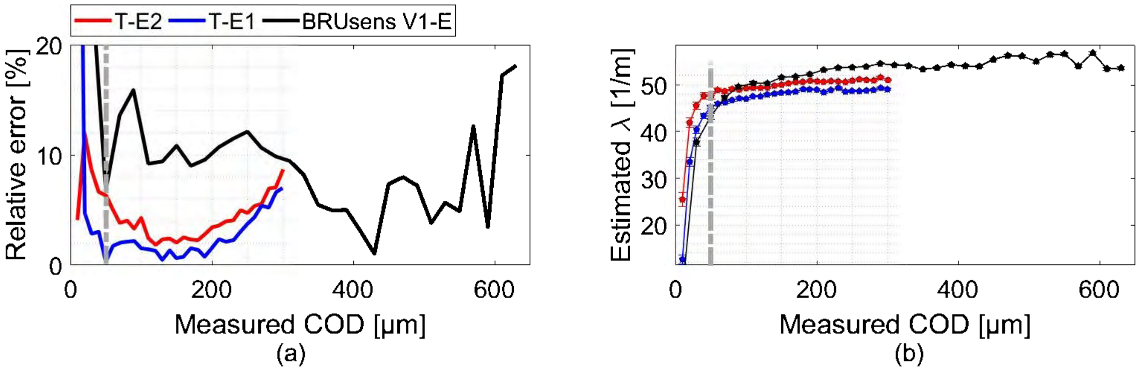

*Figure 3-18: Variation of the **(a)** relative COD estimation error and **(b)** strain lag parameter in function of the measured COD for surface for type T and V1 surface-mounted lines*

During the microcracking stage when the crack openings are smaller than 50 μm (left of the grey line), high relative error values accompanied with high variations in the strain lag parameter values could be due to the accumulation of errors at four different levels (Figure 3-18a):

- The fracture behavior of concrete: the strain measurements are affected by the heterogeneity of the concrete material, especially in the area where the main crack is more likely to appear. This fracture process zone is composed mainly of different micro discontinuities in the concrete material and not only one main crack as assumed in the model.
- The strain in host material: the fracture process zone could also figure localized strain values in the concrete host material where their contribution in the strain measured by the fiber cannot be neglected compared to the crack-induced strain part.
- The ODISI-B strain repeatability: For low measured strain values, the strain repeatability of $\pm 20\mu$m/m that leads to a spatial noise distribution affects the model fitting process and leads to very wide 95% confidence intervals.
- The reference sensor: the precision of the reference LVDT sensors is also an important factor. This precision of only 1 μm can for example generate a 10% relative error at a COD equal to 10 μm, respectively.

During the macro cracking stage, the Thorlabs embedded lines lead to accurate COD estimations with a nearly constant relative error of less than 2%. Entering the post-elastic phase at a crack opening of 200 μm, the change in the system's response leads to a degradation in COD estimation accuracy with the relative error reaching 10% at 300 μm. For the BRUsens V1 cable, the COD relative error varies around 10% when the elastic behavior of the strain transfer system prevails. It decreases to around 5% at a crack opening of 400 μm, then starts degrading progressively as the post-elastic stage starts. An error of 18% is reached at crack opening of 600 μm. It is important to mention that for crack openings between 400 and 600 μm, the fitted curves keeps providing good COD estimations as the robust fitting method reduces the influence of the strain distribution shape changes in the post-elastic region around the crack location.

On the other hand, the strain lag parameter reaches a steady level during the macro-cracking stage (Figure 3-18b) for both cable types. The layer's mechanical properties, figuring in the strain lag parameter's theoretical equation, are normally constant in the elastic domain. Thus, the observed stable trend is an additional sign of the validity or legitimacy of the estimated values and the model itself. The strain lag parameter values vary around 48 m^{-1} for Thorlabs cable and 54 m^{-1} for BRUsens V1 cables.

III.5.1.2. Surface-mounted cables

The Thorlabs and BRUsens V1 cable were also installed on the surface of the specimen by introducing the cable in the groove filled with the epoxy adhesive. Figure 3-19 shows the spatial strain profiles measured by the ODISI-B interrogator over S1 surface-mounted lines for each optical cable type, together with the fits using Equation III.2 for different measured crack openings. Similar to the two embedded optical cables, and at the beginning of the test, the measured spatial strain distribution figures an exponential variation during the linear elastic stage. In addition, the computed strain profiles are in accordance with the proposed mechanical model as the residuals vary randomly around the zero line within the strain repeatability of the ODISI-B interrogator. At the end of the test, the non-linear increase in strain measurements next to the crack location is observed. This non-linear behavior led to high number of dropouts and thus it is hard to observe the spatial strain variation in the post-elastic region. In addition, the two surface-mounted lines figure a reduced length of the post-elastic region for the same crack openings when compared to the embedded lines.

Figure 3-20 shows the variation of the strain measured at the location of the crack with respect to the measured crack opening for different surface-mounted lines. We can clearly observe a perfect

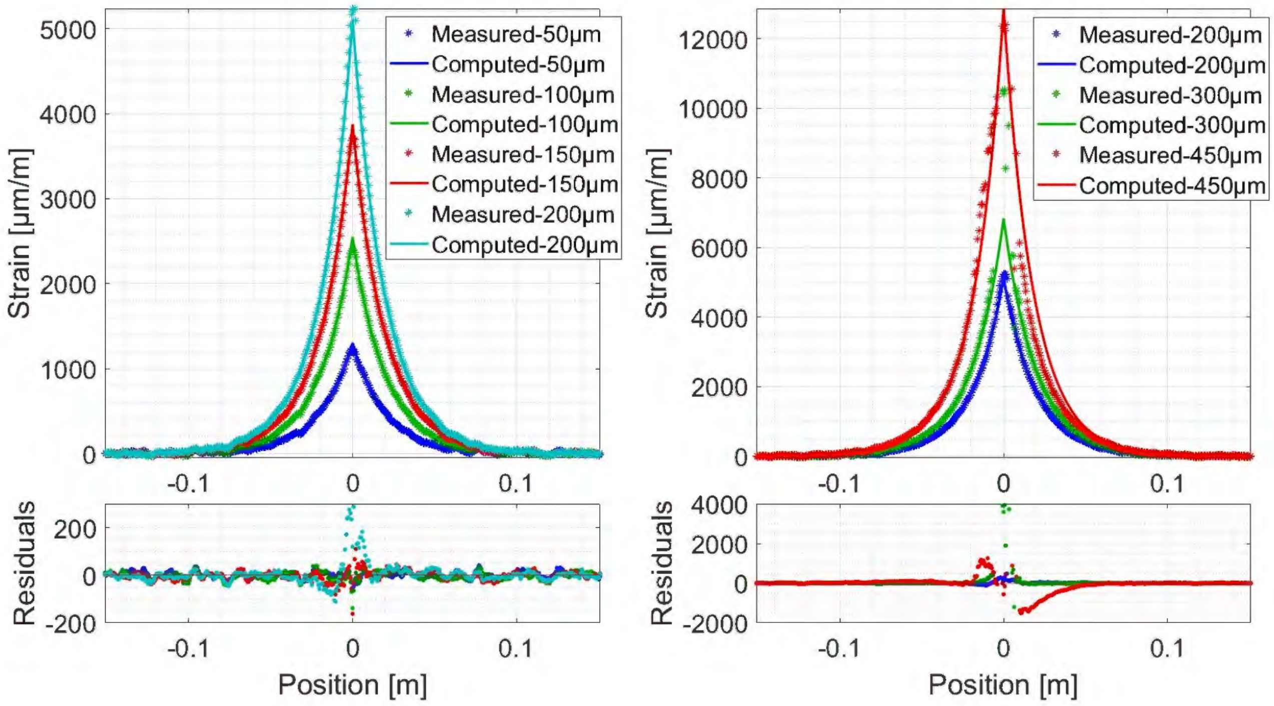

(a) S1 line from Specimen 1

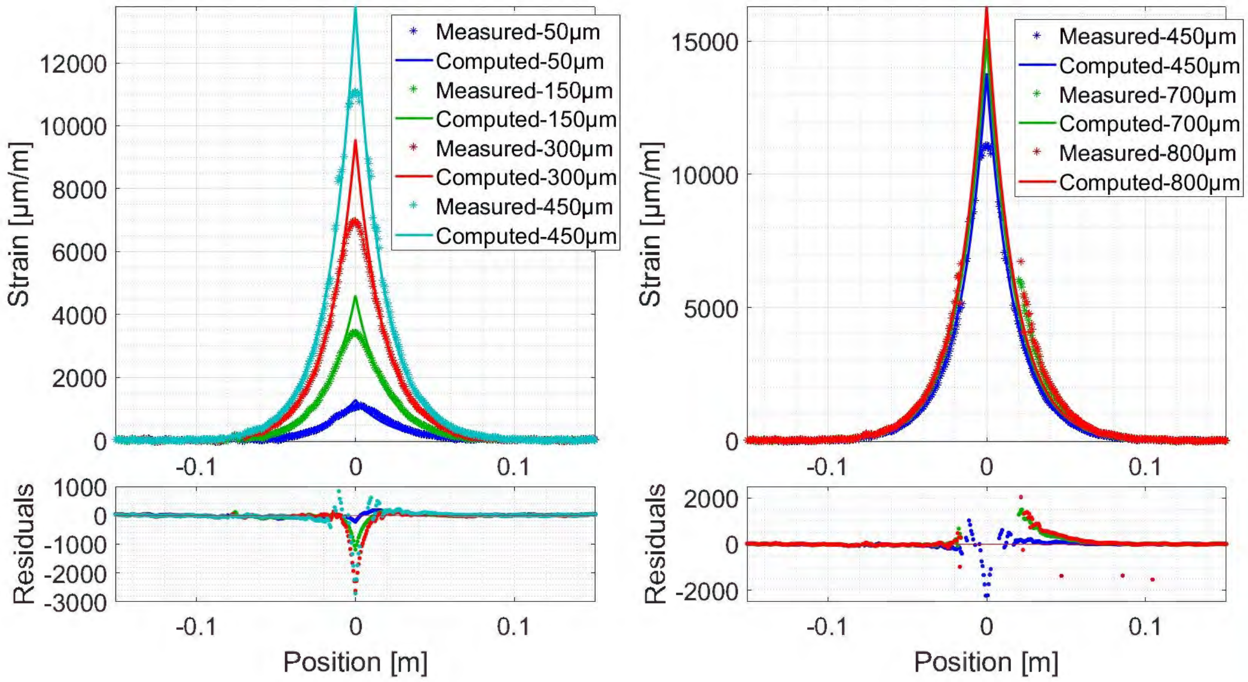

(b) S1 line from Specimen 2

*Figure 3-19: Computed strain compared to the measured strain distribution and the corresponding residuals for different crack openings over **(a)** Thorlabs and **(b)** BRUsens V1 surface-mounted lines.*

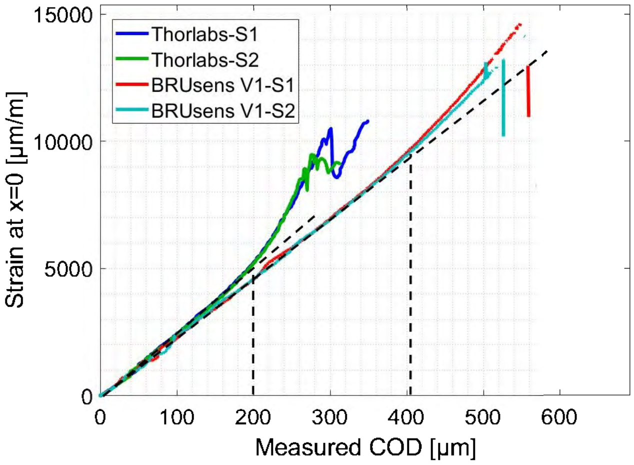

Figure 3-20: Variation of the DFOS strain measured at the location of the crack in function of the crack opening for different surface-mounted Thorlabs and BRUsens V1 cable lines.

correlation between different optical fiber lines from each optical cable type. When compared to the embedded lines for each of the Thorlabs and BRUsens V1 cables, we notice a similar linear strain variation during the elastic stage and a similar non-linear strain variation during the post-elastic stage. Moreover, the same critical crack opening value of 200 μm and 400 μm can be distinguished for Thorlabs and BRUsens V1 cables.

The estimated crack opening COD, strain lag λ parameters, corresponding to each measured strain profile from Figure 3-19, are shown in Table 3-4. In addition, Figure 3-21 shows the variation of

Thorlabs cable: S1 line from Specimen 1						
Strain lag parameter λ [m^{-1}]	49.9	50.6	50.9	51.3	50.8	55
Estimated COD [μm]	52.1	100.6	152.4	200.8	330.3	467.7
Measured COD [μm]	50	100	150	200	300	450
Absolute relative error [%]	4.3	0.6	1.6	0.38	10.1	3.9
BRUsens V1 cable: S1 line from Specimen 2						
Strain lag parameter λ [m^{-1}]	46.5	54.5	57.1	58.45	56.8	60.8
Estimated COD [μm]	55.2	169	335.1	472	869.4	826.24
Measured COD [μm]	50	150	300	450	700	800
Absolute relative error [%]	10.4	12.7	11.7	4.9	24.2	3.28

Table 3-4: Estimated parameters from the fitting and the calculated COD absolute relative error with respect to measured crack opening for Thorlabs and BRUsens V1 surface-mounted lines.

the absolute relative COD error and the estimated strain lag parameter in function of the measured COD for different surface-mounted lines. Similar COD estimation accuracy as in the case of embedded lines can be observed, precise estimations of the crack openings are achieved with relative errors varying around 0.5-2% for Thorlabs cable and 7-11% for BRUsens V1 cable. Under high crack openings exceeding the post-elastic stage limits for each cable, the estimations are less accurate as higher relative errors are observed (in red color).

In contrast, we observe an increase in the strain lag parameter to 50 m^{-1} and 57 m^{-1} for Thorlabs and BRUsens V1 cables, compared to the embedded lines. This increase of around 5-10% is due to the existence of additional epoxy adhesive layer between the sensing cable and the concrete host

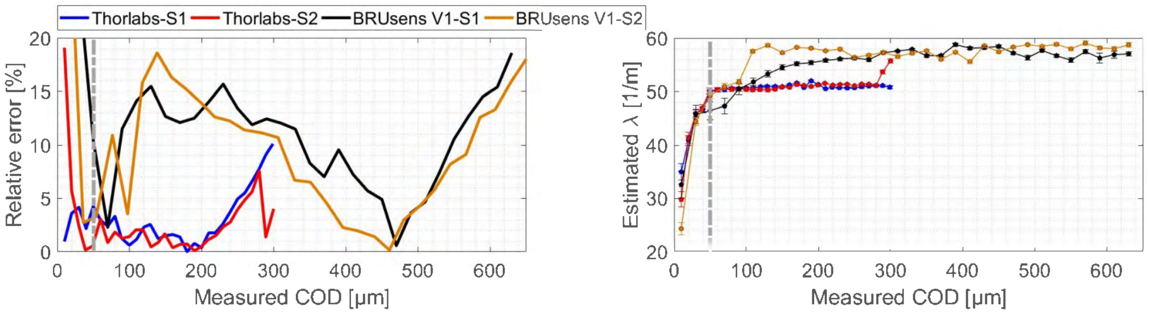

(a) (b)

Figure 3-21: Variation of the ***(a)*** *relative COD estimation error and* ***(b)*** *strain lag parameter in function of the measured COD for Thorlabs and BRUsens V1 surface-mounted lines.*

material. The strain transfer system can be modeled as illustrated in Figure 3-22, by simulating the adhesive filling the groove as a concentric cylindrical layer with an external radius r_a equal to half of the groove thickness. Thus, based on Equation II.72 from Chapter 2, the strain lag parameter

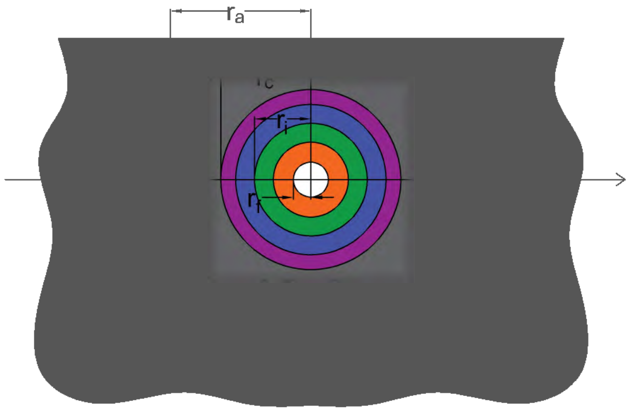

Figure 3-22: Simulated multi-layers strain transfer system for the surface-mounted instrumentation case.

resulting from the proposed imperfect bonding theory can be written as follows for the embedded and surface-mounted multi-layer systems:

$$\lambda^2_{embedded} = \frac{2}{E_f r_f^2 \left[\frac{1}{G_1} \ln\left(\frac{r_1}{r_f}\right) + \sum_{i=2}^{N} \frac{1}{G_i} \ln\left(\frac{r_i}{r_{i-1}}\right) + \sum_{i=1}^{N-1} \frac{1}{k_i r_i} \right] + \frac{E_f r_f^2}{k_{m/c} r_c}} \tag{III.4}$$

$$\lambda^2_{surface} = \frac{2}{E_f r_f^2 \left[\frac{1}{G_1} \ln\left(\frac{r_1}{r_f}\right) + \sum_{i=2}^{N} \frac{1}{G_i} \ln\left(\frac{r_i}{r_{i-1}}\right) + \sum_{i=1}^{N-1} \frac{1}{k_i r_i} \right] + \frac{E_f r_f^2}{k_{a/c} r_c} + \frac{E_f r_f^2}{k_{m/a} r_a} + \frac{E_f r_f^2}{G_a} \ln\left(\frac{r_a}{r_c}\right)} \tag{III.5}$$

Where $k_{m/c}$, $k_{m/a}$ and $k_{a/c}$ are the interfacial adhesion coefficients at the host material/cable, host material/adhesive and adhesive/cable interfaces. In addition, r_c and r_a represent the externally radius of the cable and the final radius including the adhesive layer. This system is composed of an optical fiber surrounded by N coating layers. Comparing Equation III.4 to Equation III.5 allows us to conclude than any change in the strain lag parameter values can be due to the shear deformation in the adhesive layer G_a and/or a difference between the level of epoxy glue adhesion to the cable $k_{a/c}$ and concrete $k_{m/a}$ compared to the one existing directly between the cable and the concrete $k_{m/c}$ in the embedded instrumentation case.

In order to examine the influence of the adhesive's shear deformation, we can assume a perfect bonding at different interfaces. Hence, the stiffness coefficients $k_{m/c}$, $k_{m/a}$ and $k_{a/c}$ are assumed close to $+\infty$. As a result, any difference between the strain lag parameters corresponding to the surface cable $\lambda_{surface}$ and the embedded cable instrumentation $\lambda_{embedded}$ can only result from the term $\frac{E_f r_f^2}{G_a}\ln(\frac{r_a}{r_c})$, depicting the adhesive's shear deformation effect. The strain lag parameter variation rate between the two instrumentation cases can be calculated:

$$\text{Variation rate } = 100\left(\frac{\lambda_{surface}-\lambda_{embedded}}{\lambda_{embedded}}\right) = 100\left(\sqrt{\frac{1}{1+\frac{E_f r_f^2}{G_a}ln\left(\frac{r_a}{r_c}\right)\frac{\lambda_{embedded}^2}{2}}}-1\right) \tag{III.6}$$

for different fixed $\lambda_{embedded}$ values and using the mechanical and geometrical properties of the optical fiber and the epoxy glue listed in Table 3-5: Plotting the strain lag parameter variation rate in function

Optical fiber		Adhesive			Optical cable	
E_f	r_f	G_a	r_a (T type)	r_a (V1 type)	r_c (T type)	r_c (V1 type)
73 GPa	62.5 μm	1.2 GPa	1000 μm	2000 μm	900 μm	2800 μm

Table 3-5: Mechanical and geometrical properties of the optical fiber and adhesive layers.

of $\lambda_{embedded}$ for both Thorlabs and BRUsens V1 cables shows that the shear deformation in the additional layer can only lead to a decrease in the strain lag parameter values (Figure 3-23). More importantly, the low variation rate compared to those observed from the experiment, proves that its effect can be neglected in the case of Thorlabs and BRUsens V1 cables as $\lambda_{embedded}$ varies between 48 and 58 m^{-1}.

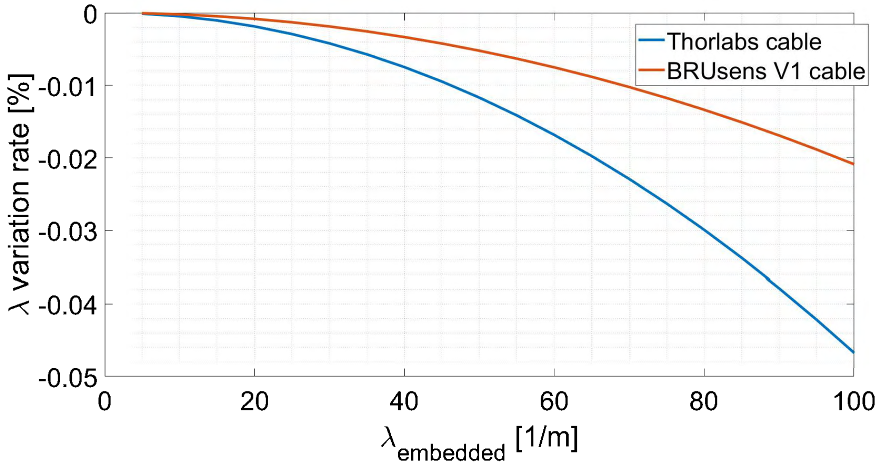

Figure 3-23: strain lag parameter variation rate due to shear deformation of the Adhesive layer for T and V1 fiber optic cable types.

Thus, by looking back to Equations III.4 and III.5, we can conclude that the reason behind the increase in the strain lag parameter values in the case of surface glued cables is mainly due to the fact that the sum of the terms related to $k_{m/a}$ and $k_{a/c}$ interfacial stiffness coefficients is less than the term related to $k_{m/c}$ coefficient. This can be explained by the fact that the epoxy adhesive layer provides higher interfacial adhesion with the cable and the concrete material compared to the one existing when the concrete and the cable are directly in contact.

III.5.2. Non-concentric cable configuration

In this section we will study the strain transfer through a more complex optical fiber cable configuration where the optical fiber is not positioned in the center of the cable and the assumption of cylindrical symmetry is no longer valid. Thus, we are interested in investigating the capacity of the two parameters model based on Equation III.4 to provide acceptable approximations of the strain distribution and the crack opening value. The chosen optical cable is a multi-layer cables composed of six fibers placed around a cylindrical tension member in order to strengthen the cable. One of the two single mode fibers is used to perform the measurements. The fibers are surrounded by a silicone filling layer, an epoxy overcoat and a Hytrel jacket with an external diameter of 2000 μm (3-24a). To strengthen the cable, a tension member is introduced in the center between the fibers as shown in Figure 3-24b. This cable is sold by Cementys company under the name “SensoLux”. As shown in Figure 3-25, Specimens 2 and 3 are instrumented with three embedded lines of the SensoLux cable (E on Specimen 2, E1 and E2 on Specimen 3) and six surface-mounted lines (S1 and S2 on Specimen 2, S1 to S4 on Specimen 3).

(a)

(b)

*Figure 3-24: **(a)** Photo of the SensoLux cable. **(b)** Micrography of different constitutive layers of SensoLux optical cable [57].*

Figure 3-26 shows the measured spatial strain profiles over the surface-mounted S1 line from Specimen 2 and embedded E2 from Specimen 3, together with the fitted curves for different measured crack openings and the residual plots. Similar to Thorlabs and BRUsens V1 concentric cables, the measured spatial strain distribution figures an exponential variation during the linear elastic stage and the computed strain profiles are in accordance with the proposed mechanical model. However, some discrepancies between the measured and fitted curves can be observed from the residuals variation over a wide area of 0 to 10 cm and -20 to 20 cm for E2 and S1 lines. These discrepancies increase with the increase in the crack opening. Contrary to Thorlabs and BRUsens V1 cables, the SensoLux has a very smooth surface that could promote slippage and could be the reason behind the distributed residuals over the bonded length of the cable and not only next to the crack location. Nevertheless, this residuals increase in a slow manner during the elastic stage and does not affect significantly the shape of the strain distribution curve.

In the case of the embedded E2 line, the residuals start propagating in a fast manner when the crack opening exceeds the 200 μm and thus, affects greatly the shape of the measured strain distribution (Figure 3-26a). The residuals propagate all over the bonded length of the fiber with no linear

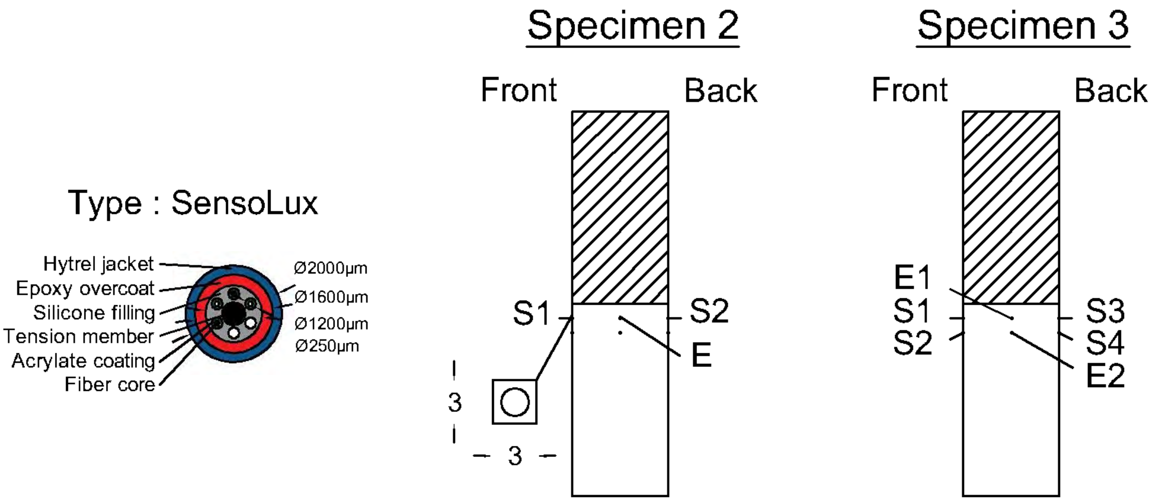

Figure 3-25: Schematic representation of the instrumentation policy of specimens 2 and 3 with SensoLux cable configuration.

spatial strain variation inside this post-elastic region. On the other hand, the crack-induced strain distribution over the surface-mounted S1 line keeps its quasi-exponential shape until a remarkable 900 μm of crack opening (Figure 3-26a). The residuals figure important variations mainly for crack openings higher than 400 μm and are distributed in the ±20 cm post-elastic region.

We can observe from Figure 3-27a that the strain measured at the location of the crack varies linearly during the elastic stage in the same manner for all different embedded lines. The critical crack opening separating the elastic and post-elastic stages can be fixed around 175μm. In the same way, the surface mounted lines shows similar linear strain variations during the elastic stage (Figure 3-27b). However, the critical crack opening varies between 220 and 400μm for the four lines instrumented on Specimen 3 and exceeded the 900 μm for the two lines instrumented on Specimen 2. The scattered results from surface mounted lines on Specimen 3 could be due to the fact that optical cable was not well positioned in the center of the groove and well surrounded by the epoxy glue, as these lines were the first glued lines during the experimental campaign.

Figure 3-28a shows that the COD estimation reaches its highest accuracy in the range of 100-400 μm with a relative error of 2-7% for embedded E1 and E2 lines from Specimen 3 and 10-15% for E line from Specimen 2. On the other hand, the COD relative errors reach less than 4% for all different surface-mounted lines as shown in Figure 3-28c. Despite the varied critical crack opening values (Figure 3-27b) for glued lines on Specimen 3, they all maintain high estimation accuracy until at least 400 μm compared to 900 μm for those glued on Specimen 2. This extremely good estimation accuracy is the most compelling evidence that the strain transfer model can be applied to non-concentric cable configurations like the SensoLux cable. Thus, there is no need for more complex and developed modeling of the cable even though it does not respond to the radial symmetry assumption adapted in the analytical model.

The effect of the additional epoxy adhesive is not only recognized with an improved crack opening estimations, it also stabilizes the strain lag parameter values as seen in Figure 3-28b and Figure 3-28d. Strain lag parameter values decrease in the case of embedded lines after reaching a peak value around 18-20 m^{-1}. On the other hand, surface glued lines maintain constant strain lag parameter values around 18-21 m^{-1}. In spite of this 15% dispersion range between the six different lines, it does not seem to affect the crack opening estimation accuracy.

Looking back to the strain lag parameter equations III.5 and III.2, the decrease in strain lag param-

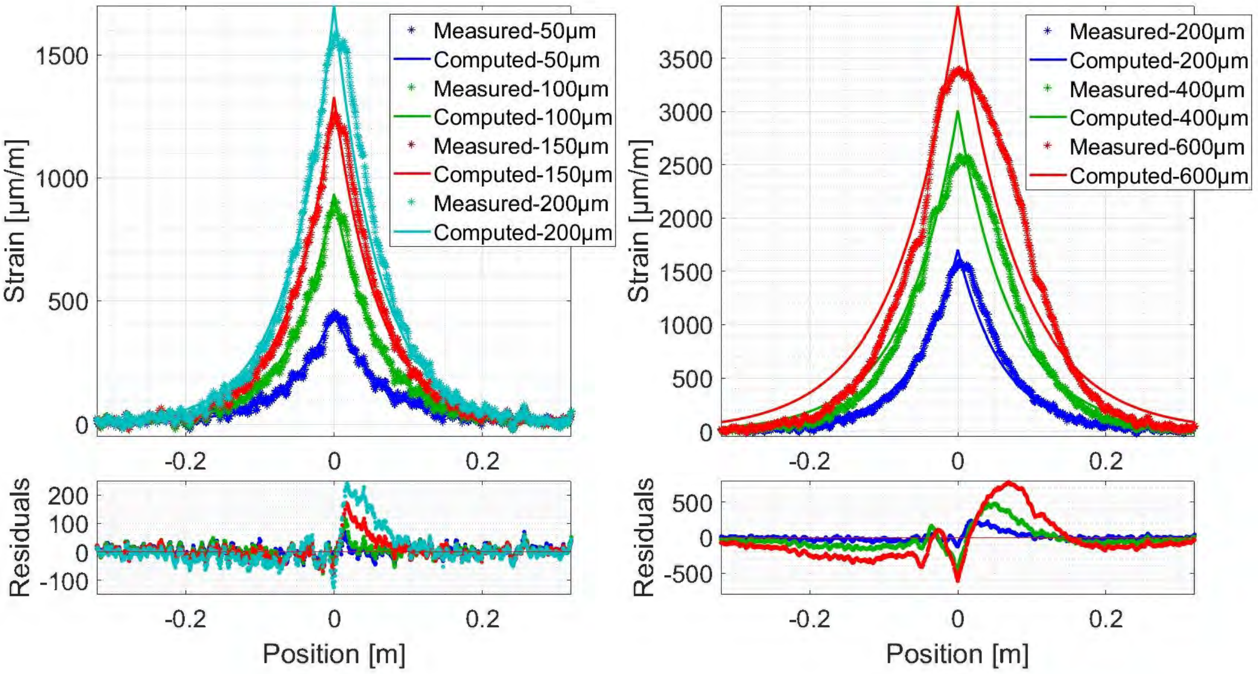

(a) E2 line from Specimen 3

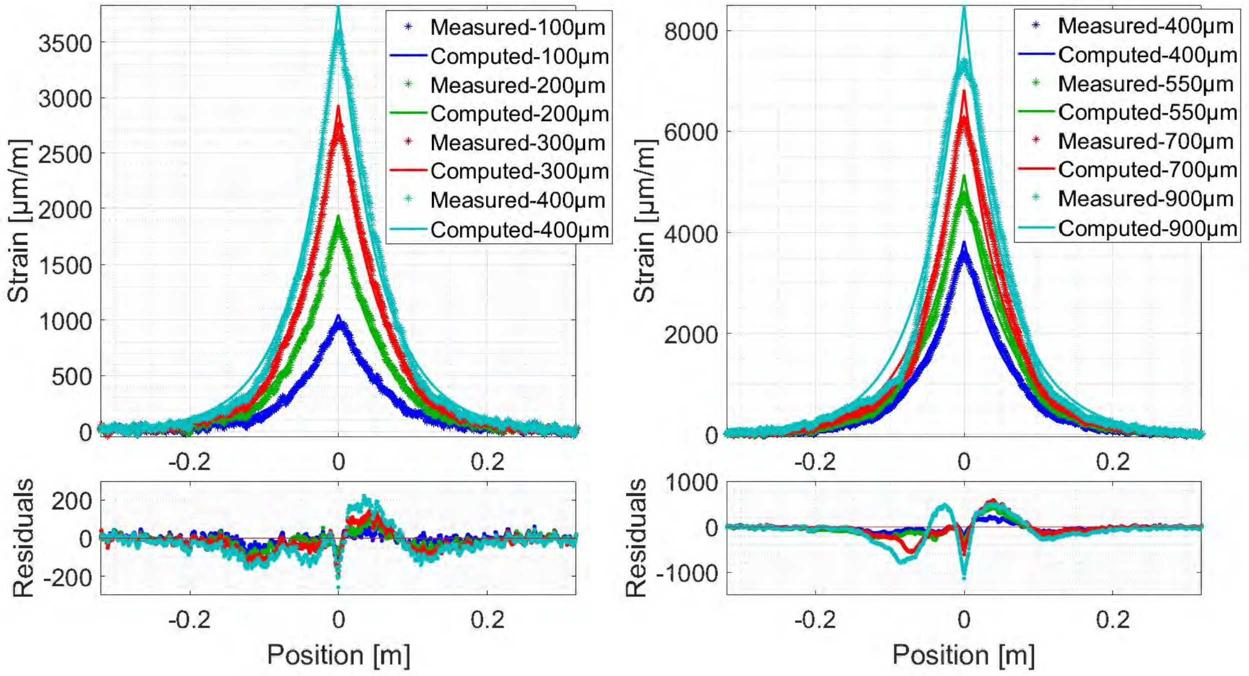

(b) S1 line from Specimen 2

*Figure 3-26: Computed strain compared to the measured strain distribution and the corresponding residuals for different crack openings over SensoLux **(a)** embedded and **(b)** surface-mounted lines.*

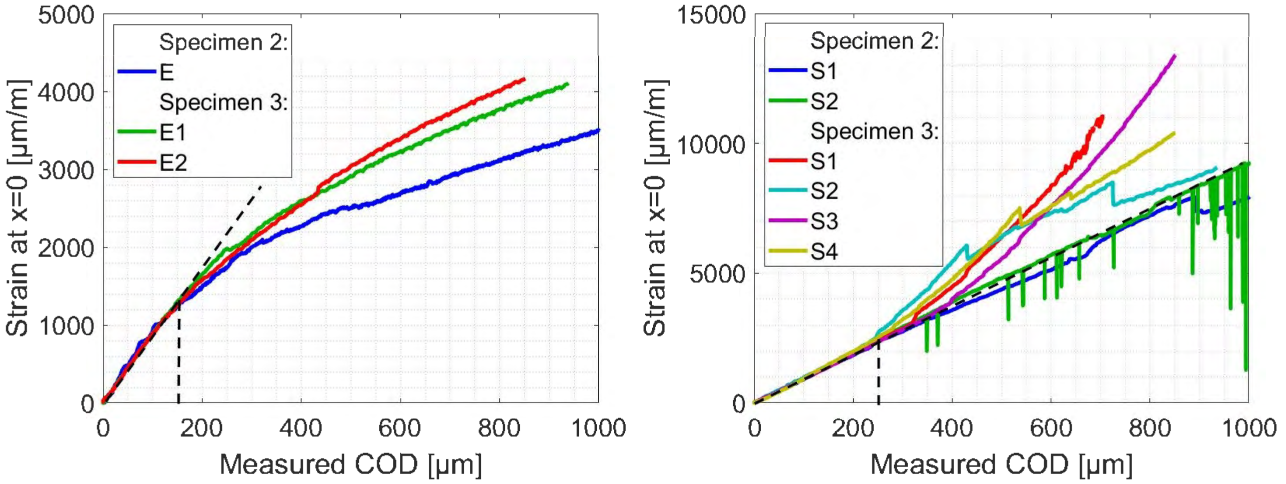

*Figure 3-27: Variation of the DFOS strain measured at the location of the crack in function of the measured crack opening for different **(a)** embedded and **(b)** surface-mounted SensoLux cable lines.*

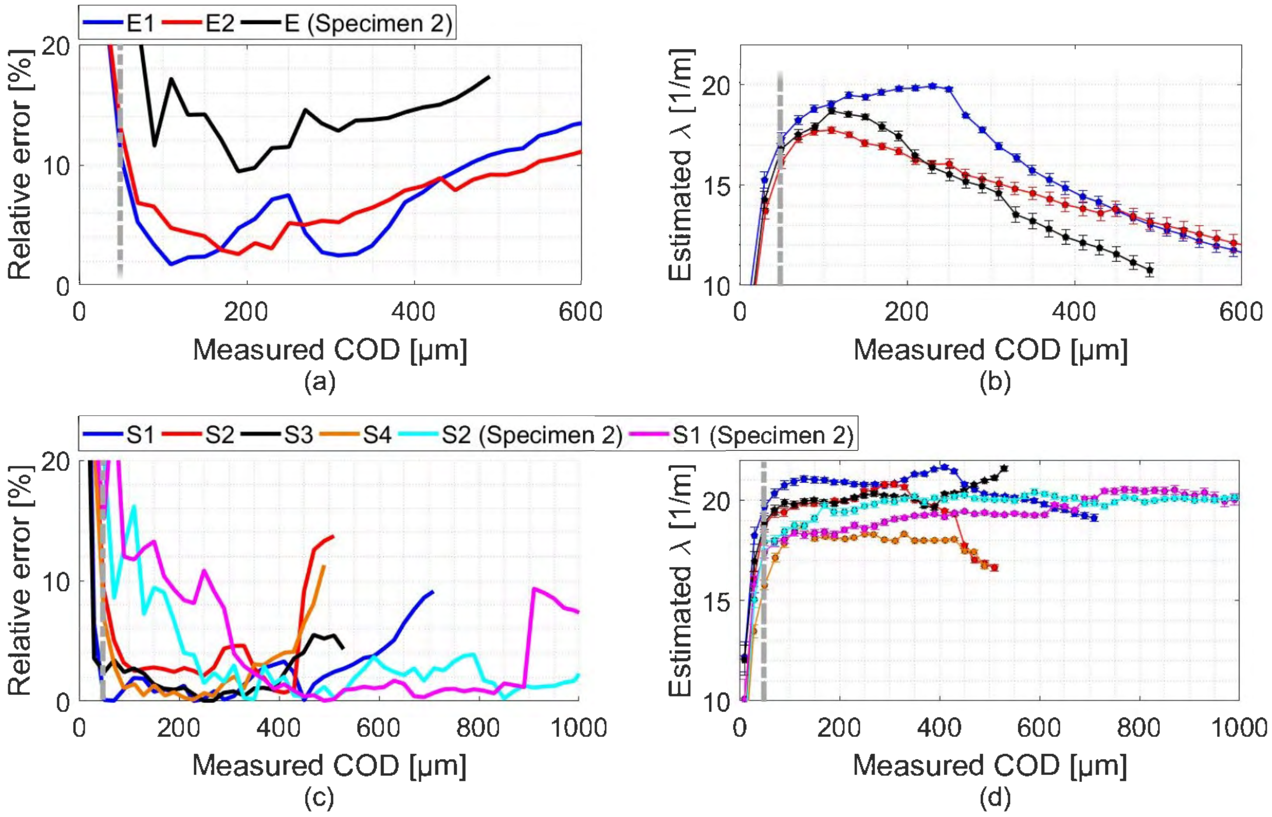

*Figure 3-28: Variation of the **(a)** relative COD estimation error and **(b)** strain lag parameter in function of the measured COD for embedded lines, and **(c)** relative COD estimation error and **(d)** strain lag parameter for surface-mounted lines.*

eter values in the case of embedded SensoLux lines should be most probably due to a degradation in the bonding stiffness at the cable/concrete interface $k_{m/c}$. This non-stable bonding response could be due to many parameters related to the cable and/or concrete and the interface conditions. As mentioned in the ACI 408R-03 code [158], concrete properties like compressive and tensile strength, aggregate type and quantity, fracture energy, mineral admixtures, consolidation, etc. can all affect its bonding capacity. However, taking into account the results from embedded Thorlabs and BRUsens V1 cables, the SensoLux very smooth external surface compared to the other two types of cables, fosters the debonding phenomenon with the concrete material and could be the main reason behind the degrading behavior of embedded lines.

III.6. Influencing conditions and model limitations

After validating the strain transfer model, this section of the chapter mainly focus on examining how instrumentation conditions and different layers properties influence the estimated parameters. In addition, some of the results, to be presented in this section, point out on the limitations of the proposed analytical model.

III.6.1. Robust optical fiber configurations

Some optical fiber cables are especially developed to be embedded in soil or concrete for the monitoring of pipelines, soil movement, tunnels, dams, etc. They include a stainless steel tube that increases the stiffness of the cable assembly and protect the optical fiber from the harsh environmental conditions present on construction sites. For this kind of cables, some potential drawbacks may arise, e.g. increased longitudinal stiffness, possible slippage between the layers within the cable or the occurrence of plastic strains in the metallic parts.

Two types of robust optical cables, named “BRUsens V4” and “BRUsens V9” are selected for testing. They are composed of an optical fiber surrounded by an Acrylate coating bonded to a stainless steel tube through a multi-layer buffer. Then, this metal tube is surrounded by a Polyamide (PA) outer sheath until the cable reaches an external diameter of 3200 μm. The outer sheath increases three times the diameter of the cable and therefore, increases its robustness. In order to examine the effect of this final layer, the metal tube without the PA outer sheath is also tested. While BRUsens V4 cable has a smooth surface, the BRUsens V9 cable has a corrugated surface in order to increase the bonding with the host material (Figure 3-29). As shown in Figure 3-30, Specimen 4 is instrumented using the metal tube by gluing two lines on the surface (S1 and S2) and embedding one line inside the concrete material (E). In the same way, Specimen 5 is instrumented using BRUsens V4 and BRUsens V9 cables, with two lines (S1 and S2) on the surface and one line (E) embedded inside the concrete.

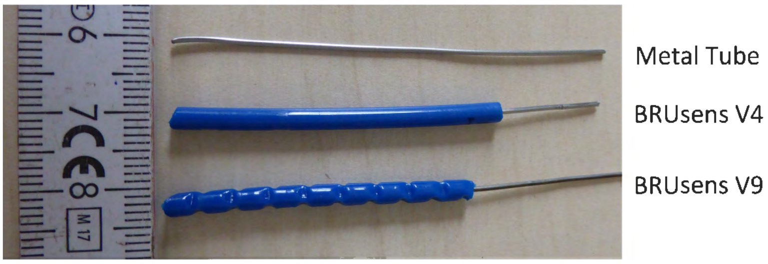

Figure 3-29: Photo of the Metal tube, BRUsens V4 and BRUsens V9.

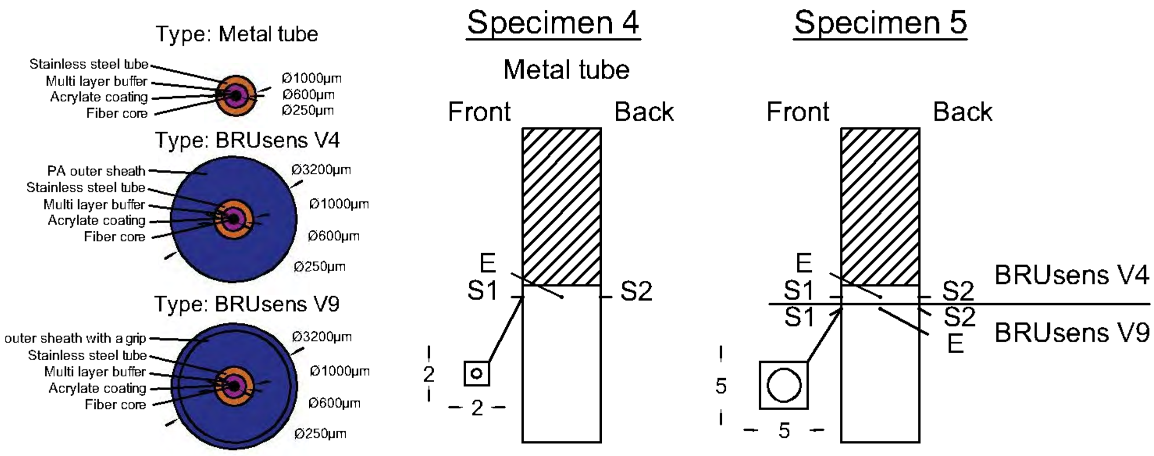

Figure 3-30: Instrumentation policy of Specimens 4 and 5 with BRUsens V4, BRUsens V9 and its metal tube configurations.

Figure 3-31 shows the measured spatial strain profiles over the metal tube surface-mounted S1 and embedded E lines (Specimen 4), together with the fitted curves for different measured crack openings and the residual plots. The surface-mounted line S1 led to spatial strain distributions in accordance with the analytical model. Residuals are observed only in the -5 cm and +1 cm area and stayed relatively constant until a 250 μm of measured crack opening (Figure 3-31a). For crack openings bigger than 250 μm, the post-elastic region starts propagating on the right side of the crack observed from the high level of residuals. On the other hand, the measured strain distribution over the embedded line E does not fit well the analytical model (Figure 3-31b) and takes a similar form to the one measured from embedded SensoLux lines during their post-elastic stage. As it keeps an exponential form near the ends, and despite its rapid shape variations, the resulting fit does always converge. This behavior can be explained due to a slippage between the cable and the concrete substrate. Together with the very smooth surface of the metal tube (Figure 3-29), the high modulus of elasticity of the stainless steel compared to concrete means that the metal tube tends to deform less than the concrete material and thus promotes a slipping behavior since the start of the macrocrack stage.

Figure 3-32a shows the peak strain variation under different crack openings. While the embedded line E figures a non-linear strain variation, the surface-mounted lines S1 and S2 figure a linear elastic response until 160μm of crack opening.

The improved adhesion due to the epoxy glue leads to a higher crack opening estimation accuracy of less than 5% in the case of S1 surface mounted line, compared to 15% in the case of embedded E line (Figure 3-33a). Moreover, the strain lag parameter reach a stable level with higher values of around 47 m^{-1}, compared to 34 m^{-1} for the embedded line E (Figure 3-33b).

For BRUsens V4 and V9 cables, Figure 3-34 shows the measured strain profiles from the instrumented lines on Specimen 5. With the additional PA outer sheath in these cable configurations, the crack-induced strain distribution takes a triangular form under different crack openings. For crack openings less than 300 μm, the strain profiles are more or less symmetric with respect to the location of the crack and the surface-mounted and embedded lines measurements correlate well. However, for high crack openings, more differences in the strain profiles are observed. For both cables, the strain amplitudes of the embedded lines become lower than those from surface-mounted lines. As discussed previously, this could be again due to the effect of the epoxy providing an increased adhe-

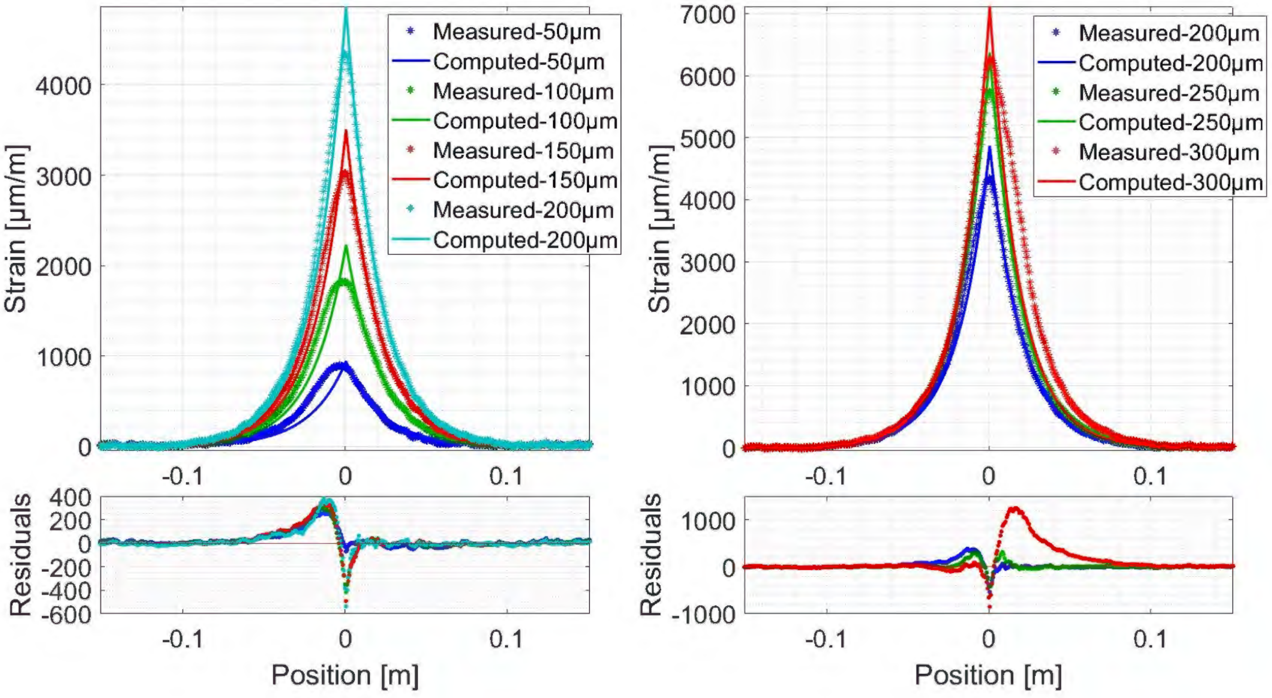

(a) S1 line

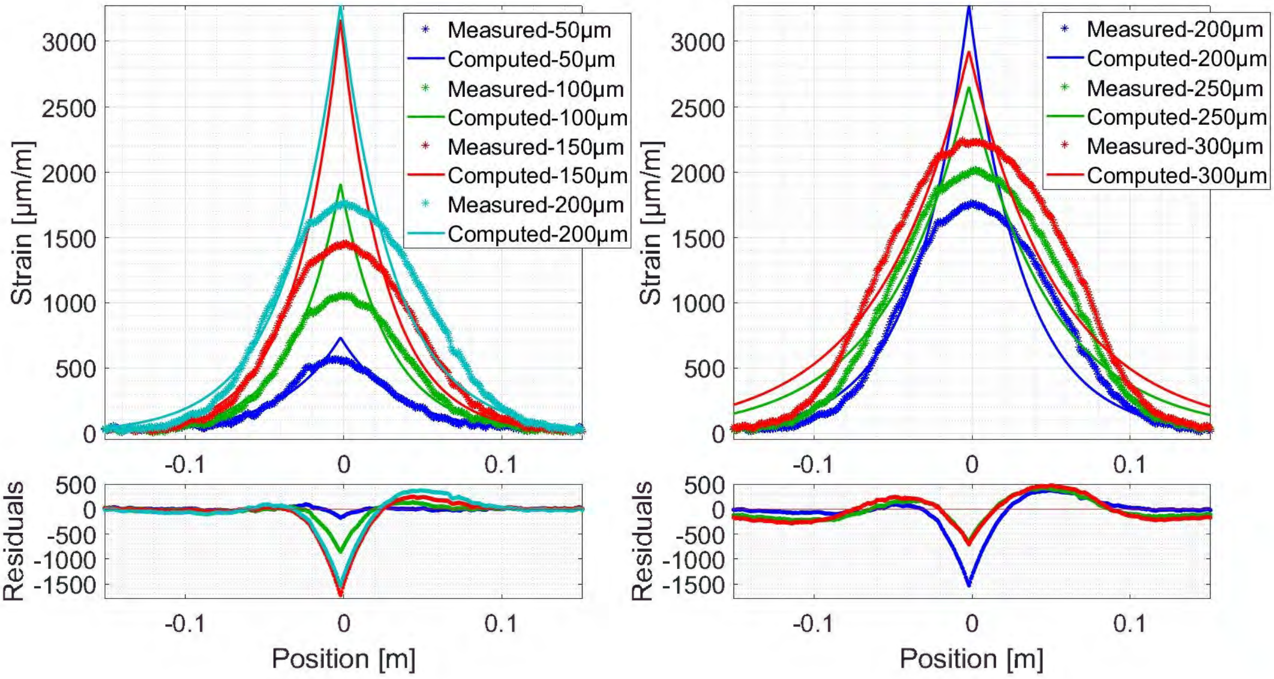

(b) E line

Figure 3-31: Computed strain compared to the measured strain distribution and the corresponding residuals for different crack openings over the Metal tube ***(a)*** *surface-mounted line S1 and* ***(b)*** *embedded line E from Specimen 4.*

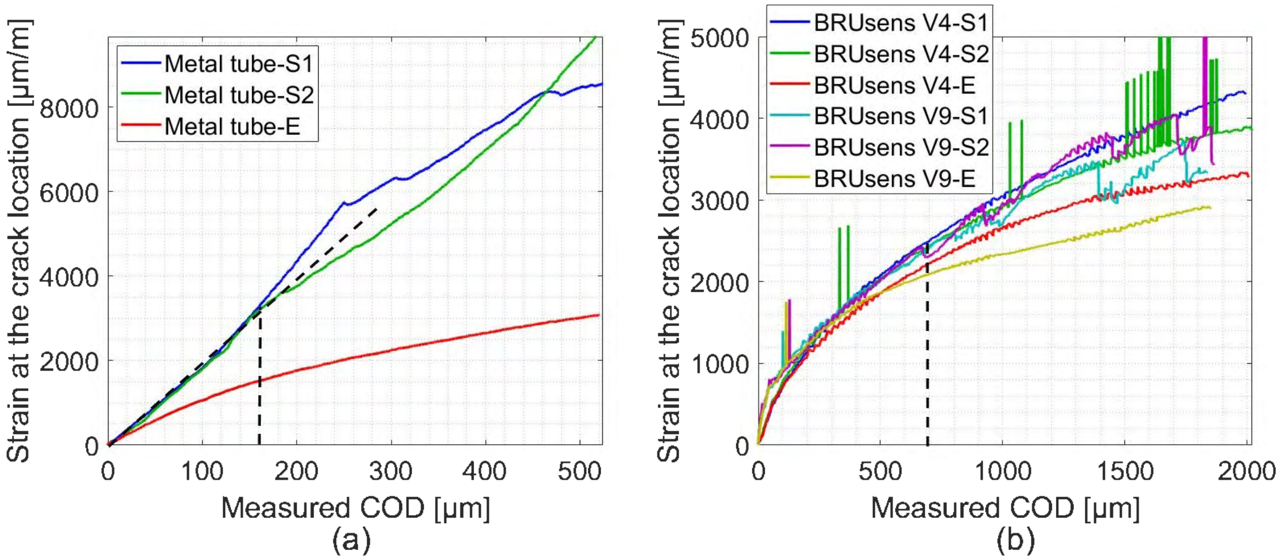

Figure 3-32: Variation of the strain measured at the crack location with the measured COD for different fiber optic lines from Specimens 4 and 5.

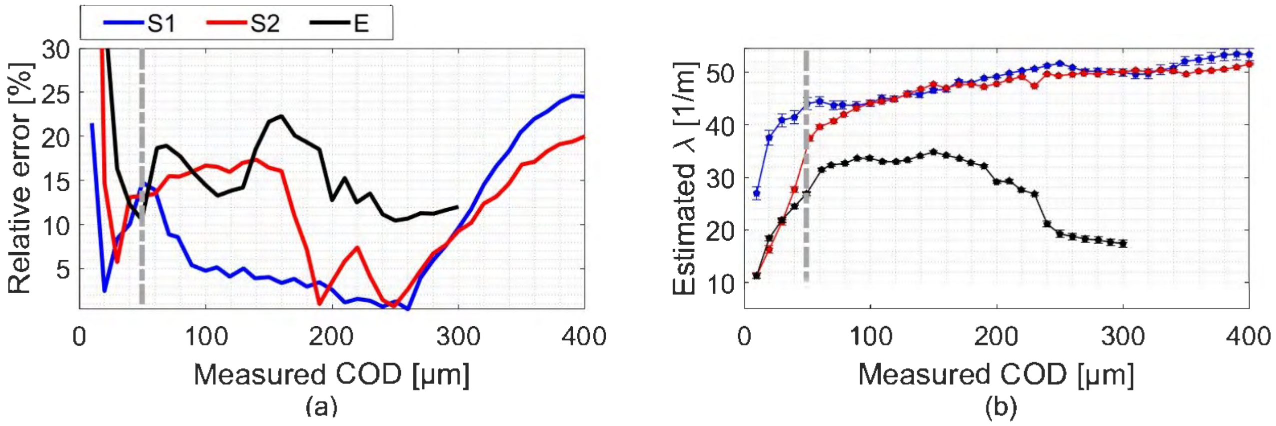

*Figure 3-33: Variation of the **(a)** relative COD estimation error and **(b)** strain lag parameter values in function of the measured COD for different Metal tube lines from Specimen 4.*

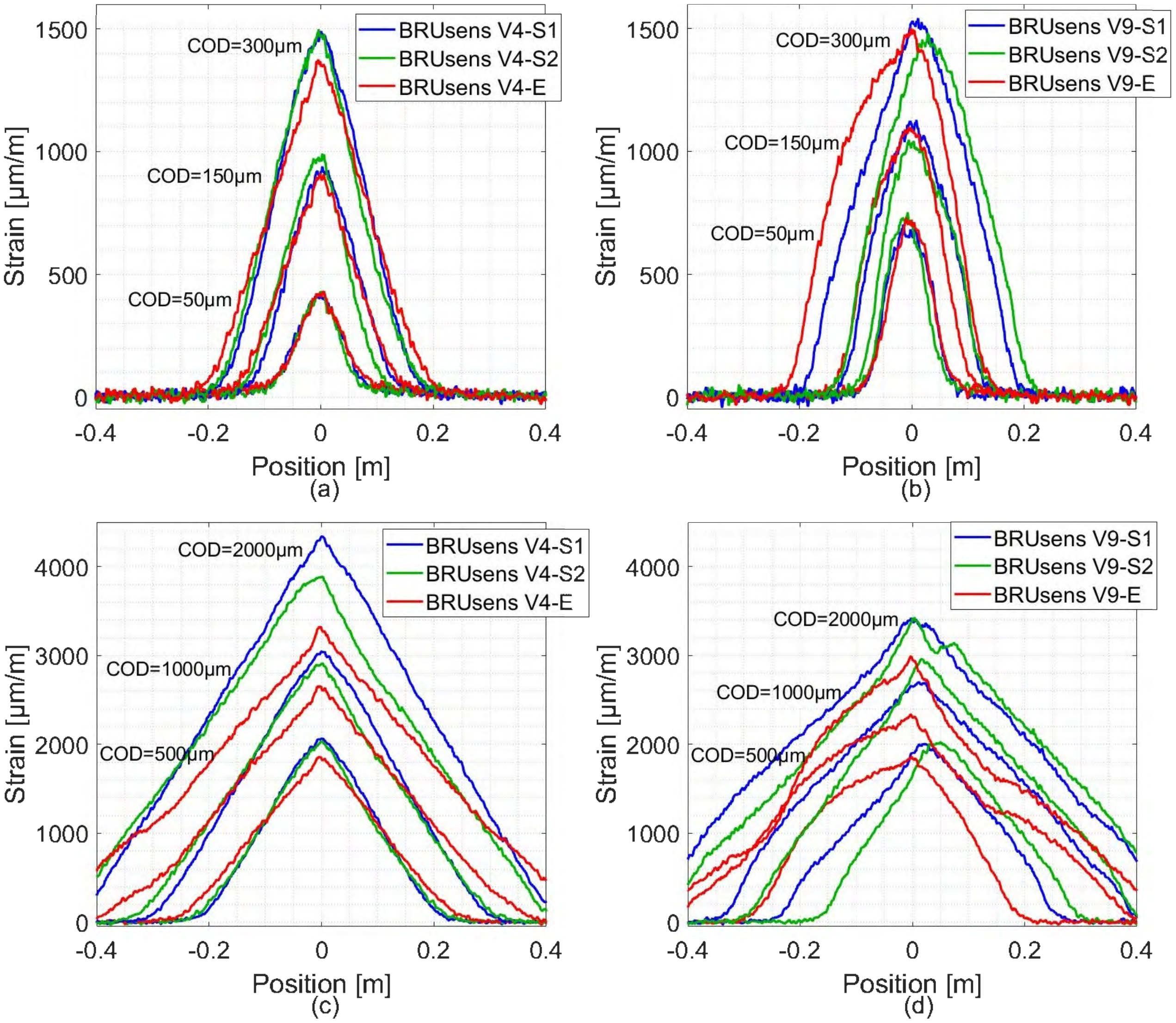

(a) (b) (c) (d)

Figure 3-34: The measured strain spatial distribution under different crack openings from fiber optic lines from Specimen 5.

sion between the cable and the concrete substrate.

The additional PA outer sheath highly decreased the optical fiber strain sensitivity to crack propagation as the BRUsens V4 and V9 lines reached a maximal strain 2000 μm/m at a COD of 500 μm, compared to a COD of 100 μm from the surface mounted metal tube. As plastic behavior of the PA outer sheath is less likely to be encountered at this small strain level, the nonlinear strain variation shown in Figure 3-33b is most probably due to a slippage at the stainless steel/outer sheath or outer sheath/concrete interfaces.

Moreover, under small crack openings ($<$300μm) the strain amplitudes from BRUsens V9 lines reach higher values than the strain measured over the V4 lines (Figure 3-34a,b). For higher crack openings, similar strain peaks can be observed from both cable types (Figure 3-34c,d). The main difference in the response of these two types of cables turns up in the consistent linearity and symmetry of the BRUsens V4's triangular shape response (Figure 3-34a,c). Contrary to V4 lines, shift in the strain peak position as well as the non-linear spatial strain variation can be observed from BRUsens V9 lines under high crack openings (Figure 3-34d). This inconsistent behavior is also observed in the sudden fall in the peak strains for BRUsens V9 S1 and S2 lines for crack openings bigger than 700 μm (Figure 3-32b). Thus we can conclude that in spite of the increased sensitivity of the BRUsens V9 cable, its corrugated surface led to inconsistent strain variation over the length of the cable and discontinuous strain variation of the peak amplitude.

It is also important to mention that the corresponding fitted curves are not plotted in Figure 3-34 as they lead to high residual levels and high error in COD estimations. Given the repeatability and consistency of the simple triangular shape obtained from the strain profiles of BRUsens V4 and V9 cables, it is later possible to propose a more adapted model. Yet another reason to do so is the cables remarkable capacity to keep this consistent simple triangular shape until high crack opening of 2 mm, contrary to other tested cable configurations.

III.6.2. Thin optical fiber configurations

Contrary to robust cables, some optical fibers are intended to be used for laboratory tests in a controlled environment and on laboratory size specimens of small dimensions. Therefore, a number of thin optical fibers characterized by thicknesses of less than 1000 μm are selected for testing. Specimen 6 is instrumented by gluing one line of each optical fiber on the concrete surface (Figure 3-35). The thinnest optical fiber is composed of an optical core surrounded by a primary Polyimide coating with an external diameter of 155 μm. The second and third types are composed of an optical core surrounded by a double layer of Acrylate coating (A1, A2) with an external diameter of 250 μm. While the Polyimide fiber is produced particularly for strain sensing (bought from Luna company), the Acrylate fibers are the well-known SMF 28 dual Acrylate coated fibers (bought from Corning company). Acrylate A2 is a recent version while Acrylate A1 is an old version bought 10 years ago. A fourth optical fiber has an Acrylate coating and a secondary Hytrel coating increasing the external diameter to 350 μm. Hytrel material is a Thermoplastics Polyester Elastomer that combines the flexibility of rubber with the strength and processability of thermoplastics. Finally, the last tested type is a tape sensing fiber consisting of two standard single mode fibers on single tape named “FutureNeuro” (provided by Neubrex Co.) .

Figure 3-36 shows the measured strain distributions at different crack openings for the Hytrel, Polyimide, Acrylate A2 and FutureNeuro fibers. Since the Acrylate A1 fiber had a very similar elastic and post-elastic behavior to Acrylate A2 fiber, the corresponding strain profiles are not presented. The crack induced strain distribution from all the optical fiber lines figured an exponential shape in accordance with the analytical model with the residuals varying randomly around the zero line during the elastic stage.

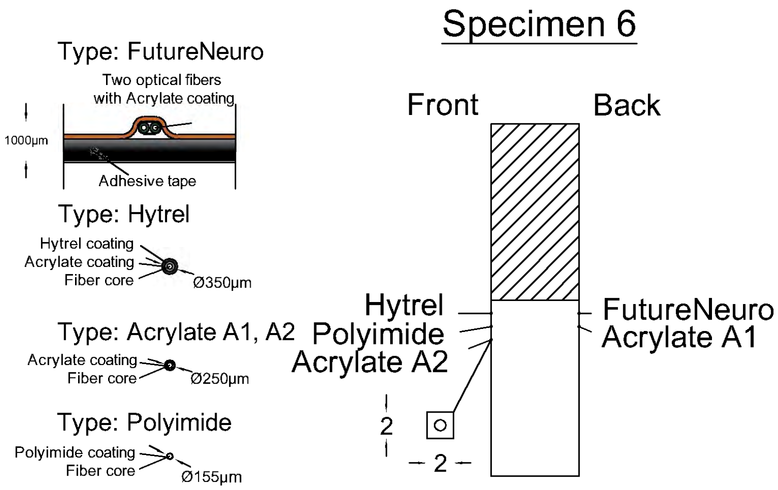

Figure 3-35: Instrumentation policy of specimen 6 with different types of thin optical fiber configurations.

The post-elastic behavior of the Acrylate A2 fiber is similar to the Thorlabs and BRUsens V1 cables presented previously, figuring a linear spatial strain variation in the post-elastic region (Figure 3-36a). The start of the post-elastic behavior along the Hytrel fiber led to high strain variations around the crack location and thus the appearance of dropouts (Figure 3-36b). This strain variation also exhibits a linear spatial strain variation in the post-elastic region that is only observed at high crack openings of around 700 μm.

The Polyimide fiber shows very high strain sensitivity to the crack propagation as the measured peak strain exceeded the 6000 μm/m at only 70 μm of crack opening (Figure 3-36c). In addition, the region affected by the crack-induced strain distribution is remarkably small of around 4 cm compared to the other fibers. In this region, an area of around 1 cm surrounding the crack location figure constant strain measurements. As discussed in Chapter 2, constant strain measurements are an indication of a full debonding behavior more likely due to the crack discontinuity propagation.

The FutureNeuro fiber reached a strain peak of 4000 μm/m at 500 μm (Figure 3-36d). The strain distribution remarkably maintained its exponential shape until very high crack opening of 1500 μm.

The linear strain variation at the crack location with the increase in crack location can be observed in Figure 3-37 for all the five types of optical fibers. The critical COD marking the start of the post-elastic stage differs between the different fiber types. It varies around 150, 180 and 200 μm for Acrylate A1, Hytrel and Acrylate A2. On the other hand, the Polyimide fiber has a very small critical COD of 80 μm and the FutureNeuro fiber has a very high critical COD of around 1400 μm (Figure 3-37b).

Figure 3-38 shows the relative COD estimation error and strain lag parameter values from the Hytrel and Acrylate A1 and A2 fiber lines. During the elastic stage, the relative error reached less than 2% for all the three fiber types and the strain lag parameter reached 31, 40 and 44 m^{-1} for the Acrylate A2, Acrylate A1 and Hytrel fiber lines, respectively. Contrary to the perfect bonding case, where an additional coating should lead to lower strain lag parameter values, the Hytrel fiber led to the highest strain lag parameter as the interfacial adhesion of the epoxy paste with the Hytrel coating seems to be better than the one with the Acrylate coating.

On the other hand, the Polyimide fiber reached a COD estimation error of less than 20% and mainly varying around 10% (Figure 3-39a). This higher percentage of relative errors compared to the three previous fibers could be attributed to the fact that the 1 cm debonded region around the

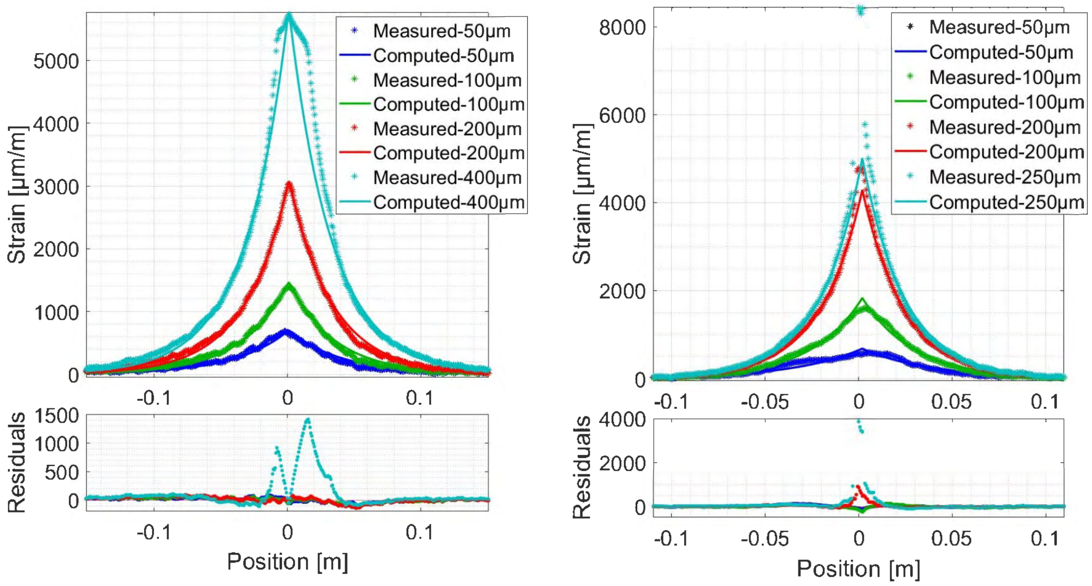

(a) Acrylate A2 fiber.

(b) Hytrel fiber.

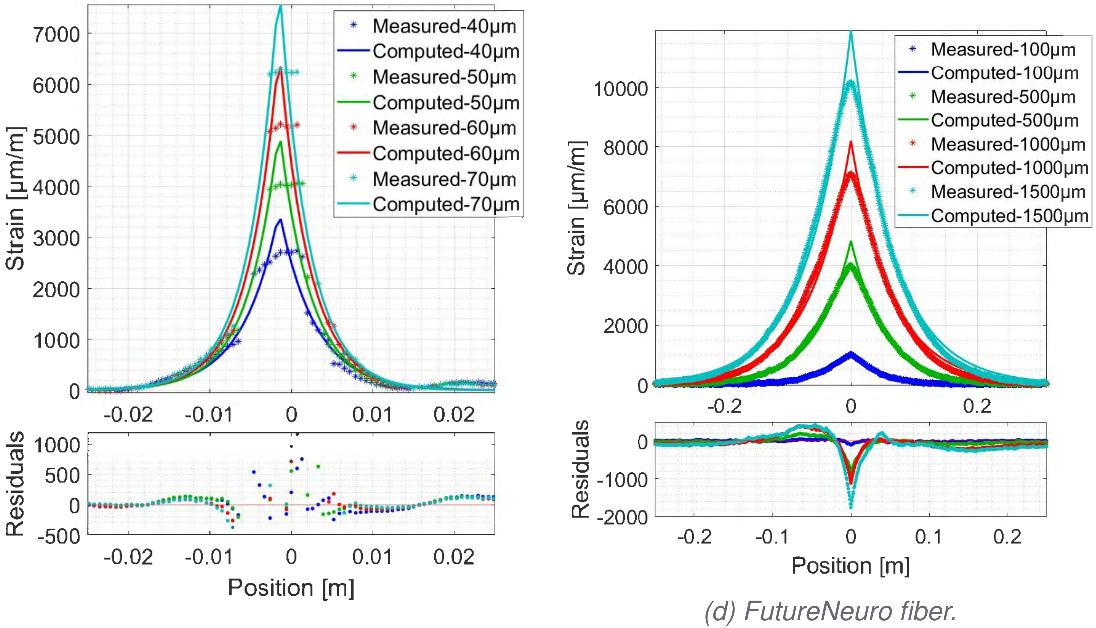

(c) Polyimide fiber.

(d) FutureNeuro fiber.

Figure 3-36: Computed strain compared to the measured strain distribution and the corresponding residuals under different crack openings for the thin optical fiber types.

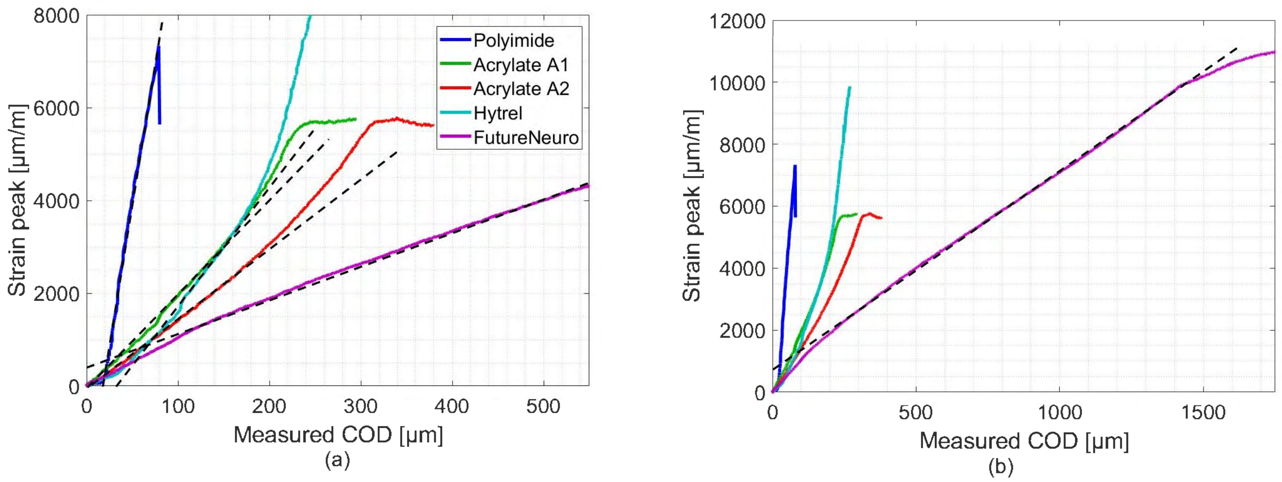

Figure 3-37: Variation of the strain measured at the crack location with the measured COD for different fiber optic lines from Specimens 6.

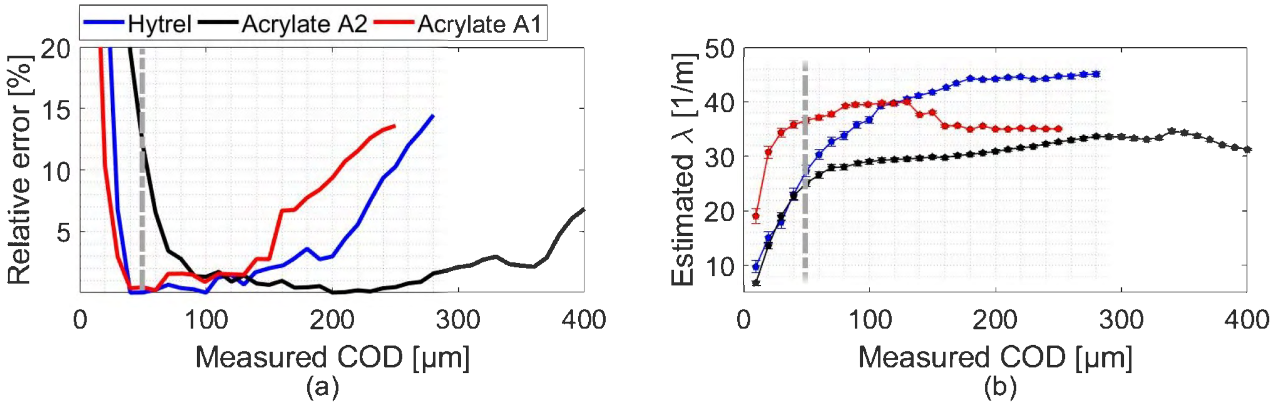

*Figure 3-38: Variation of the **(a)** relative COD estimation error and **(b)** strain lag parameter values in function of the measured COD for Hytrel, Acrylate A1 and Acrylate A2 fibers lines.*

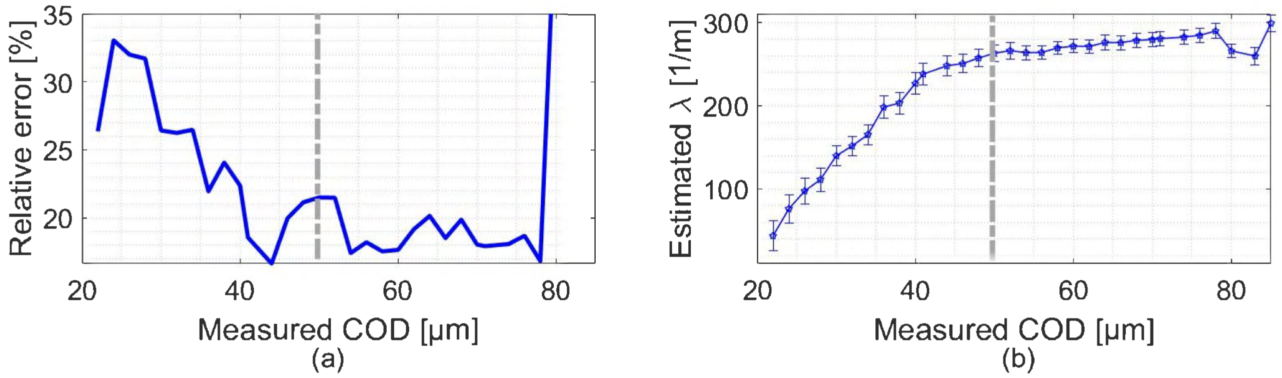

*Figure 3-39: Variation of the **(a)** relative COD estimation error and **(b)** strain lag parameter in function of the measured COD for Polyimide fiber line.*

crack forms around 25% of the total crack induced strain area and thus influences the convergence of the mechanical model fitting. The very high adherence of the polyimide coating with the fiber core, largely known in strain sensing applications, can be clearly observed from the very high strain lag parameter values of around 290 m^{-1}, exceeding at least five times the highest strain lag parameter reached by any other test optical fiber or optical cable (Figure 3-39b). All things considered, the Polyimide fiber seems to be too sensitive for a degrading material like concrete. Thus, the Polyimide fiber is not suitable for the monitoring of crack openings in concrete as long as the interrogators are still limited in terms of strain gradients and an important fiber/host material debonded area around the crack exists. This fiber could be suitable for cases where the aim is to follow small discontinuities in host materials.

The FutureNeuro fiber achieved a very good accuracy with the COD relative error reaching less than 1% for a COD=50-150 μm then degrading progressively until reaching a constant level around 6% for a COD=500-1500 μm (Figure 3-40a). In addition, the progressive decrease in the estimated strain lag parameter values from 23 m^{-1} at 150 μm to 15 m^{-1} at 1500 μm did not influence the COD estimation accuracy and the exponential shape of the strain profiles (Figure 3-36d). This could be the result of a progressive degradation of the cable's interfacial adhesion with the concrete substrate.

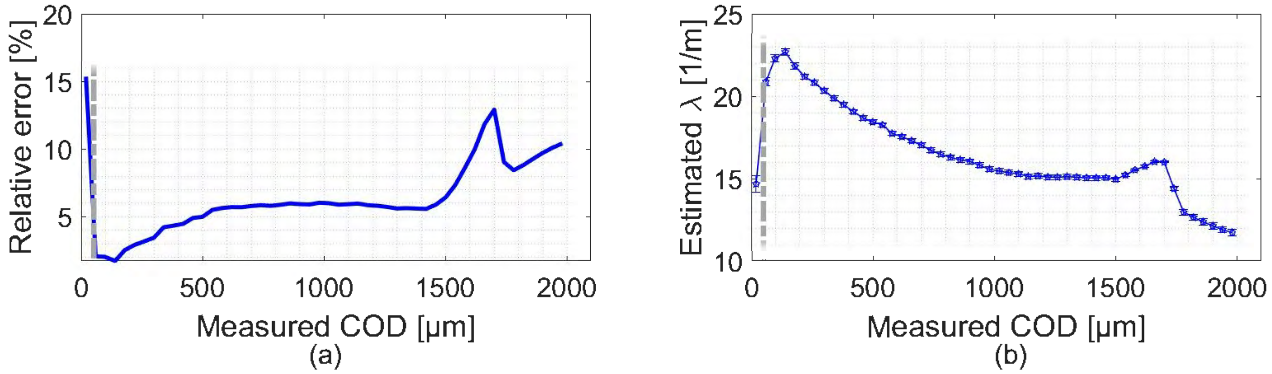

*Figure 3-40: Variation of the **(a)** relative COD estimation error and **(b)** strain lag parameter in function of the measured COD for FutureNeuro fiber line.*

III.6.3. Effect of concrete hardening

The concrete is completely fluid before the cement sets, then progressively hardens over several months. During this hardening process, the strength of the concrete material, its degradation behavior and its adhesion properties to other materials can change. Thus, in order to examine the effect of concrete hardening on the strain response of the embedded and surface-mounted sensing cables, three 40×40×20 cm Specimens 9, 10 and 11 were tested after 1, 2 and 3 months of concrete hardening, respectively. As shown in Figure 3-41, each specimen was instrumented with one embedded and one surface-mounted line of SensoLux and Thorlabs cables. It is important to mention that the grooves were made at the same day for all the three specimens and the surface-mounted lines were glued only 10 days before each test in order to eliminate any effect of epoxy adhesive aging on the strain transfer response.

Figure 3-42 compares the relative COD error and strain lag parameter values for the SensoLux cable lines embedded and glued on the surface of the three specimens.

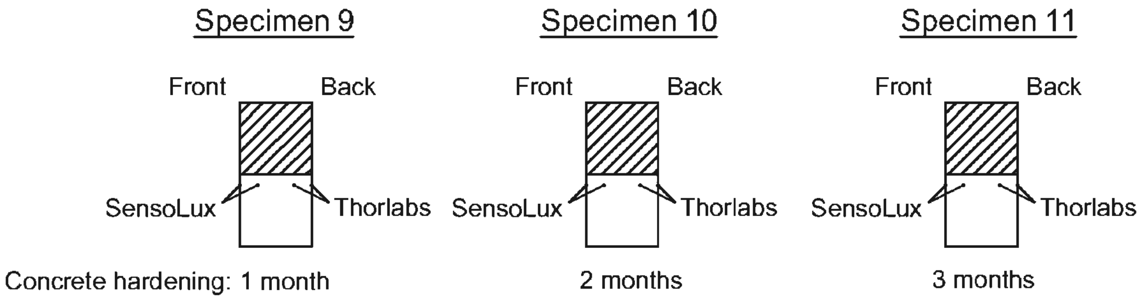

Figure 3-41: Instrumentation policy of Specimens 9, 10 and 11 with Thorlabs and SensoLux cable configurations.

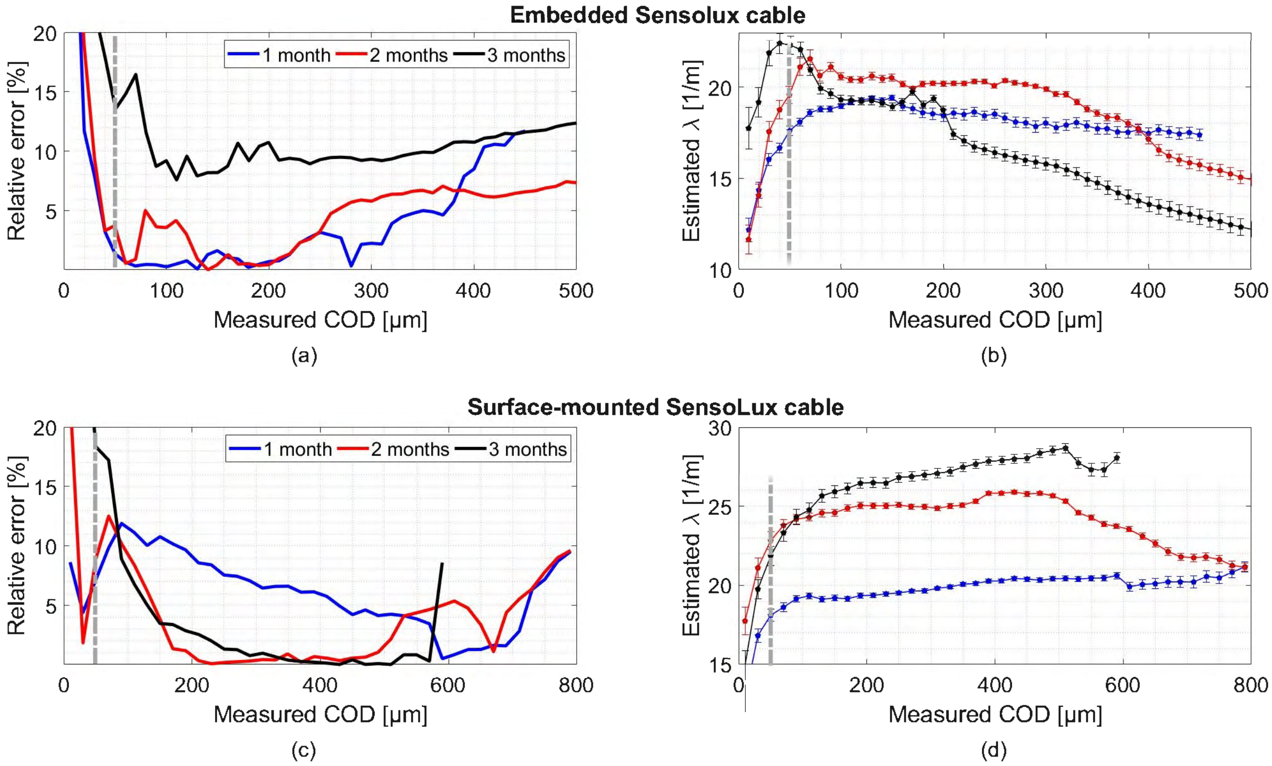

(a) (b)

(c) (d)

*Figure 3-42: Variation of the **(a,c)** relative COD estimation error and **(b,d)** strain lag parameter in function of the measured COD for SensoLux cable tested after 1, 2 and 3 months of concrete hardening.*

In the case of embedded SensoLux cable (Figure 3-42a), the relative COD estimation error increased from 2% for the lines instrumented on Specimens 9 and 10 to 10% for the line instrumented on Specimen 11 and tested after 3 months of concrete hardening. The latter led to the highest strain lag parameter peak of 22.5 m^{-1} followed by a rapid decrease, while the lines corresponding to 1 and 2 months hardened concrete figured more constant post-peak values at 19.5 m^{-1} and 21 m^{-1} (Figure 3-42b).

On the other hand, the surface-mounted line corresponding to a 1 months hardened concrete from Specimen 9 led to the highest COD estimation error of 5-10% compared to 1% for the surface-mounted lines corresponding to 2 and 3 months hardened concrete (Figure 3-42c). This improved accuracy is accompanied by an increase in strain lag parameter values from 20 m^{-1} to 25 m^{-1} and 27.5 m^{-1} for a hardened concrete of 1, 2 and 3 months, respectively (Figure 3-42d). Thus, concrete hardening could be the reason behind an increased interfacial adhesion with the Araldite epoxy adhesive that increases the strain lag parameter values and also improves the crack opening estimation accuracy.

Figure 3-43 compares the COD and strain lag estimated parameters for surface-mounted and embedded Thorlabs cable lines. For the embedded lines, the COD estimation error varied around

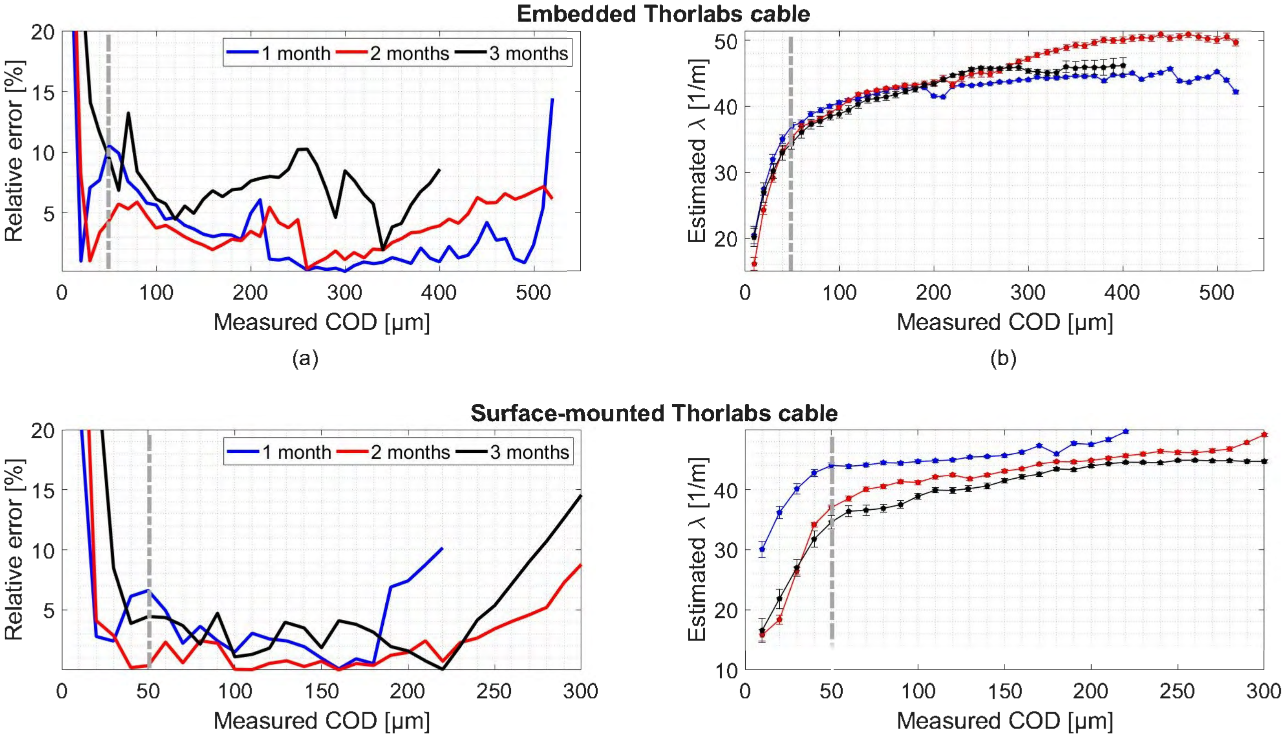

(a) (b)

(c) (d)

Figure 3-43: Variation of the ***(a,c)*** *relative COD estimation error and* ***(b,d)*** *strain lag parameter in function of the measured COD for Thorlabs cable tested after 1, 2 and 3 months of concrete hardening.*

2-4% for those corresponding to 1 and 2 months hardened concrete, with an increase to around 5-8% for the line corresponding to 3 months hardened concrete (Figure 3-43a). On the other hand, the strain lag parameter values are very well correlated for the three different lines, reaching a constant level of around 44 m^{-1} (Figure 3-43b).

Moreover, no remarkable change in the COD estimation accuracy of the surface-mounted lines is observed after 3 months of concrete hardening as the relative error varies around 4% (Figure 3-43c). Strain lag parameter values decrease from 45.5 m^{-1} to 43 m^{-1} and 41.5 m^{-1} for lines corresponding to 1, 2 and 3 months hardened concrete (Figure 3-43d). Whether embedded in concrete or glued on the surface, the Thorlabs cable seems to be less affected by concrete hardening compared to the SensoLux cable.

Finally, it is important to mention that the limited number of tests prevent us to totally affirm the tests observations. In the continuity of this work, a more systematic campaign of tests can be foreseen figuring different types of concrete with variable properties and longer concrete hardening time.

III.6.4. Effect of bonding length

As discussed in the section of the previous chapter, the crack-induced strain response is mainly distributed over a certain length of the optical fiber. As already shown in Figure 2-5, this length is dependent on the strain lag parameter. This effective bonding length 2L$_e$ can be defined as the bonding length allowing a certain strain transfer rate (STR) from the total crack induced strain distribution (Figure 3-44) as follows:

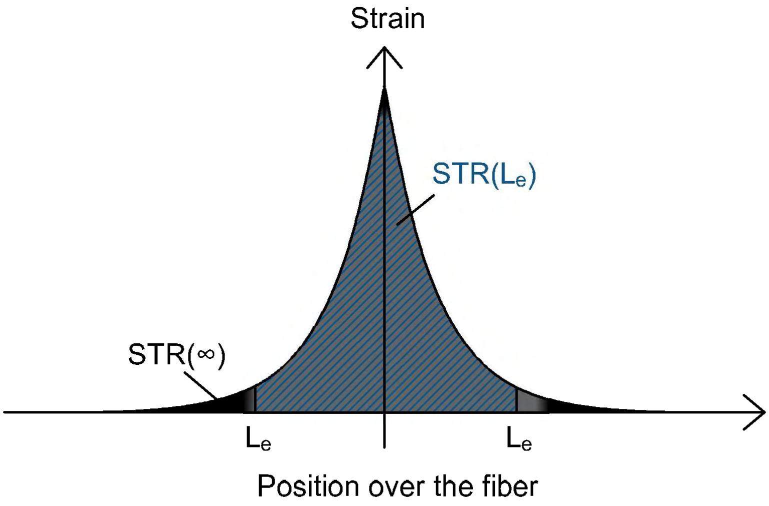

Figure 3-44: Schematic representation of the defined effective bonding length and its corresponding strain transfer rate STR.

$$\mathrm{STR}(\mathrm{L}_e) = \frac{\int_{-\mathrm{L}_e}^{+\mathrm{L}_e} \epsilon_f(x)\mathrm{d}x}{\int_{-\infty}^{+\infty} \epsilon_f(x)\mathrm{d}x} \tag{III.7}$$

Introducing the strain transfer Equation III.2 in Equation III.7 leads to:

$$\mathrm{STR}(\mathrm{L}_e) = \frac{\int_{-\mathrm{L}_e}^{+\mathrm{L}_e} \frac{\mathrm{COD}}{2}\lambda e^{-\lambda|x|}\mathrm{d}x}{\int_{-\infty}^{+\infty} \frac{\mathrm{COD}}{2}\lambda e^{-\lambda|x|}\mathrm{d}x} = 1 - e^{-\lambda \mathrm{L}_e} \tag{III.8}$$

Figure 3-45 shows the variation of the strain transfer rate STR in function of the strain lag parameter λ for different bonding lengths.

In previous works on strain transfer [108, 57, 109], the authors fixed the effective bonding length based on a STR=0.97, as defined by Yuan in 1998 [159]. However, in our case, the appropriate effective bonding length is the one corresponding to the minimum STR allowing us to estimate the

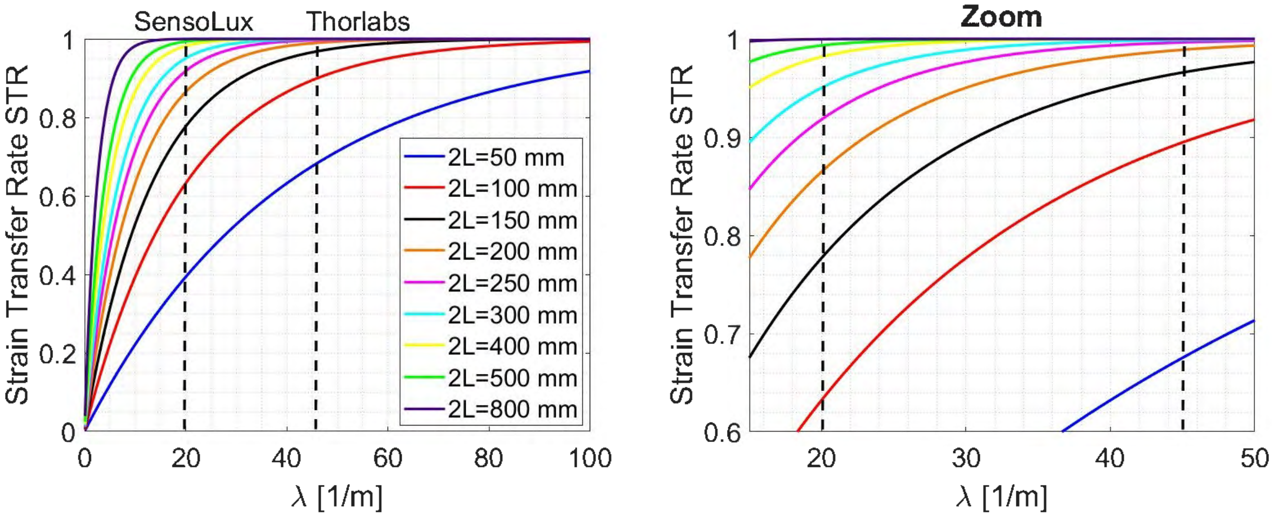

*Figure 3-45: **(a)** Variation of the strain transfer rate STR in function of the strain lag parameter λ for different bonding lengths $2L$ and **(b)** a zoom on the area covering the SensoLux and Thorlabs cables case.*

real COD and strain lag parameter values. In other words, when the bonding length 2L of a specific optical cable is bigger than its effective bonding length 2L$_e$, the estimated crack opening COD and strain lag parameter λ should not differ significantly from the true values.

In order to estimate this bonding length, Specimen 7 is instrumented with Thorlabs and SensoLux cables on the front and back sides and with bonding lengths varying from 100 to 400 mm and 100 to 800 mm, respectively (Figure 3-46). The COD estimation error and strain lag parameter values are presented in Figure 3-47 for the SensoLux and Thorlabs lines glued on the surface of the specimen with different bonding lengths. In the case of SensoLux lines, the COD estimation error reached around 2%, except for the lines bonded over 200 and 100 mm, where it increased to 6% and 22% (Figure 3-47a). In addition, and while both lines bonded over 800 and 500 mm led to an estimated strain lag parameter value of 19.5 m^{-1}, higher values were estimated from lines with lower bonding lengths (Figure 3-47b). A strain lag parameter of 25 m^{-1} is estimated from the SensoLux line bonded over 100 mm. Similar to SensoLux cable, different Thorlabs cable lines reached high COD estimation accuracy with a relative error of only 3%, except for the line bonded over 100 mm leading to higher relative errors of around 5% (Figure 3-47c). We can also observe an increase in the estimated strain lag parameter to 52 m^{-1} and 50 m^{-1} for lines bonded over 100 and 150 mm, compared to 45.5 m^{-1} for other lines with higher bonding lengths (Figure 3-47d).

Table 3-6 gives the numerical values of the strain transfer rates corresponding the each effective bonding length and for a strain lag parameter equal to 19.5 m^{-1} (for SensoLux cable) and 45.5 m^{-1} (for Thorlabs cable), extracted from Figure 3-45b. In addition, the table presents the estimated COD and strain lag parameter values resulting from the experimental test. In order to guaranty an estimation of the real crack opening values, a bonding length of 300 mm and 150 mm are enough for SensoLux and Thorlabs cables. These bonding lengths correspond to a strain transfer rate of 0.95 and 0.96, respectively. Moreover, for a real estimation of strain lag parameter values, a bonding length of 500 mm and 200 mm is needed for SensoLux and Thorlabs cables. These bonding lengths correspond to a strain transfer rate of 0.99 (Figure 3-45b).

As a conclusion, the strain transfer rate of 0.97 fixed by Yuan seems to be enough for estimating

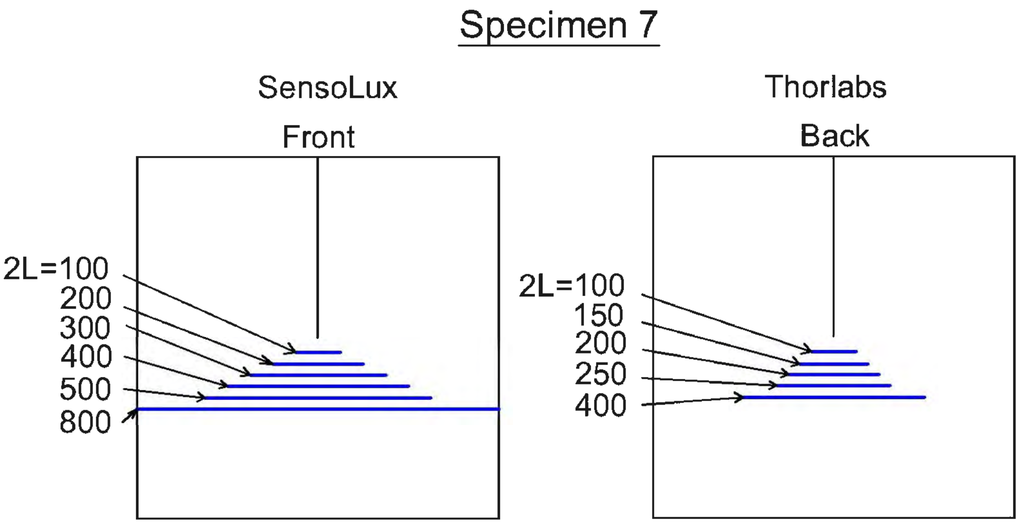

Figure 3-46: Instrumentation policy of specimen 7 with Thorlabs and SensoLux cable configurations glued over different bonding lengths.

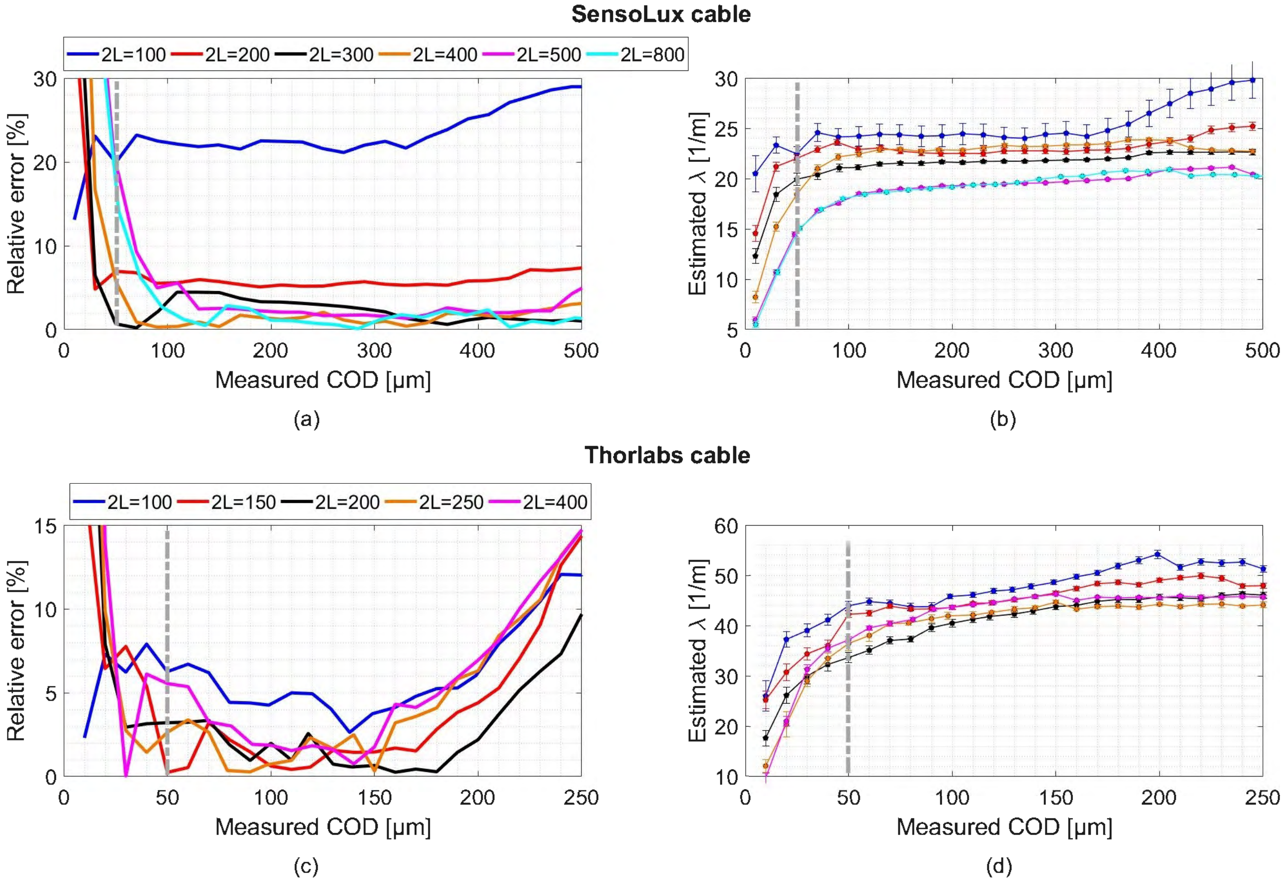

*Figure 3-47: Variation of the **(a,c)** relative COD estimation error and **(b,d)** strain lag parameter in function of the measured COD for SensoLux and Thorlabs cables under different bonding lengths.*

Thorlabs cable						
Bonding length [mm]	100	150	200	250	400	-
STR	0.89	0.96	0.99	1	1	-
Strain lag parameter λ [m^{-1}]	52	50	45.5	43.5	45.5	-
Absolute relative error [%]	5	1	1	1.5	1.5	-
SensoLux cable						
Bonding length [mm]	100	200	300	400	500	800
STR	0.63	0.87	0.95	0.98	0.99	1
Strain lag parameter λ [m^{-1}]	25	22.5	23	21.5	19.5	19.5
Absolute relative error [%]	22	6	3	2	2	2

Table 3-6: Estimated parameters from the fitting and the calculated COD absolute relative error with respect to measured crack opening for Thorlabs and BRUsens V1 embedded lines.

the real crack opening values but will lead to strain lag parameter estimation errors. For an accurate estimation of both parameters, the optical cable should be bonded over an effective bonding length corresponding to a minimum strain transfer rate of 0.99.

III.6.5. Effect of the epoxy adhesive aging

During the testing campaign, all different optical fiber lines were glued on the specimens 10 to 14 days before the test. However, in order to use this crack opening monitoring technique for an application on a real structure, it is important to study the effect of epoxy adhesive aging on the estimated parameters of the model.

Therefore, Specimen 8 was instrumented by gluing lines of SensoLux cable, 1, 2 and 3 months before the test. This short aging time was fixed due to time constraints of the PhD work. Recently, the company ”HUNTSMAN” stopped the production of the Araldite 2014-1 and released a new version called Araldite 2014-2. For this reason, we chose to glue the front side lines using the Araldite 2014-1 and the back side lines using the Araldite 2014-2, as shown in Figure 3-48. The new Araldite 2014-2

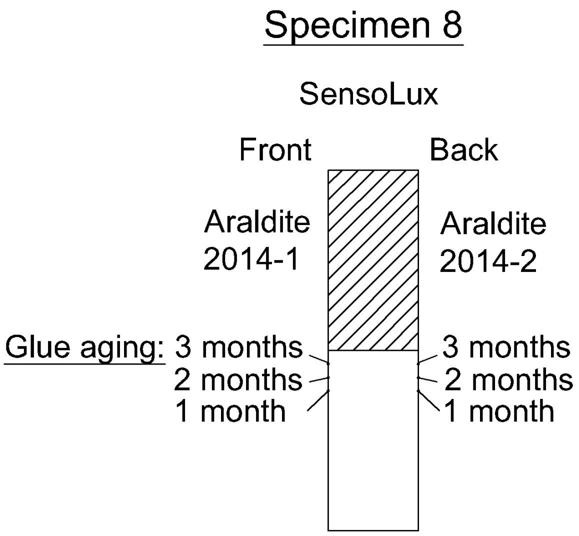

Figure 3-48: Instrumentation policy of specimen 8 with SensoLux cable configuration glued using epoxy Araldite 2014-1 and 2014-2.

is very similar to Araldite 2014-1 in terms of performance and mechanical properties listed in Table 3-7.

textbfType	**Cure time**	**Lap shear strength**	**Shear modulus**	**Tensile strength**	**Tensile modulus**	**Elongation at break**
Araldite 2014-2	5-8 hours	>14 MPa	1.2 GPa	30 MPa	3.1 GPa	10000 μm/m
Araldite 2014-1	4-7 hours	>14 MPa	1.2 GPa	26-28 MPa	3.5-4.35 GPa	7000-8000 μm/m

Table 3-7: Mechanical properties of the Araldite 2014-1 and 2014-2 epoxy adhesives at 23° C.

Figure 3-49 presents the estimation results of the COD and strain lag parameter from all the instrumented lines. The line glued for 3 months using the Araldite 2014-1 shows lower COD estimation error of less than 2% compared to 4-6% from lines glued for 1 and 2 months using the same adhesive (Figure 3-49a). Moreover, the Araldite 2014-1 layer adhesion to the cable and the concrete material seems to increase as the strain lag parameter increased from 20 m^{-1} to 22 m^{-1} and 25 m^{-1} for a glue aging of 1 to 2 and 3 months, respectively (Figure 3-49b).

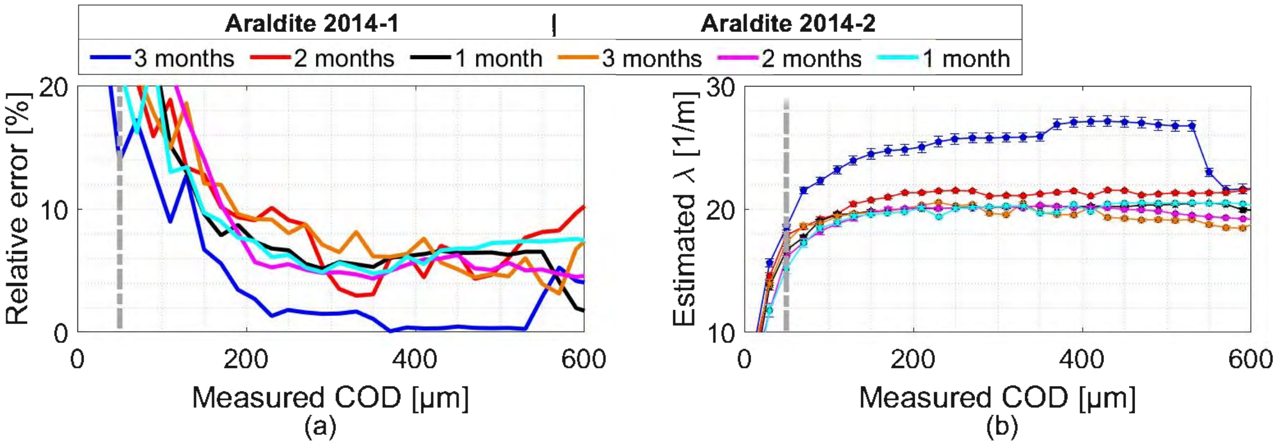

*Figure 3-49: Variation of the **(a)** relative COD estimation error and **(b)** strain lag parameter in function of the measured COD for SensoLux lines with 1, 2 and 3 months glue aging.*

The new Araldite 2014-2 seems to have more stable performance with aging time as all different lines showed equivalent COD estimation error around 4-6% (Figure 3-49a) with a corresponding strain lag parameter of 20 m^{-1} (Figure 3-49b). Thus, no effect of the Araldite 2014-2 short-term aging on the strain transfer response and the corresponding COD and strain lag parameter estimated parameters, can be observed.

III.7. Conclusion

In this chapter, the strain response of the optical fiber due to a crack propagation inside concrete material was studied. For this purpose, the wedge splitting mechanical tests were performed in order to create a single crack propagating perpendicularly to the optical fiber and up to high crack openings of 2 mm. The distributed strain profiles were measured using the ODISI-B interrogator over the length of each line of optical fiber with a high spatial resolution of 1.3 mm. The frequency of measurements and the displacement-controlled tests were adjusted in order to perform continuous strain measurements under different crack openings (at least 10 strain measurements at each 1μm of crack opening). LVDT sensors were used as a reference sensors to measure the crack openings at the optical fiber location. The proposed strain transfer model discussed in Chapter 2 was fitted to the spatial strain profiles using robust least square method and thus provided an estimation of the crack opening and strain lag parameter variable coefficients.

First, two types of multi-layer concentric cable configurations (Thorlabs and BRUsens V1) embedded inside the concrete material, were tested. Two strain transfer stages were distinguished: an elastic stage and a post-elastic stage. During the elastic stage, the distributed spatial strain profiles took an exponential form and correlated well with the fitted strain transfer equation. This has been concluded from the low residuals level and the linear strain variation at the crack location under different crack openings. In addition, a critical crack opening, marking the start of the post-elastic stage, was determined for each type of cable. The post-elastic stage was characterized by a progressively propagating post-elastic region starting from the crack location, in which the spatial strain variation takes a triangular form. During the macro-cracking stage of the concrete material (crack openings higher than 50 μm), the estimated crack openings were also in accordance with those measured from LVDT sensors and with absolute relative errors of less than 10%. In addition, the estimated strain lag parameter values shown to be mainly constant around 45 to 55 m^{-1}.

The same Thorlabs and BRUsens V1 cables were also glued on the surface of the specimens inside a groove and using the Araldite 2014-1 epoxy adhesive. Similar to the embedded lines, the distributed spatial strain profiles from the surface mounted lines correlated well with the fitted strain transfer equation with similar critical crack opening values. And thus, this new multi-layer strain transfer system can be represented by the proposed analytical model based on the cylindrical symmetry assumption. In terms of estimated parameters, and while the same crack opening estimation errors were found, higher strain lag parameter values were observed. It has been concluded that this increase is mainly caused by a better interfacial adhesion between the glue and both the cable and the concrete layers than the one existing between the cable and the concrete material.

Despite its non-concentric configuration around the optical fiber, the crack-induced strain distributions from a third cable type (SensoLux) corresponded well to the strain transfer model. When embedded in concrete, the elastic strain transfer stage was limited to a crack opening of 200 μm, compared to 1000 μm for some surface-mounted lines. Both embedded or surface-mounted, measurements from the SensoLux cable led to accurate estimation of the crack openings. Surface-mounted lines led to lower relative errors of 4%, compared to embedded lines where it varied between 4 and 15%. This difference has been attributed to degrading interfacial adhesion between the cable and the concrete material, as the strain lag parameter values decreased under increased crack openings. For surface mounted lines, the strain lag parameter values were constant and varied around 18 to 20 m^{-1} between different lines.

Model limitations were discovered through testing two robust optical cables (BRUsens V4 and BRUsens V9) including a metal tube. Whether embedded or surface-mounted, the BRUsens V4 and BRUsens V9 led to similar triangular spatial strain distribution. On the other hand, the metal tube response was in accordance with the elastic strain transfer model. Thus, it has been shown that the last Polyamide outer sheath layer of the BRUsens V4 and BRUsens V9 could be the reason behind this different response as it increase three times the diameter of the cable and could lead to slippage at the cable/concrete interface.

On the other hand, five different types of thin optical fibers, glued on the surface of the specimens, correlated well with the strain transfer model and led to very good crack opening estimations. While Acrylate A1 and A2 and Hytrel coated fibers showed similar behavior to Thorlabs and BRUsens V1 cables, the Polyimide coated fiber proved to be at least 5 times more strain sensitive to crack opening propagation. However, it is limited in terms of crack opening range (maximum 80 μm) and estimation accuracy (relative error equal to 10%). Contrary to the Polyimide fiber, the FutureNeuro fiber figures the lowest strain sensitivity to crack openings, allowing the fiber to monitor crack openings with a precision of 6% and up to 1500 μm.

The concrete hardening effect on the crack opening and strain lag parameter estimations was examined on the Thorlabs and SensoLux cable types. For embedded SensoLux cables, lower crack opening estimation accuracy as well as strain lag parameter values, were found after three months of concrete hardening compared to one month. On the opposite, better crack opening estimation accuracy and remarkably higher strain lag parameter values were observed for surface-mounted lines glued on a three months hardened concrete. For Thorlabs cable, the surface-mounted and embedded lines did not show any dependency on the concrete hardening time.

For surface-mounted lines, the bonding length can affect the crack opening and strain lag parameter estimations when it is smaller than an effective bonding length. The latter is inversely proportional to the strain lag parameter and it corresponds to a certain strain transfer rate of the total crack induced strain distribution. It was found that an effective length corresponding to 0.95 transfer rate, guarantees an estimation of the real crack opening values. For good an estimation of both crack opening and strain lag parameter values, an effective bonding length corresponding to a strain transfer rate of 0.99 is needed.

Finally, another influencing parameter for the surface mounted optical fibers is the aging of epoxy adhesive. In the case of glued SensoLux cable, the crack opening estimation error decreased from 6 to 2% after three months aging of the Araldite 2014-1 epoxy adhesive. As the strain lag parameter values increased with aging, it can be concluded to the glue adhesion to the SensoLux cable and/or concrete material increases with glue aging. The new Araldite 2014-2 proved to have more stable behavior as the same crack opening estimation accuracy and strain lag parameter values were found after three months short-term aging.

Chapter IV

Crack monitoring in reinforced concrete structures

> ”If you can not measure it, you can not improve it.”
>
> *Lord Kelvin*

Contents

IV.1. Introduction

This chapter addresses the advantages of distributed fiber optics sensing techniques can bring to the monitoring and auscultation of reinforced concrete structures, especially in terms of crack early detection and monitoring. Tests figuring the use of DFOS techniques implemented alone or combined to other types of sensors or techniques (Strain Gauge and LVDT sensors, Coda Wave Interferometry technique and Digital Image Correlation technique), will be presented.

The first part focuses on early crack detection in a reinforced concrete beam combining the distributed fiber optics sensing and coda wave interferometry techniques. It is the result of a collaboration with Xin Wang in the framework of INFRASTAR project. The second part focuses on examining its capacity to estimate small crack openings by fitting the strain transfer model to DFOS measurements. This part also tackles the influence of attaching the cables next to rebars as it is the common way for embedding optical fiber cables inside a reinforced concrete structure. The third and final part is mainly focused on studying the multiple cracking case of a real scale reinforced concrete beam. The total spatial strain distribution resulting from the formation of different neighboring cracks is investigated and the possibility of estimating the different crack openings is examined and compared to DIC technique.

IV.2. Evaluation of early crack detection

Coda Wave Interferometry (CWI) is well-known by its high sensitivity to damage propagation. Contrary to normal sonic methods and vibration measurements, the frequency range of ultrasonic measurements for SHM applications exceeds 50 kHz. Therefore, the signal wavelength can be smaller than the size of defects and aggregates in the concrete material forcing waves to enter the multiple scattering regime and interact with small heterogeneities [160]. As diffused waves travel along much longer paths than direct or simply reflected ones, they are much more sensitive to weak perturbations in the medium (Figure 4-1). For this reason, the ultrasonic Coda Wave Interferometry technique is nowadays considered one of the most promising methods for the detection of subtle changes in heterogeneous materials like concrete.

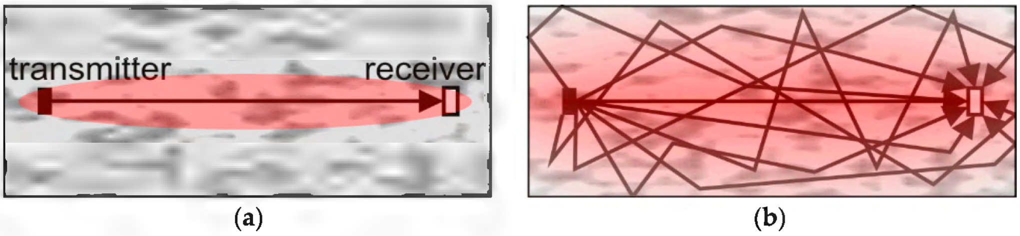

*Figure 4-1: Principle of ultrasonic measurements, propagation paths and areas of influence (red). **(a)** Direct wave (time of flight); **(b)** multiple scattering (coda) [161].*

Thus, in order to evaluate the capacity of DFOS technique to detect and follow structural damages through the measured strain profiles, it is important to study and compare its sensitivity to traditional sensors available in the market like strain gauge and LVDT sensors and a new non-destructive technique like CWI.

IV.2.1. Experimental set-up

A reinforced concrete beam instrumented with different kinds of sensors is tested under three-point bending. The test was performed with loading rate of 1 kN/min and until two cracks appeared in the specimen. As shown in Figure 4-2a, the $20\times20\times100$ cm beam is reinforced with three ∅10 longitudinal reinforcement bars (rebars) in the tension area and three ∅6 rebars in the compression area, attached together by four ∅6 stirrups. The instrumentation policy includes two SG (green color), six LVDT (grey color), four Ultra Sonic US (red color), six lines of DFO (blue color) sensors and one thermocouple (TC). Two LVDT sensors (LVDT5,LVDT6) are used to measure the deflection at the center of the beam, while four other sensors are fixed at the level of rebars for crack opening monitoring at probable propagation locations of cracks, as shown in Figure 4-2b,c. While the central LVDT sensors (LVDT1,LVDT2) cover a 3 cm area, the others cover a 6 cm area (LVDT3,LVDT4). They are the same LVDT sensors used in Chapter 3 with an accuracy of 1 μm. Moreover, two SG sensors (one from each side) were fixed 6 cm away from the center of the beam. These sensors follow strain over 5 cm of the beam with an accuracy of 1 μm/m.

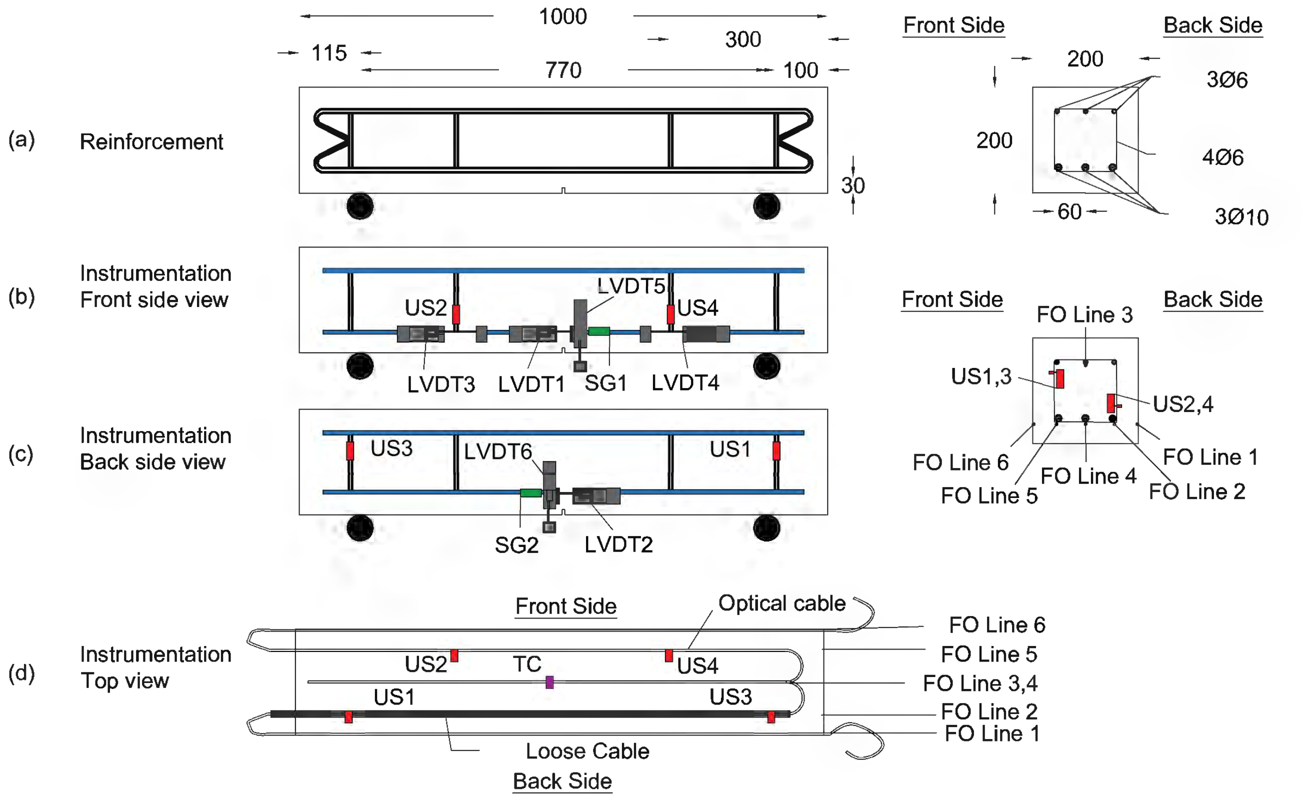

*Figure 4-2: (**a**) dimensions of the beam and different rebars positions, (**b**) front view, (**c**) back view and (**d**) top view of the sensors positions.*

One US sensor is fixed over each of the four stirrups (Figure 4-2b,c). This new embedded ultrasonic transducer “SO807” (Figure 4-3a), is designed by Acoustic Control Systems company in cooperation with and exclusively for BAM institution [162]. The sensor can work both as a transmitter or receiver with a central frequency of around 62 kHz. Contrary to classic ultrasonic sensors glued on the surface of the structure, this sensor is configured to be embedded inside the concrete material and thus records fewer surface waves and is less influenced by near-surface changes like temperature. Thus, a thermocouple (purple color) is fixed at the center of the mid bottom rebar (Figure 4-2d)

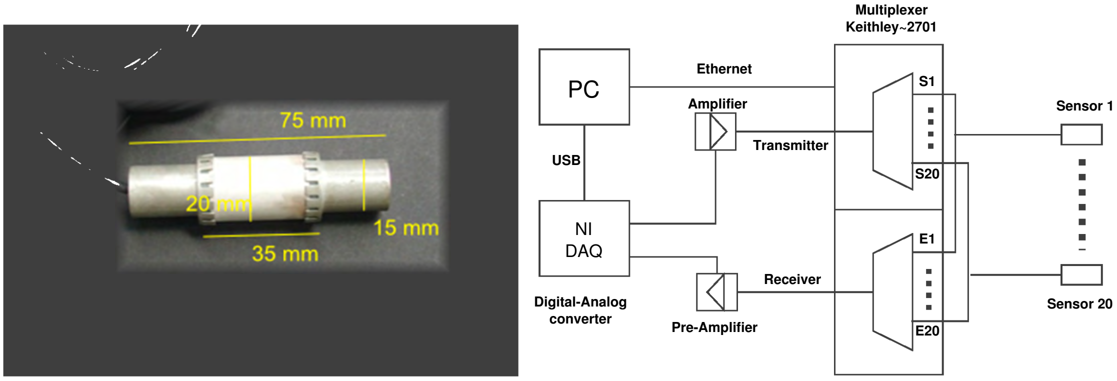

(a) (b)

*Figure 4-3: (**a**) dimensions of "SO807" [162]. (**b**) diagram of the data acquisition system [100].*

in order to monitor temperature variations during the test. As shown in Figure 4-3b, a Keithley 2701 multiplexer was used to switch between different combinations S-E (transmitter-receiver) during the test. This data acquisition system allows autonomous continuous monitoring of the structure with a sampling frequency of 1 MHz.

For DFOS strain measurements, the SensoLux cable is used as the optical fiber sensor for this experiment. The trajectory of the cable over the length of the beam is as follows (Figure 4-2d):

- Glued on the front surface (line 1).
- Attached to the front bottom rebar (line 2). This line was surrounded by a tube to create a loose part for temperature compensation.
- Attached to the mid top rebar (line 3).
- Attached to the mid bottom rebar (line 4).
- Attached to the back bottom rebar (line 5).
- Glued on the back surface (line 6).

For surface-mounted lines, the Araldite 2014-1 epoxy adhesive is used to glue the cable inside the 3×3 mm groove.

The ODISI–B interrogator working under the standard operating mode is chosen for this experiment with a spatial resolution of 5.2 mm and a sampling frequency of 10 Hz. The strain measurements reached a repeatability of ±5 μm/m compared to the ±20 μm/m with the high resolution mode (Table 3-1). This strain repeatability decreased to ±2 μm/m after calculating the rolling average of 10 consecutive measurements.

Figure 4-4b shows the embedded US sensors and SensoLux cable fixed to the rebars before concrete casting, while Figure 4-4a shows the surface instrumentation of the beam ready for testing. Finally, it is important to mention that the beam was tested after 10 months of its casting with a standard C30/37 concrete, similar to the one used for the wedge splitting specimens in Chapter 3.

IV.2.2. Coda Wave Interferometry technique

The principle of CWI technique is to compare the coda waves recorded in two different states to monitor weak velocity variations and waveform modifications. As shown in Figure 4-5, the first arrivals of the signals recorded after perturbations are similar (i.e., [0.16 ms, 0.35 ms]), while the coda waves (i.e., [1.5 ms, 1.7 ms]) show a significant difference. The most used method to evaluate these

(a) *(b)*

*Figure 4-4: (**a**) front view of the loading arrangement and the beam instrumented with sensors before testing; (**b**) Ultra Sonic (US) and Distributed Fiber optics (DFO) sensors attached to the rebars before casting of concrete.*

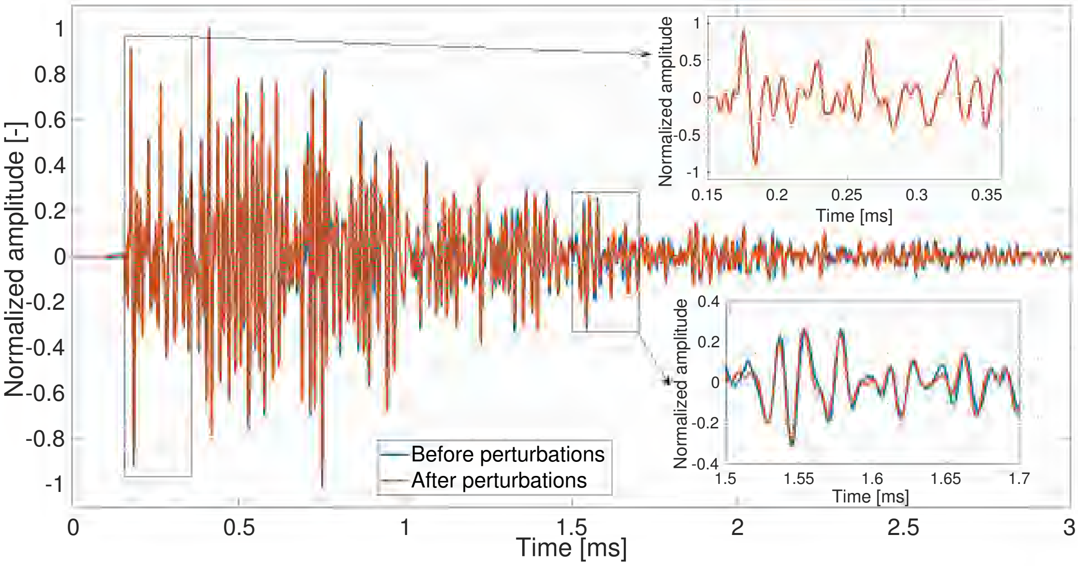

Figure 4-5: Signals recorded before and after perturbation in the medium [163].

changes is the stretching method [164], where the velocity change is considered as a dilation or compression in time by the dilation rate α. This method is based on choosing a reference signal $u_u(t)$ and then stretching it by different dilation rates α in the range $[\alpha_{min}, \alpha_{max}]$. The correlation coefficient (CC) between the signal in a new state $u_p(t)$ and all the stretched reference signals $u_u(t(1+\alpha))$ is computed as follows:

$$CC(\alpha) = \frac{\int_{t-T}^{t+T} u_u(t'(1+\alpha))u_p(t')\mathrm{d}t'}{\sqrt{\int_{t-T}^{t+T} u_u^2(t'(1+\alpha))\mathrm{d}t' \int_{t-T}^{t+T} u_p^2(t')\mathrm{d}t'}}. \tag{IV.1}$$

This cross correlation coefficient measures the similarity of the signals within a certain time window $[t-T,\, t+T]$ and therefore, indicates a change in the state of the medium (e.g., stress change or permanent local change as cracks). The parameter α, which maximizes the correlation coefficient is considered as the velocity change.

As a standard procedure, one or several fixed signals recorded before changes in the structure are chosen as reference signals and the correlation coefficient CC and velocity change α are compared to this reference. However, when the changes in the structure exceed a certain limit (i.e., wave forms change completely or wave forms shifted by more than half of the wavelength), the velocity change becomes meaningless while the correlation coefficient might still be useful. In this case, standard CWI procedure is not applicable anymore. Niederleithinger et al. [161] implemented a way to deal with this limitation by calculating the stepwise changes though comparing each signal $u_p^n(t)$ with the previous one $u_p^{n-1}(t)$, so-called stepwise CWI. Since stepwise CC can only show the similarity between current and previous signals, the stepwise CWI should be combined with standard CWI for long-term monitoring in order to detect the occurrence of any unusual behavior.

IV.2.3. Crack detection in reinforced concrete

Back and front side vertical deflections measured by LVDT sensors are plotted in Figure 4-6, in which the four marked points indicate each change in the curve shape and therefore a change in the behavior of the reinforced concrete beam. Point A (load = 22 kN) marks the end of a linear elastic phase and the start of a nonlinear behavior of the beam. The latter is normally due to the

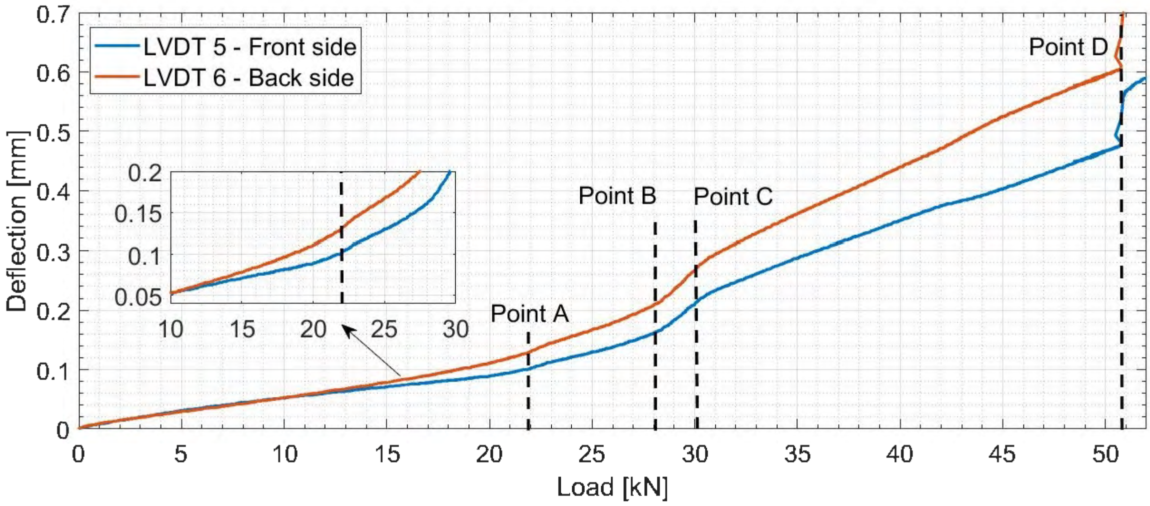

Figure 4-6: Variation of the vertical deflection in the central part of the beam measured by LVDT sensors.

initiation of small micro cracks in the central part of the beam, where the highest value of bending moment is located. Between Point B and Point C, the beam goes through a significant increase in deflection rates. This state marks a rapid reduction in the stiffness of the beam and thus significant deterioration problems. After 30kN (Point C), the deflection values increase at a smaller rate, before a steep increase is observed when at 51 kN (Point D). The jump in deflection is due to a sudden formation of a macro crack. In addition, distributed load and geometric imperfections of the beam could be the reason behind the difference in front and back side deflection values. This difference becomes more evident after the beam enters its nonlinear state.

The spatial strain distribution near the top (Line 3) and bottom rebars (Line 4) are plotted in Figure 4-7 at different load levels. In the tensioned part of the beam (Figure 4-7a), we observe high increase in the strain measured by Line 4 when load level increases from 20 kN to 28 kN. The strain profile evolves exponentially, indicating that a first crack appeared in the center of the beam. With the increase in the crack opening, the strain reigning in concrete ($<100\mu$m/m) is negligible when compared to the crack-induced strain. On the other hand, Line 3 measures a negative triangular strain distribution in the compression part of the beam corresponding to the 3-point loading arrangement (Figure 4-7b). At 35 kN load level, a strain peak at x=0, indicating that the central crack propagated over the height of the beam and reached the top rebars. When the load reaches 51 kN, the spatial strain distribution fixed next to the bottom rebars, shows a second exponential increase indicating that a second micro crack propagated around 20 cm from the center of the beam (Figure 4-7a).

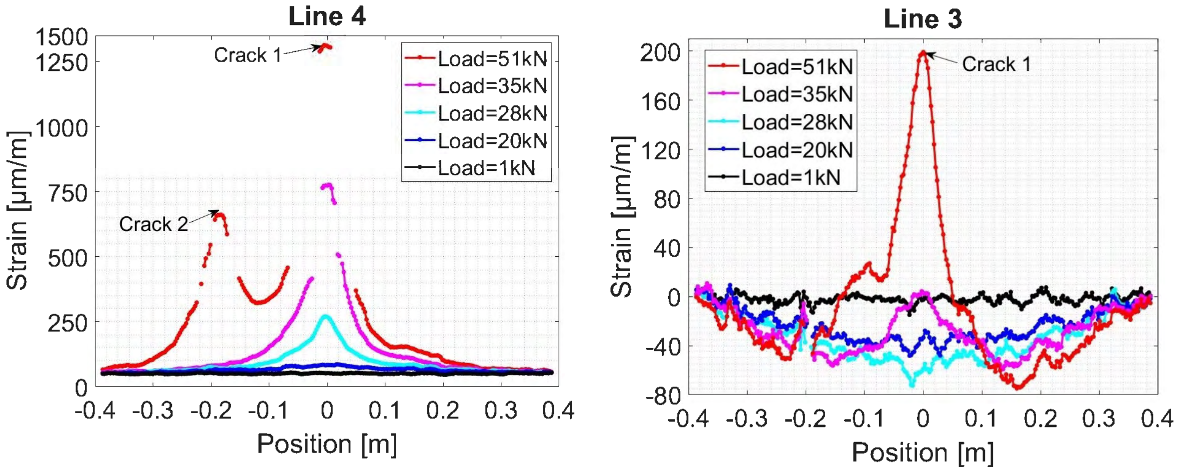

(a) At the level of bottom rebars

(b) At the level of top rebars

*Figure 4-7: Spatial strain distribution measured by the DFOS system near the top **(a)** and bottom **(b)** rebars.*

The determination of the crack appearance is usually difficult at early stages through visual observations of the strain profiles. Therefore, a simple crack detection criteria is established based on the total elongation of the optical fiber over its bonding length. This elongation e is the sum of the deformations corresponding to all the measurement points along the bonding length:

$$e = \Delta\ell \sum_{-L}^{L} \epsilon_f \tag{IV.2}$$

where $\Delta\ell$ is equal to the spatial sampling pitch. Based on the strain lag theory, and as illustrated in 4-8, the strain measured by the optical fiber ϵ_f contains the contribution of the concrete elastic strain

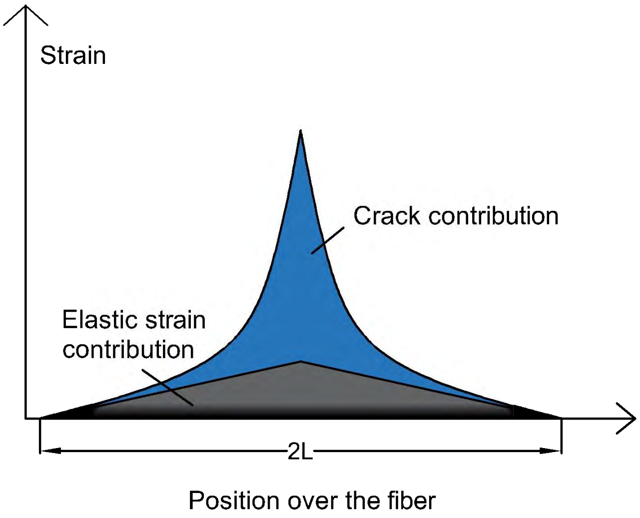

Figure 4-8: Illustration of the elastic strain and crack contributions in the measured strain over the optical fiber.

ϵ_m which has a triangular shape for three-point bending tests, and the crack-induced strain part ϵ_{crack} which has an exponential shape:

$$\sum_{-L}^{L} \epsilon_f = \sum_{-L}^{L} (\epsilon_m + \epsilon_{crack}) = \sum_{-L}^{L} \epsilon_m + \sum_{-L}^{L} \epsilon_{crack} \tag{IV.3}$$

Thus, wherever a crack crosses the optical fiber, the increase in the crack-induced strain part will lead to an increase in the total elongation of the optical fiber. The variation rate of this elongation is given by:

$$\delta e = \frac{e(t) - e(t - \Delta t)}{\Delta t} \tag{IV.4}$$

and will serve as the crack detection criteria.

DFOS, SG, LVDT and CWI measurement results are compared in Figure 4-9 in function of the applied load. Similar to the previous observations from deflection measurements, several points marking a significant change in the measurements can be distinguished:

- Point A' (Load=18 kN): Propagation of Crack 1 in the center of the beam.
- Between Point B (Load=28 kN) and C (Load=30 kN): Crack 1 propagating to the top rebars level.
- Point D (Load=51 kN): Propagation of Crack 2 at 20 cm from the center of the beam.

The formation of Crack 1 is first detected by CWI technique (Figure 4-9f). When the load exceeded 18 kN, a decrease in the stepwise velocity change calculated for six different combinations "T_xR_y" (Transmitter x and Receiver y), can be observed. The standard velocity change plots show that this steep fall in velocity change is the highest for combination T_2R_4 (Figure 4-9e), between the two closest transducers located on the bottom part of the beam. On the other hand, the smallest variations are observed for combinations T_1R_2 and T_3R_4 as the direct waves between these transducers do not bridge through the crack 1. Thus, we can deduce that the crack is propagating in the central area of the beam from its bottom side. Similar observations can be deduced from the correlation coefficient measurements for different combinations (Figure 4-9d).

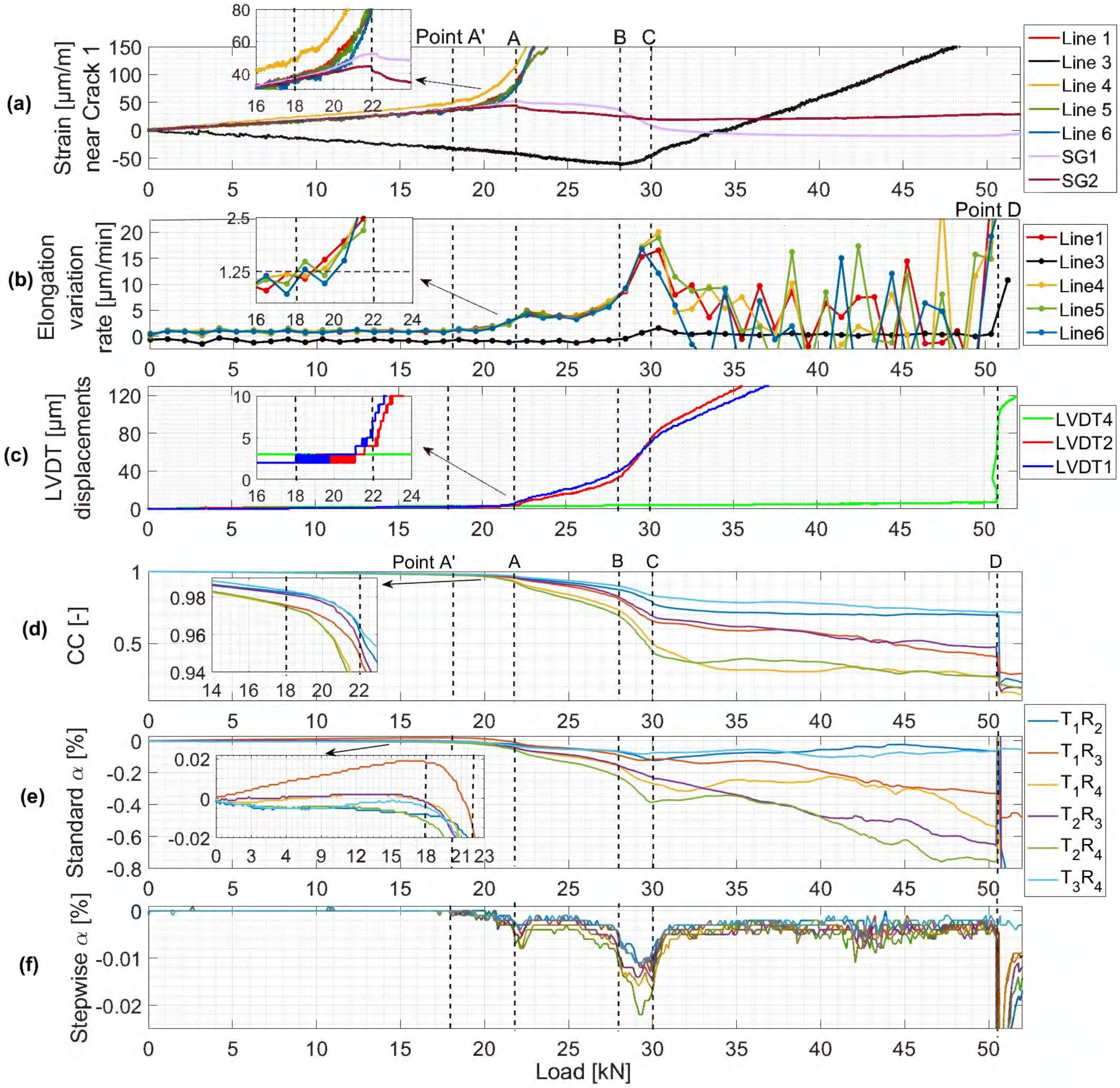

*Figure 4-9: **(a)** DFO and SG strain measurements; **(b)** optical fiber elongation variation rate measurements; **(c)** LVDT displacement measurements; **(d)** CWI correlation coefficient measurements; **(e)** CWI standard velocity change measurements; **(f)** CWI stepwise velocity change measurements.*

Another compelling evidence of the crack propagation is the increase in the elongation variation rate δe, calculated for each line over a 1 min intervals (Figure 4-9b). During the elastic stage, a constant elongation variation rate of 1 μm/min is observed. It starts increasing at 18 kN and exceeds the 2.5 μm/min at 22kN, for all the fiber optic lines. In this same load range, we can also observe a slope change in the strain measured near the location of Crack 1 (Figure 4-9a), that reaches 110μm/m at 22 kN for Line 4.

For LVDT and strain gauge sensors, a high increase in LVDT 1 and LVDT 2 displacement measurements is only observed after the load reached 22 kN (Figure 4-9c), accompanied with a decrease in SG1 and SG2 strain measurements (Figure 4-9a).

A linear decrease in velocity change and correlation coefficient values are observed between 18 kN and 28 kN (Figure 4-9e) indicating a stable propagation of Crack 1 over the height of the beam.

At about 28 kN, the strain measured over Line 3 (Figure 4-9a) started increasing accompanied with an increase in the elongation variation rate (Figure 4-9b), and therefore indicates that Crack 1 reached the level of top rebars. When Crack 1 approaches top rebars, a higher decrease in the velocity change and correlation coefficient are observed (Figure 4-9d,e), signaling a rapid crack propagation between the top rebars level and top of the beam. At a load level of 30 kN. The beam is then divided into two parts leading to an increase in velocity change values for combinations T_1R_2 and T_3R_4 (Figure 4-9e). The fact that the top rebars started working in tension could be the reason behind a sort of asymmetrical damage propagation in the beam. This can be observed from LVDT (1,2) and SG (1,2) measurement plots where the displacements and strain values measured on the back side of the beam exceeded those on the front side at 29 kN (Figure 4-9c).

When load reached 51 kN, Crack 2 suddenly appears 20 cm from the center of the beam. The velocity change and correlation coefficient change significantly for all combinations (Figure 4-9d,e,f), except for T_3R_4 combinations. The later is not affected by the appearance of Crack 2, as transducers 3 and 4 are located on the other side of the beam and thus, only small part of the propagating waves cross through the second crack as the beam is divided into two parts. The fact that the crack reached instantaneously a crack opening of 100 μm measured by LVDT 4, led to a sudden increase in the elongation variation rate for all the fiber optics lines (Figure 4-9b).

These results confirm once again that CWI technique is highly sensitive to crack activity. This technique could be the most advantageous for crack detection as it can cover an important volume of the concrete structure, contrary to to DFOS technique which requires that the crack cross the optical fiber sensor. Although this may be true, fixing a distributed optical fiber sensor at the level of bottom rebars allows us the detect the crack propagation in the reinforced concrete beam as early as the CWI technique. This high sensitivity is related to the strain lag parameter of the SensoLux cable, which is around 20m^{-1}. For special applications, and if earlier crack detection is needed, cables like Thorlabs and BRUsens V1, tested in Chapter 3, could be used as they figure higher strain lag parameter values of around 50m^{-1}.

As conclusion, the combination of DFOS and CWI techniques confirmed the crack detection in the reinforced concrete beam and helped acquiring more detailed information about the damage propagation. While DFOS technique is able to locate the cracks, CWI technique gave preliminary indications about the propagation of the cracks over the height of the beam.

IV.2.4. Monitoring crack opening and strain lag parameter

Based on the previous work in Chapter 2 and 3, an additional advantage of using DFO sensing techniques is the capacity of monitoring crack openings. Fitting the mechanical strain transfer equation to the strain profiles measured over line (1,4,5,6) leads to the estimation of the strain lag parameter

λ and the crack opening COD values presented in Figure 4-10. In order to take the strain in the host material into account, the strain gauge measurements were used to consider a linear spatial strain distribution, depicting the three point loading case. The surface mounted FO lines 1 and 6 lead to the lowest relative COD estimation errors of around 2%. On the other hand, and as FO line 5 reach stable 10% of error, FO line 4 shows decrease from 15% to 2% between a COD=25-160μm.

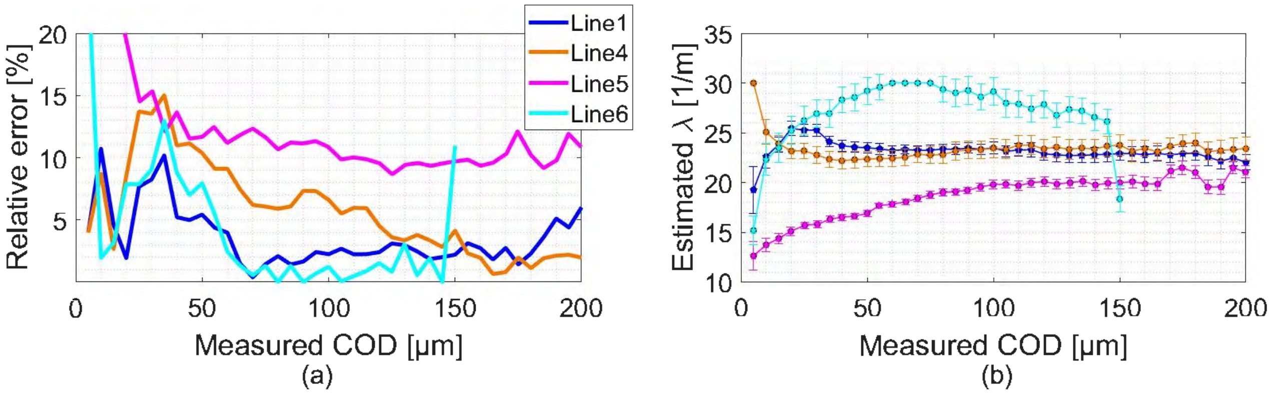

*Figure 4-10: Variation of the **(a)** COD relative error and **(b)** λ values with respect to the measured COD.*

FO line 6 reached the highest λ values with a maximum of 30m^{-1}, followed by FO lines (1,4,5) reaching 24, 23 and 20m^{-1}, respectively. As the beam is tested after 10 months of concrete hardening, this high levels of λ is due to good adhesion between the cable and the concrete material for embedded lines and the adhesion of the glue with both the cable and concrete for surface mounted lines.

IV.3. Estimation of small micro crack openings

Micro cracks are usually neglected in durability design of reinforced concrete structures. However, recent findings have proven that water can penetrate into the damaged zone of the fictitious crack ahead of the formation of the real macrocrack [165]. They suggest that the corrosion of steel in concrete might be more affected by these microcracks than the macrocracks when considering the durability design of reinforced concrete structures in chloride exposure environments [166].

Thus, monitoring small crack openings at different depth inside the reinforced concrete structure seems of paramount importance. For this reason, we focus in this section on studying our capacity to estimate small micro cracks openings on the surface and inside reinforced concrete structures, when fixed next to the reinforcement bars.

IV.3.1. Experimental tests

Similar to the previous section, three-point bending tests were performed on four reinforced concrete beams tested after 1, 2, 4 and 10 months of concrete hardening. The beams have a 1000×200×100 mm geometrical dimensions (Figure 4-11a). While Beam 1 and 3 were reinforced with three ∅6 longitudinal rebars fixed at 3 cm from the bottom side, Beam 2 and 4 were reinforced with two ∅10 longitudinal rebars.

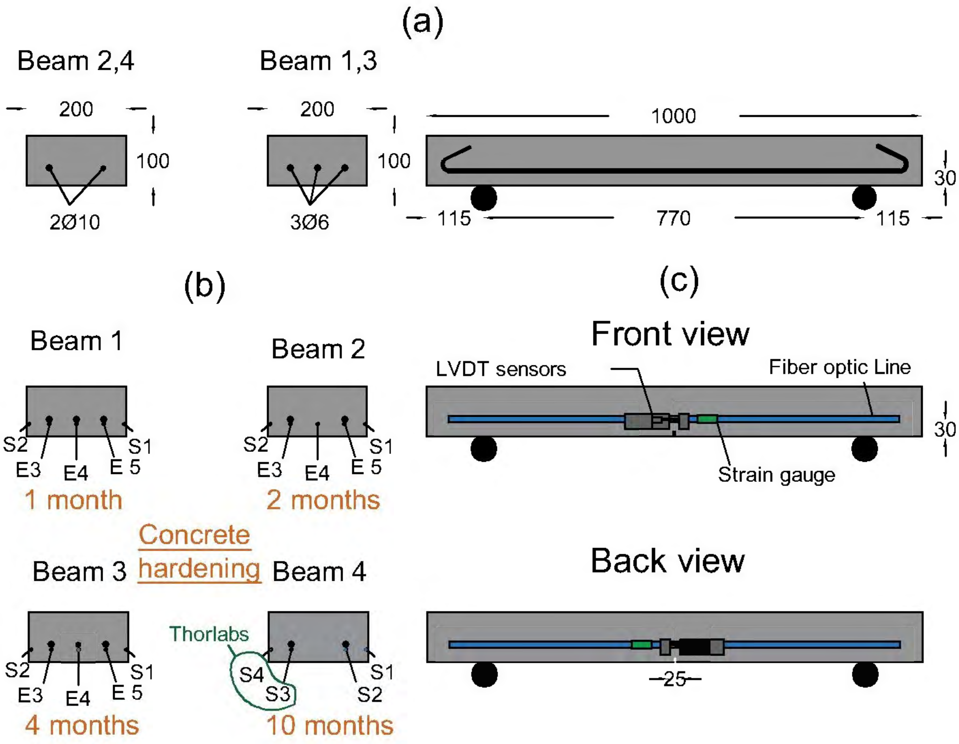

*Figure 4-11: **(a)** Dimensions and reinforcements of the beams; **(b)** Fiber optics instrumentation policy Beam 1, **(c)** Beam 2, **(d)** Beam 3, **(e)** Beam 4.*

Each beam was instrumented at the level of rebars with a LVDT sensor on the front and back side of the beam, covering an area of 25 mm (Figure 4-11c). In addition one 50 mm strain gauge is glued on each side, 60 mm from the center. For DFO sensors, an optical cable is attached all over the length of different rebars and then glued using Araldite 2014-1 epoxy inside a 3×3 mm groove at the same level of rebars. The central line 4 in Beam 2 was strained and fixed to the two side of the formwork using dominos (Figure 4-11b). In total, each of Beams 1, 2 and 3 is instrumented with five lines of SensoLux cable, with two lines glued on the surface and three lines embedded inside the concrete material. Beam 4 is instrumented with one surface-mounted and one embedded line from each of the SensoLux and Thorlabs cable types. Figure 4-12a and Figure 4-12b show the optic cable attached to rebars and fixed to the formwork, as well as the prepared groove filled with epoxy before inserting the optical cable.

The same ODISI–B interrogator is used for these experiments. However, the standard operating mode is chosen for Beams 1, 2 and 3 for an improved strain spatial dispersion and temporal repeatability. On the other hand, the high resolution mode was used for Beam 4 to avoid dropouts over the Thorlabs cable lines, characterized by high strain lag parameter values. The sampling rate is fixed to 10 Hz and a rolling average is performed over 10 consecutive measurements.

Figure 4-13 shows one of the beams in the testing machine instrumented with the LVDT and SG sensors. The beams were loaded under a fixed displacement rate of 0.1 mm/min until reaching vertical displacement of 5 mm with all the tested beams entering their full multiple cracking phase.

(a) (b)

*Figure 4-12: **(a)** Optical fiber cable attached next to the rebars and fixed to the formwork. **(b)** Filling the groove with the epoxy glue.*

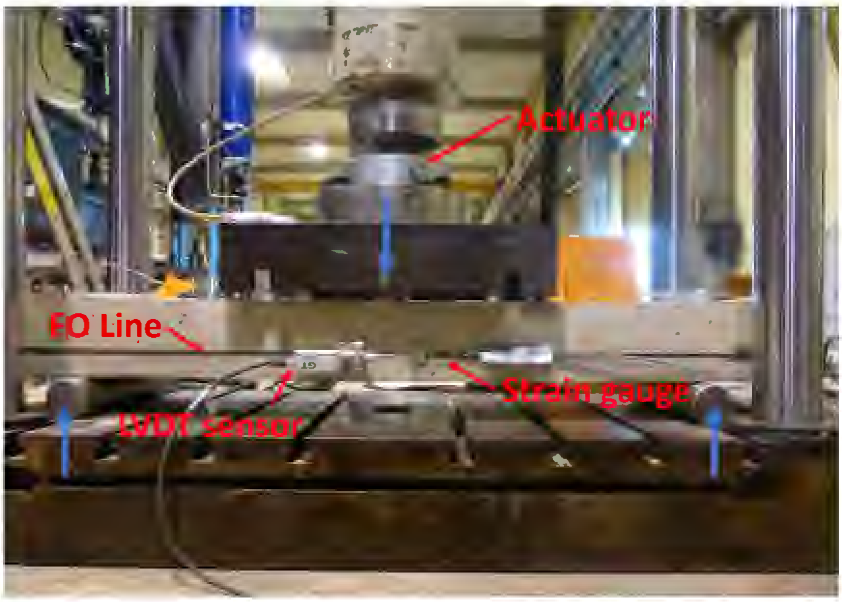

Figure 4-13: Three-point bending test setup.

IV.3.2. DFO strain measurements

Figure 4-14 shows the spatial strain distributions measured by the ODISI-B interrogator over Line 1, from each tested beam and at different load levels. Five cracks appeared at the end of each test, except for Beam 3 where only three primary cracks propagated. As Beam 3 has the same reinforcement rate as Beam 1, the lower number of cracks could be due to the hardening of concrete leading to more dissipated energy at the moment of crack propagation (Figure 4-14c - right) and less distributed cracks. On the other hand, despite testing Beam 4 after 10 months of concrete hardening, higher reinforcement rate than Beam 3 (2∅10 $>$ 3∅6) is the reason behind the propagation of five cracks and less energy dissipation due to cracks.

The same distance between cracks can be observed for all the tested beams, varying around 10 cm. On the other hand, the crack-induced strain affects around 40 cm of the cable's length. As a result, the final spatial strain distributions due to multiple crack formations is a combination of the induced strains from each crack. As the first crack appears, the strain level rapidly exceeds the strain reigning in the concrete material measured by the strain gauges in the order of 30 $\mu\mathrm{m}$. Rapid strain transitions near the crack location led to the of dropout points, especially in Beam 3. It is worthwhile mentioning that dropout points also appeared over Line 3 and Line 4 where Thorlabs cables, despite the use of the high resolution mode.

IV.3.3. Influence of strain in concrete on the estimated parameters

As illustrated in Figure 4-15a, the strain distributions corresponding to the strain transfer model (red color) is fitted to the measured strains (blue color) using robust least square method.

In the literature, the strain in host material was considered either equal to zero due to energy release near the crack location [167, 168] or the last reigning strain in the specimen just before the crack formation [57]. Contrary to the wedge splitting test where strain in concrete is mainly localized in the fracture process zone, the three-point bending test leads to a triangular strain distribution with a peak value in the center of the two supports. Moreover, after the formation of a crack, the strain release is only localized in the area surrounding the crack position, due to the existence of rebars. As a result, for small crack openings, strain in concrete can still form an important part of the measured strain distribution and should be taken into account.

For this reason, and while the crack opening COD and strain lag parameter λ were selected as variable parameters, triangular strain distribution in concrete (orange color) is continuously estimated using the strain gauge measurements (green color). Thus, the crack-induced strain CIS can be extracted from the difference between the measured strain ϵ_{fiber} and the estimated strain in concrete $\epsilon_{concrete}$.

Figure 4-15 shows clearly that the model (red color) describes well the measurement data. The residuals figure several strain peaks in the range 10 μm/m distributed all over the length of the beam. These small residual strains could be due to the heterogeneous concrete material as strain in fine aggregates could differ from the one in coarse aggregates. In the previous wedge splitting tests, this phenomenon was hidden by the important spatial dispersion of the measurements of $\pm$20 μm due the use of high resolution mode.

In order to study the influence of the strain in concrete on the estimation results, three different ways to account for the strain in concrete are considered:

- Case 1: A triangular distribution consistent with the three-point loading test, is assumed;

$$\epsilon_f(z) = \epsilon_{crack}(z) + \epsilon_m(z) = \lambda \frac{\mathrm{COD}}{2} e^{-\lambda|z|} + k|\mathrm{L} - z| \tag{IV.5}$$

  where COD, λ and k are the variable coefficients.

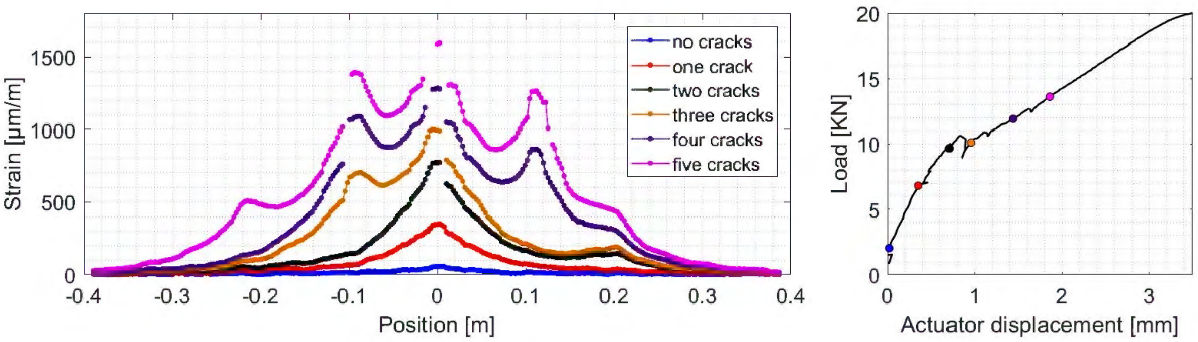

(a) Beam 1

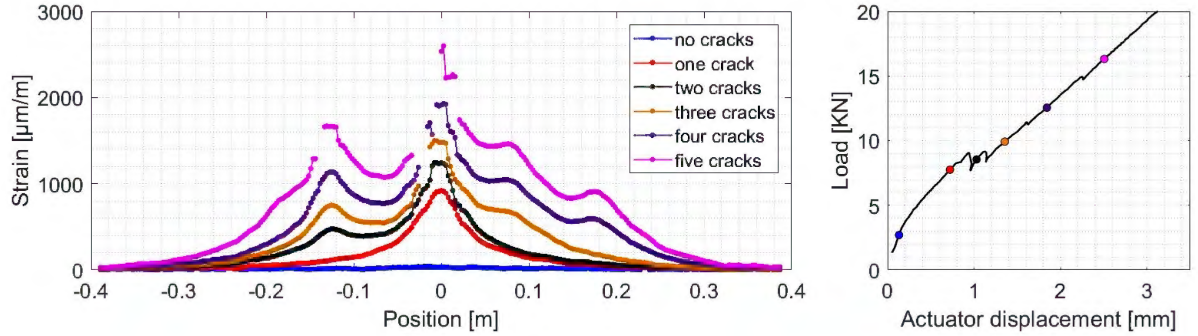

(b) Beam 2

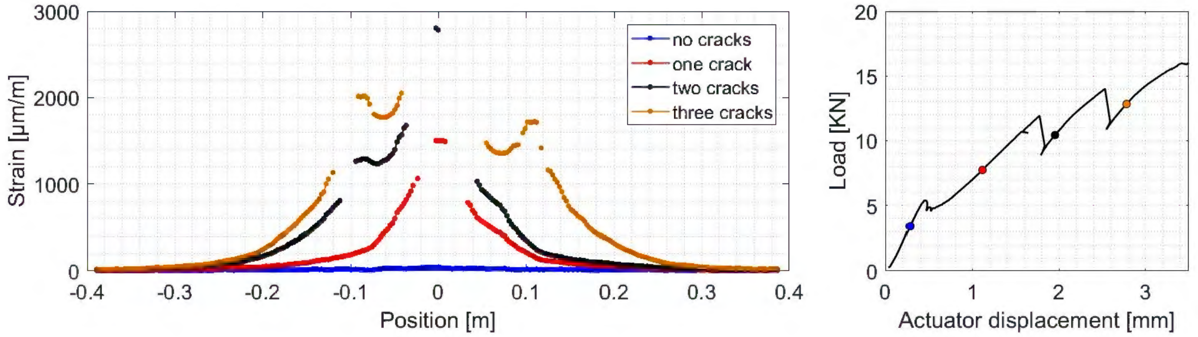

(c) Beam 3

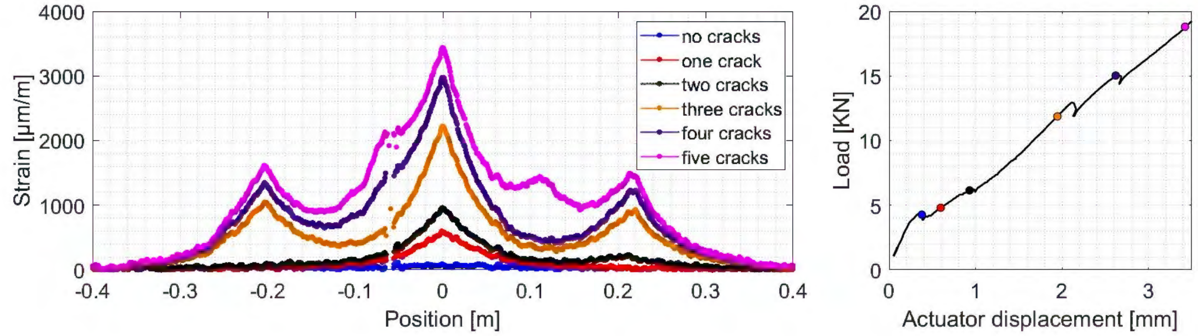

(d) Beam 4

Figure 4-14: (Left) The measured spatial strain distributions over the length of the SensoLux surface-mounted Line 1; (Right) The corresponding actuator load and displacement, for each of the four tested beams.

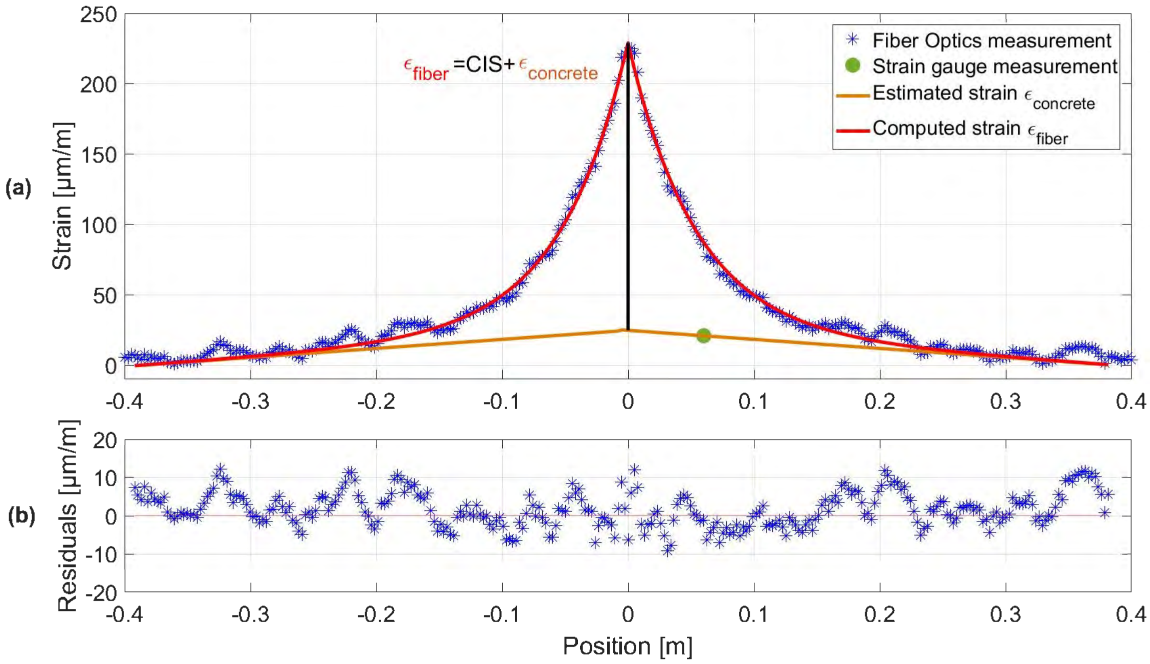

Figure 4-15: Computed strain compared to the measured strain profiles over FO line1 from Beam1.

- Case 2: The same triangular distribution is chosen.

$$\epsilon_f(z) = \lambda \frac{\mathrm{COD}}{2} e^{-\lambda|z|} + k|\mathrm{L} - z| \tag{IV.6}$$

  where COD, λ are the variable coefficients and k value is updated from the strain gauge measurements.

- Case 3: The strain in concrete is neglected compared to the crack-induced strain:

$$\epsilon_f(z) = \lambda \frac{\mathrm{COD}}{2} e^{-\lambda|z|} \tag{IV.7}$$

Figure 4-16 compares the estimation results for each case, corresponding to the SensoLux surface-mounted lines S1 from Beam 1 and Beam 4.

For the standard mode measurements, Figure 4-16a shows that the estimated strain in the host material ϵ_m from Case 1, diverges from the strain values measured by the strain gauge. As a result, strain lag parameter values of around 20 m^{-1} with a relative COD estimation error of around 11% are observed. On the other hand, using the strain gauge measurements for estimating the strain in concrete ϵ_m, led to a strain lag parameter value around 18-20 m^{-1} and a relative error of around 1%. Thus, in both cases, the estimated strain lag parameter values are in accordance with the previous results from SensoLux lines glued using Araldite 2014-1 leading to a range of values of 17-30 m^{-1}. However, adding the strain in concrete as a third variable leads to a 10% increase in the crack opening estimation errors. Neglecting the strain in concrete in Case 3 leads to strain lag parameter estimations of around 15 m^{-1}, lower than the strain lag parameter range values. In addition, high relative errors around 20-30% are observed. These relative errors keep decreasing with the increase of crack openings, as the strain in concrete ϵ_m becomes more negligible compared to the crack-induced strain distribution. Similar estimation results are observed for the rest of fiber optic lines.

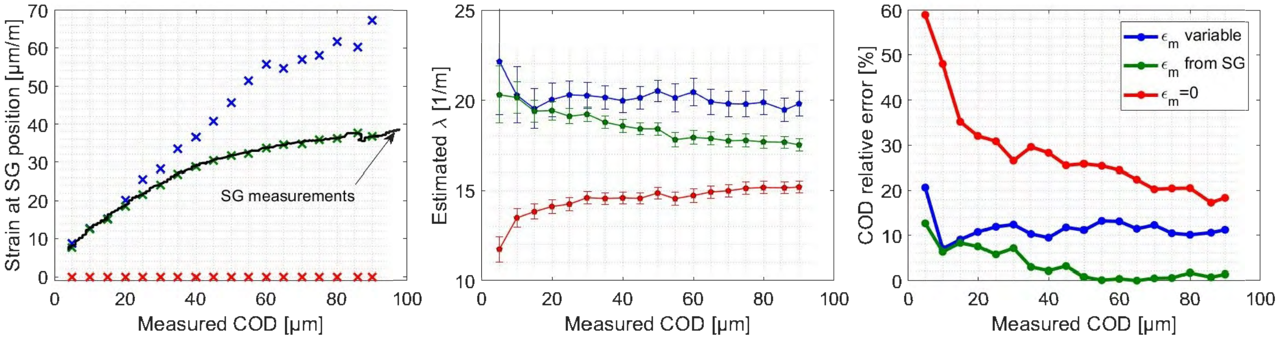

(a) (b) (c)

Standard mode: surface-mounted S1 from Beam 1.

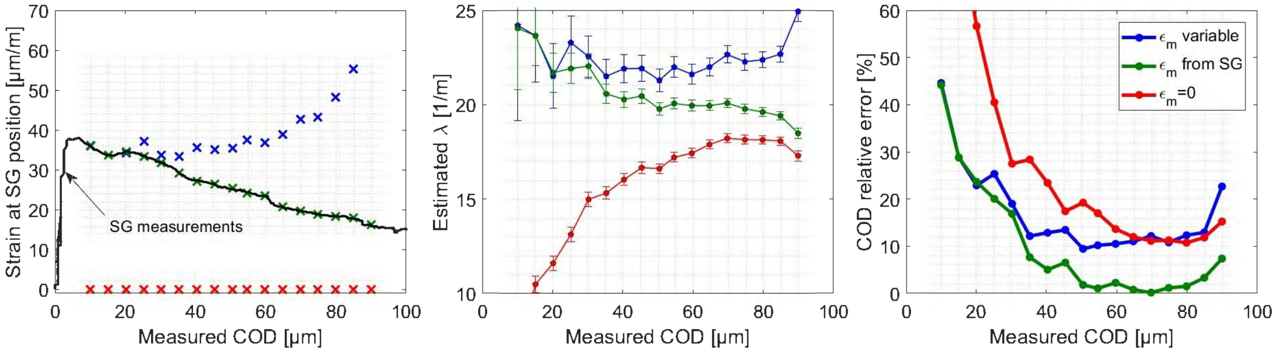

(a) (b) (c)

High resolution mode: surface-mounted S1 from Beam 4.

Figure 4-16: Influence of the strain in concrete ϵ_m on the estimated crack openings COD and their corresponding strain lag λ parameter for standard and high resolution modes.

For the high resolution mode measurements, the lower level of strain repeatability compared to the standard leads degrades influences the estimations for crack openings less than 40 μm. In this zone, and for Case 2, the COD estimations reach is lower than 10% starting from a minimal COD of 10 μm for standard operating mode, compared to 35 μm for high resolution mode.

To conclude, and as the strain release happens only in a small area compared to the CIS affected area around the crack, the strain in host material ϵ_m should be taken into account in a reinforced concrete structure. Neglecting ϵ_m or introducing it as a variable parameters lead to important discrepancies in the estimated crack openings COD and strain lag λ parameters. Using strain gauge measurements to account for ϵ_m during the fitting process proved to be the best option for monitoring small crack openings.

IV.3.4. Influence of rebars and concrete hardening

Figure 4-17 presents the estimated COD and strain lag parameters λ by fitting the strain transfer equation and updating the strain in concrete triangular distribution using the strain gauge measurements. For each test, the fitting is performed only during the single central crack propagation in order to isolate any influence of the formation of other cracks.

The measured COD for embedded lines is determined by assuming a linear crack opening variation between the front and back side LVDT measurements:

$$\mathrm{COD}(x) = \mathrm{COD}_{front} + \frac{x}{t}(\mathrm{COD}_{back} - \mathrm{COD}_{front}) \tag{IV.8}$$

where x is the position over the thickness t of the beam.

For surface-mounted SensoLux cable lines (S1 and S2 from Beam 1, 2 and 3, S1 from Beam 4), an accuracy of 4% is reached for crack openings exceeding the 50 μm. In addition, the strain lag parameter values varied between 19-22 m^{-1}, corresponding well to the wedge splitting test results. A small influence of concrete hardening can be observed with lines from Beam 1 and 2 figuring lower average values closer to 19 m^{-1}, compared to 22 m^{-1} for lines from Beam 3 and 4.

For SensoLux embedded lines (E3,E4,E5 from Beam 1, 2 and 3, E2 from Beam 4), the COD relative errors decrease from 40% after 1 month of concrete hardening to 15% after 2 months. Figure 4-18 compares the fitted and measured strain profiles corresponding to Line E3 after 1 and 2 months of concrete hardening. The measured strain profile corresponds well to the fitted curve after 2 months of concrete hardening, while the one measured after 1 month figures important variation in the residuals not only around the crack location. These residuals are distributed over the bonded right side of the cable. These residuals can be due to the phenomenon of concrete degradation at the interface with the rebars shown in Figure 1-24. Distributed secondary cracks can develop all over the length of the beam and lead to additional strains not taken into account in the fitting process.

As for the strain lag parameter, Beam 3 and 4 figured higher values than Beam 1 and 2. this increase in the strain lag parameter is more likely due to an increased adhesion between the cable and concrete due to the hardening process. However, as can be seen from Beam 3, this increased adhesion could happen at different rates.

As only two lines (E3 and S4) of Thorlabs cable were tested in Beam 4, it is hard to explain the high relative errors of 15% and 20%, compared to the 2% derived from the wedge splitting tests.

It is important to mention that the assumption of linear COD variation (Equation IV.8) over the thickness of the beam could not be always true, especially in the existence of rebars, and no accurate models to estimate this variation exist in the literature. Thus, the COD estimation errors presented in this section can be influenced by the fact that the reference COD measurements exhibit a certain error. For this reason more experimental tests should be performed to validate the conclusions drawn in this section.

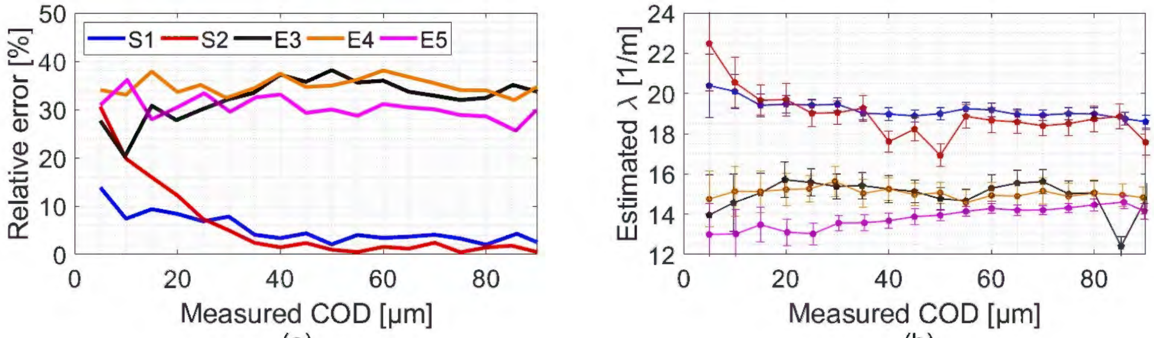

(a) (b)

Beam 1 - 1 month of concrete hardening

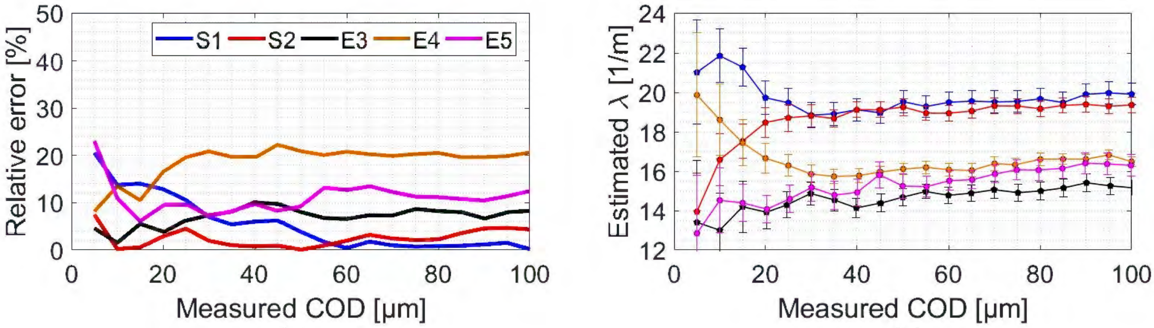

(a) (b)

Beam 2 - 2 months of concrete hardening

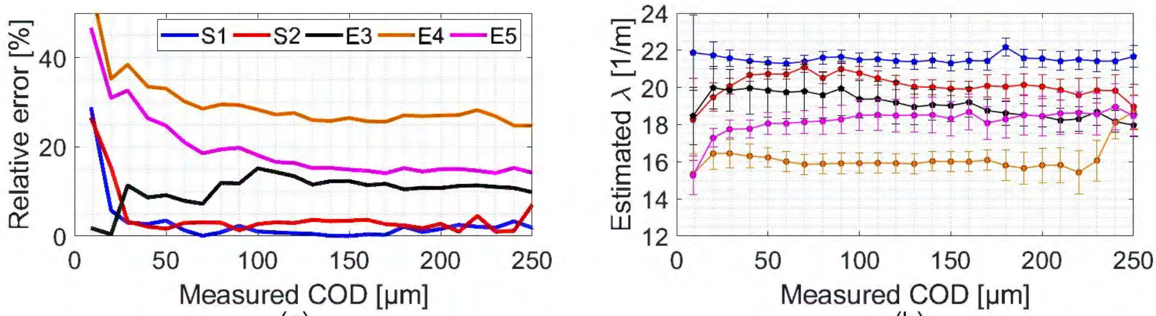

(a) (b)

Beam 3 - 4 months of concrete hardening

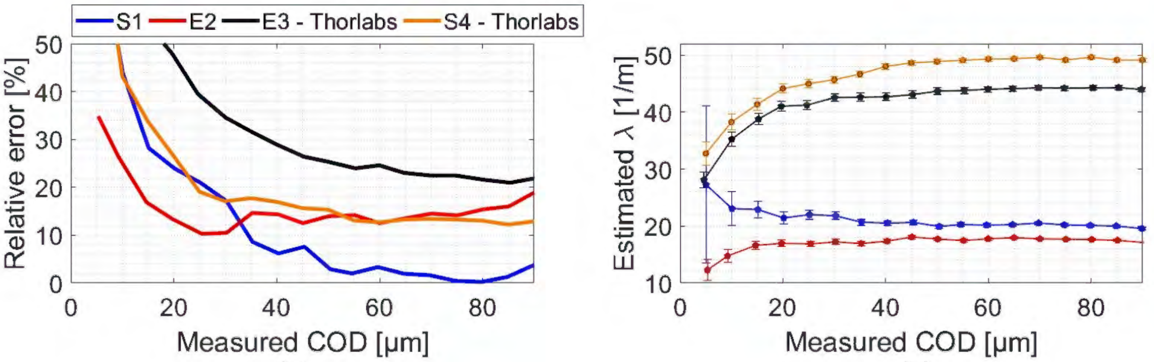

(a) (b)

Beam 4 - 10 months of concrete hardening

Figure 4-17: Variation of the estimated ***(a)*** *crack opening COD relative error and* ***(b)*** *strain lag parameter λ values.*

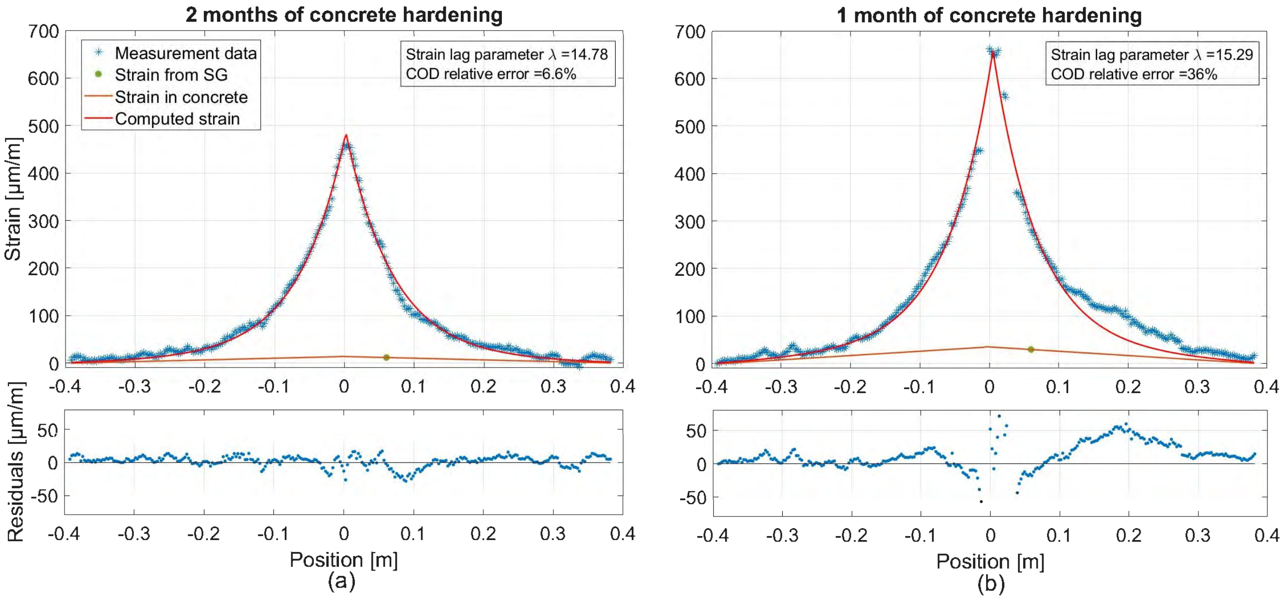

*Figure 4-18: Fitted and measured strain distribution for a crack opening of 60 μm corresponding to Line E3 from **(a)** Beam 2 and **(b)** Beam 1.*

IV.3.5. Influence of surrounding microcrack formations

During the multiple cracking stage, the mechanical transfer function can be fitted to the strain profiles using the following equation:

$$\epsilon_f(z) = \epsilon_m(z) + \sum_{i=1}^{n} \lambda \frac{\mathrm{COD}_i}{2} e^{-\lambda|z-z_i|} \tag{IV.9}$$

where COD$_i$ (for each crack i) and λ are selected as variable parameters. The parameters n and z_i, representing respectively the total number of cracks and their position, are fixed manually for each load step to simplify the fitting process. Figure 4-19a shows the computed strain profiles taking into account the five propagating cracks from Beam 1, compared to the measured strain profiles over surface-mounted Line 1. The low residuals level, randomly scattered around the zero line, indicate that the model describes well the measured strains (Figure 4-19b).

The COD estimation error and the strain lag parameter λ values corresponding to the primary crack are presented in Figure 4-20. The accuracy of COD estimations appears to be stable as the relative error varies around 5% until a crack opening of 400 μm. In addition, the strain lag parameter values are also stable around 18.5m^{-1}, except at the moment the 3$^{\text{rd}}$ and 4$^{\text{th}}$ cracks appeared. The latter correspond to Crack 2 and Crack 4 noted in Figure 4-19a. Thus, the steep fall in λ to 17.25m^{-1} could be due to the fact that the mentioned cracks are close to Crack 3 and figure lower λ values at small crack openings.

IV.4. Evaluation of a multiple crack monitoring system

IV.4.1. Experimental set-up

A 2900×400×200 mm real scale reinforced concrete beam is tested under four-point loading, four months after its casting with standard C30/37 concrete mix. Contrary to a three-point bending test that

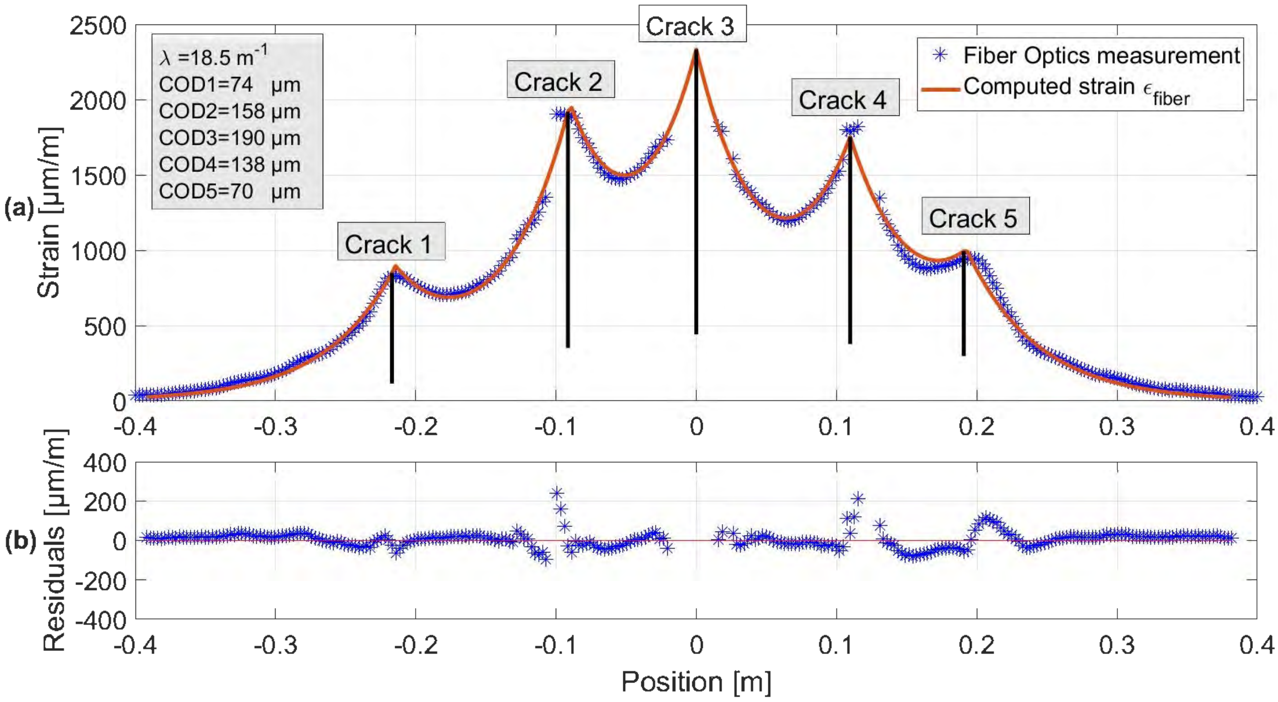

*Figure 4-19: **(a)** The computed strains compared to those measured over the surface-mounted Line 1 from Beam 1 and **(b)** the corresponding residual plots for multiple cracking case.*

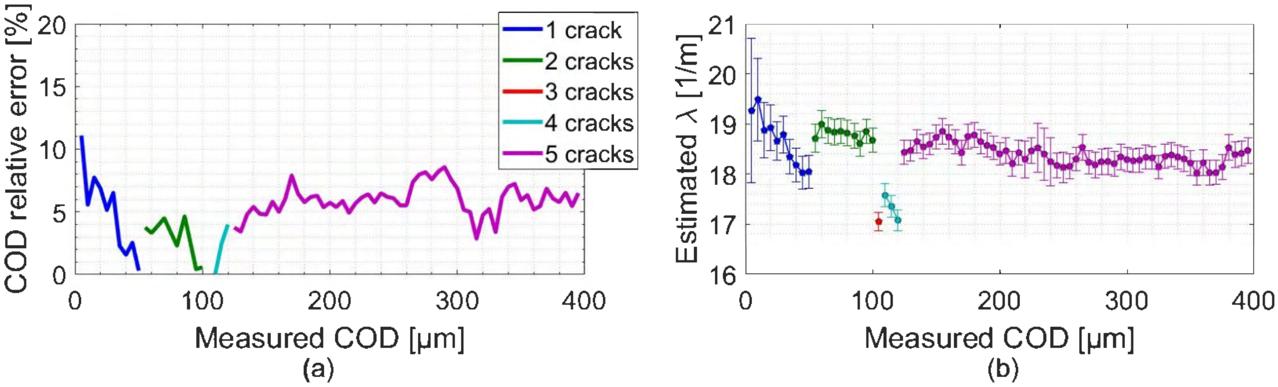

(a)

(b)

*Figure 4-20: Variation of the **(a)** COD relative error and **(b)** the strain lag parameter λ during multiple crack propagation over Line 1 from Beam 1.*

leads to successive cracks formation, a four-point bending test leads to a simultaneous appearance of multiple micro cracks, mainly in the constant strain zone between the two loading points.

Figure 4-21a shows the reinforced concrete beam and the position of different rebars. The distance between the two supports and the two loading points are respectively 2500 mm and 800 mm. On the front side, the beam is textured for DIC between the two loading points (Figure 4-21b). On the back side, two LVDT sensors are fixed 400 mm from the center on the left and right side of two other central LVDT sensors fixed 45 mm (bottom level) and 95 mm (top level) from the bottom side of the beam (Figure 4-21c). The LVDT sensors have an accuracy of 1 μm and covers an area of 100 mm or 200 mm as shown in Figure 4-21c.

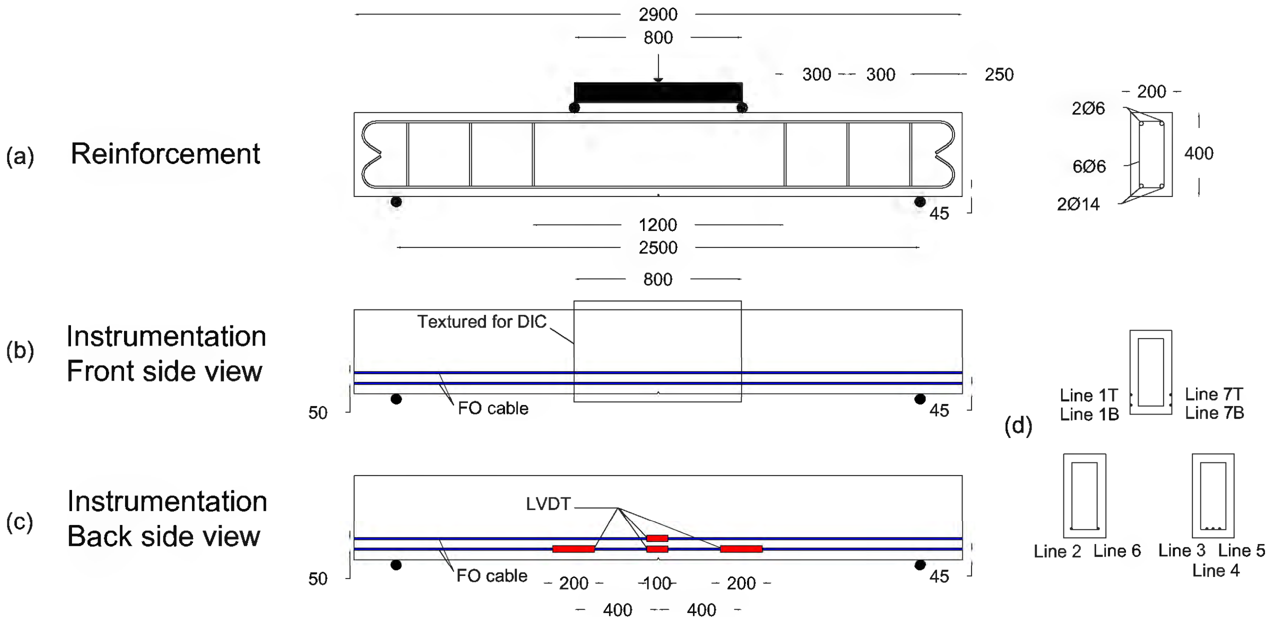

*Figure 4-21: **(a)** Dimensions of the beam and different rebars positions **(b)** Front view with DIC textured surface position **(c)** Back view with LVDT sensors positions **(d)** Section view of different fiber optic lines positions.*

A SensoLux optical cable is fixed over the length of the beam at the top and bottom levels (Figure 4-21d). Five fiber optic lines (Line 2,3,4,5,6) are embedded inside the concrete material (Figure 4-22a). Four fiber optic lines are mounted on the front (Line 1B,1T) and back (Line 7B,7T) sides by gluing the optical cable inside a 3x3 mm groove using Araldite 2014-1 epoxy adhesive (Figure 4-22b). The test was performed in BAM's research labs and therefore the available OBR 4600 interrogator is used for performing the measurements. Similar to the ODISI-B, this interrogation unit is also based on Optical Backscattering Reflectometry (OBR) technique. The OBR 4600 strain measurements has better repeatability of ± 1 μm/m and accuracy of ± 4.1 μm/m, than the ODISI-B interrogator. However, continuous measurements cannot be performed as each strain measurement should be taken manually with a measurement period of around 3 s. The measurements are performed with a spatial resolution of 10 mm and a sampling rate of 5 mm.

A step-wise loading is performed until reaching an applied load of 80 kN. Between the total 64 loading steps, the first 4 steps had an amplitude of 5 kN each, while the following 60 steps had an amplitude of 1 kN. At each step, the spatial strain profiles along the optical cable were measured using the OBR4600 interrogator and an image was taken using the two DIC cameras.

(a) (b)

*Figure 4-22: **(a)** Embedded optical fiber lines before concrete casting. **(b)** Front view of the loading arrangement and the textured area for DIC.*

IV.4.2. Digital Image Correlation DIC technique

The DIC technique is based on the observation of a light-dark pattern using a camera. The image of the pattern is divided into sub-image areas (so-called facets). These facets and their movement, due to the applied load, are identified and followed using the images taken during the test. There is two types of DIC: 2D-DIC and stereo DIC. For 2D-DIC, the test piece is assumed to be planar, to remain planar throughout the test, to be perpendicular to the camera optical axis and to maintain constant stand-off distance throughout the test. Any inadvertent out-of-plane motion (i.e. due to test piece thinning or buckling, rotations or translations induced by misaligned grips, etc.) will cause errors in 2D-DIC [169, 170, 171]. For this reason, the stereo DIC with two synchronously triggered cameras is used in our experiment. Since the cameras are calibrated photogrammetrically in a stereo arrangement (Figure 4-23), the 3D coordinates of the corresponding material areas can be determined from the image positions of the facets, which lead to calculating vertical and horizontal displacement and deformation parameters. Facet size of 15x15 mm has been fixed for this experiment.

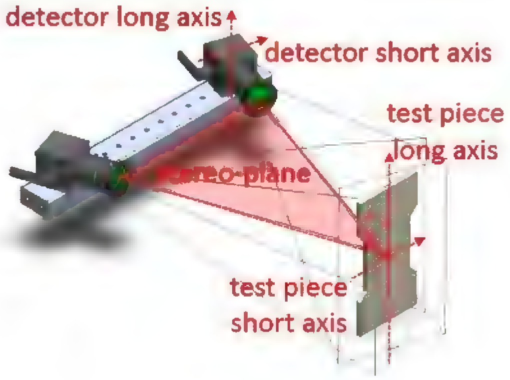

Figure 4-23: An isometric view of the orientation of the cameras detectors in a stereo camera pair with respect to the test piece [172].

IV.4.3. Beam's cracking behavior

Figure 4-24 presents the actuator's vertical displacement measurements plotted in function of the load. Two different stages can be distinguished: a first elastic stage until a 40 kN load level characterized by a linear load/vertical displacement variation followed by a post-elastic cracking stage usually characterized by multiple crack propagation.

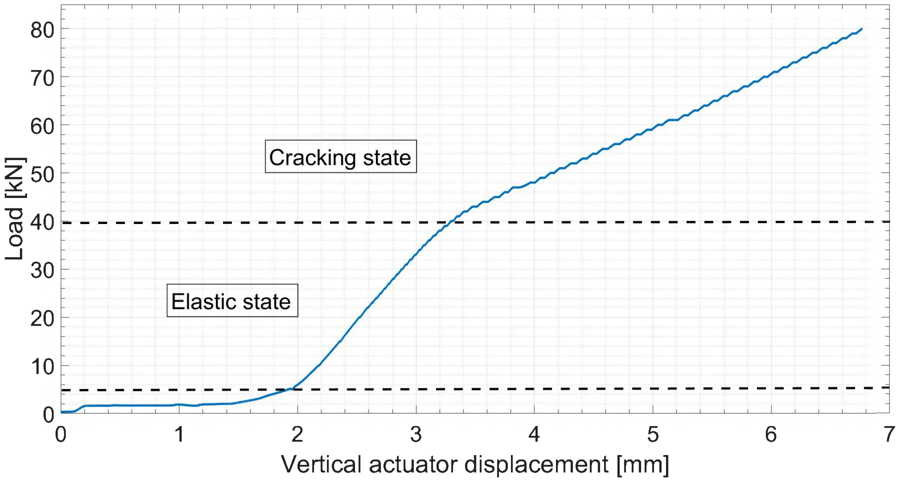

Figure 4-24: Variation of the actuator vertical displacement in function of the load.

Figure 4-25a,b shows the horizontal strain calculated using the DIC technique at the level of rebars. During the elastic state, the strain measurements figure high noise levels in the range of 1500 μm/m. At the end of this state, three strain peaks exceed the noise range and could correspond to microcracks in the concrete material (Figure 4-25a). During the cracking state, the detection of the cracks becomes more evident with seven strain peaks exceeding the 10000 μm/m range in the DIC area (Figure 4-25b).

Figure 4-25c shows DFOS strain measurements from Line 1B glued on the surface of the beam at the bottom level. This line exhibits a trapezoidal strain distribution during the linear elastic state before the load reaches 22kN. Afterwards, the appearance of multiple strain peaks, corresponding to microcracks location in the concrete material, can be clearly detected. Nine cracks can be distinguished at the end of this stage, with six of them localized in the DIC area. While these small micro crack discontinuities propagate during the cracking state, new cracks appear reaching a total number of 14 cracks at the end of the test (Figure 4-25d). The position of the seven DFOS strain peaks in the DIC area correlate well with that of the DIC strain peaks.

Moreover, based on visual observations at the end of the test, a crack map of the front and back sides of the beam is created by means of manual crack mapping (Figure 4-26). The location of all fourteen cracks are in accordance with the DFOS strain peaks. In addition, the propagation of the seven central cracks 4-10, correspond well to the DIC crack mapping in Figure 4-26. Thus, the results show that both DFOS and DIC techniques are able to separate all different microcracks.

On the back side, LVDT sensors were able to monitor crack 4, 7 and 10.

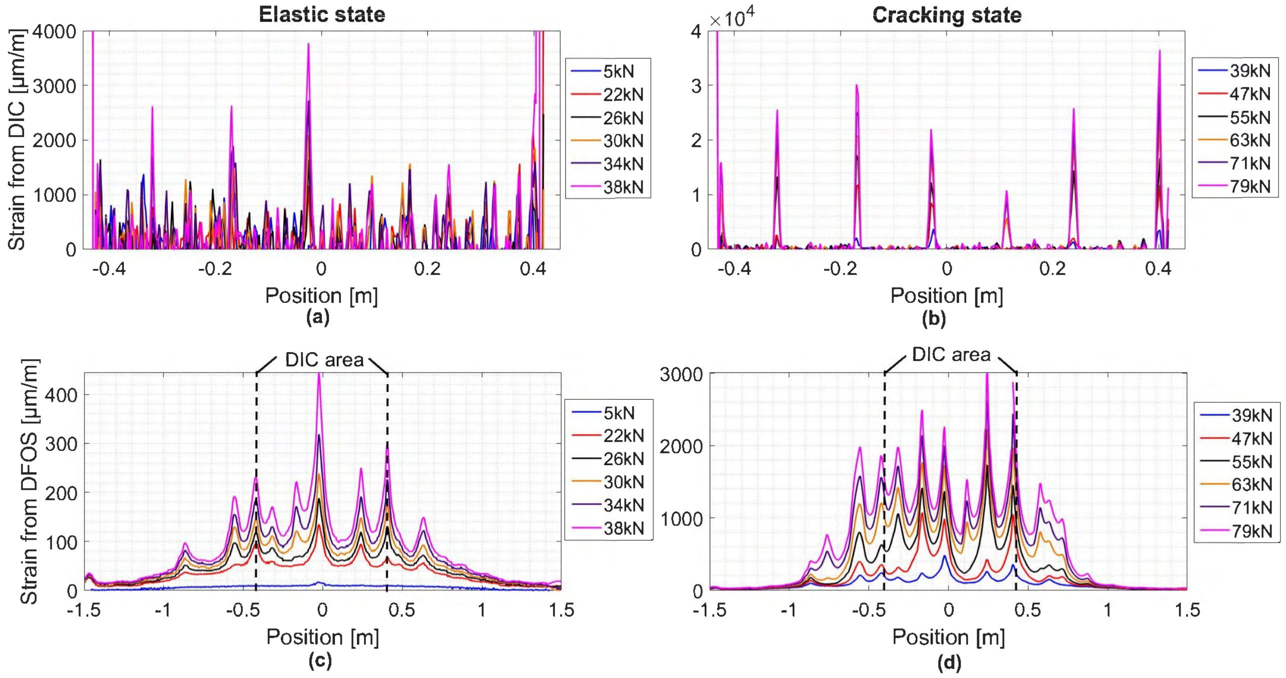

Figure 4-25: Spatial strain distribution measured by the DIC and DFOS at the fiber optic bottom level during ***(a,c)*** *the elastic state and* ***(b,d)*** *the cracking state.*

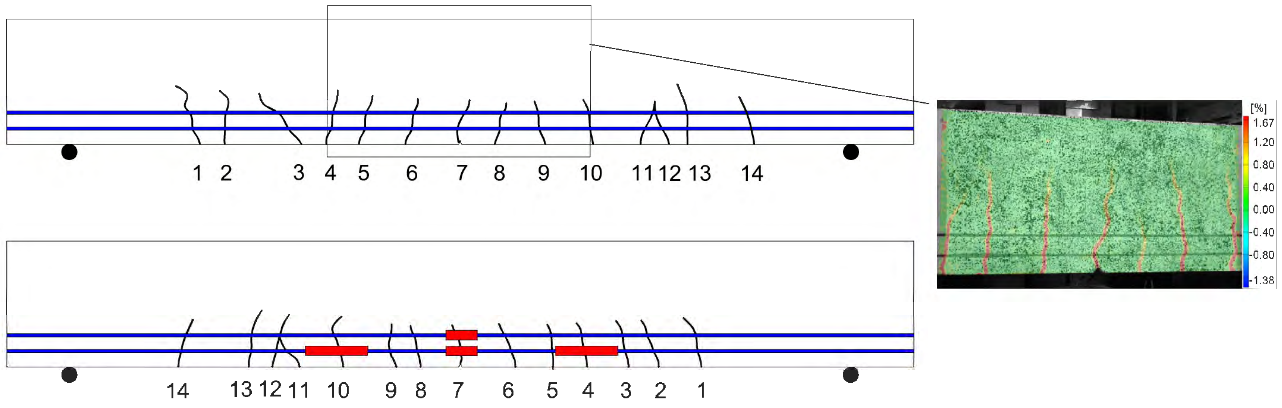

Figure 4-26: A cracks map of the beam's front and back sides by means of manual crack mapping (left) and in the central area using DIC technique (right).

IV.4.4. Monitoring of the cracks openings and strain lag parameter

The mechanical strain transfer equation can be adapted for multiple crack propagation case as follows:

$$\epsilon_f(x) = \epsilon_m(x) + \sum_{i=1}^{k} \lambda \frac{\mathrm{COD}_i}{2} e^{-\lambda|x-x_i|} \tag{IV.10}$$

where COD_i (for each crack i) and λ are selected as variable parameters. A trapezoidal approximation of $\epsilon_m(x)$ is adopted based on the strain level before the appearance of the multiple microcracks. The parameters k and x_i, representing respectively the total number of cracks and their position, are fixed manually for each load step to simplify the fitting process.

Figure 4-27 shows that the fitted strain transfer equation is clearly in accordance with the measured strain distribution using the DFO system even at early stages (load=26 kN), with low residual levels randomly scattered around zero.

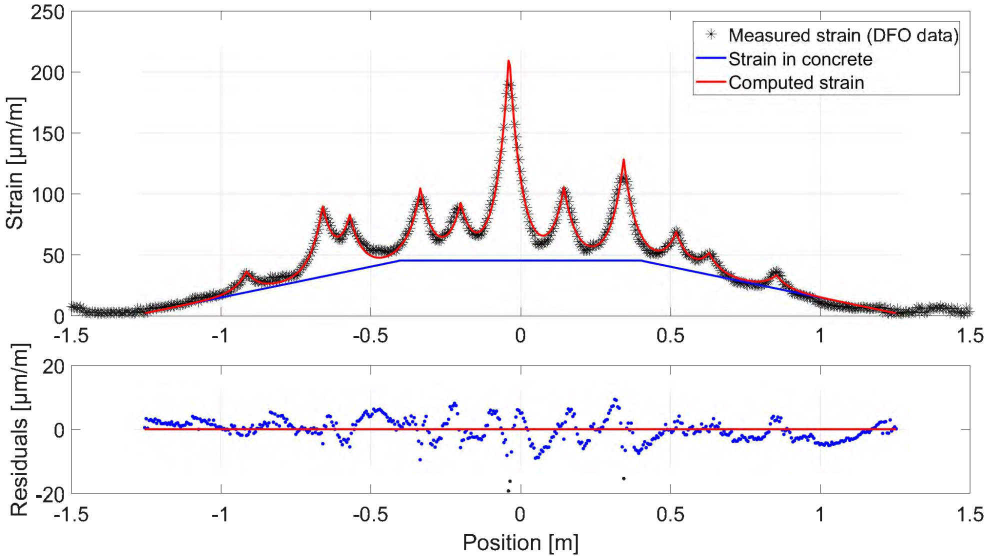

Figure 4-27: Computed strain spatial distribution using the strain transfer function compared to FO line7T measured profiles at Load=26 kN.

Figure 4-28 shows the variation of the global strain lag parameter value for all the optical fiber lines. High strain lag parameter variations can be observed during the linear elastic phase. As discussed previously on many occasions, this can be attributed to the beginning of the concrete cracking process were discontinuities in the material are starting to develop in the so-called fracture process zone, and end up leading to the creation of a macrocrack. When the load reaches 40 kN, the strain lag estimations from the SensoLux lines glued on the surface of the beam (Lines 1B,1T,7B,7T) become stable around 20 m^{-1} (Figure 4-28a). On the contrary, the strain lag parameters for the four embedded lines decrease slightly. These lines can be divided into two groups: those fixed next to the rebars (Lines 2, 6) with a decrease from 17 m^{-1} to 14 m^{-1} (Figure 4-28b), and those far from the rebars (Lines 3, 5) with a decrease from 25 m^{-1} to 18 m^{-1} (Figure 4-28c). The rebars could be the reason behind a reduced adhesion between the cable and the concrete material more likely due to the cement not being able to completely surround the optical fiber. As the global strain lag parameter varies in the same range as the previous results on one single crack for the surface-mounted and embedded SensoLux cable, we can conclude that all different cracks have a similar

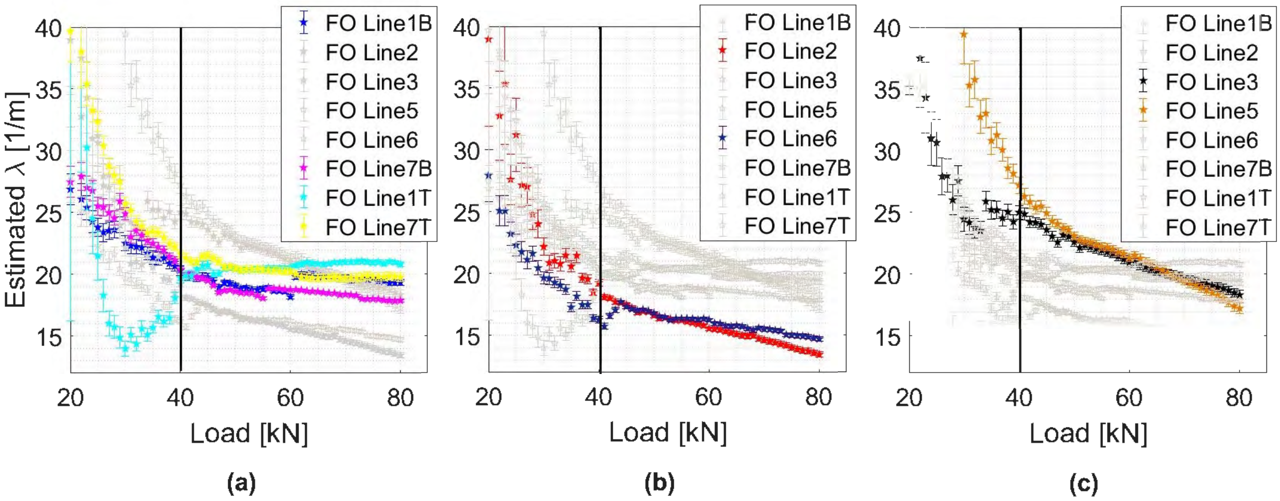

*Figure 4-28: Estimated λ for **(a)** surface mounted FO lines, **(b)** embedded FO lines next to the rebars and **(c)** embedded FO lines fixed far from the rebars.*

strain lag parameter.

Crack 4, 7 and 10 propagated inside the range covered by LVDT sensors on the back side of the beam (Figure 4-26). Crack 4 crosses the two central LVDT sensors at the top and bottom levels. However, a problem with the LVDT sensor fixed on the bottom level led to inaccurate measurements. Figure 4-29a and Figure 4-29b show the estimated values of the three cracks compared to LVDT measurements at the top and bottom level. It is clear that the estimated crack openings are in accordance with those measured from LVDT sensors, since the difference of less than 5% for crack openings that exceeds 20 μm. In fact, the sharp rise in relative difference for lower crack openings could be mainly due to the LVDT sensors limited accuracy of 1μm. This confirms the validity of the crack opening measurements from the DFOS technique.

Figure 4-30a and Figure 4-30b show the estimated openings for cracks 4 to 10 from DFO measurements at the bottom (Line 1B) and top levels (Line 1T), compared to those estimated from DIC technique. There is again a remarkable agreement between the values estimated by both techniques. However, DFO crack openings estimations have a better repeatability as they lead to more stable estimations than DIC estimations. Relative differences remain smaller than 15% for the majority of the micro cracks starting from a crack opening of 50 μm (Figure 4-30c,d). The estimated openings for crack 10 have higher relative differences due to its position at the border of the DIC textured surface that seem to have lead to inaccurate and low repeatable estimations. Another exception is the COD estimations for crack 8 where relative differences are inconsistent with the majority of the results. This can be attributed to the harsh crack propagation (seen from the sudden increase in COD) that could be the reason behind a debonding next to the crack location.

Due to the difficulty in finding crack meters that can be embedded inside the concrete material and are small enough to be accurate in terms of position, it is hard to validate crack opening estimations from embedded lines 2, 3, 5 and 6. Many theories were proposed to model the crack opening variation inside the reinforced concrete structures. These relationships, are based on rebar/concrete interaction like ”no slip” theory, ”debonded length” theory, ”fracture mechanics” theory, etc. Alone, these empirical relationships are not accurate enough to follow the crack opening distribution inside a reinforced concrete structure. Strain in rebars, concrete cover, distance from the neutral axis and between rebars can all be factors that affect crack opening in-depth variations. As all the embedded lines are at the same distance from the neutral axis and the distance between rebars and the concrete

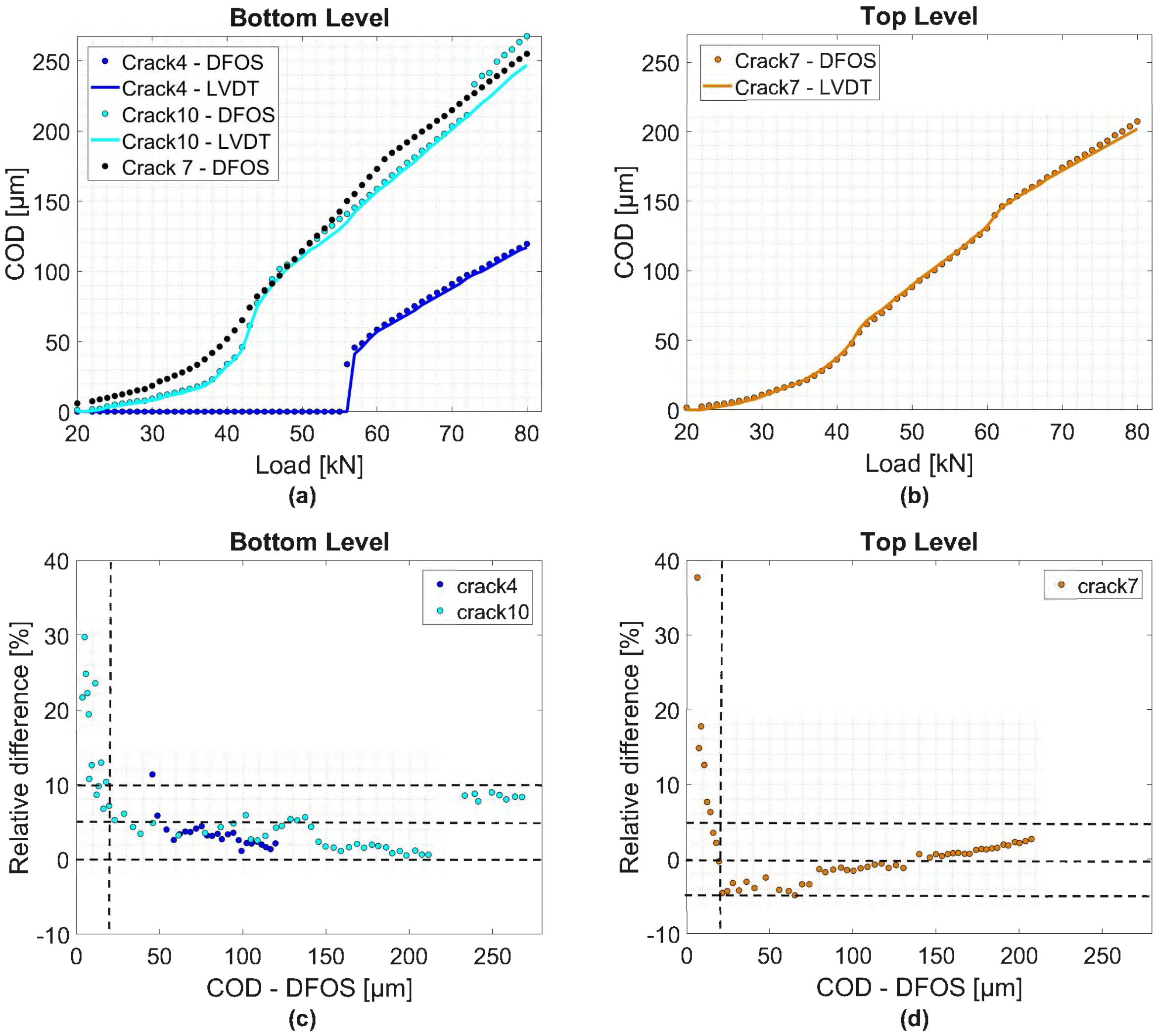

(a)

(b)

(c)

(d)

Figure 4-29: Variation of the estimated COD from LVDT and DFOS techniques for cracks (4,7,10) at the Bottom (FO line7B) and Top (FO line7T) levels.

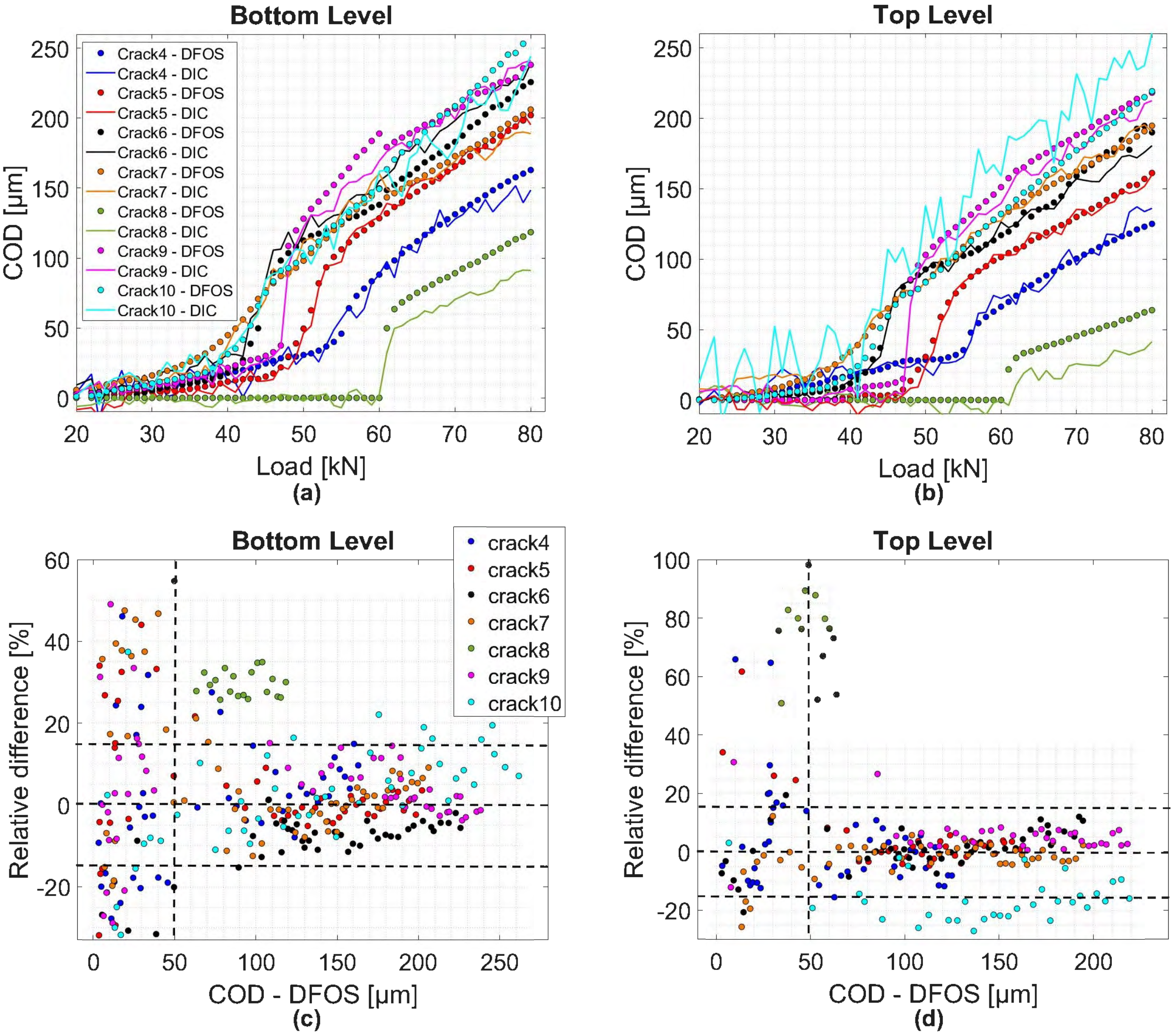

Figure 4-30: Variation of the estimated COD from DIC and DFOS techniques for cracks (4 to 10) at the Bottom (FO line1B) and Top (FO line1T) levels.

cover is relatively small, a bond-slip model can be adopted in our case, where only the loading and geometry asymmetries between the front and back side can cause variations in the crack opening.

Thus, assuming a linear crack opening variation over the thickness of the beam, it is possible to calculate a theoretical crack opening value at each of line's position using the front and back side crack opening estimations from FO line 1B and FO line 7B. As shown in Figure 4-31, comparing these theoretical values to those estimated for crack 4 and crack 10, where front and back side opening estimations were previously validated, shows a good correlation with relative differences of less than 10% starting from a crack opening of 40μm.

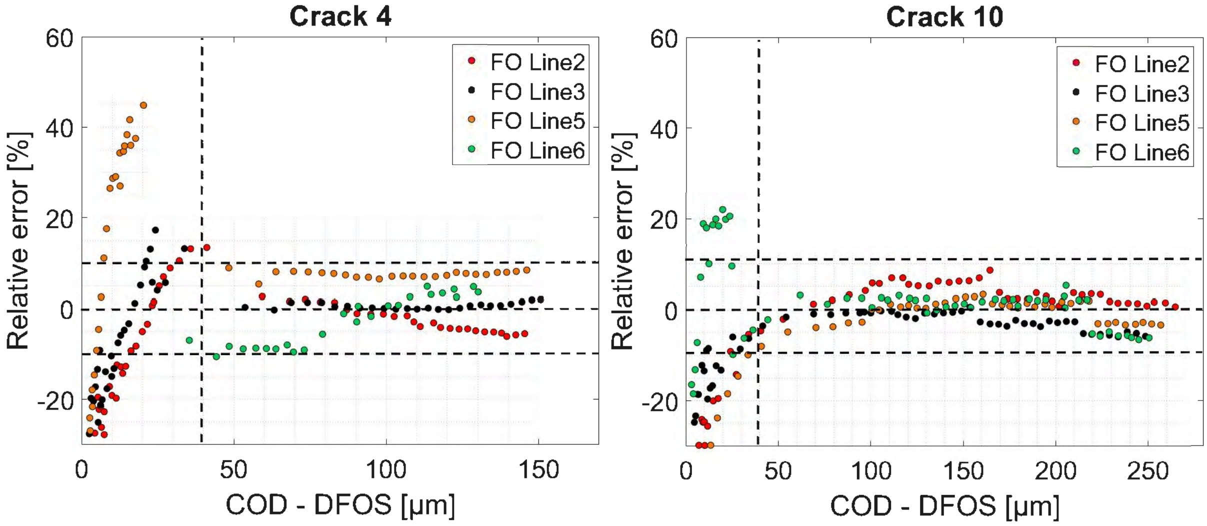

Figure 4-31: Relative error between estimated COD values from FO lines (2,3,5,6) and theoretical values based on the simple linear variation assumption crack 10.

IV.4.5. View of a full crack monitoring system

In view of the results presented in the previous section, the Rayleigh-based DFOS system shows that it could be a promising tool to perform multiple crack identification in reinforced concrete structures. In terms of crack detection and localization, this sensing system achieved early crack detection during the linear elastic phase and was able to separate and localize all different microcracks.

By embedding the optical cable inside the structure, it is also possible to monitor in-depth crack propagation as shown in Figure 4-32. In order to plot this figure, we assumed the existence of a crack when a peak is detected with a strain amplitude of 20 μm/m. During the linear elastic state, microcracks appeared mainly in the central area while propagating from the surface to the inside part of the beam. At full cracking state, the cracks are distributed over the hole length of the beam with a distance of 10-15 cm separating each two consecutive cracks.

More importantly, this system is able to quantify and continuously monitor the crack openings. Figure 4-33a presents the fiber optics spatial strain distribution over the length of the tested beam. By using the mechanical strain transfer model, the cracks openings variations can be extracted from the strain profiles as shown in Figure 4-33b. The microcracks can be divided into two categories. At an applied load of 80 kN, we can separate main cracks with an average crack opening of around 200 μm and secondary cracks with an average crack opening of around 50 μm.

Figure 4-34 presents the in-depth variation of the estimated crack opening. While cracks like

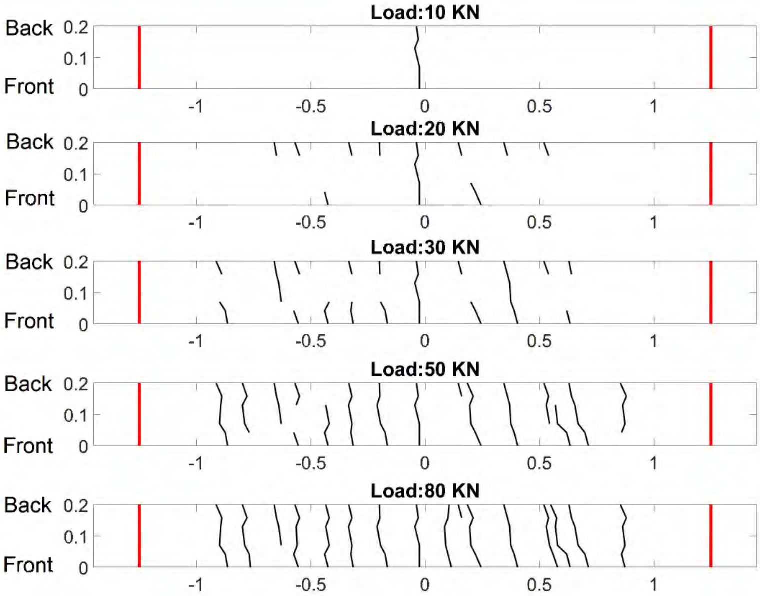

Figure 4-32: Crack propagation over the thickness of the tested beam for different load levels.

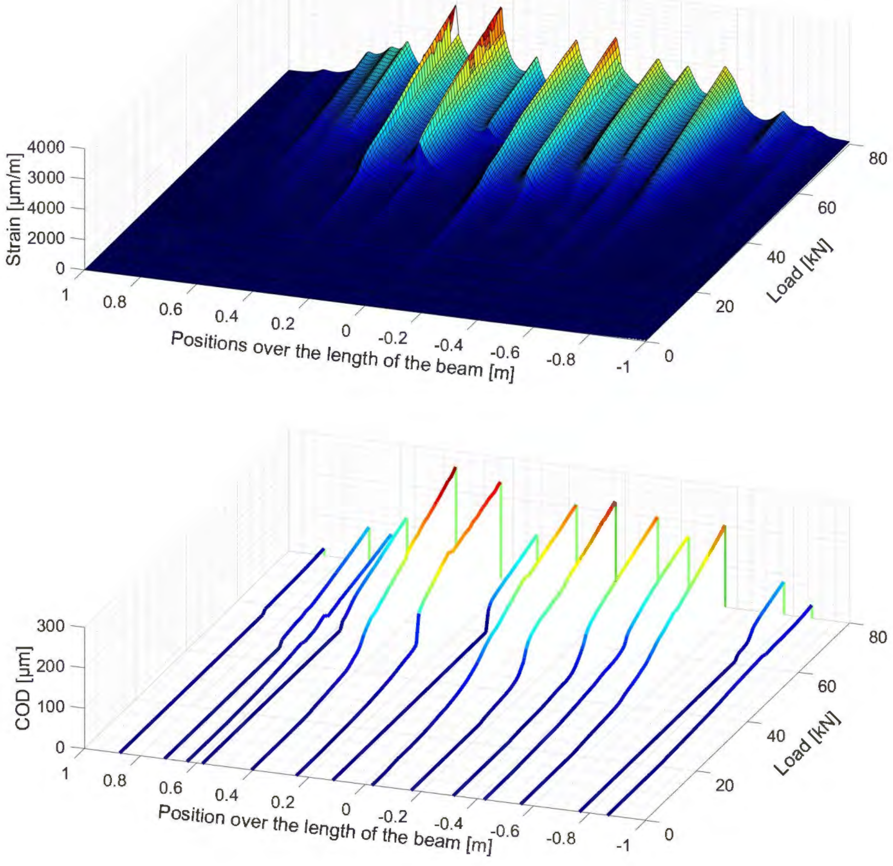

Figure 4-33: Measured strain variation from FO line 1B transformed to COD distribution over the full length of the beam.

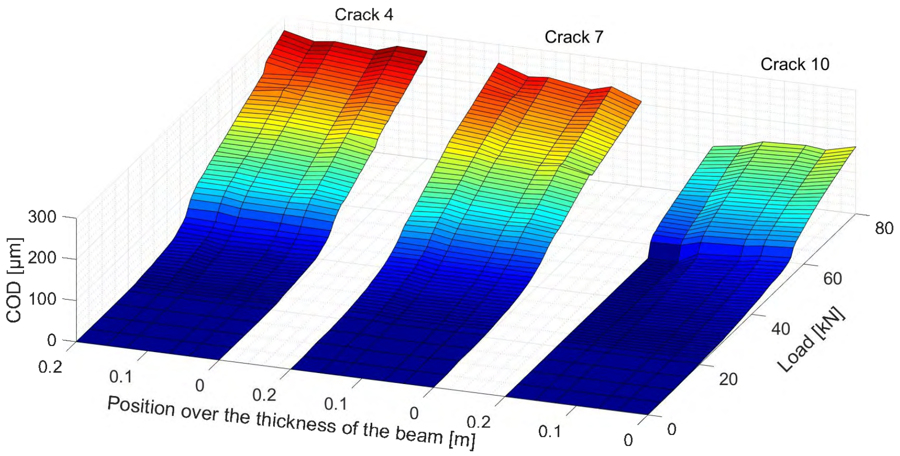

Figure 4-34: In-depth COD distribution for crack 4, 7 and 10.

crack 4 figured constant crack openings over the thickness of the beam, cracks like crack 7 and 10 figured a linear COD variations from the front to the back side of the beam.

With the continuous improvements in the interrogation units characteristics, real time on-site strain monitoring using DFOS techniques is now available with more user friendly interfaces. All things considered, civil engineers can used this techniques to monitor different aspects of a cracking behavior of a reinforced concrete structure.

IV.5. Conclusion

We addressed in this chapter the advantages of distributed fiber optic sensing techniques for damage monitoring in reinforced concrete structures by following the microcracks formation and propagation.

First, we evaluated the crack detection using this sensing technique. A three-point bending test on a reinforced concrete beam figuring ultrasonic, LVDT and strain gauge sensors, was performed. together with the CWI technique, the DFO sensing technique achieved prior crack detection to standard LVDT and strain gauge sensors. The ODISI-B interrogator working on standard operating mode, measured high strain variations over the SensoLux cable and was able to detect and localize the main central crack reaching both bottom and top rebars, as well as a second crack at a later stage. This high sensitivity is due to the crack-induced strains dependent on the strain lag parameter of the sensing cable. Thus, based on the family of sensing cables tested in Chapter 3 with their wide range of strain lag parameter, the suitable sensor can now be selected for each type of application demanding a specific crack sensitivity. The combination of the CWI and DFOS techniques gave more detailed information about different crack propagation aspects.

Second, we examined our capacity to monitor small micro crack openings. Four three-point bending tests were performed on laboratory size reinforced concrete beams. We showed that even low level of strain in concrete affects the estimation of small crack openings and the strain lag parameter. Neglecting the strain in concrete or introducing it as a variable parameter into the fitting process lead to discrepancies in the estimated parameters. The best option is to account for this strain using a strain gauge measurements.

An influence of the rebars and concrete hardening was also observed. ODISI-B strain measurements over surface-mounted SensoLux cable lines achieved very good accuracy of less than 4%. A 10% accuracy is reached starting from crack openings as low as 20 μm. For these lines, crack opening estimations were not influenced by concrete hardening, contrary to embedded SensoLux cable lines figuring variation in the accuracy of the COD estimations. The COD estimation errors reached 30-40% for short concrete hardening time of 1 month, and decreased to 10-15% for 2 to 10 months of concrete hardening. Moreover, the strain lag parameter values increased with concrete hardening and the results suggest that a relation between the strain lag parameter and the crack opening accuracy could exist. More tests should be performed to validate these conclusions.

In terms of surrounding microcrack formations, only adjacent microcracks, located 10 cm from the main crack, led to a decrease in the strain lag parameter values. However, no influence of the surrounding micro cracks on the estimated crack opening, was observed.

The third and final part is mainly focused on studying the multiple cracking case of a real scale reinforced concrete beam. A four-point bending test was performed figuring the use of LVDT sensors and DIC technique for comparison of different crack openings.

From the strain profiles measured over the length of SensoLux cable lines and resulting from the formation of different neighboring cracks, we were able to separate and localize all different cracks. Contrary to DIC technique, the cracks were easily detected during the elastic stage.

The model is fitted to the spatial strain distributions and low residual levels are observed. The global strain lag parameter was consistent with the previous embedded and surface-mounted values for the SensoLux cable. In terms of crack openings, relative differences of less than 5% with LVDT sensors are deduced. By comparing the DFO estimated crack openings with those estimated from DIC technique, relative differences of 15% are observed. This high level of relative differences is mainly due to the repeatability of the DIC estimations. Moreover, the relative differences between the crack openings estimated from embedded and surface-mounted lines did not exceed the 10%. This forms a compelling evidence that surface and in-depth multiple crack opening monitoring can be performed using the DFO sensing technique.

Based on these results, one can imagine a structural health monitoring system based on the implemented DFOS system. In addition to the possibility to monitor strain over the length of the structure with a good accuracy almost equal to strain gauge sensors, the spatial strain measurements from this DFOS system can be used to accurately detect and localize all the microcracks at early stages and estimate their crack openings. Thus, this strain monitoring system can also function as a multiple cracks opening monitoring system. The novelty of this SHM system could be in its capacity to monitor continuously the full length of a medium size civil infrastructure, like a bridge.

Conclusion

The main functionality that civil engineers want to preserve in time is the mechanical strength of structures. The tools implemented must allow the assessment of their safety. They must also provide elements to detect the appearance of harmful pathologies in the structure and to monitor their evolution. Strain and displacements measurements, as well as crack propagation in concrete material, are indicators of the mechanical strength of the structure. DFOS systems, composed of an interrogator and optical cable, allow spatial distributed strain measurements forming an undeniable asset for health monitoring on civil infrastructures. These techniques can replace many thousands of traditional sensors with only one optical fiber. Recently, the possibility of crack identification in terms of detection, localization using these sensing systems was also demonstrated with some researchers interested in quantifying crack openings. This has been possible due to the significant improvement in the interrogation unit properties during the last decade. On the other hand, the behavior of optical cables designed for strain measurements is still poorly understood on short-term as well as the long-term. Hence, in this PhD work, some of these challenges has been approached.

The first part of this work was devoted to the theoretical study of the strain transferring. We presented a strain transfer model proposed by D. Li for a system with three layers (optical fibre, coating, host material) that behave in an elastic manner and perfectly adhere to each other. Then we proposed an improved model that takes into account an imperfect bonding at the sensor/host material interface and we have extended it to multi-layer systems. This more realistic analytical model includes the slip or discontinuities at the interfaces by introducing an interfacial stiffness parameter. The key result of our calculations is that in all these cases, the crack-induced strain can take the form of:

$$\epsilon_{crack}(z) = \frac{\mathrm{COD}}{2}\lambda e^{-\lambda |z|} \tag{IV.11}$$

which depends on only two parameters: COD and λ. The parameter COD represents the opening of the crack. The parameter λ, or strain lag parameter, is related to the characteristics of the studied system: it depends on the mechanical properties of the different layers and the adhesion between the layers. Its evolution therefore provides information on the evolution of the system under study.

Having a single law of behavior covering a wide range of configurations is of undeniable interest from an experimental point of view. Indeed, to analyze the measurements, we only need in many practical cases to fit the measurements with the mechanical strain transfer function composed of the crack induced strain part (Equation IV.11) and the elastic strain in the host material. If the fit is relevant, the crack opening is obtained directly, without the need to know precisely the internal composition of the system and the interactions between layers, and without the need to perform prior calibration tests. Depending on each structure's behavior, proper approaches to take the elastic strain into account should be adapted in order the improve the small crack openings estimations.

A second part of this work focused on experimental studies for model validation. Wedge splitting tests were performed on specimens instrumented with optical fiber cables on the surface and inside the concrete material, together with LVDT extensometers which serve as reference sensors. The spatial strain distribution was measured by a Rayleigh based interrogation unit and fitted using the strain transfer function to estimate the crack opening and strain lag parameter. Crack openings were compared to the reference measurements showing low relative errors close to 2% and up to a crack opening of 200-1000 μm, for concentric optical cables glued in a U-groove on the surface of specimen. The same results where demonstrated for cables with non-concentric more complex stack of layers. Optical cables embedded in concrete show less accurate results with relative errors of 10%. Through monitoring the strain lag parameter variation, we were able to associate this discrepancy in crack opening estimation accuracy to different level of bonding at the interfaces. The increased interfacial adhesion between the added adhesive layer and both the cable and concrete material increases the strain lag coefficient and in some case, it guarantees the steadiness and stability of the interfacial bonding.

A thorough study on the model limitations and its influencing parameters was also conducted. We were able to show that robust cable configurations with additional metallic and thick Polyamide layers could revoke the model assumptions. In addition, we proved that the concrete hardening affects the strain transfer between the concrete material and the optical cable. It is mainly dependent on the interfacial state condition, as an increase in the adhesion leads to higher strain lag coefficient and better crack opening estimations. Finally, we investigated the effect of bonding length on the crack induced spatial distribution. A bonding length corresponding to a 99% of strain transfer rate guarantees the best crack opening and strain lag parameters estimations.

To definitively validate the model, we applied it to reinforced concrete beams, similar to those that exist in real structures. The objective was threefold: to prove its ability to detect cracks at early stage, to measure the opening of small cracks and to monitor the evolution of multiple cracks.

We submitted a 20×20×100 cm beam to a three points bending test. The beam was instrumented with optical fibers, ultra sonic sensors, strain gauges and LVDT sensors. The ultra sonic signal was analysed with the coda wave interferometry (CWI) technique known to be very sensitive to subtle changes in the concrete material. The capacity of crack detection using DFO sensing technique has proven to be as sensitive as CWI technique. Henceforth, these two techniques detected cracks earlier than the traditional strain gauge and displacement sensors and their combination helped monitoring changes in the behavior of the damaged reinforced concrete beam.

In a second time, we submitted four 10×20×100 cm beams equipped with optical fibers, LVDT sensors and strain gauges to a three point bending test. We showed that it is possible to improve estimation accuracy of microcracks of less than 100 μm, by separating the strain in host material from the crack-induced strain. We also investigated the case of embedded cables instrumentation next to rebars. Over estimations of crack openings can be observed that could be due to the degradation of concrete over the length of the longitudinal rebars. This estimation error reduced with concrete hardening.

Then a four point bending test on a 20×40×290 cm reinforced concrete beam has been performed, leading to multiple micro crack propagation. The beam was instrumented with optical fibers and LVDT sensors and also monitored by a stereo Digital Image Correlation system (DIC). We proved that it is possible to detect all different microcracks at early stage and localize them. In addition, crack opening estimations from surface-mounted cables led to relative errors of less than 5% when compared to displacement sensors. Moreover, DFO estimations led to more accurate and stable estimations than the DIC technique with those estimated through embedded cables close and far from rebars showing less then 10% variations.

From all these results, it can be concluded that the distributed optical fiber strain sensing associated with the law of behaviour IV.11 is an effective method for detecting, localizing and monitoring the opening of cracks in concrete structures.

As a next step, the durability of the system should be examined. The behavior of the optical cable under mechanical and environmental cyclic loading should be studied. Finally, the possibility of employing optical cables with different levels of shear lag parameter and therefore different levels of sensitivity to microcracks can be of use to investigate more complex cracking behaviors in novel materials like ultra high performance fiber reinforced concrete.

Appendix A

Data sheets of tested optical cables

THORLABS

Single Mode Fiber with Ø900 µm Hytrel Jacket

SMF-28-100

Description

Thorlabs' single mode SMF-28-100 fiber jacketed with Ø900 µm yellow Hytrel tubing delivers high performance across a broad spectral range in the telecom region, and also features exceptional core / clad concentricity specifications.

Specifications

Geometrical & Mechanical	
Core Diameter	8.2 µm
Cladding Diameter	125 ± 0.7 µm
Coating Diameter	242 ± 5 µm
Core-Clad Concentricity	≤0.5 µm
Coating-Clad Concentricity	<12 µm
Fiber Curl	≥4.0 m Radius of Curvature
Operating Temperature	-60 to 85 °C
Proof Test Level (245 coat)	≥100 kpsi (0.7 GN/m^2)
Fiber Length	100 m
Jacket	Ø900 µm Hytrel

Optical	
Numerical Aperture (nominal)	0.14
Attenuation*	≤0.32 dB/km @ 1310 nm ≤0.32 dB/km @ 1383 nm** ≤0.21 dB/km @ 1490 nm ≤0.18 dB/km @ 1550 nm ≤0.20 dB/km @ 1625 nm
Operating Wavelength	1260 - 1625 nm
Mode Field Diameter	9.2 ± 0.4 µm @ 1310 nm 10.4 ± 0.5 µm @ 1550 nm
Dispersion	≤18.0 ps/(nm·km) @ 1550 nm ≤22.0 ps/(nm·km) @ 1625 nm
Polarization Mode Dispersion, Link Design Value	≤0.04 ps/√km
Polarization Mode Dispersion, Maximum Individual Fiber	≤0.1 ps/√km
Bend Loss for 100 Turns on 25 mm Mandrel	≤0.01 dB @ 1550 nm

*Maximum specified attenuation value available within the stated ranges.
** Attenuation values at this wavelength represent post-hydrogen aging performance.

Technical Response

Customer / Reference:	DNS-0470
Products:	SENSORNET
Requester:	Adrian Parsons
Author:	Daniela Giron
Checked:	Jon Sherhod
Date Submitted:	29th April 2014
File Reference Number:	Tr-14-184

Revision History

Revision	**Date**	**Reason for Change**
01	29/04/14	New Issue

Technical Response
DNS-0470 2.0mm Fibre Strand Unit, Blue – 2 X SM, 2 X 50um MM fibres, (+two mechanical fibres)

MM Fibres:

Quantity	Colour	Max Attenuation @ 850nm	Max Attenuation @ 1300nm
2	1.Blue 2.Orange	2.8 dB/km	0.8 dB/km

SM Fibres:

Quantity	Colour	Max Attenuation @ 1310nm	Max Attenuation @ 1550
2	3.Green 4.Brown	0.35 dB/km	0.25 dB/km

2 Mechanical Fibres

Minimum Bend Radius of Cable: 100mm
Tensile limit: 600g

BRUsens DSS 2.8mm V1 non-metallic

3_50_2_004

LLK-BSST V1 2.8 mm

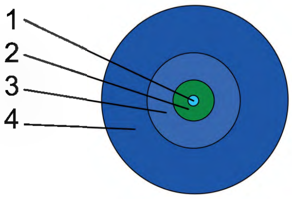

SublineFiber optic strain sensing cable, extra small, lightweight, sensitive, non metallic, one optical up buffered fiber, protection and strain transfer layer, EPR outer sheath, strain range up to 1% (10000 µstrain).

Application

- Strain
- Soil movement
- Pipeline monitoring
- Stuctural monitoring
- Precision measurement and alarm systems

Technical data

Type	Max. no. of fibres units	Cable ø mm	Weight kg/km	Installation Max. tensile strength N	Typical Load at 1 % elongation N
1F	1	2.8	5.9	5	26

Type	with tensile load Min. bending radius mm	without tensile load Min. bending radius mm	Max. crush resistance N/cm
1F	≤0.5	≈ 4.2	10.5

Optical fiber data (cabled) at 20°C

Fiber Type	Attenuation dB/km 1550 nm	Temperature sensitivity df_B/dT Typical Brillouin parameters BOTDR or BOTDA at 1550 nm MHz/°C	Strain sensitivity $df_B/dT\varepsilon$ Typical Brillouin parameters BOTDR or BOTDA at 1550 nm MHz/°C	Centr. Brillouin Freq. Typical Brillouin parameters BOTDR or BOTDA at 1550 nm GHz
SMF	≤0.5	≈ 4.2	≈ 450	10.5

BRUsens DSS 3.2mm V4 metallic

3_50_2_003

LLK-BSST V4 3.2 mm

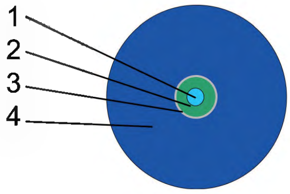

SublineFiber optic strain sensing cable, mini, flexibel, armored with central metal tube, PA outer sheath, one optical fiber, strain range up to 1% (10000 µstrain).

Application

- Strain
- Soil movement
- Pipeline monitoring
- Stuctural monitoring
- Precision measurement and alarm systems
- Brillouin, FBG
- Outdoors, harsh environment, subsea
- Direct burial in soil, concrete, composite structures

Technical data

Type	Max. no. of fibres units	Cable ø mm	Weight kg/km	Installation Max. tensile strength N	Typical Load at 1 % elongation N
1F	1	3.2	10.5	260	470

Type	with tensile load Min. bending radius mm	without tensile load Min. bending radius mm	Max. crush resistance N/cm
1F	64 (20xD)	48 (15xD)	250

Optical fiber data (cabled) at 20°C

Fiber Type	Attenuation dB/km 1550 nm	Temperature sensitivity df_B/dT Typical Brillouin parameters BOTDR or BOTDA at 1550 nm MHz/°C	Strain sensitivity $df_B/dT\varepsilon$ Typical Brillouin parameters BOTDR or BOTDA at 1550 nm MHz/°C	Centr. Brillouin Freq. Typical Brillouin parameters BOTDR or BOTDA at 1550 nm GHz
SMF	≤0.5	1.1	450	10.6

BRUsens DSS 3.2mm V9 grip

3_50_2_005

LLK-BSST V9 3.2 mm

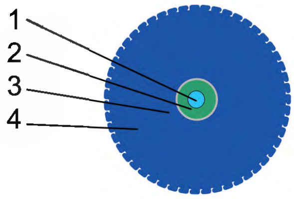

SublineFiber optic strain sensing cable, mini, flexible, armored with central metal tube, structured PA outer sheath, one optical fiber, strain range up to 1 % (10000 µstrain).

Application

- Strain
- Soil movement
- Pipeline monitoring
- Stuctural monitoring
- Precision measurement and alarm systems
- Brillouin, FBG
- Outdoors, harsh environment, subsea

Technical data

Type	Max. no. of fibres units	Cable ø mm	Weight kg/km	Installation Max. tensile strength N	Typical Load at 1 % elongation N
1F	1	3.2	10.5	260	470

Type	with tensile load Min. bending radius mm	without tensile load Min. bending radius mm	Max. crush resistance N/cm
1F	64 (20xD)	48 (15xD)	250

Optical fiber data (cabled) at 20°C

Fiber Type	Attenuation dB/km 1550 nm	Temperature sensitivity df_B/dT Typical Brillouin parameters BOTDR or BOTDA at 1550 nm MHz/°C	Strain sensitivity $df_B/dT\varepsilon$ Typical Brillouin parameters BOTDR or BOTDA at 1550 nm MHz/°C	Centr. Brillouin Freq. Typical Brillouin parameters BOTDR or BOTDA at 1550 nm GHz
SMF	≤0.5	1.1	450	10.6

FutureNeuro™ FN-SSL-3

Surface-taped Sensing Fiber

FEATURES

- **Two single-mode optical fibers**
- **Easy to install: just stick tape to surface**
- **Temperature range: -40 to +80 C**
- **Minimum bending radius: 15 mm**

*T*he FN-SSL-3 tape sensing fiber consist of two standard SM fibers on single tape. It is designed for temperature and/or strain measurements, exhibiting very good sensitivity and durability.

Sticking tape-like sensing fiber

The thickness of fibers supporting back-sheet is less than 1.0 mm. It allows the sensing fibers to be attached to an object, while providing a medium for transferring strain and temperature between object and fibers.
The FN-SSL-3 surface film covers fibers and protects them from damage. This film also supports the fibers while bending. The minimum bending radius is 15 mm, making it suitable for all types of objects and installation schemes.

Easy installation. Excellent durability

The FN-SSL-3 surface-tape sensing fiber is easy to use; just peel off the release liner and attach the fiber to the object. Specially designed adhesive starts solidifying after sticking and pressing the tape. It becomes ready for measurement in 24 hours. The adhesive of the tape is designed for many years of use.

Specifications FN-SSL-3

Fiber Type	10 / 125 μm Single-Mode Fiber
Fiber count	2
Attenuation	< 0.5 dB/km
Bending Radius	> 15 mm
Dimension (W x H)	8.0 x 1.0 mm
Length (standard, per reel)	15 m
(custom made, per reel)	< 100m
Weight	3.5 g /m
Working Temperature	-40 to +80 °C

All specifications above are subject to change without notice.

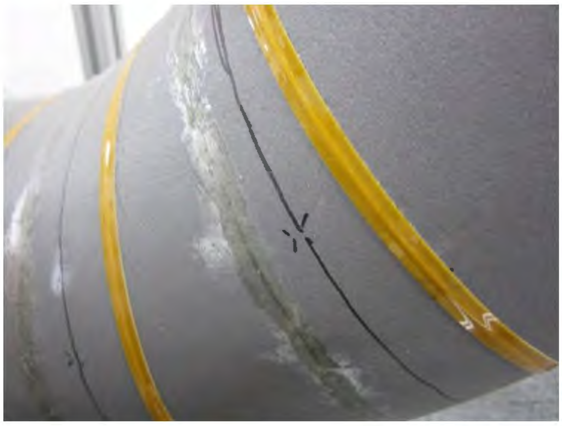

Application example: stuck spirally on the steel pipe for detecting strain

Configurations

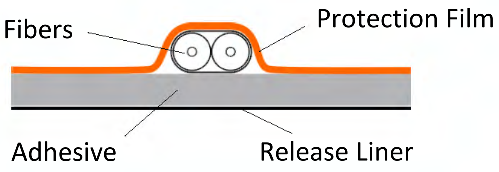

Delivery Reel

(The Standard type for 15m)

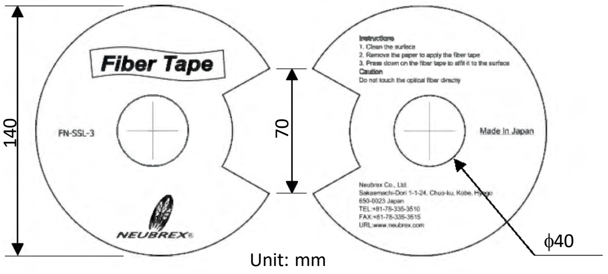

Neubrex Co., Ltd.

Sakaemachi-dori 1-1-24, Chuo-ku, Kobe
Hyogo 650-0023, Japan
Tel: +81-78-335-3510
www.neubrex.com

DEFYING IMPOSSIBLE

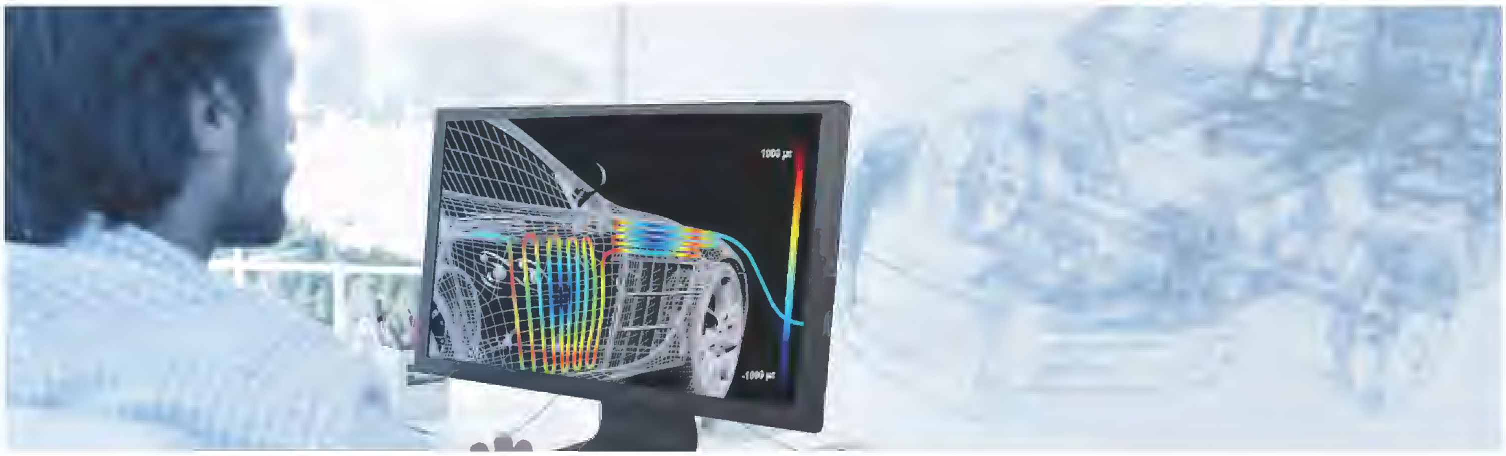

High-Definition Fiber Optic Strain Sensors

Unlike conventional strain gages that only measure strain at a discrete point, Luna's high definition fiber optic strain gages provide continuous, high resolution (~1mm) measurements of strain along the entire length of the sensor (up to 50m). A single sensor provides more than one thousand strain measurements per meter of sensor. This breakthrough measurement technology enables an entirely new dimension of stress and strain analysis. High-Definition (HD) Sensors for static environments offer unprecedented resolution and strain range, while High-Speed CFG Sensors are ideal for fatigue testing and more dynamic environments.

BENEFITS

Low profile for embedding
Embed sensor within structures without influencing test results

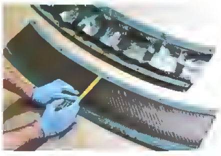

High density measurements
Characterizes strain gradients and validates finite element models

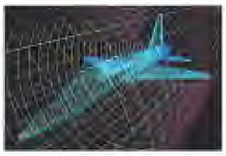

Dielectric and EMI/EMC immune
Ideal for instrumenting electronic assemblies

Corrosion proof
A robust sensor that introduces no source of ignition to hazardous environments

High-Definition (HD)

Uses standard unaltered fiber. Gage length and location are configurable through software.

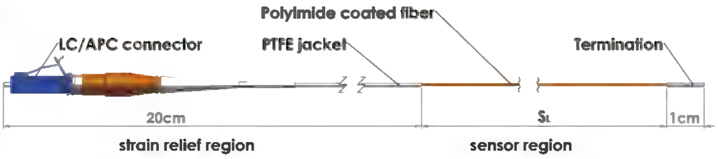

High-Speed CFG (HS)

Uses a proprietary continuous grating pattern that offers both high spatial resolution and improved dynamic performance.

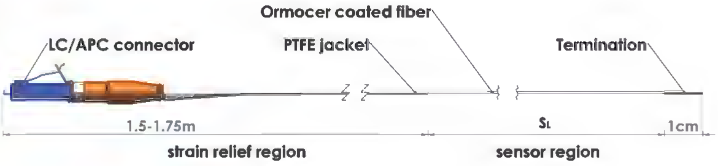

Corning® SMF-28e® Optical Fiber Product Information

Optical Fiber

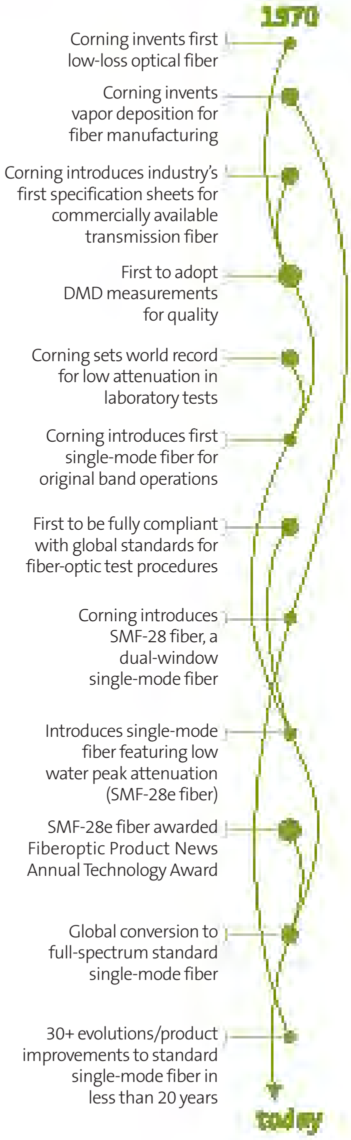

Evolving Networks Now

At Corning Optical Fiber, we are continually pushing single-mode fiber to new performance levels. Building on our leadership position in the optical fiber industry, Corning is evolving our already formidable products to meet customer requirements like never before. As the first manufacturer to upgrade standard single-mode fiber worldwide, we're providing our customers with greater value today and in the future. Corning® SMF-28e® optical fiber is:

- Corning's standard single-mode fiber offering, delivering optimized capability, network design flexibility and confidence in long-term performance
- The world's most widely demanded full-spectrum fiber
- In compliance with or exceeding the industry's most stringent requirements, including:
  - ITU-T G.652 (Categories A, B, C & D)
  - IEC Specifications 60793-2-50 Type B1.3
  - TIA/EIA 492-CAAB
  - Telcordia's GR-20
- The industry leader in comprehensive standard single-mode fiber specifications

As Corning's premier standard single-mode fiber, SMF-28e fiber is one in a long line of optical innovations. Corning SMF-28e, an ITU-T G.652.D-compliant optical fiber, is expanding the capability of the world's most dynamic metropolitan and access networks.

PI1344 | ISSUED: JANUARY 2005 | SUPERSEDES: NOVEMBER 2004 | ISO 9001 REGISTERED

References

[1] LA Bisby et al. *An Introduction to Structural Health Monitoring*. Tech. rep. ISIS Canada and SAMCO Network of the European Comission, 2005.

[2] Esequiel Mesquita et al. “Global overview on advances in structural health monitoring platforms”. In: *Journal of Civil Structural Health Monitoring* 6.3 (2016), pp. 461–475.

[3] Branko Glisic and Daniele Inaudi. *Fibre optic methods for structural health monitoring*. John Wiley and Sons, 2008.

[4] AASHTO. “342 standard method of test for determining dynamic modulus of hot-mix asphalt concrete mixtures”. In: *American Association of State Highway and Transportation Officials* (2011).

[5] Jerome P Lynch, Charles R Farrar, and Jennifer E Michaels. “Structural health monitoring: technological advances to practical implementations”. In: *Proceedings of the IEEE* 104.8 (2016), pp. 1508–1512.

[6] Kinzo Kishida, Yoshiaki Yamauchi, and Artur Guzik. “Study of optical fibers strain-temperature sensitivities using hybrid Brillouin-Rayleigh system”. In: *Photonic Sensors* 4.1 (2014), pp. 1–11.

[7] Denis Breysse and Odile Abraham. *Méthodologie d’évaluation non destructive de l’état d’altération des ouvrages en béton*. Ed. Presse des ponts et Chaussées, 2005.

[8] Odile Abraham et al. “Monitoring of a Large Cracked Concrete Sample with Non-Linear Mixing of Ultrasonic Coda Waves”. In: *EWSHM - 7th European Workshop on Structural Health Monitoring*. July 2014.

[9] Ernst Niederleithinger, Martin Herbrand, and Matthias Müller. “Monitoring von Querkraftversuchen an Spannbetondurchlaufträgern mit Ultraschall- und Codawelleninterferometrie”. In: *Bauingenieur* 92 (Nov. 2017), pp. 474–481.

[10] Kentaro Ohno and Masayasu Ohtsu. “Crack classification in concrete based on acoustic emission”. In: *Construction and Building Materials* 24.12 (2010), pp. 2339–2346.

[11] Dimitrios G Aggelis. “Classification of cracking mode in concrete by acoustic emission parameters”. In: *Mechanics Research Communications* 38.3 (2011), pp. 153–157.

[12] Archana Nair and CS Cai. “Acoustic emission monitoring of bridges: Review and case studies”. In: *Engineering structures* 32.6 (2010), pp. 1704–1714.

[13] TM Roberts and M Talebzadeh. “Acoustic emission monitoring of fatigue crack propagation”. In: *Journal of Constructional Steel Research* 59.6 (2003), pp. 695–712.

[14] Alexis Courtois et al. “La surveillance en exploitation des enceintes de confinement et des aérorefrigérants à tirage naturel du parc nucléaire d’EDF”. In: *Revue Generale Nucleaire* 2 (2011), pp. 49–59.

[15] Alexandre Simon and A Courtois. “Structural monitoring of prestressed concrete containments of nuclear power plants for ageing management”. In: *Structural Mechanics in Reactor Technology* 21 (2011), pp. 6–11.

[16] Catherine Larive. “Apports combinés de l’expérimentation et de la modélisation à la compréhension de l’alcali-réaction et de ses effets mécaniques”. PhD thesis. Ecole des Ponts et Chaussées, 1997.

[17] Pierre Ferdinand. “The Evolution of Optical Fiber Sensors Technologies During the 35 Last Years and Their Applications in Structure Health Monitoring”. In: *EWSHM - 7th European Workshop on Structural Health Monitoring*. IFSTTAR, Inria, Université de Nantes. Nantes, France, July 2014.

[18] Wolfgang R. Habel and Katerina Krebber. “Fiber-optic sensor applications in civil and geotechnical engineering”. In: *Photonic Sensors* 1.3 (2011), pp. 268–280.

[19] KS Thyagarajan and Ajoy Ghatak. *Fiber optic essentials*. Vol. 10. John Wiley & Sons, 2007.

[20] “Streicker Bridge: a comparison between Bragg-grating long-gauge strain and temperature sensors and Brillouin scattering-based distributed strain and temperature sensors”. In: *Sensors and Smart Structures Technologies for Civil, Mechanical, and Aerospace Systems*. Vol. 7981. 2011.

[21] José Miguel Lopez-Higuera. *Handbook of optical fibre sensing technology*. Wiley, 2002.

[22] B Zhang et al. “Evaluation of fibre optic sensors for structural condition monitoring”. In: *Materials and structures* 35.6 (2002), pp. 357–364.

[23] Xiongxing Zhang et al. “Two-Parameter Elliptical Fitting Method for Short-Cavity Fiber Fabry–Perot Sensor Interrogation”. In: *Sensors* 19.1 (2019), p. 36.

[24] XW Ye, YH Su, and JP Han. “Structural health monitoring of civil infrastructure using optical fiber sensing technology: A comprehensive review”. In: *The Scientific World Journal* 2014 (2014).

[25] Qingbin Li, Guang Li, and Libo Yuan. “Calibration of embedded fiber optic sensor in concrete under biaxial compression”. In: *Measurement* 35.3 (2004), pp. 303–310.

[26] Daniele Posenato et al. “Model-free data interpretation for continuous monitoring of complex structures”. In: *Advanced Engineering Informatics* 22.1 (2008), pp. 135–144.

[27] A Hartog. “Distributed fiber-optic sensors: principles and applications”. In: *Optical Fiber Sensor Technology*. Springer, 2000, pp. 241–301.

[28] Russell Ellis. “Explanation of reflection features in optical fiber as sometimes observed in OTDR measurement traces”. In: *Corning White Paper* (2007).

[29] Brian J Soller et al. “High resolution optical frequency domain reflectometry for characterization of components and assemblies”. In: *Optics Express* 13.2 (2005), pp. 666–674.

[30] Luca Palmieri and Luca Schenato. “Distributed optical fiber sensing based on Rayleigh scattering”. In: *The Open Optics Journal* 7.1 (2013).

[31] Dennis Denney. “DTS Technology: Improving Acid Placement”. In: *Journal of Petroleum Technology* (2012), pp. 96–99.

[32] Gerard Glasbergen et al. “Fluid-Diversion Monitoring: The Key to Treatment Optimization”. In: *SPE Production & Operations* 25.03 (2010), pp. 262–274.

[33] Dhirendra K Nath, Riki Sugianto, Doug Finley, et al. “Fiber-Optic Distributed Temperature Sensing Technology Used for Reservoir Monitoring in an Indonesia Steam Flood”. In: *SPE International Thermal Operations and Heavy Oil Symposium*. Society of Petroleum Engineers. 2005.

[34] Tsuneo Horiguchi, Toshio Kurashima, and Mitsuhiro Tateda. “Tensile strain dependence of Brillouin frequency shift in silica optical fibers”. In: *IEEE Photonics Technology Letters* 1.5 (1989), pp. 107–108.

[35] M. Nikles, L. Thevenaz, and P. A. Robert. “Brillouin gain spectrum characterization in single-mode optical fibers”. In: *Journal of Lightwave Technology* 15.10 (1997), pp. 1842–1851.

[36] T. R. Parker et al. “Simultaneous distributed measurement of strain and temperature from noise-initiated Brillouin scattering in optical fibers”. In: *IEEE Journal of Quantum Electronics* 34.4 (Apr. 1998), pp. 645–659.

[37] Kinzo Kishida et al. “Hybrid brillouin-Rayleigh distributed sensing system”. In: *OFS2012 22nd International Conference on Optical Fiber Sensors*. Vol. 8421. International Society for Optics and Photonics. 2012.

[38] Yongsheng Tang and Zhishen Wu. “Distributed Long-Gauge Optical Fiber Sensors Based Self-Sensing FRP Bar for Concrete Structure”. In: *Sensors* 16.3 (2016).

[39] Pierre Ferdinand et al. “Brillouin sensing for perimetric detection: the SmartFence project”. In: *22nd International Conference on Optical Fiber Sensors*. Vol. 8421. 2012.

[40] Daniele Inaudi and Branko Glisic. “Distributed Fiber optic Strain and Temperature Sensing for Structural Health Monitoring”. In: *The Third Int’l Conference on Bridge Maintenance, Safety and Management* (2006).

[41] Daniele Inaudi and Branko Glisic. “Overview of fibre optic sensing applications to structural health monitoring”. In: *Symposium on Deformation Measurement and Analysis*. 2008, pp. 1–10.

[42] Branko Glisic et al. “Damage detection and characterization using long-gauge and distributed fiber optic sensors”. In: *Optical Engineering* 52.8 (2013).

[43] Filippo Bastianini et al. “Discontinuous Brillouin strain monitoring of small concrete bridges: comparison between near-to-surface and smart FRP fiber installation techniques”. In: *Smart Structures and Materials 2005: Sensors and Smart Structures Technologies for Civil, Mechanical, and Aerospace Systems.* Vol. 5765. International Society for Optics and Photonics. 2005, pp. 612–623.

[44] A. Minardo et al. “Bridge Monitoring Using Brillouin Fiber-Optic Sensors”. In: *IEEE Sensors Journal* 12.1 (Jan. 2012), pp. 145–150.

[45] Wei Zhang et al. “Health Monitoring of Rehabilitated Concrete Bridges Using Distributed Optical Fiber Sensing”. In: *Computer-Aided Civil and Infrastructure Engineering* 21.6 (2006), pp. 411–424.

[46] Dorotea Hoeg Sigurdardottir. “Strain-based monitoring methods for beam-like structures”. PhD thesis. Princeton University, 2015.

[47] Gerardo Rodriguez, Joan R.casas, and Sergi Villalba. “SHM by DOFS in civil engineering: a review”. In: *Structural monitoring and maintenance* 2.4 (July 2015), pp. 357–382.

[48] Jon Harald L Grave, Magnus L Håheim, and Andreas T Echtermeyer. “Measuring changing strain fields in composites with Distributed Fiber-Optic Sensing using the optical backscatter reflectometer”. In: *Composites Part B: Engineering* 74 (2015), pp. 138–146.

[49] Jean-Marie Hénault et al. “Quantitative strain measurement and crack detection in RC structures using a truly distributed fiber optic sensing system”. In: *Construction and Building Materials* 37 (2012), pp. 916–923.

[50] Sergi Villalba and Joan R. Casas. “Application of optical fiber distributed sensing to health monitoring of concrete structures”. In: *Mechanical Systems and Signal Processing* 39.1–2 (Aug. 2013), pp. 441–451.

[51] Alfredo Güemes, Antonio Fernández-López, and Brian Soller. “Optical fiber distributed sensing-physical principles and applications”. In: *Structural Health Monitoring* 9.3 (2010), pp. 233–245.

[52] Sylvie Delepine-Lesoille et al. “Validation of TW-COTDR method for 25km distributed optical fiber sensing”. In: vol. 8794. 2013.

[53] Ryan Regier and Neil A Hoult. “Distributed strain behavior of a reinforced concrete bridge: Case study”. In: *Journal of Bridge Engineering* 19.12 (2014), p. 05014007.

[54] Andre Brault et al. “Monitoring of Beams in an RC Building during a Load Test Using Distributed Sensors”. In: *Journal of Performance of Constructed Facilities* 33.1 (2019).

[55] António Barrias et al. “Application of distributed optical fiber sensors for the health monitoring of two real structures in Barcelona”. In: *Structure and Infrastructure Engineering* 14.7 (2018), pp. 967–985.

[56] Olivier Artieres, Laurent Briançon, and Alain Robinet. “Auscultation d’ouvrages avec un capteur géotextile à fibres optiques”. In: *Sciences Eaux Territoires* 3 (2012), pp. 30–37.

[57] Jean-Marie Henault. “Approche méthodologique pour l’évaluation des performances et de la durabilité des systèmes de mesure répartie de déformation: application à un câble à fibre optique noyé dans le béton”. PhD thesis. Université Paris-Est, 2013.

[58] James Dupont. “Comportements de Capteurs à Fibres Optiques, noyés ou fixés en surface d’ouvrages en béton”. PhD thesis. Ecole des Ponts ParisTech, 2002.

[59] Sylvie Delepine-Lesoille et al. “Quasi-distributed optical fibre extensometers for continuous embedding into concrete: design and realization”. In: *Smart Materials and Structures* 15.4 (2006), p. 931.

[60] Dominik Hauswirth. “A study of the novel approaches to soil displacement monitoring using distributed fiber optic strain sensing”. PhD thesis. ETH Zurich, 2015.

[61] Hao Zhang and Zhishen Wu. “Performance Evaluation of PPP-BOTDA-Based Distributed Optical Fiber Sensors”. In: *International Journal of Distributed Sensor Networks* 8.12 (2012), p. 414692.

[62] Javier Oliver et al. “Two-dimensional modeling of material failure in reinforced concrete by means of a continuum strong discontinuity approach”. In: *Computer Methods in Applied Mechanics and Engineering* 197.5 (2008), pp. 332–348.

[63] B Gerard, HW Reinhardt, and B Breysse. “Measured transport in cracked concrete”. In: *Rilem report* 16 (1997), pp. 265–324.

[64] “Ouvrage d’art - réparation et renforcement des ouvrages en béton et en maçonnerie — traitement des fissures et protection du béton.” In: *AFNOR, NF* (1993), pp. 95–103.

[65] Yukimasa Goto. “Cracks formed in concrete around deformed tension bars”. In: *Journal Proceedings*. Vol. 68. 4. 1971, pp. 244–251.

[66] Adorjan Borosnyoi and Ivan Snobli. “Crack width variation within the concrete cover of reinforced concrete members”. In: *Epitoanyag* 3 (2010), p. 70.

[67] A Michou et al. “Reinforcement–concrete bond behavior: Experimentation in drying conditions and meso-scale modeling”. In: *Engineering Structures* 101 (2015), pp. 570–582.

[68] Ludovic Jason et al. “Cracking behavior of reinforced concrete beams: experiment and simulations on the numerical influence of the steel-concrete bond”. In: *International Journal of Fracture* 180.2 (2013), pp. 243–260.

[69] Syed Yasir Alam et al. “Use of the digital image correlation and acoustic emission technique to study the effect of structural size on cracking of reinforced concrete”. In: *Engineering Fracture Mechanics* 143 (2015), pp. 17–31.

[70] G Ruiz, M Elices, and J Planas. “Experimental study of fracture of lightly reinforced concrete beams”. In: *Materials and Structures* 31.10 (1998), pp. 683–691.

[71] A Raharinaivo et al. “Relationships between concrete deterioration and reinforcing-steel corrosion”. In: *Durability of building materials* 4.2 (1986), pp. 97–112.

[72] P Laurencet et al. “Fissuration, étancheité et durabilité des structures en béton armé”. In: *Annales du Bâtiment et des Travaux Publics*. 6. 2000.

[73] “Eurocode 2, EN 1992-1-1. October 2005: Design of concrete structures - Part 1-1: General rules and rules for buildings”. In: *Eur. Comm. Stand* (2005).

[74] William Henry Mosley, Ray Hulse, and John Henry Bungey. *Reinforced concrete design: to Eurocode 2*. Macmillan International Higher Education, 2012.

[75] JF Lataste et al. “Electrical resistivity measurement applied to cracking assessment on reinforced concrete structures in civil engineering”. In: *Ndt and E International* 36.6 (2003), pp. 383–394.

[76] OL Manzoli and PB Shing. “A general technique to embed non-uniform discontinuities into standard solid finite elements”. In: *Computers and Structures* 84.10-11 (2006), pp. 742–757.

[77] Arun Mohan and Sumathi Poobal. “Crack detection using image processing: A critical review and analysis”. In: *Alexandria Engineering Journal* 57.2 (2018), pp. 787–798.

[78] Benniu Zhang et al. “Sensitive skin and the relative sensing system for real-time surface monitoring of crack in civil infrastructure”. In: *Journal of intelligent material systems and structures* 17.10 (2006), pp. 907–917.

[79] Benniu Zhang et al. “Online bridge crack monitoring with smart film”. In: *The Scientific World Journal* 2013 (2013).

[80] M A Caminero et al. “Damage monitoring and analysis of composite laminates with an open hole and adhesively bonded repairs using digital image correlation”. In: *Composites Part B: Engineering* 53 (2013), pp. 76–91.

[81] Simon Rouchier et al. “Damage monitoring in fibre reinforced mortar by combined digital image correlation and acoustic emission”. In: *Construction and Building Materials* 38 (2013), pp. 371–380.

[82] Syed Yasir Alam. “Experimental study and numerical analysis of crack opening in concrete”. PhD thesis. Ecoles centrale de Nantes, 2011.

[83] Rashid Hameed. “Apport d’un Renfort de Fibres sur les Performances des Structures en Béton Armé pour les Applications Parasismiques”. PhD thesis. Université Toulouse III-Paul Sabatier, 2010.

[84] Michael A Sutton et al. “Determination of displacements using an improved digital correlation method”. In: *Image and vision computing* 1.3 (1983), pp. 133–139.

[85] David Corr et al. “Digital image correlation analysis of interfacial debonding properties and fracture behavior in concrete”. In: *Engineering Fracture Mechanics* 74.1-2 (2007), pp. 109–121.

[86] S Choi and SP Shah. “Measurement of deformations on concrete subjected to compression using image correlation”. In: *Experimental mechanics* 37.3 (1997), pp. 307–313.

[87] Karl F Voss and Keith H Wanser. “Fiber sensors for monitoring structural strain and cracks”. In: *Second European Conference on Smart Structures and Materials*. Vol. 2361. International Society for Optics and Photonics. 1994, pp. 144–147.

[88] Christopher KY Leung, Xinyang Wang, and Noah Olson. “Debonding and calibration shift of optical fiber sensors in concrete”. In: *Journal of engineering mechanics* 126.3 (2000), pp. 300–307.

[89] Noah Olson, Christopher KY Leung, and Aidong Meng. “Crack sensing with a multimode fiber: experimental and theoretical studies”. In: *Sensors and Actuators A: Physical* 118.2 (2005), pp. 268–277.

[90] Kai Tai Wan and Christopher KY Leung. “Applications of a distributed fiber optic crack sensor for concrete structures”. In: *Sensors and Actuators A: Physical* 135.2 (2007), pp. 458–464.

[91] TengFei Bao, JiaLin Wang, and Yuan Yao. “A fiber optic sensor for detecting and monitoring cracks in concrete structures”. In: *China Technological Sciences* 53.11 (2010), pp. 3045–3050.

[92] HaoWu Liu et al. “Theoretical analysis and experiment of micromechanics and mechanics-optics coupling of distributed optic-fiber crack sensing”. In: *Science China Technological Sciences* 54.1 (2011), pp. 185–191.

[93] Assaf Klar and Raphael Linker. “Feasibility study of automated detection of tunnel excavation by Brillouin optical time domain reflectometry”. In: *Tunnelling and Underground Space Technology* 25.5 (2010), pp. 575–586.

[94] Xin Feng et al. “Theoretical and experimental investigations into crack detection with BOTDR-distributed fiber optic sensors”. In: *Journal of Engineering Mechanics* 139.12 (2013), pp. 1797–1807.

[95] Xiaoyi Bao and Liang Chen. “Recent progress in Brillouin scattering based fiber sensors”. In: *Sensors* 11.4 (2011), pp. 4152–4187.

[96] Michio Imai et al. “Crack detection application for fiber reinforced concrete using BOCDA-based optical fiber strain sensor”. In: *Journal of structural engineering* 136.8 (2010), pp. 1001–1008.

[97] Michio Imai and Maria Feng. “Sensing optical fiber installation study for crack identification using a stimulated Brillouin-based strain sensor”. In: *Structural Health Monitoring* (2012), pp. 501–509.

[98] Hao Zhang and Zhishen Wu. “Performance Evaluation of BOTDR-based Distributed Fiber Optic Sensors for Crack Monitoring”. In: *Structural Health Monitoring* 7.2 (2008), pp. 143–156.

[99] J Casas, Sergi Villalba, and Vicens Villalba. “Management and safety of existing concrete structures via optical fiber distributed sensing”. In: *Maintenance and Safety of Aging Infrastructure: Structures and Infrastructures book Series; CRC Press: Boca Raton, FL, USA* 10 (2014), pp. 217–245.

[100] Antoine Bassil et al. “Distributed fiber optics sensing and coda wave interferometry techniques for damage monitoring in concrete structures”. In: *Sensors* 19.2 (2019), p. 356.

[101] Gerardo Rodriguez, Joan Ramon Casas, and Sergi Villalba. “Assessing Cracking Characteristics of Concrete Structures by Distributed Optical Fiber and Non-Linear Finite Element Modelling”. In: *EWSHM - 7th European Workshop on Structural Health Monitoring*. Ed. by Vincent Le Cam, Laurent Mevel, and Franck Schoefs. IFSTTAR, Inria, Université de Nantes. Nantes, France, July 2014.

[102] Gerardo Rodríguez, Joan R. Casas, and Sergi Villaba. “Cracking assessment in concrete structures by distributed optical fiber”. en. In: *Smart Materials and Structures* 24.3 (2015), p. 035005.

[103] Andre Brault and Neil Hoult. “Monitoring Reinforced Concrete Serviceability Performance Using Fiber-Optic Sensors”. In: *ACI Structural Journal* 116.1 (2019), p. 57.

[104] Oliver Fischer, Sebastian Thoma, and Simone Crepaz. “Quasicontinuous Fiber Optic Strain Measurement for Crack Detection in Concrete Structures”. In: *concrete and reinforced concrete construction* 114.3 (2019), pp. 150–159.

[105] Rafal Sienko et al. “Strain and crack analysis within concrete members using distributed fibre optic sensors”. In: *Structural Health Monitoring* 18.5-6 (2018), pp. 1510–1526.

[106] YL Beck et al. “Distributed measurements with optical sensors in the EDF group: experience feedback and perspectives”. In: *Proceedings of the International Conference on Smart Infrastructure and Construction, June, Cambridge, UK*. 2016, pp. 3–8.

[107] Neil A Hoult, Omurden Ekim, and Ryan Regier. “Damage/deterioration detection for steel structures using distributed fiber optic strain sensors”. In: *Journal of Engineering Mechanics* 140.12 (2014), p. 04014097.

[108] JM Henault et al. “Analysis of the strain transfer mechanism between a truly distributed optical fiber sensor and the surrounding medium”. In: *3rd International Conference on Concrete Repair, Rehabilitation and Retrofitting, ICCRRR-3*. CRC Press. 2012, p. 266.

[109] Astrid Billon et al. “Qualification of a distributed optical fiber sensor bonded to the surface of a concrete structure: a methodology to obtain quantitative strain measurements”. In: *Smart Materials and Structures* 24.11 (2015), p. 115001.

[110] Ji-long Li, Zhi Zhou, and Jin-ping Ou. “Interface transferring mechanism and error modification of embedded FBG strain sensor based on creep: Part I. linear viscoelasticity”. In: *Smart Structures and Materials*. International Society for Optics and Photonics. 2005, pp. 1061–1072.

[111] Guang-dong Zhou et al. “Influencing parameters analysis of strain transfer in optic fiber bragg grating sensors”. In: *Nondestructive Evaulation for Health Monitoring and Diagnostics*. International Society for Optics and Photonics. 2006.

[112] Ramzyzan Ramly, Wahyu Kuntjoro, and Mohd Kamil Abd Rahman. “Using embedded fiber Bragg grating (FBG) sensors in smart aircraft structure materials”. In: *Procedia Engineering* 41 (2012), pp. 600–606.

[113] G Pereira et al. “On the improvement of strain measurements with FBG sensors embedded in unidirectional composites”. In: *Polymer Testing* 32.1 (2013), pp. 99–105.

[114] YM Gebremichael et al. “Integration and assessment of fibre Bragg grating sensors in an all-fibre reinforced polymer composite road bridge”. In: *Sensors and Actuators A: Physical* 118.1 (2005), pp. 78–85.

[115] Li Sun et al. “Strain Transfer Analysis of Embedded Fiber Bragg Grating Strain Sensor”. In: *Journal of Testing and Evaluation* 44.6 (2015).

[116] Sham-Tsong Shiue et al. “The effect of polymeric coatings on the static fatigue of tightly jacketed double-coated optical fibers”. In: *Materials chemistry and physics* 83.2 (2004), pp. 239–244.

[117] Sham-Tsong Shiue and Ting-Ying Shen. “Effect of thermal stresses on the static fatigue of double-coated optical fibers”. In: *Materials chemistry and physics* 89.1 (2005), pp. 159–163.

[118] Haw-Long Lee, Win-Jin Chang, and Yu-Ching Yang. “Viscoelastic analysis of optical effects in double-coated optical fibers induced by axial strain and hydrostatic pressure”. In: *Materials chemistry and physics* 91.1 (2005), pp. 80–87.

[119] Zhi Zhou, Zhenzhen Wang, and Lian Shao. “Fiber-Reinforced Polymer-Packaged Optical Fiber Bragg Grating Strain Sensors for Infrastructures under Harsh Environment”. In: *Journal of Sensors* 2016 (2016).

[120] Shiuh-Chuan Her and Chang-Yu Tsai. “Experimental measurement of fiber optic strain sensors”. In: *Smart Structures and Materials 2006: Smart Sensor Monitoring Systems and Applications*. Vol. 6167. International Society for Optics and Photonics. 2006, pp. 404–415.

[121] Shiuh-Chuan Her and Chih-Ying Huang. “Effect of coating on the strain transfer of optical fiber sensors”. In: *Sensors* 11.7 (2011), pp. 6926–6941.

[122] Hai-tao Zhao et al. “Strain transfer of surface-bonded fiber Bragg grating sensors for airship envelope structural health monitoring”. In: *Journal of Zhejiang University SCIENCE A* 13.7 (2012), pp. 538–545.

[123] Daniel C Betz et al. “Advanced layout of a fiber Bragg grating strain gauge rosette”. In: *Journal of lightwave technology* 24.2 (2006), p. 1019.

[124] Kai Tai Wan, Christopher KY Leung, and Noah G Olson. “Investigation of the strain transfer for surface-attached optical fiber strain sensors”. In: *Smart Materials and Structures* 17.3 (2008), p. 035037.

[125] Jianhua Zhou, Z Zhou, and D Zhang. “Study on strain transfer characteristics of fiber Bragg grating sensors”. In: *Journal of Intelligent Material Systems and Structures* 21.11 (2010), pp. 1117–1122.

[126] Li Sun et al. “Strain Transfer Analysis of a Clamped Fiber Bragg Grating Sensor”. In: *Applied Sciences* 7.2 (Feb. 2017).

[127] Graham Duck, Guillaume Renaud, et al. “The mechanical load transfer into a distributed optical fiber sensor due to a linear strain gradient: embedded and surface bonded cases”. In: *Smart materials and structures* 8.2 (1999), p. 175.

[128] Libo Yuan, Limin Zhou, and Jingshen Wu. “Investigation of a coated optical fiber strain sensor embedded in a linear strain matrix material”. In: *Optics and lasers in engineering* 35.4 (2001), pp. 251–260.

[129] Hang-yin Ling et al. “Embedded fibre Bragg grating sensors for non-uniform strain sensing in composite structures”. In: *Measurement science and technology* 16.12 (2005), p. 2415.

[130] Rujun Wu et al. “Study on strain transfer of embedded fiber Bragg grating sensors”. In: *Optical Engineering* 53.8 (2014).

[131] Farhad Ansari and Yuan Libo. “Mechanics of bond and interface shear transfer in optical fiber sensors”. In: *Journal of engineering mechanics* 124.4 (1998), pp. 385–394.

[132] O Volkersen. “The Niektraftverteilung in Zugbeanspruchten with constants Laschenquerschritten. Aviation Research”. In: *volume* 15 (1938), pp. 41–47.

[133] Dongsheng Li et al. “Strain transferring analysis of fiber Bragg grating sensors”. In: *Optical engineering* 45.2 (2006).

[134] Dongsheng Li, Hongnan Li, and Liang Ren. “Mechanical property and strain transferring mechanism in optical fiber sensors”. In: ed. by Mohammad Yasin. INTECH Open Access Publisher, 2012. Chap. 18, pp. 439–458.

[135] Raymond M. Measures. *Structural monitoring with fiber optic technology*. Academic, 2001.

[136] Huaping Wang and Ping Xiang. “Strain transfer analysis of optical fiber based sensors embedded in an asphalt pavement structure”. In: *Measurement Science and Technology* 27.7 (2016).

[137] Graham Duck and Michel LeBlanc. “Arbitrary strain transfer from a host to an embedded fiber-optic sensor”. In: *Smart materials and structures* 9.4 (2000), p. 492.

[138] C. Wang et al. “A novel DdTS technology based on fiber optics for early leak detection in pipelines”. In: *2016 IEEE International Carnahan Conference on Security Technology (ICCST)*. Oct. 2016, pp. 1–8.

[139] Qingbin Li et al. “Elasto-plastic bonding of embedded optical fiber sensors in concrete”. In: *Journal of engineering mechanics* 128.4 (2002), pp. 471–478.

[140] Qingbin Li, Guang Li, and Guanglun Wang. “Effect of the plastic coating on strain measurement of concrete by fiber optic sensor”. In: *Measurement* 34.3 (2003), pp. 215–227.

[141] H Linsbauer and E Tschegg. “Fracture energy determination of concrete with cube-shaped specimens”. In: *Zem. beton* (1986), pp. 38–40.

[142] E. Brühwiler and F.H. Wittmann. “The wedge splitting test, a new method of performing stable fracture mechanics tests”. In: *Engineering Fracture Mechanics* 35.1 (1990), pp. 117–125.

[143] E Denarie et al. “Concrete fracture process zone characterization with fiber optics”. In: *Journal of engineering mechanics* 127.5 (2001), pp. 494–502.

[144] Sara Korte et al. “Static and fatigue fracture mechanics properties of self-compacting concrete using three-point bending tests and wedge-splitting tests”. In: *Construction and Building Materials* 57 (2014), pp. 1–8.

[145] Zhifang Zhao, Seung Hee Kwon, and Surendra P Shah. “Effect of specimen size on fracture energy and softening curve of concrete: Part I. Experiments and fracture energy”. In: *Cement and Concrete Research* 38.8-9 (2008), pp. 1049–1060.

[146] Seung Hee Kwon, Zhifang Zhao, and Surendra P Shah. “Effect of specimen size on fracture energy and softening curve of concrete: Part II. Inverse analysis and softening curve”. In: *Cement and Concrete Research* 38.8-9 (2008), pp. 1061–1069.

[147] José Pacheco et al. “Assessment of cracks in reinforced concrete by means of electrical resistance and image analysis”. In: *Construction and Building Materials* 65 (2014), pp. 417–426.

[148] Ingemar Löfgren, Henrik Stang, and John Forbes Olesen. “The WST method, a fracture mechanics test method for FRC”. In: *Materials and Structures* 41.1 (2008), pp. 197–211.

[149] M Elser, EK Tschegg, and SE Stanzl-Tschegg. “Fracture behaviour of polypropylene-fibre-reinforced concrete under biaxial loading: An experimental investigation”. In: *Composites Science and Technology* 56.8 (1996), pp. 933–945.

[150] Maissa Gharbi, Mai Lan Nguyen, and Armelle Chabot. “Experimental evaluation of the interface fracture energy for composite pavements”. In: *EATA 2017, 7th International EATA Conference*. 2017.

[151] Maissa Gharbi et al. “Characterization of the bond between asphalt layers and glass grid layer with help of a Wedge Splitting Test”. In: 2017.

[152] Maissa Gharbi, Mai Nguyen, Armelle Chabot, et al. “Characterization of debonding at the interface between layers of heterogeneous materials coming from roads”. In: *Congres francais de mécanique*. AFM, Association Francaise de Mécanique. 2017.

[153] Eugen Brühwiler. “Bruchmechanik von Staumauerbeton unter quasi-statischer und erdbebendynamischer Belastung”. PhD thesis. EPFL, 1988.

[154] EK Tschegg. “New equipments for fracture tests on concrete”. In: *Materialprüfung* 33.11/12 (1991), pp. 338–342.

[155] B Trunk. “Experimental investigation into the size dependence of fracture mechanics parameters”. In: *Proc. 3rd Int. Conf. Fracture Mechanics Concrete Structures*. Vol. 3. 1998, pp. 1937–1948.

[156] B Hillemeier and HK Hilsdorf. “Fracture mechanics studies on concrete compounds”. In: *Cement and Concrete Research* 7.5 (1977), pp. 523–535.

[157] Matthew Gerber et al. “Strain transfer for optimal performance of sensing sheet”. In: *Sensors* 18.6 (2018), p. 1907.

[158] ACI 408 Committee et al. “Bond and development of straight reinforcing bars in tension (ACI 408R-03)”. In: *American Concrete Institute, Detroit, Michigan, US* (2003), p. 49.

[159] Libo Yuan and Limin Zhou. “Sensitivity coefficient evaluation of an embedded fiber-optic strain sensor”. In: *Sensors and Actuators A: Physical* 69.1 (1998), pp. 5–11.

[160] T. Planès and E. Larose. “A review of ultrasonic Coda Wave Interferometry in concrete”. In: *Cement and Concrete Research* 53 (2013), pp. 248–255.

[161] Ernst Niederleithinger et al. “Processing Ultrasonic Data by Coda Wave Interferometry to Monitor Load Tests of Concrete Beams”. In: *Sensors* 18.6 (2018).

[162] Ernst Niederleithinger et al. “Embedded ultrasonic transducers for active and passive concrete monitoring.” In: *Sensors (Basel, Switzerland)* 15 (2015), pp. 9756–9772.

[163] Xin Wang and Ernst Niederleithinger. “Coda Wave Interferometry used to detect loads and cracks in a concrete structure under field conditions”. In: *EWSHM 2018, The 9th European Workshop on Structural Health Monitoring Series, Manchester, England, 10-13 June, 2018*, pp. 10–13.

[164] C. Sens-Schönfelder and U. Wegler. “Passive image interferometry and seasonal variations of seismic velocities at Merapi Volcano, Indonesia”. In: *Geophysical Research Letters* 33.21 (2006).

[165] Junjie Wang et al. “Influence of service loading and the resulting micro-cracks on chloride resistance of concrete”. In: *Construction and Building Materials* 108 (2016), pp. 56–66.

[166] Junjie Wang et al. “Influence of micro and macro cracks due to sustained loading on chloride-induced corrosion of reinforced concrete beams”. In: *4th International Conference on the Durability of Concrete Structures*. 2014.

[167] Dewei Meng, Farhad Ansari, and Xin Feng. “Detection and monitoring of surface micro-cracks by PPP-BOTDA”. EN. In: *Applied Optics* 54.16 (June 2015), pp. 4972–4978.

[168] Dewei Meng and Farhad Ansari. "Interference and differentiation of the neighboring surface microcracks in distributed sensing with PPP-BOTDA". EN. In: *Applied Optics* 55.34 (Dec. 2016), pp. 9782–9790.

[169] Michael A Sutton et al. "The effect of out-of-plane motion on 2D and 3D digital image correlation measurements". In: *Optics and Lasers in Engineering* 46.10 (2008), pp. 746–757.

[170] Lukas Wittevrongel et al. "Evaluation of methodologies for compensation of out of plane motions in a 2D digital image correlation setup". In: *Strain* 51.5 (2015), pp. 357–369.

[171] Bing Pan, Liping Yu, and Dafang Wu. "High-accuracy 2D digital image correlation measurements using low-cost imaging lenses: implementation of a generalized compensation method". In: *Measurement Science and Technology* 25.2 (2013).

[172] I Jones and ME Iadicola. "A good practices guide for digital image correlation". In: *International Digital Image Correlation Society* (2018).

UNIVERSITE
BRETAGNE SCIENCES
LOIRE POUR L'INGENIEUR

UNIVERSITÉ DE NANTES

Titre : Mesures Réparties par Fibres Optiques pour le suivi des Fissures dans les Structures en Béton

Mots clés : Fibres Optiques, Mesures Réparties, Détection, Ouverture de Fissures, Béton

Résumé : Le travail de thèse présenté dans ce mémoire vise à développer et valider une technique de suivi d’ouvertures de fissures à l'aide de mesures réparties de déformation par fibres optiques.

Dans un premier temps les différentes théories existantes sur le transfert de déformation du matériau hôte vers la fibre optique sont présentées avec leurs domaine de validité. Le problème de l’adhésion parfaite entre couche est ensuite étudié et un modèle analytique à trois couches tenant compte d’une adhésion imparfaite est élaboré. Ce modèle est ensuite généralisé aux systèmes multicouches.

Les études expérimentales validant ce nouveau modèle sont alors présentées. Elles montrent qu’il est possible de suivre les ouvertures de fissures jusqu’à 1000 µm avec une erreur inférieure à 10% avec un câble à fibre optique collé en surface. Les câbles noyés dans le béton donnent des résultats moins justes. La justesse des mesures est aussi influencée par le type de câble, la longueur d’ancrage et le durcissement du béton.

Enfin, les résultats des études de cas sur des échantillons en béton armé de laboratoire sont présentés. Elles montrent la capacité des fibres à détecter des fissures aussi précocement que les capteurs acoustiques à ultrasons et de surveiller l’ouverture de micro fissures multiples.

Title : Distributed Fiber Optics Sensing for Crack Monitoring of Concrete structures

Keywords : Optical Fiber, Distributed Sensing, Crack detection, Crack opening, Concrete.

Abstract : This thesis work aims to develop and validate a method for monitoring crack openings using distributed fiber optics strain measurements.

First, the various existing theories on strain transfer from the host material to the optical fiber are presented, with their validity domain. The problem of perfect interfacial bonding is then studied and a three-layer analytical model capable of handling imperfect bonding case is proposed. This model is then generalized to multi-layer systems.

Experimental studies validating this new model are presented. They show that it is possible to monitor crack openings up to 1 mm with an error of less than 10% for a fiber optic cable glued on the surface. Cables embedded in concrete show less accurate results. The type of cable, the bonding length and the hardening of the concrete material also influence the accuracy of the estimated crack openings.

Finally, the results of case studies on laboratory-size reinforced concrete samples are presented. They show the optical fibers capacity to detect cracks as early as ultrasonic sensors and to monitor the opening of multiple micro cracks.